Exploiting a new catalogue of ultraluminous X-ray sources

ANGUS DUNCAN ALAN MACKENZIE

Exploiting a new catalogue of ultraluminous X-ray sources

Duncan MacKenzie

A Thesis presented for the degree of
Doctor of Philosophy

Centre for Extragalactic Astronomy
Durham University
United Kingdom
June 2024

Abstract

Ultraluminous X-ray sources (ULXs) are objects with extreme X-ray luminosities ($L_{\rm X} > 10^{39}\,{\rm erg\,s^{-1}}$) outside galaxy centres. They are now thought to be a heterogenous class of astronomical object, with individual sources powered either by sub-Eddington accretion onto intermediate mass black holes or super-Eddington accretion onto stellar mass black holes and neutron stars. We build and present a large, cleaned, multi-mission catalogue of 1843 ULX candidates in 951 different host galaxies. Comparing with former, concurrent and subsequent ULX catalogues, it is the largest ULX catalogue ever compiled at the time of publication. While some catalogues published since are larger, our candidates are more likely to be reliable due to our use of stricter constraints during assembly. Having utilised data from three distinct X-ray missions, we reveal 689 new ULX candidates, one of which we present in detail and 71 HLX candidates which we explore as a sub-population of the ULX class. Further cleaning to remove our HLX sub-sample of interlopers leaves 37 good HLX candidates, which we then whittle down to the 20 best candidates. We compare these to two well-established members of the HLX class, an intermediate mass black hole and a pulsating source, as potential archetypes of the wider population. Our findings instead indicate that they are perhaps at the extremeties of a highly heterogeneous class and while some of our HLX candidates are found to be comparable, the majority of our sources fall somewhere in between or carve out their own portion of parameter space. Finally, we present the findings from two successful observing proposals targeting a ULX candidate identified both within our catalogue and the all-sky surveys from the *eROSITA* mission. We explore the source's validity as a ULX candidate, search for the presence of a neutron star accretor and the possible existence of a surrounding bubble nebula.

Declaration

The work in this thesis is based on research carried out at the Centre for Extragalactic Astronomy, Durham University as the author was a research student under the supervision of Prof. Timothy Roberts between 2019 and 2024. No part of this thesis has been submitted elsewhere for any other degree or qualification and it is all my own work unless referenced to the contrary in the text. Portions of this work have appeared in the following papers:

- Chapter 2 and the subsection on ULXs in Chapter 1: Walton et al. (2022)

The author carried out the work in this thesis with the following exceptions: (1) Dom Walton was project lead on the multi-mission catalogue of ULXs in Chapter 2 and lead author of the published paper. (2) Dom Walton assembled the galaxy catalogue. (3) Harry Gully constructed the *Swift* portion of the multi-mission catalogue. (4) Nency Patel was responsible for the initial *XMM-Newton* ULX catalogue. The author also contributed to the following works:

- Roberts et al. (2023) - (*Chapter 4*) - Digging a little deeper: characterizing three new extreme ULX candidates. MNRAS, Volume 525, Issue 3

- MacKenzie et al. (2023) - (*Chapter 3*) - The hyperluminous X-ray source population. Astronomische Nachrichten, Volume 344, Issue 4

Acknowledgements

To Aurélie, my wife. Just that alone shows how much has happened in these four years. You're one of the greatest things to ever happen to me. You have changed the rhythm of my life forever and this couldn't have been done without you. You continue to vex me, perplex me, delight and amaze me. When I look back in the years ahead, it won't be with thoughts of science or pandemics, these four years will be the moment in my life when I fell in love with you and asked you to marry me.

To my supervisor, Tim, without whom this wouldn't have been written at all. You were firm and fair in equal measure as needed. Your teachings, critiques, positive remarks and corrections have made me a better scientist and a better writer. I will take the best of those lessons onward with me wherever I go. Thank you for all the opportunities you helped me secure, from conferences, external collaborations and observing proposals. No two PhDs are the same, no doubt they all end up as a bit of a wild ride, but we saw it through in a global age that really felt like no other.

To my family, Tasha & Rob & Finlay, you are the foundation for all that I do. Mum and Dad, each and every achievement, accomplishment and all that I am can be traced back to my start and that's you. I can only continue to move forward and take upward leaps of faith knowing I have a solid footing and your loving support. Fin, as closest kin we are often of one wavelength - our tastes so frequently the same, of course sometimes they differ, but through wit and wile and guts and guile there is nothing we cannot do. Just by being yourself you inspire me to greatness. Thanks to you three for always standing with me.

To my officemates across the years, the best remedy for the trials of a long road is good company. Ugnė, Tom, Alice, Cameron and Suttikoon our time together probably only got us as far as the garden fence before the world turned upon its head, but I could not have asked for a better start. The first strides set the pace, those first steps set the tone. Thanks to my interim office, Sergio, Will, Victor and visitors from far reaches of the globe in Blessing and Tenyo, as we all tried to figure out what it meant to be back on the road. Finally, to Nency, Victor (again - what a mistake that was!) and Marcus... the ground we have covered is immense. From

the “Southern Bangladeshian Steppes” (metaphysically) to personal balconies, from coffee trips to whiteboard adventures we have seen and said it all. The science may be a given, but we brought the magic. I am not entirely convinced that a greater group of workplace colleagues/comrades/friends shall ever exist again. Thank you for helping me keep things chaotic.

To friends, Conor (with such wonderful news just recently) and Emmy (an honourary office member really) - for always being able to keep up with me when we needed to nerd out.

To so many great people around the department, Raj, Jack, Vicky, the Joaquins, Scott, Shaun and Sunny to name but a few. To staff volleyball, my physical health and sanity saver - sometimes you’ve just got to get up and vent - Matt, Phil, Craig, Holly, Megan, Seb, Stacy and anyone else who has ever joined us for a session. To external collaborators and staff keeping an eye on things at home and abroad. Dom and Matt for telling ghost stories about my supervisor. Chris’ last minute thesis advice meeting by stroke of fortune. My fellow peripheral physicists from before now that brought me here, Josh, Ben, Dominik etc. content to skirt around the edge, always ready to tango with the material and cast it away as appropriate.

Thank you all.

Contents

Dedication

To all those that feel lost.
Let not the wants and will of others steer the needle of your compass.
You will find your path again in the end.
And you shall know yourself all the more, for having been lost in the first place.

To acquire knowledge, one must study;
but to acquire wisdom, one must observe.

- Marilyn vos Savant

CHAPTER 1

Introduction

The work in this thesis primarily looks to improve our understanding of a class of astronomical objects, the ultraluminous X-ray sources (ULXs; see also Kaaret et al. 2017 and King et al. (2023) for full reviews). ULXs are bright X-ray sources, predominantly observed in other galaxies, which consist of a compact object, likely a black hole or neutron star, in a binary system with a non-degenerate stellar counterpart. As the pair orbit their common centre of mass, material from the companion star is accreted onto the neutron star or black hole through the first Lagrange point. The change in the material's gravitational potential energy is predominantly released in the form of high energy, X-ray photons. However, their characteristically extreme luminosities at X-ray wavelengths suggests ULXs are accreting matter at rates above the theoretical upper limit for accretion onto a stellar-mass compact object. This makes them very physically interesting objects.

We begin this introduction with an overview of the field of X-ray astronomy (Section 1.1), then introduce the instrumentation involved in observing and detecting astronomical objects at X-ray wavelengths (Section 1.2). We do this because there is little science without the history and observatories that make it possible. We then trace the photons back to their origin, discussing the physical processes

in accreting objects (Section 1.3), ending with an overview of what is known about ULXs and super-Eddington accretion (Section 1.4).

1.1 X-ray astronomy

The field of astronomy can be traced back to ancient civilisations, most notably in Egypt, Mesopotamia, Greece, Persia, India, China, and Central America. The focus of this early astronomy was mapping the positions of celestial objects, both the stars and the planets. The planets themselves appeared as bright stars but were named *planetes* or $\pi\lambda\alpha\nu\eta\tau\epsilon\sigma$ by the ancient Greeks, meaning "wanderer", given their relative motions against the background of the night sky (Pedersen 1993). From this astrometry, early cultures and civilisations found ceremonial uses, marked the passage of the seasons, determined the best time to plant crops, performed calculations for the length of the year and explored the philosophy of the Sun, Earth and Moon as a part of a vaster cosmos. However, this early astronomy only consisted of the observation of the motions of objects visible to the naked eye. Even with the invention of the first telescopes, observations were limited to optical wavelengths, where optical or visible light is defined as the range over which the human eye is sensitive ($\sim 400 - 700\,\mathrm{nm}$). There are three reasons early astronomy was limited in this way. Firstly, no knowledge of an electromagnetic spectrum which spans beyond the optical. Then, the absence of detectors working outside the visible regime - with the human eye being the only available photon detector of the time. Thirdly, the Earth's atmosphere is largely opaque to many of the other wavelengths of electromagnetic radiation (as shown in Figure 1.1).

Since X-rays cannot penetrate the atmosphere deeper than $\sim 30\,\mathrm{km}$ above sea level, X-ray astronomy was not possible until the advent of space flight. Early X-ray instruments aboard rockets were deployed with the scientific intent of studying solar X-rays, both directly from the Sun and reflected off the lunar surface. At the time it was thought that X-rays emitted from outside our Solar System would not be detectable. In 1962, Giacconi et al. (1962) did manage to observe X-ray fluorescence off the Moon's surface, however, the data was dominated by an X-ray source detected

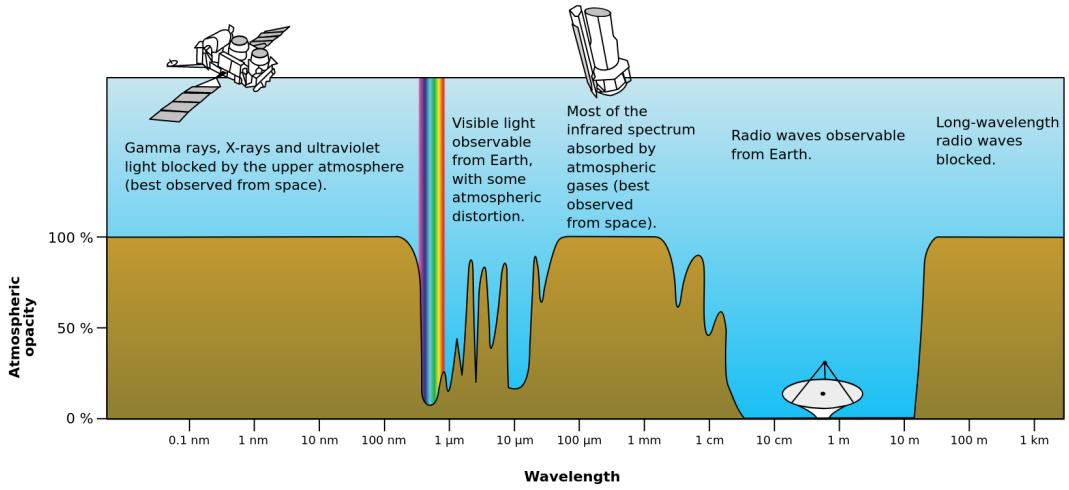

Figure 1.1: Illustration of the Earth's atmospheric opacity to different photon wavelengths across the electromagnetic spectrum. Higher energy photons, those with wavelengths narrower than 100 nm, cannot penetrate beyond the upper atmosphere. Hence, space observatories are necessary for X-ray astronomy. (Image credit: NASA).

in the Scorpius constellation, since labelled Sco X-1, and a contribution from a diffuse component spread across the sky that we now know as the X-ray background.

With the discovery of Sco X-1 a new population of astronomical sources presented itself. Over the decades that followed, missions were launched with the sole dedication of X-ray astronomy and exploring this new population (see also Bradt et al. 1992). The *Uhuru* mission (Giacconi et al. 1971), launched from Kenya in 1970, was the first to complete a scan of the sky in the 2 - 20 keV energy range. From this, Forman et al. (1978) built the first all-sky X-ray source catalogue and constructing such catalogues remains an important part of X-ray astronomy with each new mission.

Following *Uhuru* were the launches of *Ariel V* (Smith and Courtier 1976) in 1974, the *High Energy Astrophysics Observatory-1* (*HEAO-1*) in 1977 (see Fig. 1.2) and *HEAO-2* (known more colloquially as the *Einstein* telescope) in 1978 (Giacconi et al. 1979). Across the *Ariel V* and *HEAO-1* missions it was found that many X-ray sources were variable and several bright, transient sources were discovered (Wood et al. 1984). However, in the context of this thesis, the contributions of the *Einstein* observatory were of particular importance. *Einstein* was the first mission to carry an imaging X-ray telescope that used grazing incidence reflection of X-rays

by nested mirrors to focus the X-rays into an image. This was significant progress for X-ray telescopes and nested mirrors became the standard aboard the current soft, X-ray missions (see also Giacconi 2003). Furthermore, the results from the *Einstein* mission revealed a new class of non-nuclear X-ray sources in external galaxies, with greater X-ray luminosities than is typical of Galactic sources (Fabbiano, 1989). The nomenclature of this new class went through several iterations, including: extraluminous X-ray binaries (Colbert and Mushotzky 1999), superluminous X-ray sources (Roberts and Warwick 2000), and intermediate-luminosity X-ray objects (Colbert and Ptak 2002); but the title that ultimately stuck was ULXs.

The *ROSAT* mission (Truemper 1982) was launched in the early 90s and was the predecessor to the *eROSITA* mission which will be discussed as part of the next section on current X-ray telescopes. The early lifespan of *ROSAT* was dedicated to providing a novel all-sky survey, complementing and improving on the datasets from prior missions such as *Uhuru* (see Fig. 1.3). The result was a survey containing of the order 150,000 X-ray sources, massively increasing the number of detected X-ray sources three times over. This all-sky survey marked only the first phase of the *ROSAT* mission, and from the subsequent pointed observations during phase two came the assembly of ULX catalogues which identified the first samples of ULX candidates (Colbert and Mushotzky 1999; Colbert and Ptak 2002; Liu and Bregman 2005; Roberts and Warwick 2000).

1.2 The suite of current X-ray observatories

Among the current generation of X-ray telescopes, the work in this thesis focuses on data taken from *Chandra* (Weisskopf et al. 2002), *Swift* (Gehrels et al. 2004) and *XMM-Newton* (Jansen et al. 2001). There is also work undertaken as part of an external collaboration on the *eROSITA* mission (Predehl and eROSITA Consortium 2021). Beyond these, there is a further multitude of X-ray observatories, including missions such as *NuSTAR* (Harrison et al. 2013). However for the sake of a succinct narrative we only give details on those missions pertinent to this work, which are those listed above and a full list of properties can be found in Table 1.1. For those

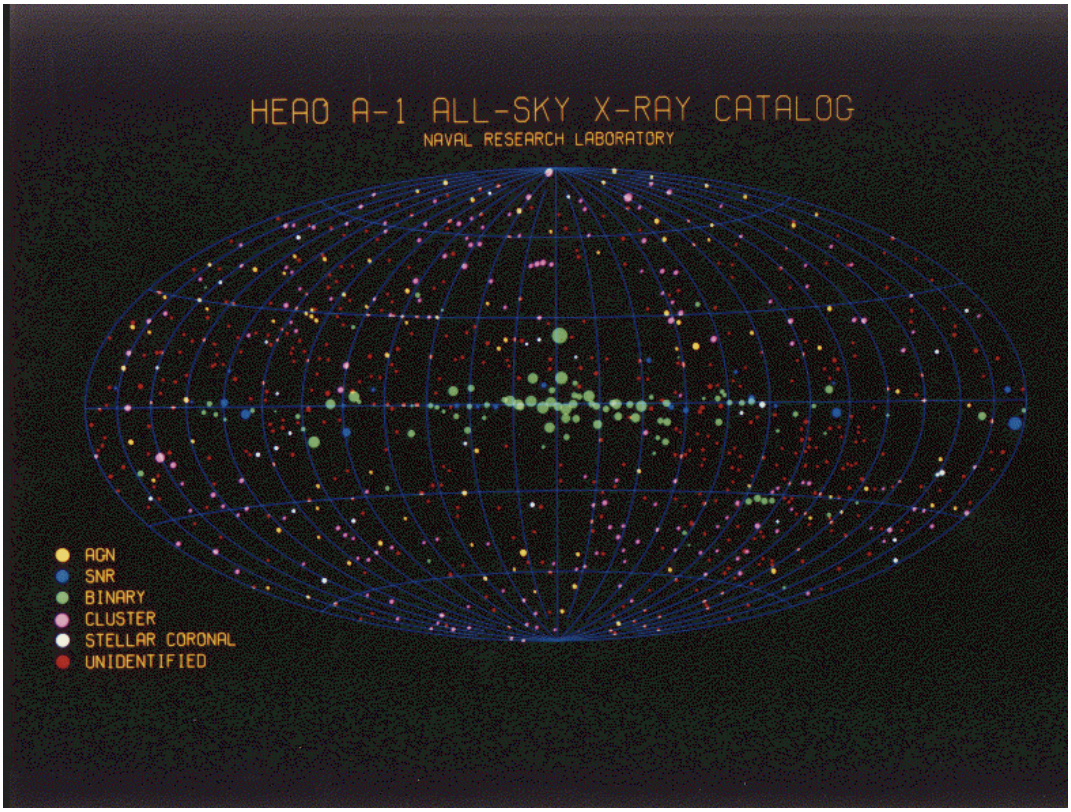

Figure 1.2: Projection depicting the sources detected as part of the *HEAO-1* all-sky survey (https://heasarc.gsfc.nasa.gov/Images/heao1/heao1.gif). The all-sky coverage was across the 0.25 - 25 keV energy range with a limiting flux of 250 nJy at 5 keV, or ∼0.25 UFU (historically 1.1 μJy at 5 keV = 1 UFU, for a Crab-like spectrum; Wood et al. 1984).

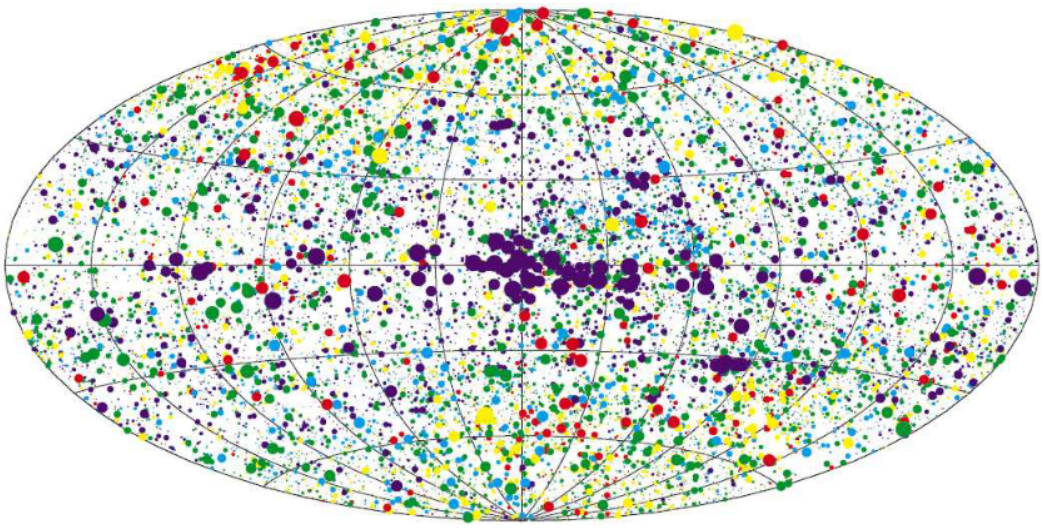

Figure 1.3: Projection of the *ROSAT* all-sky survey bright source catalogue (RASS-BSC) in the 0.1 - 2.4 keV energy range. Sensitivity extends down to a limiting count-rate of 0.05 cts s^{-1} in the 0.1-2.4 keV energy band (Voges et al. 1999). The size of the markers represents the count-rate and the colours represent different HR values: red (-1 $\leq$ HR $<$ -0.6); yellow (-0.6 $\leq$ HR $<$ -0.2); green (-0.2 $\leq$ HR $<$ 0.2); blue (0.2 $\leq$ HR $<$ 0.6) and purple (0.6 $\leq$ HR $\leq$ 1.0).

of particular interest to UK astronomy, see Pounds (2020).

1.2.1 *Chandra*

The *Chandra X-ray Observatory*, henceforth referred to as *Chandra*, is a NASA mission. Launched in 1999 under its initial title of *Advanced X-ray Astrophysics Facility* or *AXAF* (Holt 1993), *Chandra* represents the X-ray coverage within the "Great Observatories" NASA programme. It contains four instruments: the High Resolution Camera (HRC), the Advanced CCD Imaging Spectrometer (ACIS), and two high resolution spectrometers (the Low Energy and High Energy Transmission Gratings, LETG and HETG respectively). These four instruments cannot all operate simultaneously due to being on the same focal plate which is shifted according to which one is to be used. This work primarily uses the ACIS instrument (Garmire et al. 2003a), made up of two arrays of CCDs (the ACIS-I and ACIS-S), most sensitive over the energy range 0.5–8 keV. The ACIS-I array contains four CCDs and is used for imaging, and the ACIS-S array contains six CCDs that can either be used for imaging or as a read-out array for the high resolution spectrometers (see Fig. 1.4 for the layout). While its lower effective area (the characteristic of a mirror's

performance which reflects its ability to collect radiation at different photon energies) and smaller field of view make it less efficient than *XMM-Newton* for collecting data, *Chandra* has a superior angular resolution with a full-width half maximum (FWHM) of the point spread function (PSF) of 0.5 arcseconds for the ACIS instrument (Jerius et al. 2000). This makes it a powerful complement to *XMM-Newton*, with the ability to determine source positions with very high precision and to resolve sources close to one another that are blended in *XMM-Newton* observations. It also allows for better isolation of emission from a point source, with less contamination from its environment.

1.2.2 *XMM-Newton*

In 1982, prior to the 1983 launch of *EXOSAT*, *XMM-Newton's* predecessor, a proposal was generated for a "multi-mirror" X-ray telescope mission (Jansen et al. 2001). At a European Space Agency (ESA) organised workshop, held in Lyngby, Denmark, in June 1985, it was determined that high quality X-ray spectroscopy on faint sources was the next major step beyond a series of X-ray missions flown in the 1990s. This became the primary objective for the *XMM-Newton* mission. The X-ray Multi-Mirror Mission, now referred to as *XMM-Newton*, was launched at the end of 1999 by the European Space Agency. It is composed of an optical telescope and three X-ray telescopes which operate simultaneously. The three instruments aboard the *XMM-Newton* mission are the European Photon Imaging Camera (EPIC), the reflection grating spectrometer (RGS) and the optical monitor (OM). The EPIC instrument is made up of three charge-coupled device (CCD) cameras, one for each X-ray telescope, which are capable of recording the position, time and energy of each photon arrival event – data which can later be converted into images, spectra and light curves. Two of these cameras are seven-chip arrays of Metal Oxide Semiconductor CCDs, referred to as MOS1 and MOS2, which both share their telescope with one of the RGS gratings and therefore receive about 44% of the incident flux of their telescope (Turner et al. 2001). The third camera is a twelve-chip array of pn CCDs, referred to as the pn, which receives the entirety of the flux from its telescope (Strüder et al. 2001). A graphical layout of the chips for the MOS and pn cameras

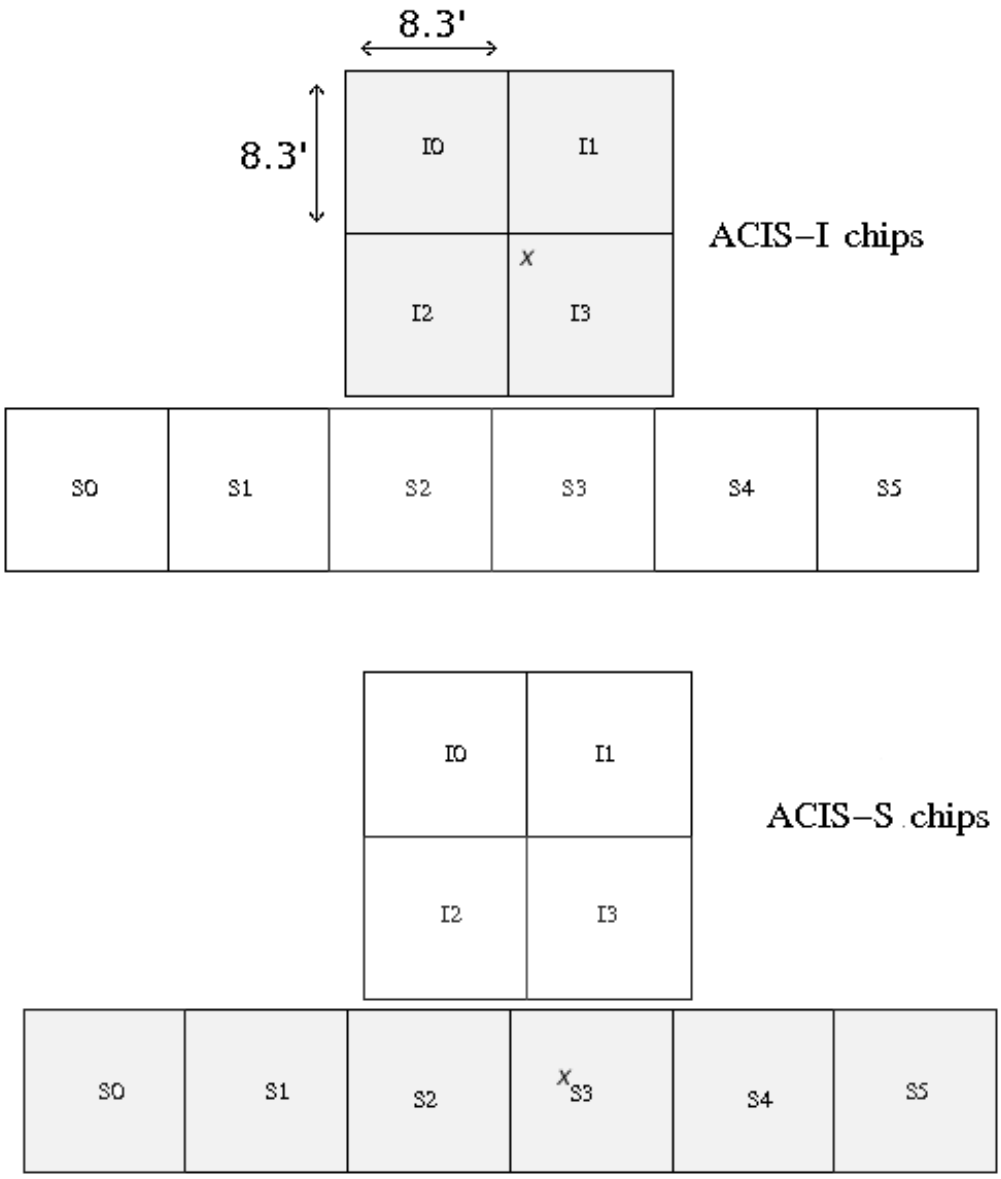

Figure 1.4: The *Chandra* ACIS-I and ACIS-S chip layout, taken from the *Chandra* Proposers' Observatory Guide. ACIS-I and ACIS- S can both be used for X-ray imaging. Only the ACIS-S chips can operate in conjunction with the HETG or LETG for high resolution spectroscopy. The default aimpoints are indicated by the **x**.

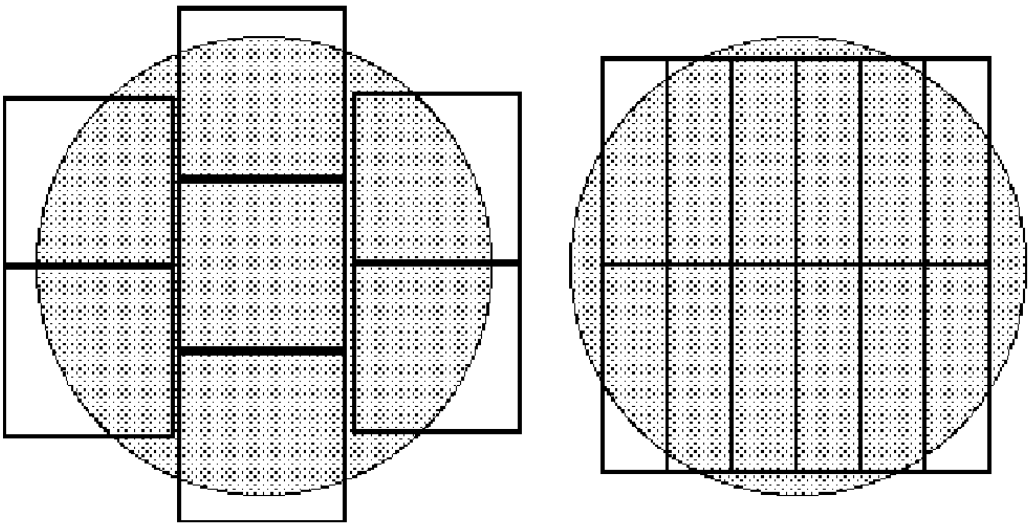

Figure 1.5: The *XMM-Newton* field of view for the EPIC-pn and EPIC-MOS cameras (taken from the *XMM-Newton* User's Handbook). Both dark circles are 30 arcminutes across and the lines depict the layouts of the chips for EPIC-MOS (left) and EPIC-pn (right).

is depicted in Fig. 1.5.

1.2.3 *Swift*

Compared to the previously discussed missions of *Chandra* and *XMM-Newton* the *Neil Gehrels Swift Observatory*, previously called the *Swift Gamma-Ray Burst Explorer* and henceforth referred to in this work as *Swift*, was proposed with a different primary objective. *Swift* is a NASA space observatory for detecting gamma-ray bursts (GRBs) and monitoring their afterglow in X-ray and UV/Visible light at the location of a burst (Gehrels et al. 2004). *Swift* is designed to have response times on the order of minutes to ensure being on target as quickly as possible and so observe the GRB afterglow. For effective multiwavelength follow-up, all three instruments comprising the *Swift* telescope payload can operate in tandem. The Burst Alert Telescope (BAT) handles the detection of the GRB themselves, computing burst positions with arcminute positional accuracy. BAT operates in the 15 - 150 keV energy range (higher energies than we're concerned with in this work) with a large field of view and high sensitivity. The UV/Optical Telescope (UVOT) is a close equivalent of the OM on-board *XMM-Newton*. This work is most concerned with

data taken from the *Swift* X-ray Telescope (XRT), which operates in the 0.3 - 10 keV energy range (Burrows et al. 2005). The *Swift* XRT has a lower effective area than *Chandra* and *XMM-Newton* and does not sit on-target for single, long-exposure observations. Instead, *Swift* takes multiple shallower, short burst observations. This makes *Swift* highly suited for long-term (on the order of months) monitoring programmes which can then trigger deeper observations from another X-ray mission. However, the nature of the short observations means few X-ray photons are collected, so faint or distant sources are not usually detected.

1.2.4 *eROSITA*

eROSITA (extended ROentgen Survey with an Imaging Telescope Array) is the primary instrument on the Spectrum-Roentgen-Gamma (SRG) mission, which was successfully launched on July 13, 2019, from the Baikonour cosmodrome. The *eROSITA* instrument consists of seven identical Wolter-1 mirror modules, each with a diameter of 360 mm, and a detector system consisting of 7 CCD cameras. Following the commissioning of the instrument and a subsequent calibration and performance verification phase, *eROSITA* started a survey of the entire sky on December 13, 2019 (Predehl and eROSITA Consortium 2021). The initial mission parameters postulated that by the end of 2023, eight complete scans of the celestial sphere would have been performed, each lasting six months. At the end of this program, the *eROSITA* all-sky survey would then be about 25 times more sensitive than the *ROSAT* All-Sky Survey in the soft X-ray band (0.2–2.3 keV), while in the hard band (2.3–8 keV) it would provide the first ever true imaging survey of the entire sky. However, ongoing geopolitical tension resulted in a suspension of the mission (beginning around March 2022) partway through its fifth all-sky scan.

Catalogues of both point-like and extended sources using the data acquired in the first six months of survey operations (eRASS1; completed June 2020) have been published (Merloni et al. 2024). These covered the half of the sky whose proprietary data rights lie with the German *eROSITA* Consortium. eRASS1 has increased the number of known X-ray sources in the published literature by more than 60% in the energy range over which it is most sensitive, 0.3-2.3 keV (Merloni et al. 2024).

The portion of the catalogue detected above this, in the harder 2.3-5 keV where *eROSITA* is less sensitive, is smaller but represents the first true imaging survey of the entire sky above 2 keV. An all-sky map of the first data release (DR1) of the *SRG/eROSITA* all-sky survey is shown in Fig. 1.6. To have complete all-sky coverage every 6 months, observations are shallow so, like *Swift*, *eROSITA* cannot usually detect faint or distant sources. However, by stacking data from eRASS1 - eRASS5 we can reach a greater sensitivity and still retain individual eRASS data to track transient sources.

A suite of publications were released alongside eRASS1, showing the impact of this data across different branches of X-ray astronomy. In our galaxy, eRASS1's coverage can map out the local interstellar medium (ISM) by 3D mapping from the X-ray absorption spectroscopy profile (Gatuzz et al. 2024b). Further afield, the intergalactic medium (IGM) can be characterised via the observed absorption in blazar spectra (Gatuzz et al. 2024a) and the warm-hot circumgalactic medium (CGM) surrounding the Milky Way is 3D mapped around the O VIII line (Locatelli et al. 2024). The all-sky coverage impacts studies from dark energy (Grandis et al. 2024), through AGN feedback in galaxy groups (Bahar et al. 2024) and down to individual point sources such as the detection of a new, supersoft, ultra-compact binary in the direction of the LMC (Maitra et al. 2024). The temporal coverage of *eROSITA* data across 4 complete all-sky surveys helps study transient phenomena, such as tidal disruption events (TDEs; Goodwin et al. 2024) and quasi-periodic eruptions (QPEs; Arcodia et al. 2024).

1.3 Accretion physics in compact objects

X-ray astronomy is a field in which astronomers are photon-starved when compared to longer wavelengths. The production of photons with such high energies requires the most extreme, violent and energy efficient mechanisms in the Universe. Primarily this is the accretion of matter onto compact objects, where the extreme gravitational potential energy of in-falling material is released as photons.

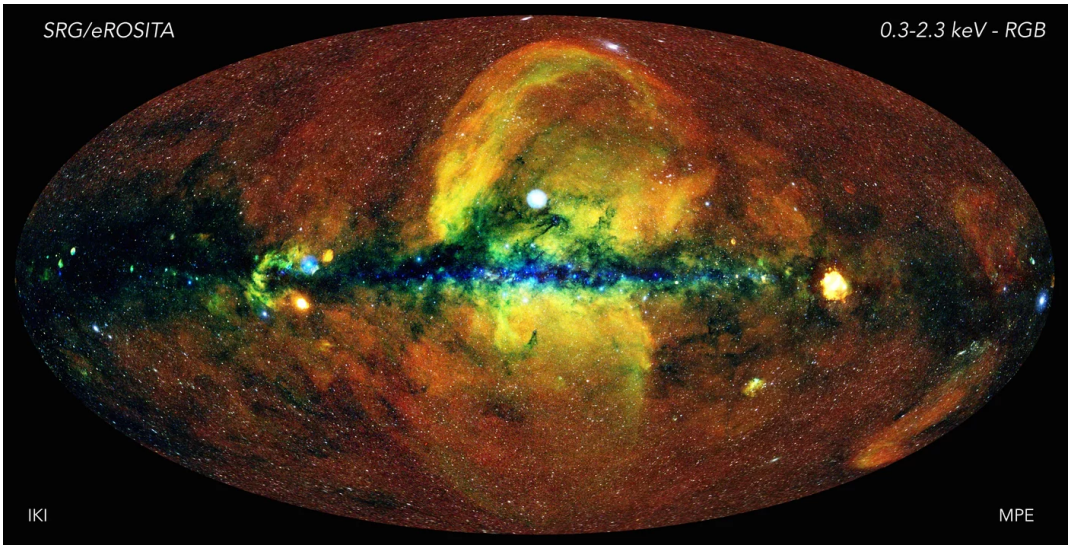

Figure 1.6: The *eROSITA* first all-sky survey (eRASS1) map in the 0.3-2.3 keV energy range (`https://www.mpe.mpg.de/7461761/news20200619`).

Table 1.1: Properties of the instruments used in this work aboard the X-ray space telescopes *XMM-Newton*, *Chandra* and *Swift*.

Instrument	FoV[a]	Energy[b] (keV)	Eff. Area[c] (cm^2) at 1 keV	Pixel Size (arcsec)
Swift XRT	23.6 × 23.6'	0.3-10	110	2.36
Chandra ACIS-I	16.9 × 16.9'	0.5-8	340	0.5
Chandra ACIS-S	8.3 × 50.3'	0.5-8	340	0.5
XMM-Newton EPIC-pn	30' radius	0.2-12	1227	4.1
XMM-Newton EPIC-MOS	30' radius	0.2-12	922	1.1

[a] The full instrument field of view.
[b] Energy range over which the instrument is most sensitive.
[c] The on-axis effective area.

1.3.1 A mathematical proof to describe the brightness of ULXs in the X-ray regime

Let us consider an element of mass m moving in a circular orbit at a radius $r + dr$ around an accreting compact object of mass M and the energy released as it moves inward to a circular orbit at radius r. The gravitational potential energy, E_g, is given by:

$$E_g = \frac{-GMm}{2r}$$

so the energy released is:

$$E = \frac{GMmdr}{2r^2}$$

For now we consider the radial dependence:

$$dE_g = \frac{GMmdr}{r^2}$$

this means the luminosity contribution produced by this annulus given a mass accretion rate of $\dot{m}$ is represented by:

$$dL = \frac{GM\dot{m}dr}{r^2}$$

and under the assumption that the annulus radiates its energy as a blackbody and obeys $L = \sigma AT^4$ where A is the surface area (which is $2\pi rdr$ for our annulus) and T is the blackbody temperature, we find a relation between temperature and our other parameters:

$$T^4 \sim \frac{M\dot{m}}{r^3}$$

This reveals a number of properties. The temperature of the accreting material increases as it moves in closer to the central accreting compact object (corresponding to a decreasing value of r). The temperature also shares a relationship to the mass of the central accreting compact object, M. If we consider general relativity and

the innermost stable circular orbit (ISCO) of a non-rotating black hole we find how r is related to M:

$$r_{ISCO} = \frac{6GM}{c^2}$$

this in turn relates to the Schwarzchild radius $r_{ISCO} = 3R_S$ but more on that in the following subsection. By substituting in for r and $\dot{m}$ we can observe how the temperature of material at the ISCO varies with the mass of the compact object:

$$T \sim M^{-\frac{1}{4}}$$

This shows that as black holes get bigger, emission from their accretion discs get cooler, all else being equal. For example, a stellar-mass black hole accreting at nearly the Eddington rate has an inner disc temperature near 10^7 K, but a supermassive 10^8 $M_\odot$ black hole accreting near Eddington has only a $\sim 10^5$ K temperature (Liu and Qiao 2022). From this, we can consider Wien's displacement law, which describes how the blackbody radiation curve for higher temperatures will peak at shorter wavelengths:

$$\lambda_{peak} = \frac{b}{T}$$

where the peak wavelength λ_{peak} is inversely proportional to the absolute temperature T and b is the Wien's displacement constant ($b \sim 2898\,\mu$m K). This shows that for a supermassive black hole the observed radiation is peaked in the ultraviolet while a stellar-mass black hole will peak in the X-ray regime.

Returning to the luminosity in a previous form:

$$L = \frac{GM\dot{m}}{r} = \frac{\dot{m}c^2 R_S}{2r} = \eta \dot{m} c^2$$

where $\eta = R_S/2r$ is the efficiency, a measure of what fraction of the accreting mass (which is equivalent to energy, $E = mc^2$) can be radiated away. For a black hole, this is the most efficient process in the Universe, with $\eta \sim 0.1 - 0.5$, depending upon the black hole spin parameter. By comparison nuclear fusion in stars has

efficiency values $\epsilon \sim 0.01$, converting around 1% of the reactant mass into energy via the mass–energy equivalency, where accretion yields above 10%.

1.3.2 Creating a neutron star or black hole

Accretion onto a degenerate, compact object first requires the death of a star. The terminology of compact and degenerate refer to an astrophysical object which has high density, its large mass is occupying a small volume, and is hence compact. In quantum physics, degeneracy describes the degree to which different states occupy the same energy. Degenerate matter is a highly dense state of fermionic matter in which the Pauli exclusion principle exerts significant pressure in addition to, or in lieu of, thermal pressure. This concept applies in astronomy to both white dwarfs (WDs) and neutron stars (NS).

WDs are the remnants of low mass ($< 8\ M_\odot$) progenitor stars that are held up against collapse by the degeneracy pressure from electrons (Mukai 2017), provided that their mass is smaller than the Chandrasekhar limit ($1.4\ M_\odot$). However, when the progenitor star has a mass greater than $8\,M_\odot$, the sheer mass of collapsing material will overcome the electron degeneracy pressure. The work in this thesis focuses on remnants formed from more massive progenitors. For the $8 < \mathrm{M} < 25$ $M_\odot$ case (Heger et al. 2003), the remnant object is extremely dense, with a final mass of 1.4–3 $M_\odot$ confined to a radius of $\sim$10 km following the collapse. In this instance, with the electron degeneracy pressure overcome, the protons undergo electron capture and form neutrons. Given their close proximity, the neutrons occupy higher energy states to avoid violating the Pauli exclusion principle and this forms the neutron degeneracy pressure which holds the core up against further collapse (Shapiro and Teukolsky 1983). This resultant object is a NS. Due to conservation of angular momentum, as the NS collapses down to a size far smaller than that of its progenitor, the collapsing material obtains a higher rotation velocity and the formed NS spins very rapidly. Initial spin periods for NS following formation are of the order 10–100 ms (Kaplan et al. 2004; Migliazzo et al. 2002). Furthermore, with the magnetic flux also conserved during the star's collapse, any moderate magnetic field present in the young, massive progenitor becomes a $10^8 - 10^{15}$ G magnetic field

for the NS (Ostriker and Gunn 1969). In a NS the spin and magnetic axes can be misaligned, resulting in radio (Hewish et al. 1968) and X-ray (Giacconi et al. 1971) pulsations as radiation is beamed along the open magnetic field lines, which can be detected in observations.

Some further forms of degenerate matter have been postulated in theory, such as quark stars (Alcock et al. 1986; Weissenborn et al. 2011) or strange stars (Haensel et al. 1986; Kettner et al. 1995). Where, under even more extreme temperature and pressure, the degeneracy pressure of the neutrons is overcome and the neutrons are forced to merge and dissolve into their constituent quarks acting freely. Individual candidates have even been proposed (Drake et al. 2002; Pons et al. 2002). Quark matter consisting of up and down quarks in a free state has a very high Fermi energy compared to ordinary atomic matter and is stable only under extreme temperatures and/or pressures. This theory suggests that the only stable quark stars will be neutron stars with a quark matter core, while quark stars consisting entirely of quark matter will be highly unstable and undergo spontaneous rearrangement (Weissenborn et al. 2011). Stars made of strange quark matter are known as strange stars, forming a distinct subtype of quark stars. Since baryonic matter is observed primarily of the lowest mass and most stable quarks, up and down, encountering the heavier quark flavours; strange, charm, bottom and top, in nature is highly uncommon. However, in theory, quark stars may also be created in the early cosmic phase separations following the Big Bang (Witten 1984). If these primordial quark stars transform into strange quark matter before the external temperature and pressure conditions of the early Universe makes them unstable, they might turn out stable and thus long-lived up to the observable present.

However, the prevailing current theory predicts that for the most massive progenitor stars, M $> 25\ M_{\odot}$, the resultant collapse moves beyond degenerate matter. The gravitational force acting on such significant mass overcomes any counteracting force due to degeneracy and continues to collapse down into an infinitely dense singularity, a black hole (BH). BHs have no surface (at least not an identifiable or observable one) and were first postulated by Einstein in his theory of general relativity (GR). The resultant spacetime curvature induced by such a massive ob-

ject is thought to be so immense that, prior to reaching any form of surface, there is a boundary condition where the escape velocity is equal to the speed of light ($c = 3 \times 10^8\,\mathrm{m\,s^{-1}}$). This boundary is defined as the event horizon.

From Einstein's GR, Karl Schwarzschild computed the event horizon for a non-spinning BH:

$$R_S = \frac{2GM}{c^2} = 2R_g$$

where G is the gravitational constant, M is the BH mass and c is the speed of light. The result was defined to be the Schwarzschild radius ($\mathrm{R_S}$), which is set to be double the gravitational radius ($\mathrm{R_g}$), and is an exact solution to Einstein's field equations (Schwarzschild 1916). As with the NS case, a BH with some non-zero value for spin is more physically realistic due to the conservation of angular momentum. Kerr (1963) found the rotating solution in which the event horizon shrinks down and a region of spacetime defined by the ergosphere is formed outside the event horizon where particles are forced to corotate with the BH.

BHs can only be defined by three parameters; mass, angular momentum (also called spin) and charge as is described in the 'no-hair theorem' (Misner et al. 1973). With so few descriptive properties, all other information carried by in-falling matter appears to be lost and a BH constitutes a highly disordered state or maximal entropy (at least under the Bekenstein bound; Bekenstein 1972). It is extremely difficult to calculate the black hole entropy based solely on statistical mechanics, which associates entropy with a large number of microstates. In fact, the 'no-hair' theorem suggests that black holes can have only a single microstate. It is only with the advent of more exotic theories exploring higher dimensions, such as string theory or loop quantum gravity, that we begin to resolve the inconsistencies. The supposed condition of maximal entropy (Bekenstein 1972) which scales with area instead of volume, has given rise to the holographic principle. The seemed destruction of information at the boundary (which violates quantum mechanics) is resolved by the advent of a firewall - a searing barrier of high energy bound at or near to the event horizon; see Almheiri et al. (2013). But, ultimately, the exact nature of BHs remains under intense, theoretical scrutiny.

However, while it seems observationally impossible to detect BHs directly due to the event horizon, their existence has been inferred indirectly by their impact on their surroundings. Two sub-populations of BHs have been found; supermassive black holes (SMBHs) with masses $\sim 10^5$-10^{10} $M_\odot$ and stellar remnant BHs, with masses ranging from M < 20 $M_\odot$ (Charles and Coe 2006) up to ~ 100 $M_\odot$ (Belczynski et al. 2010). For the latter, we adopt the naming convention of BH for the entire sub-population since they are the focus of this thesis and may thus still be differentiated from SMBHs.[1]

Following the trajectories of stars near the centre of the Milky Way revealed that they must be bound into an orbit around an unseen massive object (M $\sim 10^6$ $M_\odot$) (Ghez et al. 2005). This led to the conclusion that the central object is a SMBH. Indeed, such objects are currently thought to reside in the nucleus of all high mass galaxies. And, while BHs themselves cannot be directly observed, we can observe the accretion of matter towards the BH outside the event horizon, both in the stellar remnant and SMBH case (see following section for the former). However, two recent strides have led to the strongest observational evidence for the existence of BHs and SMBHs. Firstly, the detection of gravitational waves from a BH–BH merger (with masses 36 $M_\odot$ and 29 $M_\odot$) seen by LIGO (Abbott et al. 2016) and subsequent similar BH merger detections (Abbott et al. 2020). Second, the Event Horizon Telescope (EHT) radio image of the SMBH at the centre of the galaxy M87, constructed from radio interferometry with unprecedented angular resolution (shown in Fig. 1.7). This image captured a direct view of the shadow of a SMBH for the first time (Event Horizon Telescope Collaboration 2019).

1.3.3 Mass transfer in an accreting binary

In our universe, stars do not only exist in isolation. Often, stars can be found in binary systems and the more massive of the two stars will evolve faster. If a NS

[1] There is a third population, the intermediate mass black holes (IMBHs), existing between the two. These have been observed at the lower end of the mass range by LIGO at $\sim$150 $M_\odot$ (Abbott et al. 2020), and it is thought their masses range up to $\sim 10^4 M_\odot$, which likely occurs in the BHs at the centre of dwarf galaxies (Mezcua 2017; Moran et al. 2014).

Figure 1.7: EHT image of the M87 SMBH from observations on 2017 April 11 as a representative example of the images collected in the 2017 campaign. The ring structure is $42 \pm 3\mu$as across (Event Horizon Telescope Collaboration 2019).

or BH is formed they can accrete material from their companion star, provided the system survived the supernova explosion. These accretion systems can be divided into two sub-classes; low mass X-ray binaries (LMXBs) or high mass X-ray binaries (HMXBs) depending on the relative mass of the companion star. LMXBs typically have companion stars of $\leq 1\ M_{\odot}$ (White et al. 1995). In LMXBs the companion star fills its Roche lobe, the region where material is gravitationally bound to the star, as it evolves and mass transfer takes place as matter passes through the first Lagrange point (L1) into an accretion disc around the compact object (Tauris and van den Heuvel 2006). This mechanism is called Roche Lobe Overflow (RLOF). LMXBs are more commonly associated with old regions of galaxies where star-formation occurred in the past, leading to the presence of the low-mass (and therefore long-lived) companion (Avakyan et al. 2023). In HMXBs, typically with $M_X < M_{Opt}; M_{Opt} \leq 5\,M_{\odot}$ (Neumann et al. 2023), the accretion is usually fuelled by capture of the stellar wind that is released from the O- or B-type companion star by radiation pressure, or from the compact accretor passing through the gaseous excretion disc around a Be star. Given that more massive, hotter main sequence

stars evolve more rapidly than low mass stars, both the stars in the HMXB system are short-lived. As a result, observed HMXBs are younger than LMXBs and so are found in recent/ongoing star-forming regions of their host galaxies. A graphical representation of both LMXBs and HMXBs can be found in Fig. 1.8.

The energy distribution of X-rays (characterised by X-ray spectra) of accreting binary systems containing a BH have two components: a thermal, disc-like component and a non-thermal (power-law) component (Remillard and McClintock 2006). The presence of a surface and powerful magnetic field makes the NS case more complex (see below). The thermal component originates from the disc and is modelled as concentric annuli, each with a blackbody spectrum, summed up over the disc. The non-thermal component comes from inverse Compton scattering of the soft X-ray photons by relativistic electrons in the surrounding corona and is often modelled as a power-law (Sunyaev and Truemper 1979; Sunyaev and Titarchuk 1980). This non-thermal component can be characterised as either an advection-dominated accretion flow (ADAF) or an accretion disc corona depending the accretion rate. The occurence of an ADAF state was also referred to in the past as the quiescent state and occurs only at very low accretion rates. The theoretical Eddington limit on accretion and the ratio between an observed source luminosity and its theoretical 'maximal' luminosity (both of which are a function of mass accretion rate) given by the Eddington ratio are fully described subsequently, see Section 1.4. Various combinations of the two components give rise to four canonical sub-Eddington accretion states: the quiescent state, the low/hard state, the high/soft state, and the very high or steep power-law state. The quiescent state occurs at the lowest Eddington ratios, in this state the X-ray spectrum of the accreting binary is characterised as both faint and non-thermal, being dominated by the ADAF and thus best represented by a hard power-law (Remillard and McClintock 2006). The low/hard state is also described by a non-thermal power-law spectrum, but has an additional contribution from a cool thermal component. The low/hard state may be best understood as a truncated disc which is coupled to an inner disc corona (Done et al. 2007). X-ray spectra of the high/soft state are dominated by the thermal component. The proposed evolution from the low/hard to the high/soft state may be consistent with the

inner edge of the (formally) truncated accretion disc moving in towards the innermost stable circular orbit (ISCO), and the breaking down of the ADAF (Esin et al. 1997; Poutanen et al. 1997). Finally, the very high state corresponds to the accreting binary approaching it's Eddington limit (see following section) and exhibits significant contributions from both the thermal and non-thermal components. Physically this can be viewed as a disc carried all the way down to the ISCO and embedded within an ADAF / X-ray corona.

However, these four states do not always characterise the observed parameters in an accreting BH binary, this led to the proposition of additional intermediate states, which exhibit features from across multiple states. A graphical representation of all the states is provided in Fig. 1.9.

For a NS accretor, complications arise and we move to different (but comparable) defined accretion states. There are two broad spectral state groups in the NS case, Z sources and atoll sources. The two are classified based on their X-ray spectral and timing properties and were named after the patterns that they trace out in colour-colour diagrams (Hasinger and van der Klis 1989, see Fig. 1.10). Some atoll sources can have Z-like patterns (Gierliński and Done 2002), but the two classes remain largely distinct. Atoll sources are less luminous and have both hard and soft spectral states, while Z sources' spectra are mostly soft. Each class is then broken down into further sub-types. Z sources have three distinct branches; the horizontal (HB), normal (NB) and flaring (FB) branches. Atoll sources can occupy the island state (IS), the lower banana (LB) or upper banana (UB) branches (Linares 2009). For comparison, the NS atoll sources correspond to the low/hard and high/soft states seen in the BH accretion case (Muñoz-Darias et al. 2014). They cover a lower and larger luminosity range ($\sim$0.001–0.5 L_{Edd}) than the Z sources and are soft at high luminosities, but hard when faint. Z sources are more akin to the BH very high state, typically radiating at luminosities close to the Eddington limit, especially in the normal and flaring branches (see Fig. 1.11 for comparison). The spectra of Z sources are very soft on all three branches of the "Z" shape. NS and BH accretion states are remarkably comparable with respect to their X-ray spectra and rapid aperiodic X-ray variability.

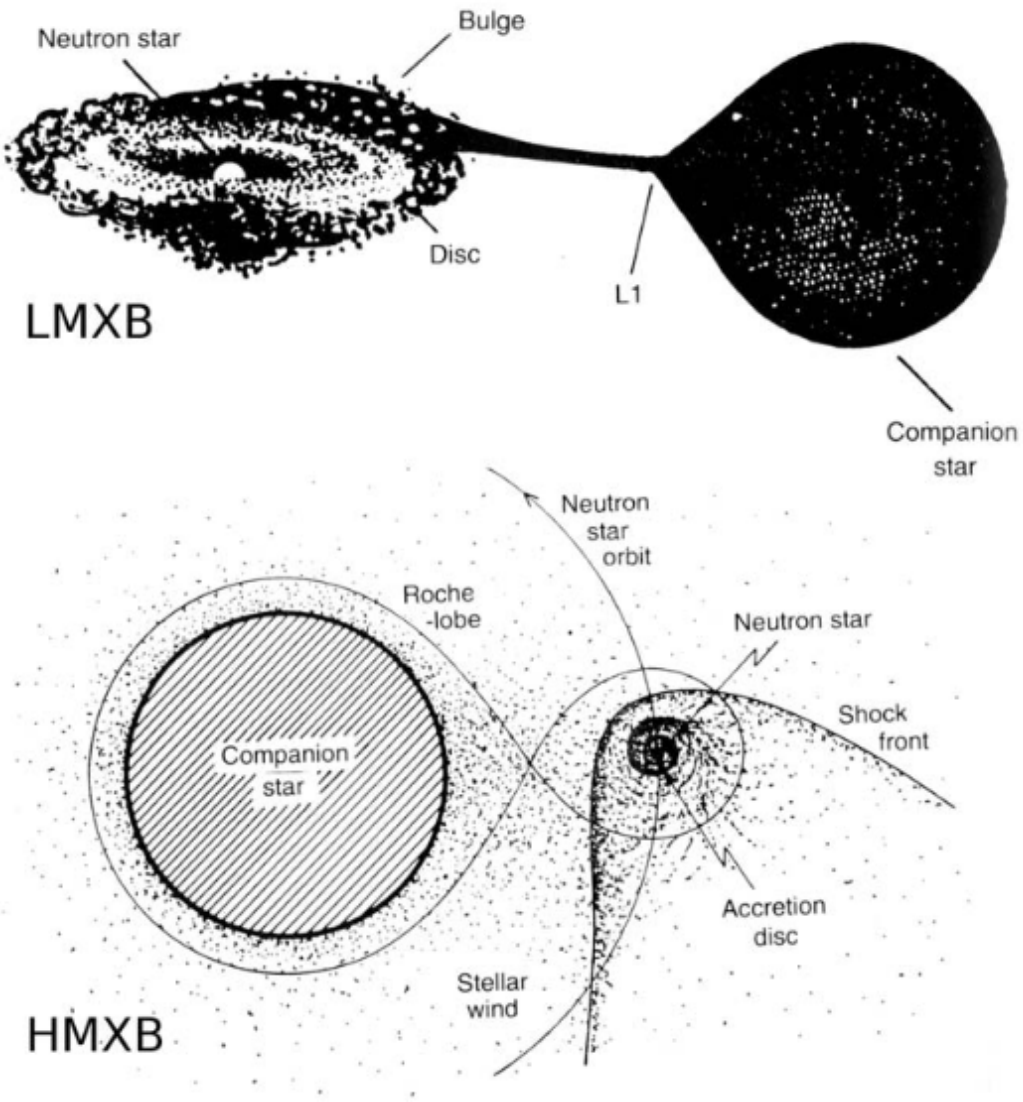

Figure 1.8: A schematic of a LMXB (top) and a HMXB (bottom) taken from Lewin and van der Klis (2006). In both instances, the compact object (labelled as NS in this case) can be a NS or BH, although in the BH case we note that the relative masses and scale of the system will be different. In the LMXB, the companion star fills its Roche lobe, causing mass transfer to occur. In the HMXB, a stellar wind is emitted from the companion star (indicated by the spots of material in the image), some of which is then captured by the compact object.

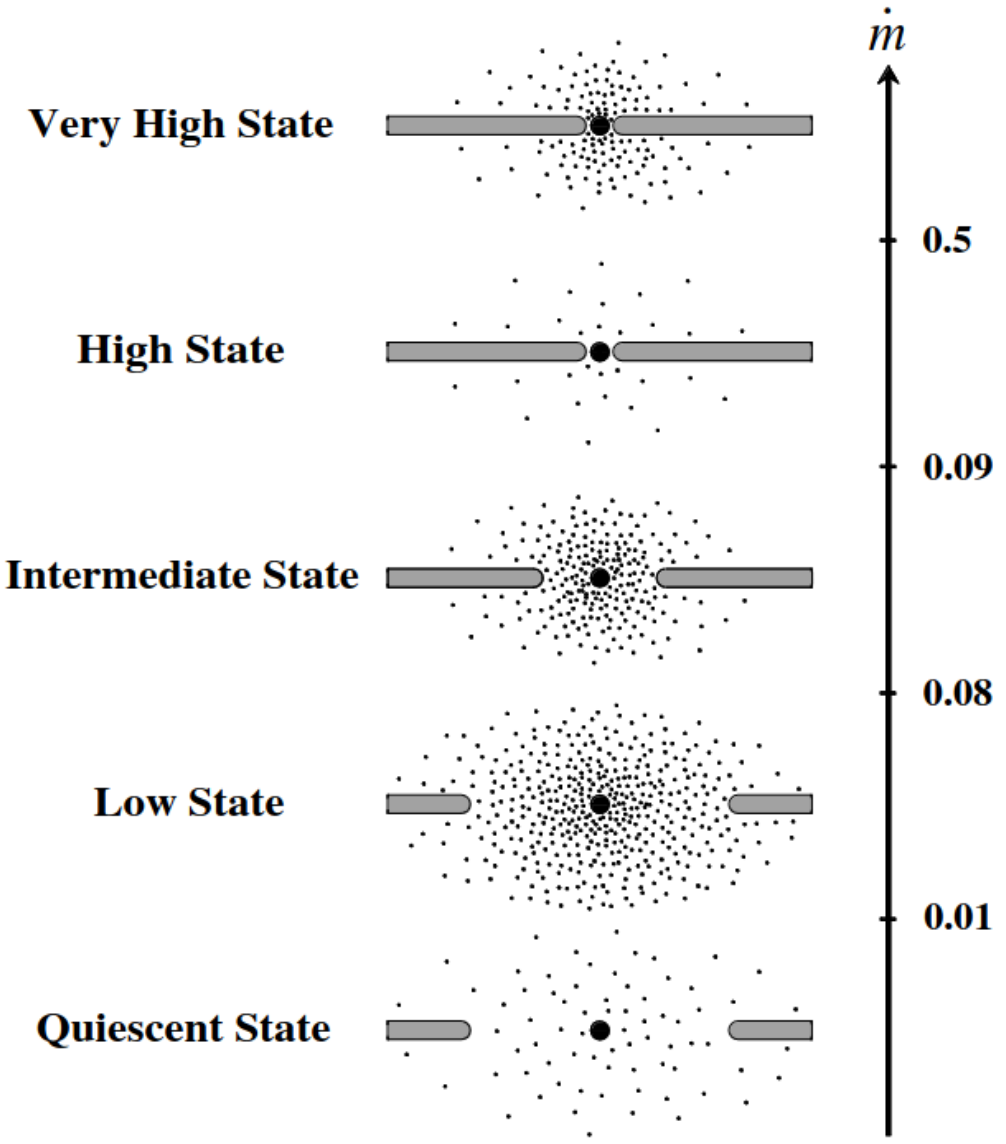

Figure 1.9: Schematic sketch of the accretion flow in different spectral states as a function of the total Eddington-scaled mass accretion rate $\dot{m}$. The ADAF/corona is represented by dots and the thin disk by the horizontal bars (Lewin and van der Klis 2006).

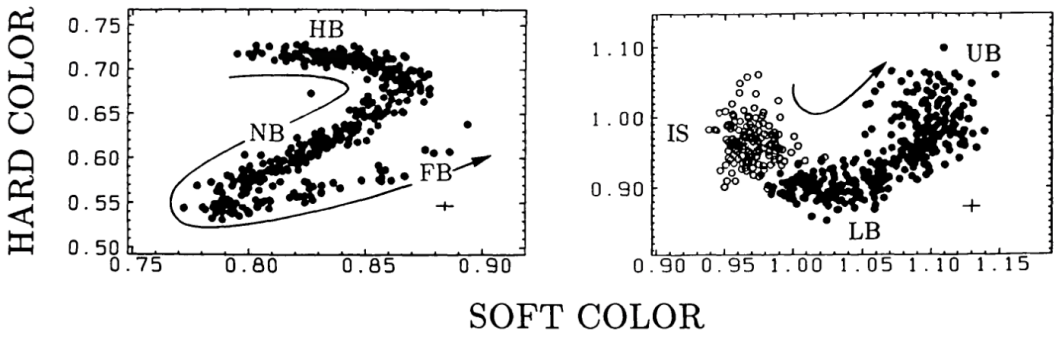

Figure 1.10: X-ray color-color diagrams of Z (left) and atoll (right) sources. The arrows in the upper diagrams indicate the direction of increasing mass accretion rate (Hasinger and van der Klis 1989).

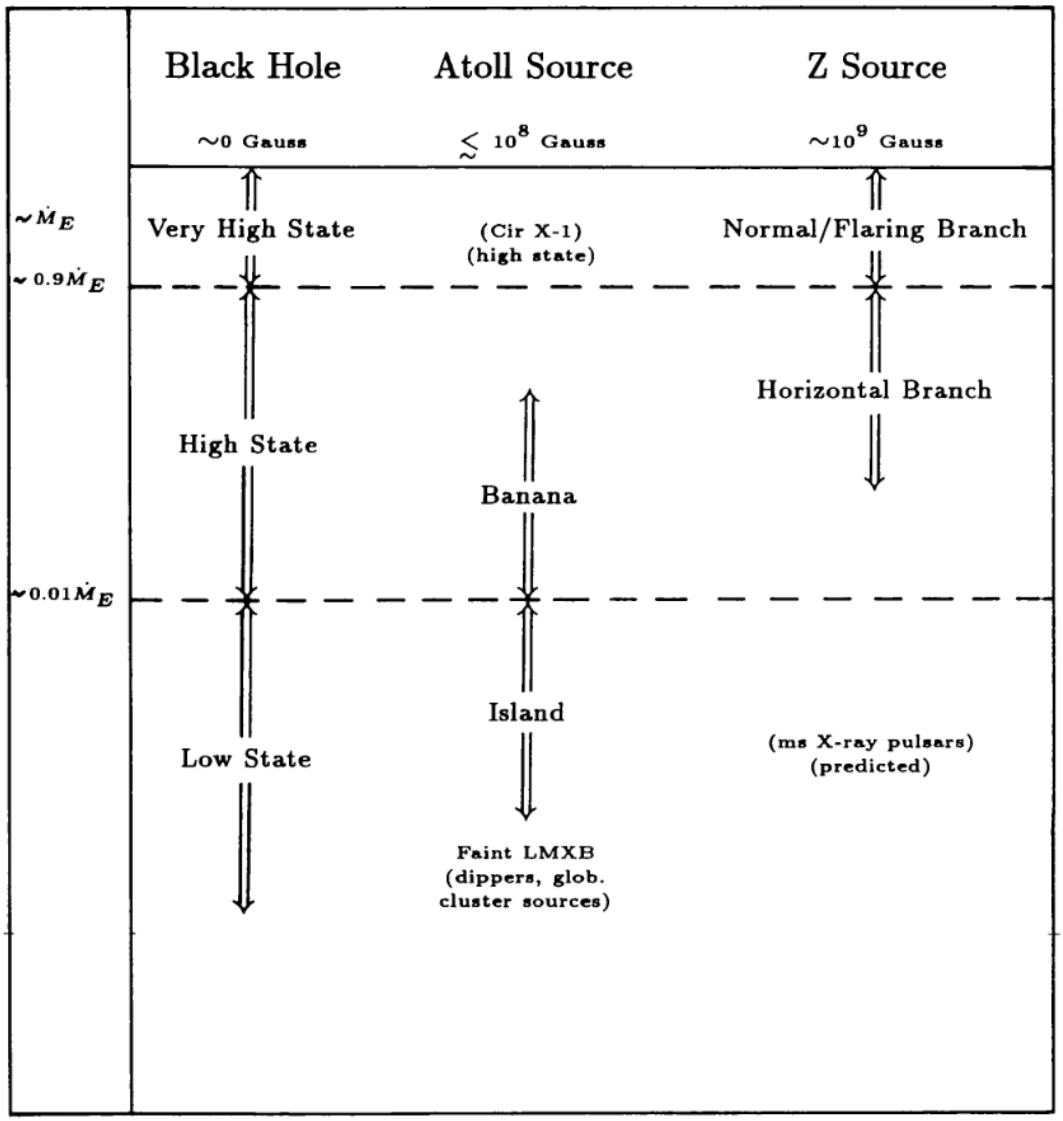

Figure 1.11: Classification of NS (both atoll and Z cases) and BH accretion states (van der Klis 1994). The mass accretion rate $\dot{M}$ is the primary determinant of which state a given source is in.

1.4 ULXs and super-Eddington accretion

Having discussed the wider physics behind accretion and mass transfer, in this section we discuss the physical theory behind the threshold which is still used to define the ULX class and how the previously defined accretion mechanisms can change above this limit.

1.4.1 The Eddington Limit

The Eddington limit is a crucial criterion in the process of accretion. It defines a theoretical upper, maximal limit on the rate at which a compact object can accrete material. This is also sometimes referred to as the Eddington luminosity, simply being the luminosity of a given source if it were to accrete at its Eddington limit. The fundamental issue lies in the fact that as material accretes it free-falls into the gravitational potential well of the compact object and thus loses gravitational potential energy. Since energy is not destroyed, this energy is released in the form of radiation (emission of photons). This radiation generates an outward pressure on the subsequent in-falling matter and surrounding material, which is acting against the gravity due to the compact object. Eddington's original calculation (which was first specified for a star) was derived assuming that the in-fall of matter is spherically symmetric about the compact object and that the accreting material was composed solely of ionised hydrogen. From this, it was determined that the radiation pressure force acting on a proton-electron pair at some distance R from the compact object was given by:

$$F_{Rad} = \frac{\sigma_T L}{4\pi c R^2}$$

where σ_T is the Thomson scattering cross section and L is the accretion luminosity[2]. Since electrons have a larger Thompson scattering cross section to photons than protons do, the electrons feel the radiation pressure more strongly. The protons then follow the movement of the electrons due to the force of electrostatic attraction

[2]Sometimes this equation also features a Q factor corresponding to the efficiency but we consider the Hyrdogen atom case and assume $Q \sim 1$.

between them. Meanwhile, the counteracting force of gravity impacts the protons more due to their greater mass (m_p):

$$F_{Grav} = \frac{GMm_p}{R^2}$$

and M is the mass of the accreting compact object. It then stands to reason that by equating these two forces, there comes a point (the proposed Eddington limit) where the outward radiation pressure is sufficiently strong to halt the accretion due to gravity. So we equate the two and rearrange for L which gives the Eddington luminosity:

$$L_{Edd} = \frac{4\pi GcMm_p}{\sigma_T}$$

While the real case will not accrete material isotropically or have accreting material composed solely of hydrogen, this theoretical limit presents a good baseline for understanding the point at which accretion onto a compact object enters the extreme and may seemingly begin to violate this rule, moving beyond the four canonical accretion states already described.

1.4.2 ULXs

Our understanding of ultraluminous X-ray sources (ULXs) – extragalactic X-ray sources with luminosities in excess of $10^{39}\,\mathrm{erg\ s^{-1}}$ (not including those associated with galaxy nuclei) – has evolved significantly over the past few years. Historically, the debate regarding the nature of these sources has focused on whether they represent a population of sub-Eddington 'intermediate mass' black holes (IMBHs with $M_{\mathrm{BH}} \sim 10^{2-5}\,M_{\odot}$; *e.g.* Colbert and Mushotzky 1999; Miller et al. 2004; Strohmayer and Mushotzky 2009) or a population of super-Eddington but otherwise normal stellar remnants (*e.g.* King et al. 2001; Middleton et al. 2015; Poutanen et al. 2007); see Kaaret et al. (2017) for a recent review. Physically, since ULXs are observed in external galaxies away from the centre of their hosts, which designates them as off-nuclear, they cannot be powered by a SMBH since such a massive object would have sunk into the host galaxy centre via dynamical friction. Although evidence

for large black holes is now being seen by LIGO (most notably the recent detection of a BH–BH merger resulting in a $\sim$150 $M_{\odot}$ remnant; Abbott et al. 2020), the general consensus is now that the majority of ULXs represent a population of super-Eddington accretors, thanks in particular to the broadband spectral and timing studies possible in the *NuSTAR* era (Harrison et al. 2013) and the high-resolution spectra and timing provided by *XMM-Newton* (Jansen et al. 2001).

As stated at the end of the previous section, the Eddington luminosity was based on the assumption of spherical accretion, so does not truly hold for the disc accretion case. For accretion disc geometry, while outgoing radiation diffuses primarily perpendicular to the disc, the matter flows inward radially, allowing an overall, observed accretion rate which exceeds the critical Eddington rate. We specify 'overall' since this can be done without violating the 'local' Eddington limit which varies as a function of radial distance from the central object and height above the plane of the disc. When a specific region of the accretion disc begins to approach the local Eddington limit, defined as occurring at the spherisation radius, the disc inflates due to the radiation pressure. This drives that portion of the disc to a larger scale height above the disc plane, causing that region to be 'puffed-up', see Fig. 1.12 (Shakura and Sunyaev 1973, Poutanen et al. 2007).

The broadband spectra obtained early in the *NuSTAR* mission demonstrated that ULX spectra are clearly distinct from standard modes of sub-Eddington accretion (*e.g.* Bachetti et al. 2013; Mukherjee et al. 2015; Rana et al. 2015; Walton et al. 2013, 2014, 2015), confirming prior indications from *XMM-Newton* (*e.g.* Gladstone et al. 2009; Stobbart et al. 2006), and instead revealed high-energy spectra consistent with broad expectations for super-Eddington accretion (*i.e.* spectra that appear to show a strong contribution from hot, luminous accretion discs, *e.g.* Abramowicz et al. 1988; Poutanen et al. 2007; Shakura and Sunyaev 1973) as shown in Fig. 1.13.8.3 $\times$ 50.3 Such spectral behaviour, unlike that seen from the sub-Eddington accretion case, could contain a supercritically accreting BH with mild geometric beaming through the funnel of a geometrically thick disc and strong radiatively driven winds (Poutanen et al. 2007). Beamed emission is non-isotropic and if the majority of emission favours the observer, by benefit of the system's inclination, can

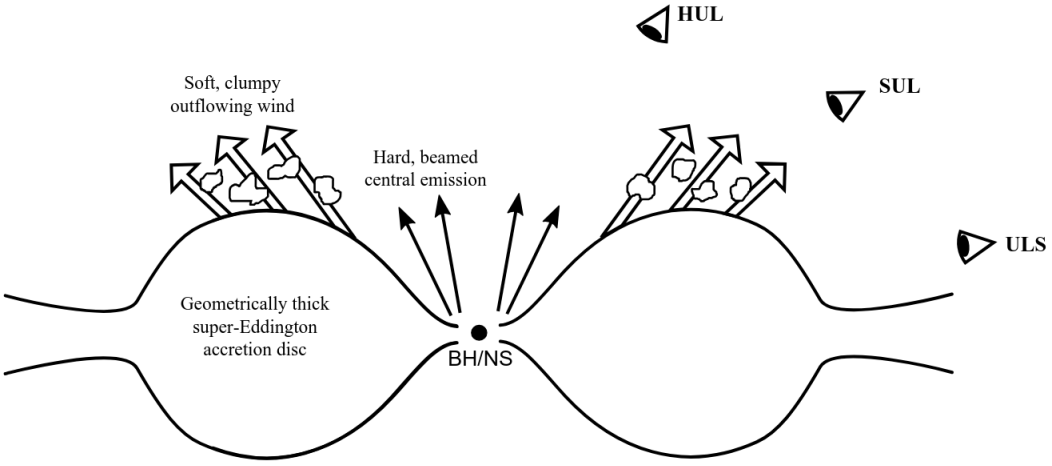

Figure 1.12: Schematic of a super-Eddington accretion state. The compact object is in the centre, surrounded by a geometrically thick accretion disc (at the spherisation radius) from which a clumpy outflowing wind is driven off. This wind manifests as any loosely bound material on its surface is ejected by radiation pressure, resulting in relativistic outflows. The eyes represent different positions of a potential observer, which we correlate to different observed spectral states.

give the appearance of a greater luminosity. This also introduces a viewing angle dependence on the observed spectral shape.

We may unify the hard and soft ultraluminous spectral states, as well as the ultraluminous supersoft regime, under a single model due to the super-Eddington, inflated accretion disc. When an observer views the ULX system from a low inclination angle (in this case - low inclination denotes face-on, *i.e.* looking down the funnel at the emission from the hot inner disc not a low inclination in-line with the plane of the disc), the spectrum is dominated by hard central emission, manifesting as the hard UL regime in Fig. 1.13. However, to an alternate observer viewing the same system at higher inclinations, the softer energy wind dominates the spectrum whilst simultaneously occulting the higher energy emission from the hot inner disc, resulting in the soft UL regime. Such a model may also extend to supersoft ULXs (SSUL in Fig. 1.13). These are characterised by a luminous and very soft black body spectrum with little to no hard emission at all. These sources may be due to observing a supercritically accreting BH system as described above at a relatively high inclination angle, labelled as ULS in Fig. 1.12, such that virtually all central emission is obscured and down-scattered through a geometrically thick disc that

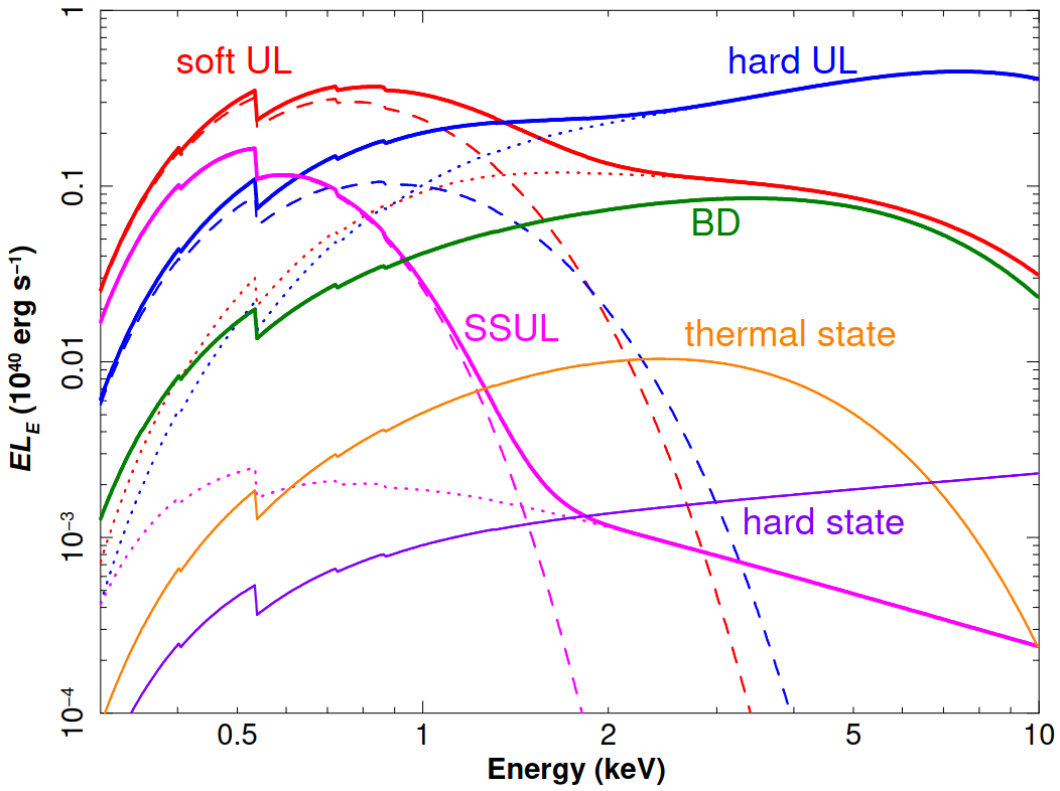

Figure 1.13: Spectra for the BH accretion states and ULX super-Eddington accretion states from Kaaret et al. (2017). The ULX states are broadened disc (BD - green), supersoft ultraluminous (SSUL - magenta) and ultraluminous (UL - red and blue). In broadened disc the ULX is accretion-disk like, but are too broad to be fitted by simple accretion disk models such as the standard multicolor disk blackbody. Supersoft ULX spectra are dominated by their cool, low energy component. Ultraluminous spectra have a soft excess and a hard component turns over at high energies. UL spectra are classified as hard (blue) versus soft (red) according to which component dominates. Disc blackbody and corona models are represented by the dashed and dotted lines respectively.

appears to completely envelope the source.

The super-Eddington nature of at least some ULXs was then spectacularly confirmed with the discovery that the ULX M82 X-2 ($L_{\rm X,peak} \sim 2 \times 10^{40}\,{\rm erg\ s^{-1}}$) is actually powered by a highly super-Eddington neutron star, following the detection of coherent X-ray pulsations (Bachetti et al. 2014). Five more ULX pulsars have since been discovered (Carpano et al. 2018; Fürst et al. 2016; Israel et al. 2017a,b; Rodríguez Castillo et al. 2020; Sathyaprakash et al. 2019b), revealing an accretion regime that extends up to $L/L_{\rm E} \sim 500$. An example of the first pulsation detection from Bachetti et al. (2014) and the power density spectrum used to identify the weak coherent pulsations found in NGC 1313 X-2 by Sathyaprakash et al. (2019b) are shown in Figs. 1.14 and 1.15 respectively. In addition to the broadband spectra and the discovery of ULX pulsars, we now have evidence in ULX data for the powerful outflows ubiquitously predicted by models of super-Eddington accretion via the detection of blueshifted atomic features (see Fig. 1.16). These have been seen primarily in the low-energy *XMM-Newton* RGS data, but also in the iron K band in a couple of cases (Kosec et al. 2018a,b; Pinto et al. 2017, 2016, 2020; Walton et al. 2016b). These outflows exhibit extreme velocities ($\sim$0.1–0.3c), implying they carry a significant additional energetic output from these already extreme X-ray binary systems.

Nevertheless, important questions still remain regarding the ULX population. Although it is now speculated that ULX pulsars could actually make up a significant fraction of these sources (*e.g.* Koliopanos et al. 2017; Pintore et al. 2017; Walton et al. 2018b), their exact contribution is still highly uncertain. Is there also a significant population of black hole ULXs, and if so could these be the progenitors of the BH–BH mergers now regularly being seen by LIGO (Inoue et al. 2016; Mondal et al. 2020)? Given the history of the field, it is easy to forget that we still do not have a single ULX with a well-constrained mass function that unambiguously requires the accretor to be a black hole. Can black hole ULXs (assuming they exist) reach the same extreme Eddington ratios as ULX pulsars, or is this somehow related to the magnetic nature of these objects (as suggested by Dall'Osso et al. 2015; Mushtukov et al. 2015)? What fraction of the total energetic output is radiative, and what

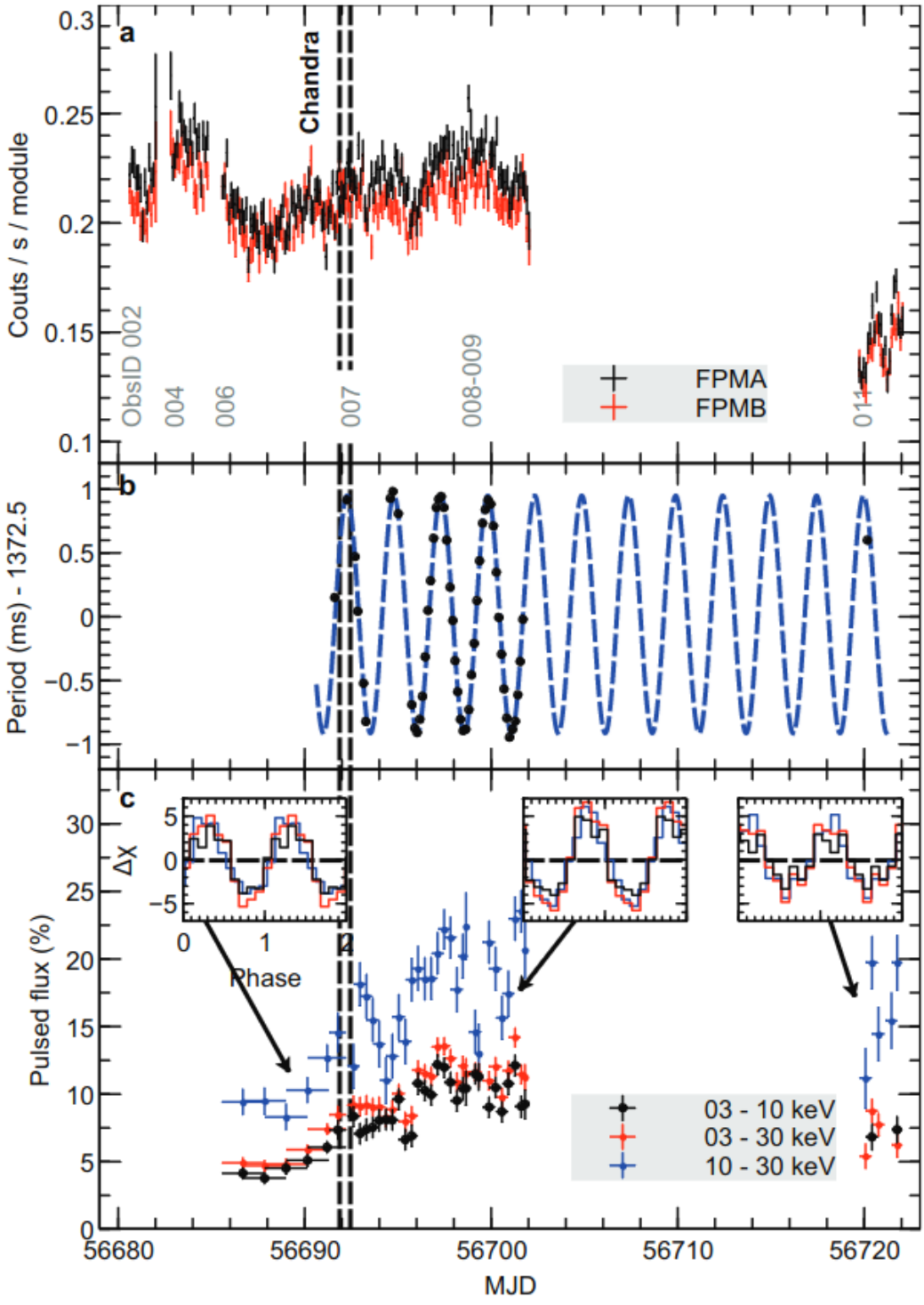

Figure 1.14: Pulsation detection in M82 X-2 from Bachetti et al. (2014). (Top): the background-subtracted 3 – 30 keV lightcurve with black and red corresponding to the count rates in each of the two *NuSTAR* telescopes (errors shown are 1σ). (Middle): detections of the pulse period (black points) and best sinusoidal fit (blue dashed line). The dashed vertical lines mark the window of coverage from an additional *Chandra* observation. (Bottom): shows the pulsed flux as a fraction of the emission from the 70 arcsec extraction region. The enhanced square inserts show the pulse profile.

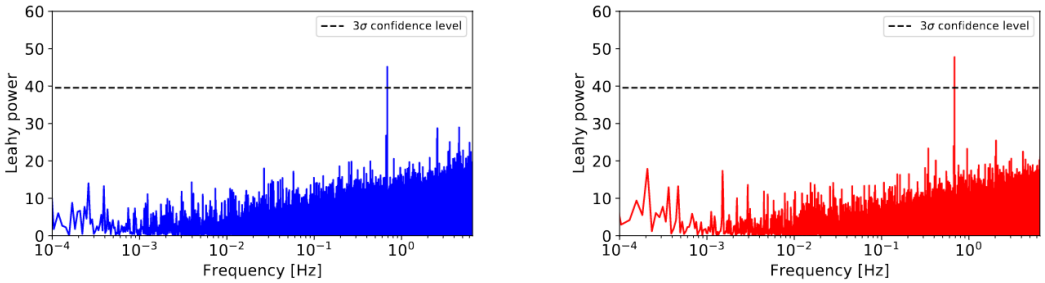

Figure 1.15: Power density spectra (corrected for acceleration) of the two *XMM-Newton* observations during which Sathyaprakash et al. (2019b) detected coherent pulsations from NGC1313 X-2. The horizontal dashed line represents the 3σ confidence level.

fraction is kinetic (*i.e.* carried by winds/outflows) at these extreme accretion rates? Understanding this last issue may in turn be critical for understanding early-universe SMBH growth (and associated feedback), given that $\sim 10^9\,M_\odot$ black holes are now being observed when the universe was only ~ 0.7 Gyr old (*e.g.* Bañados et al. 2018).

Furthermore, although the overall population is now expected to be dominated by super-Eddington accretors, there are still rare individual sources among the ULX population that remain good IMBH candidates. Most notable among these is the case of ESO 243-49 HLX-1, which reaches an astonishing luminosity of $L_{\rm X,peak} \sim 10^{42}\,{\rm erg\ s^{-1}}$ (Farrell et al. 2009). In contrast to the vast majority of the ULX population, this source does behave as expected for a scaled-up sub-Eddington X-ray binary (Servillat et al. 2011; Webb et al. 2012). Furthermore, M82 X-1 has long been thought of as an IMBH candidate because of its X-ray properties (*e.g.* Feng and Kaaret 2010; Pasham et al. 2014, although see Brightman et al. 2020b for caveats), and NGC 2276–3c has also been suggested as an IMBH candidate owing to its position on the radio–X-ray fundamental plane (Mezcua et al. 2015). Identifying further IMBH candidates remains of significant interest, given the scarcity of compelling cases among the ULX population.

1.4.3 Multiwavelength counterparts to ULXs

The optical counterparts of ULXs are generally harder to identify and characterise than Galactic sources due to their distance. Indeed, only the excellent angular resolution of the Hubble Space Telescope (*HST*) is currently able to resolve them from

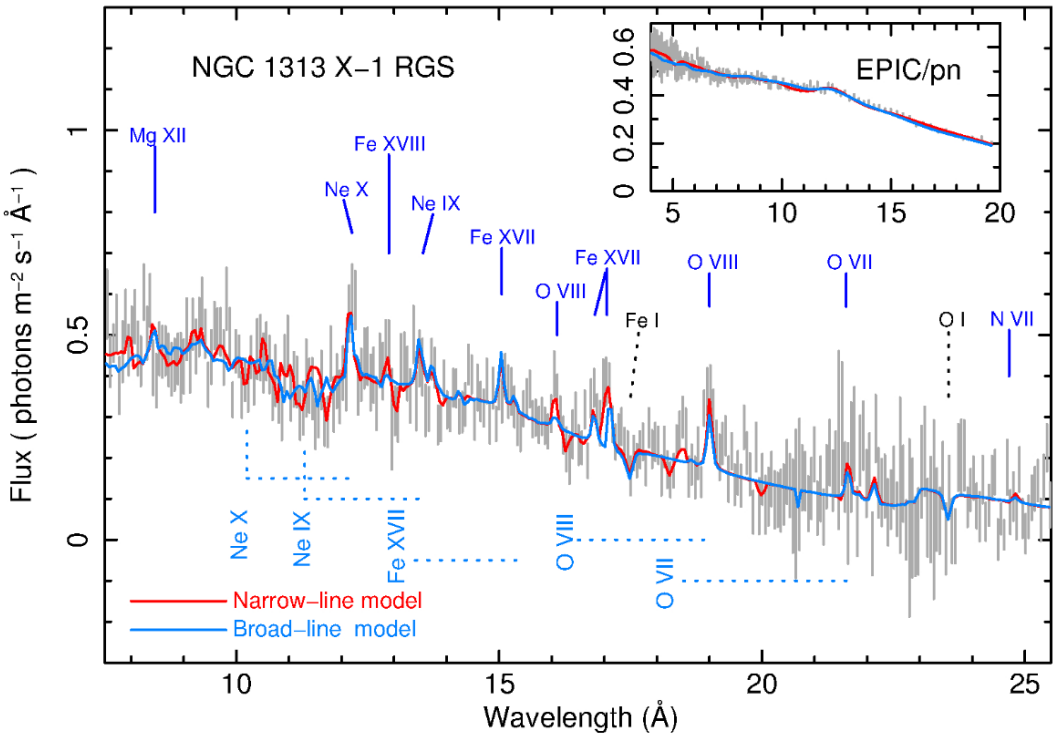

Figure 1.16: *XMM-Newton* RGS and EPIC-pn spectra of NGC 1313 X-1 (RGS stacked spectrum in main frame and EPIC-pn stacked spectrum in small top right insert; Pinto et al. 2016). The rest-frame wavelengths of the most relevant transitions and some blueshifted lines are labelled. The red line model consists of rest-frame absorption and emission and a relativistically-outflowing (v = 0.2c) photoionized absorber. The blue line is a model which includes an additional broadened absorber (v = 0.25c). Errorbars are given at the 1σ level.

other stars (Gladstone et al. 2013) and that becomes increasingly difficult beyond a few Mpc distance. Detecting point-like optical counterparts to ULXs, which are typically very faint in the optical ($m_V \geq 21$, Kaaret et al. 2017), is the crucial first step towards determining their properties and obtaining dynamical mass measurements through spectroscopic observations. Currently, with all known ULXs being extragalactic objects, only the supergiant donor stars can be spectroscopically characterised. In ULX systems containing faint, low-mass companions, where the donor star alone would not be detected, the only way to identify an optical counterpart is by observing the accretion disc of the compact object (Roberts et al. 2011; Tao et al. 2011). Despite these limitations, supergiant donors have been identified using optical and near-infrared data, for example for P13 in NGC 7793 (Motch et al. 2011), CXOU J140314.3+541807 in NGC 5457 (Lopez et al. 2020), Holmberg II X-1 and NGC 5408 X-1 (Heida et al. 2014).

Multiwavelength studies of ULXs are not limited to studies of the disc and the compact donor star, recent observations have revealed the presence of an increasing number of large bubble nebulae around ULXs. These bubble nebulae can evolve to be hundreds of parsecs across (Pakull and Mirioni 2002 and are generated by both ionisation from the ULX X-ray continuum and shocks driven by relativistic disc winds or jets carving out the surrounding ISM (López et al. 2019; Pakull et al. 2006; Roberts et al. 2003; Urquhart et al. 2018).

1.5 Thesis Overview

Understanding astrophysical populations is largely a matter of statistics. A larger sample size can better reveal trends in the data which identify sub-classes and indicates whether the behaviour of a given source is an exception among the population, or a defining feature. As stated in sub-section 1.4.2, the contribution from NS or BH accretors to the ULX population remains unknown. To better answer this question requires assembling new ULX catalogues from the latest (and largest) data releases from currently operational X-ray observatories. From there, different subpopulations can be analysed and grouped into different archetypes of the wider ULX

class. Then, individual sources can be identified for thorough study with deeper, targeted observations to search for evidence of a NS or BH accretor. These findings can then be traced back to the entire population to check for similar behaviour.

The work in this thesis aims to exploit the latest *Swift*, *XMM-Newton* and *Chandra* data to assess the NS and BH contributions to the ULX population. It is structured in an inverted-pyramid hierarchy, incrementally increasing depth of possible study due to decreasing population sample size as we progress. This also largely follows chronological order with which the scientific studies were carried out. Chapter 2 presents our new catalogue of ULXs built from recent catalogue releases from three different X-ray observatories and includes a comparison with concurrent and subsequently released ULX catalogues (Bernadich et al. 2022; Tranin et al. 2024). Then in Chapter 3 we focus on the HLX sub-class from our catalogue. Hyperluminous X-ray sources (HLXs) are the most extreme members of the ULX population with luminosities above 10^{41} erg s^{-1}. With a smaller sample size than the complete catalogue, we explore the individual source data more deeply. After separating out any remaining contaminants, we explore our strong HLX candidates in the context of two well-known HLXs, one with a confirmed NS accretor and the other as a strong IMBH candidate. In Chapter 4 we present a targeted study of an individual source from our catalogue and *eROSITA* data. The given target is selected as a candidate for observations with sufficient data quality (high counts in a reasonable exposure) to perform a search for coherent pulsations and identify a NS accretor. However, the data from the *XMM-Newton* observation is impacted by background flaring. Final, concluding remarks are given in Chapter 5.

No stream rises higher than its source. What ever man might build could never express or reflect more than he was. He could record neither more nor less than he had learned of life when the buildings were built.

- Frank Lloyd Wright

CHAPTER 2

A Multi-Mission Catalogue of Ultraluminous X-ray Source Candidates

In this chapter we present a new, multi-mission catalogue of ULX candidates, based on recent data releases from each of the *XMM-Newton*, *Swift* and *Chandra* observatories (the 4XMM-DR10, 2SXPS and CSC2 catalogues, respectively). The results of this work were largely published in Walton et al. (2022) and the final catalogues of ULX candidates produced here are publicly available via the VizieR archive[1]. As stated in the Declaration, I led the assembly of a stand-alone ULX catalogue from the CSC2.0 *Chandra* data, and then combining each individual catalogue across the three observatories into our final, published multi-mission catalogue.

Further to the work originally published as Walton et al. (2022) some additional, supplementary material can be found at the end of the chapter, where we discuss our work in light of two other ULX catalogues published concurrently and/or subsequent to our work. These are the simultaneous publication of an *XMM-Newton* ULX catalogue built from the 4XMM-DR9 data release by Bernadich et al. (2022) and the Tranin et al. (2024) multi-mission ULX catalogue that was published subsequently.

[1] `https://cdsarc.cds.unistra.fr/viz-bin/cat/J/MNRAS/509/1587`

Our multi-mission ULX catalogue has been compiled by cross-correlating each of these X-ray archives with a large sample of galaxies primarily drawn from the HyperLEDA archive. Significant efforts have been made to clean the sample of known non-ULX contaminants (e.g. foreground stars, background AGN, supernovae), and also to identify ULX candidates that are common to the different X-ray catalogues utilized, allowing us to produce a combined 'master' list of unique sources. Our sample contains 1843 ULX candidates associated with 951 different host galaxies, making it the largest ULX catalogue compiled at time of publication. Of these, 689 sources are catalogued as ULX candidates for the first time. Our primary motivation is to identify new sources of interest for detailed follow-up studies, and within our catalogue we have already found one new extreme ULX candidate that has high S/N data in the archive: NGC 3044 ULX1. This source has a peak luminosity of $L_{\rm X,peak} \sim 10^{40}\,{\rm erg\ s^{-1}}$, and the *XMM-Newton* spectrum of the source while at this peak flux is very similar to other, better-studied extreme ULXs that are now understood to be local examples of super-Eddington accretion. This likely indicates that NGC 3044 ULX1 is another source accreting at super-Eddington rates. We expect that this catalogue will be a valuable resource for planning future observations of ULXs – both with our current and future X-ray facilities – to further improve our understanding of this enigmatic population.

2.1 Introduction

There are still many important questions surrounding the composition of the ULX population. Much of this was covered in the previous chapter, but we shall review a few areas of concern here. What is the numerical contribution of ULX pulsars to the population? Can we identify black hole ULXs with a well-constrained mass function and if so, can they reach the same extreme Eddington ratios as ULX pulsars, or is a magnetic field required? In ULXs what fraction of the total energetic output is radiative, and what fraction is kinetic?

Key to advancing our understanding of these issues are efforts to grow the broader ULX population and provide larger samples with which to undertake statistical

studies of ULXs and identify notable individual sources for follow-up study. Most previous efforts have focused on searching for ULXs in individual mission archives, using in particular *ROSAT* (Colbert and Ptak 2002; Liu and Bregman 2005; Roberts and Warwick 2000), *Chandra* (Gong et al. 2016; Kovlakas et al. 2020; Liu 2011; Swartz et al. 2004) and *XMM-Newton* (Earnshaw et al. 2019b; Walton et al. 2011b). Focusing on data from a single mission has the advantage that everything (source selection, energy bands) can be treated in a uniform manner, which is important for performing population-based studies where selection biases need to be carefully controlled. However, this comes at the expense of limiting the sky area/temporal coverage utilized relative to that available in the full, multi-mission X-ray archive, both of which are key factors in terms of identifying individual sources that may be of particular interest.

Here, we present the results of a search for new ULX candidates, combining data from all of the public archives from the major soft X-ray imaging observatories currently operational: *XMM-Newton* (Jansen et al. 2001), *Chandra* (Weisskopf et al. 2002) and the *Neil Gehrels Swift Observatory* (hereafter *Swift*; Gehrels et al. 2004). In particular, we make use of the 4XMM-DR10, CSC2 and 2SXPS source catalogues (Evans et al. 2020a,b; Webb et al. 2020). Although combining the data from these facilities does formally introduce some non-uniformity to the selection, our primary aim is to compile the largest raw sample of ULX candidates to date, facilitating searches for sources that are bright enough for detailed follow-up with current and future X-ray facilities, as well as searches for sources with multi-wavelength counterparts. This is of particular interest with both *XRISM* (XRISM Science Team 2020) and *Athena* (Nandra et al. 2013) on the horizon, as well as the new facilities due to come online at longer wavelengths (*e.g.* thirty-metre class optical telescopes, *JWST*, the SKA, *etc.*).

This chapter is structured as follows: in Section 2.2 we outline the galaxy sample within which we search for ULX candidates, and in Section 2.3 we discuss our procedure for identifying ULX candidates from the individual archives. Section 2.4 presents our final, merged sample of ULX candidates, and we highlight the case of NGC 3044 ULX1 – a new extreme ULX discovered here – in Section 2.5. Finally,

we summarise our findings in Section 2.6.

2.2 Galaxy Sample

In addition to the various X-ray archives considered here, the other major input required for this work is a catalogue of galaxies within which to search for ULXs. Here, we primarily use the HyperLEDA database (Makarov et al. 2014), initially selecting everything labelled as a galaxy. We focus on HyperLEDA because this is one of the largest homogenized compilations of known galaxies available in the literature. However, we further supplement these galaxies with the latest version of the Catalogue of Nearby Galaxies (CNG; Karachentsev et al. 2018).

For our work here, we need to be able to define the sky area subtended by the galaxy (in order to positionally match X-ray sources) as well as the distance to the galaxy (in order to compute source luminosities). For the galaxy areas, we assume the extent of each galaxy is determined by the elliptical region defined by its D_{25} isophote (*i.e.* the best elliptical fit to the area over which B-band surface brightness of the galaxy exceeds 25 mag arcsec^{-2}), which is given in HyperLEDA (where this information is available). However, CNG uses the Holmberg radius to define the semi-major axis of the galaxy ellipse instead, which corresponds to a surface brightness of 26.5 mag arcsec^{-2}. For the subset of galaxies included in both HyperLEDA and CNG, we therefore calculate an empirical correction between the D_{25} semi-major axes ($R_{D_{25}}$) and the Holmberg radii ($R_{\rm Holm}$), and then apply this to any remaining galaxies that are only included in CNG in an attempt to normalise these to the D_{25} definition. On average, we find $R_{\rm Holm} = (1.26 \pm 0.02)R_{D_{25}}$ (where the uncertainty quoted here is the 1σ standard error on the mean). Although the full set of D_{25} information (semi-major axis, semi-minor axis, position angle) is obviously required to search the full sky area subtended by the galaxy, in cases where the position angle is missing it is still possible to search for ULX candidates within a circular region defined by the semi-minor axis, as this will always be within the galaxy area regardless of the orientation of its full elliptical region. We therefore also retain these galaxies in our input sample. However, any galaxies in the Hyper-

LEDA/CNG catalogues that do not have sufficient information that we can compute at least their D_{25} semi-minor axes are discarded.

For the majority of the galaxies considered, we compute distances based on their measured redshifts (z) assuming they adhere to the Hubble flow. However, where redshift-independent distance estimates are available, we prioritise these measurements. HyperLEDA and CNG both include these based on a variety of different methods (via *e.g.* Cepheid variables, the tip of the red giant branch, the Tully-Fischer relationship), and we further supplement these with distance measurements from the latest version of the Cosmicflows galaxy catalogue (Tully et al. 2016). Such measurements are particularly critical for very nearby galaxies (recession velocities $cz < 1000$ km s^{-1}), where peculiar motions can dominate over the Hubble flow. For these galaxies, we therefore also collected further redshift-independent distance from the NASA Extragalactic Database where such measurements were not available in any of the HyperLEDA/CNG/Cosmicflows catalogues. Where there are multiple distance estimates available among these catalogues, we prioritise them in the following order: Cosmicflows > CNG > Hyperleda > NED > Hubble flow, but we stress that in the majority of cases there is generally good agreement between the different catalogues regarding the redshift-independent distance estimates. However, since a reasonably reliable distance estimate is in turn critical for a reliable luminosity calculation, we therefore discard galaxies with recession velocities $cz < 1000$ km s^{-1} where there is no redshift-independent distance estimate available in any of the above (similar to both Walton et al. 2011b and Earnshaw et al. 2019b).

The final galaxy sample utilized here consists of 966,010 entries, after accounting for the requirements outlined above, the vast majority of which come from HyperLEDA (only 215 of these galaxies are found in CNG but not HyperLEDA). Just under half of these galaxies have morphology estimates available in the form of the Hubble type, T. Following Walton et al. (2011b), for these galaxies we make the distinction between spiral galaxies ($T \geq 1$, including irregular galaxies) and elliptical galaxies ($T < 1$, including lenticular galaxies). We show the distance distributions for the full galaxy sample utilized here, as well as some of these subsets, in Figure 2.1. The majority of the galaxies considered are within a Gpc, although the galax-

ies for which morphology information is not available do have larger distances on average than those where the morphology has been identified.

2.3 Selection of ULX Candidates

2.3.1 Basic Approach

We take the same basic approach to selecting ULXs for each of the three X-ray source catalogues utilized here (4XMM-DR10, 2SXPS and CSC2). Our initial analysis of these individual archives can be broadly summarised into 5 main steps, as described below. Many of the specific details differ for the different catalogues utilized, owing to the differences between the different X-ray observatories they are derived from and the different formats in which the data are provided; these details are discussed in Section 2.3.2.

Step 1 – positional match: First, we perform a positional cross-match between our input galaxy list and each X-ray catalogue; as noted above, for galaxies where the full set of spatial information is available (both the major and minor axes, and the position angle) we perform a standard elliptical match around the position of the galaxy (*i.e.* utilizing the full sky area it subtends), while for galaxies where the position angle is missing we perform a circular match within the radius set by the semi-minor axis (and thus potentially only utilize a fraction of its sky area). Where relevant, only X-ray sources listed as being point-like are retained (both CSC2 and 4XMM-DR10 also contain extended sources, while in principle 2SXPS only includes point sources).

There are inevitably a small subset of X-ray sources that are consistent with being associated with more than one galaxy in our initial matched source lists. In these cases, we make sure to retain only one of the repeat entries in order to avoid individual X-ray sources/detections appearing more than once. To do so, we initially associate the X-ray source with the galaxy for which it is closest to the centre. This is because we expect the majority of these cases to be interacting galaxies, which by definition will be at essentially the same distance, and on average the density of ULXs is known to increase as you approach the galaxy centre (Swartz et al. 2011).

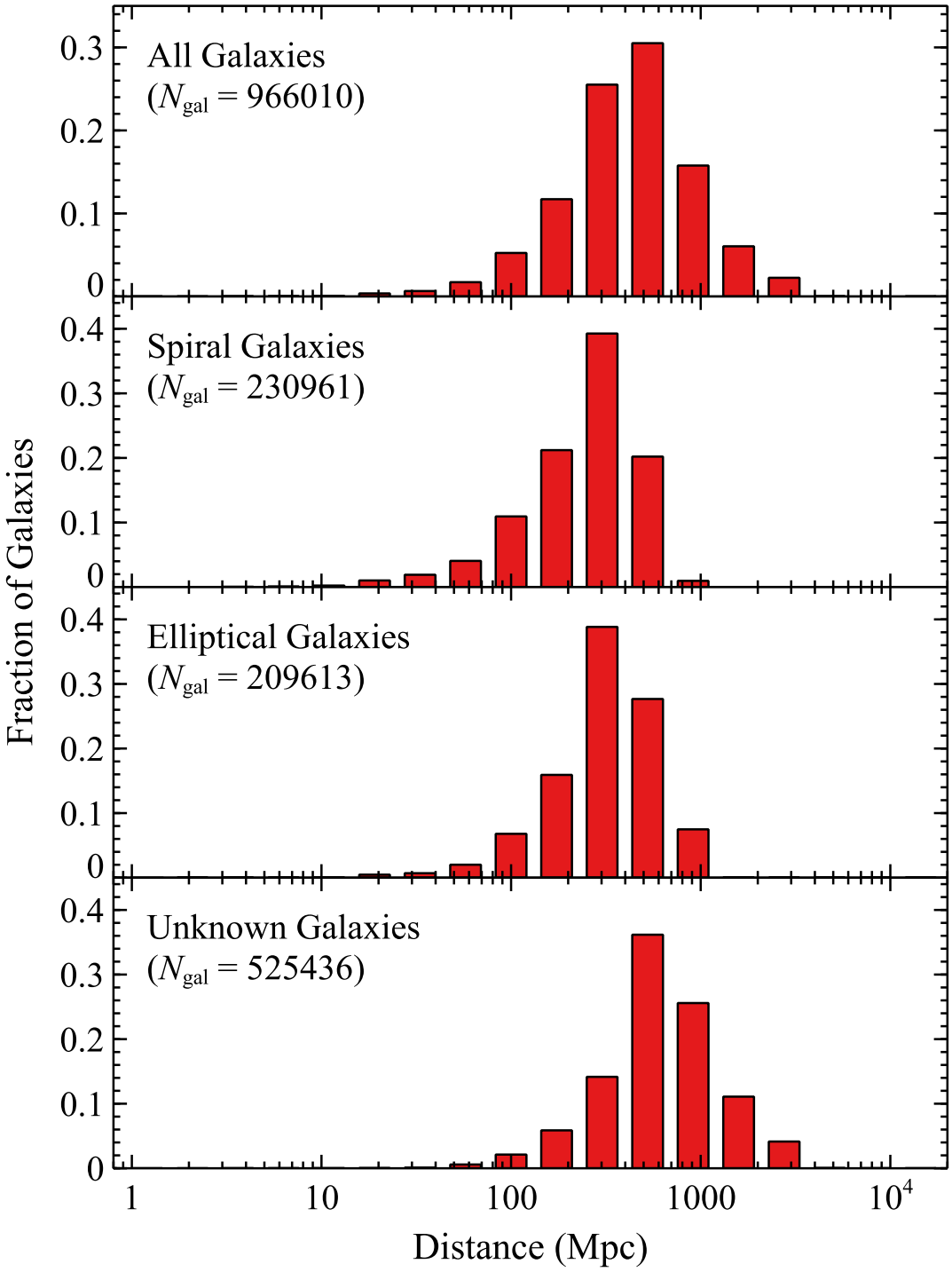

Figure 2.1: Distance distributions for the full galaxy sample utilized here (top panel), galaxies identified as spiral ($T \geq 1$) and elliptical ($T < 1$) galaxies (upper-middle and lower-middle panels, respectively), and for galaxies where morphology information is not available (bottom panel).

However, we re-visit this assumption at the end of our analysis of the individual archives (i.e. after step 5), and assess whether the different galaxy distances really are similar for any remaining sources that are potentially associated with more than one galaxy. Here, we treat galaxies with distances that differ by <15% as having similar distances. Where this is not the case, such that the potential host galaxies appear to be un-associated galaxies that happen to overlap when viewed in projection, we switch the association of the X-ray source to the less distant galaxy. This is both a conservative approach, resulting in lower X-ray luminosities, and also probably a more realistic assumption in these situations, as the enhanced absorption by gas and dust in the foreground galaxy would mean sources in the background galaxy are less likely to be seen as ULXs based on their observed luminosities. For any sources where the association is changed at this stage, the luminosities are re-evaluated (see step 2), and any sources that no longer meet the ULX criterion are excluded.

Step 2 – luminosity cut: With our positionally matched source lists, we then compute X-ray luminosities using our preferred galaxy distance. Here, we use the full band fluxes available in each of the individual X-ray catalogues (see Section 2.3.2). These bandpasses are not precisely identical, but are sufficiently similar that we consider this a reasonable compromise for the sake of simplicity, particularly in light of the simple spectral forms assumed when estimating these fluxes (see Section 2.3.2). Attempting to correct all of the fluxes to have a common treatment is non-trivial, particularly given the time-dependent nature of the *Chandra* instrumental responses (owing to the long-term build-up of the ACIS contamination layer; Plucinsky et al. 2018). With the luminosities in hand, we retain only sources with a full band luminosity that exceeds 10^{39} erg s^{-1}, the standard definition of a ULX. In particular, we select sources that have exhibited luminosities in excess of 10^{39} erg s^{-1} during any individual observation of the source, allowing us to select both persistent and transient/highly variable ULXs. This is a key consideration here, since the latter are now being detected in increasing numbers as our X-ray archives continue to grow (*e.g.* Brightman et al. 2020a; Earnshaw et al. 2019a, 2020; Middleton et al. 2013, 2012; Pintore et al. 2018, 2020; Soria et al. 2012; van Haaften et al. 2019;

Walton et al. 2021), and may be of particular interest in the context of identifying good ULX pulsar candidates (*e.g.* Earnshaw et al. 2018; Song et al. 2020; Tsygankov et al. 2016).

Step 3 – quality flag cut: Each of the X-ray catalogues utilized here contain a variety of information that relate to the robustness of the X-ray detection included and the source properties derived. In each case, we make use of this information to ensure that we only consider sources for which the available X-ray information is reliable, further discarding sources where there are concerns that this may not be the case. The approach taken here is necessarily specific to each of the individual catalogues considered, and is detailed below for each in turn (Section 2.3.2).

Step 4 – nuclear exclusion: By definition, ULXs are off-nuclear sources, and so we attempt to exclude sources that may be associated with the nuclei of their host galaxies. However, this is made challenging by the fact that low-luminosity AGN can exhibit similar luminosities to ULXs (Ghosh et al. 2008; Zhang et al. 2009). We therefore exclude potential AGN through their position relative to the centre of the galaxy instead, following the approach taken in Earnshaw et al. (2019b). In brief, for each X-ray source we compute the minimum separation from the central galaxy position, $R_{\rm min}$, based on its 3σ positional uncertainty (*i.e.* we define $R_{\rm min}$ = nuclear separation − 3σ position error). We then select sources with $L_{\rm X} > 10^{42}\,{\rm erg\ s^{-1}}$, as these sources are almost certainly AGN (only one ULX, ESO 243-49 HLX-1, has exhibited such luminosities to date; Farrell et al. 2009), and calculate the cumulative distribution of their $R_{\rm min}$ values. Unsurprisingly, these typically exhibit very small minimum nuclear separations, and we determine the value of $R_{\rm min}$ that contains >99% of these sources, which we take to be our exclusion criterion for nuclear sources, $R_{\rm min,excl}$ (see Section 2.3.2). All sources with $R_{\rm min} < R_{\rm min,excl}$ are subsequently excluded from our analysis. We repeat the assessment of $R_{\rm min}$ with both our input galaxy catalogue, where we have a requirement for a minimum amount of information regarding the extent of the galaxy (Section 2.2), and also with the full HyperLEDA/CNG/Cosmicflows galaxy catalogues (as for this stage, only the position of the galaxy is required), such that sources with $R_{\rm min} < R_{\rm min,excl}$ for *any* galaxy included in these databases are excluded from our source lists. This empirical

approach allows us to conservatively account for the uncertainty associated with the fact that for some galaxies it can be difficult to precisely identify its central/nuclear position (*e.g.* irregular or merging galaxies, and/or offset nuclei).

Step 5 – removal of other known contaminants: In addition to the nuclei of the apparent host galaxies for our sources, we also attempt to remove other known contaminants. At this stage, we particularly focus on background AGN and foreground stars that coincidentally appear to be associated with a host galaxy in projection. We therefore positionally match our remaining source lists against lists of known stars and quasars. For the former, we use the Tycho2 catalogue (Høg et al. 2000) while for the latter we use the GAIAunWISE quasar catalogue (Shu et al. 2019) and the quasar catalogue of Véron-Cetty and Véron (2010). The search radii we use vary depending on the X-ray archive, as detailed in Section 2.3.2. Any source that matches with either a known star or a known quasar is excluded from our analysis.

2.3.2 Specific Catalogue Details

2.3.2.1 4XMM-DR10

The 4XMM catalogue (Webb et al. 2020) is formatted such that every row entry represents a unique detection of an X-ray source by the EPIC detectors (pn, MOS1, MOS2; Strüder et al. 2001; Turner et al. 2001), meaning that the observation-by-observation information needed to determine the peak flux for sources that have been observed on multiple occasions is already incorporated. For the initial position match (step 1), we specifically use the RA_SC and DEC_SC columns in the 4XMM catalogue for the X-ray position, which give the catalogue-averaged position for sources that have been detected on multiple occasions. 4XMM includes both point sources and extended sources, and we exclude observations in which the detection is marked as extended[2]. When computing detection luminosities (step 2), we use the

[2]Note that we primarily use the observation-by-observation measures of source extent here, as opposed to the mission averaged measure (SC_EXTENT), as variable/transient point sources embedded in diffuse emission can still mistakenly be flagged as extended in the latter. As such, there are some sources included that have non-zero values for SC_EXTENT, but we stress that we

full band flux provided in the catalogue (i.e. 4XMM band 8, spanning 0.2–12.0 keV); these fluxes are computed by summing the fluxes of the 4XMM sub bands, which are themselves computed assuming a standard spectral shape (an absorbed powerlaw continuum with $\Gamma = 1.7$ and $n_{\rm H} = 3 \times 10^{20}$ cm^{-2}).

For the quality flags (step 3), we largely follow the approach taken in Earnshaw et al. (2019b). In brief, detections with a summary flag ≥ 2 are excluded to reduce spurious detections in general, and sources with the out-of-time event flag (Flag 10) set and a total count rate < 0.05 ct s^{-1} are also excluded as these are likely to be artefacts of out-of-time events that are associated with a nearby bright source. However, in addition to these cuts, we also filter out entries where the MASKFRAC flag (Flag 1) is set to be true for each of the EPIC detectors that registered the detection. This helps to further limit spurious detections seen at chip edges, and also spurious 'new' detections at the edge of the field-of-view (FoV) that are really associated with known bright sources just outside the FoV. When filtering out sources consistent with being the nuclei of the host galaxies (step 4) and identifying likely matches with known foreground stars/background quasars, we again make sure to use the RA_SC and DEC_SC columns for the X-ray positions. For the former, we find $R_{\rm min,excl} = 9''$ following the empirical approach described above. This is a pretty conservative cut, compared to previous works involving *XMM-Newton* data (Earnshaw et al. 2019b; Walton et al. 2011b). In the latter case, since we are simply matching point-source positions, we use a matching radius for the various star/quasar catalogues of $5''$, roughly corresponding to the typical 3σ positional accuracy for point sources in 4XMM-DR10 (Webb et al. 2020).

2.3.2.2 2SXPS

By definition the 2SXPS catalogue (Evans et al. 2020b) only includes point sources detected by the XRT (Burrows et al. 2005), and the main table of the catalogue is formatted such that every row entry represents a unique X-ray source, with

have inspected the *XMM-Newton* images from the observations listed as being point-like for these sources that are included in our final sample, and visually confirmed the presence of a point-like source.

the observation-by-observation detection information contained in a separate table. However, the primary source table includes information on the peak flux seen by the XRT for each source included, and so we mainly use this table for our analysis. As such, for the initial position match (step 1), we are naturally using the best-fit position determined from all of the available observations of a given source. When computing the relevant source luminosity (step 2), we primarily select sources based on the peak flux given for each source in the full XRT band (spanning 0.3–10.0 keV) assuming again an absorbed powerlaw continuum (fluxes for various potential spectral models are provided, but of these the absorbed powerlaw is the most appropriate choice for ULXs below 10 keV). Here, the powerlaw parameters adopted when computing the catalogued fluxes are either fit directly, derived from the 2SXPS hardness ratios, or a photon index of $\Gamma = 1.7$ and the Galactic column in the direction of the source are assumed (see Evans et al. 2020b for details).

In contrast to both *XMM-Newton* and *Chandra*, typical *Swift* observations are very short exposures ($\sim$1–2 ks). Furthermore, these observations themselves are often split up into several shorter 'snapshots', and the peak flux included in the catalogue can in principle be drawn from the count rate seen during one of these snapshots instead of the full observation. As such, the peak flux often has large uncertainties, being based on only a handful of counts. For sources where the peak luminosity has a fractional error of >40% (averaging the positive and negative errors quoted), corresponding to a detection with $\sim$10 counts based on the approximation for the Poisson distribution presented in Gehrels (1986), we therefore also require that the source meet at least one of three additional criterion for inclusion. Either: 1) the average luminosity is also consistent with the ULX regime, assuming that the average and peak luminosities are not identical, or 2) there are two or more independent detections of the source in the ULX regime, based on the observation-by-observation data, or 3) the source has also previously been detected in the ULX regime by some other facility (*i.e.* the detection is spatially consistent with an entry in one of the archival ULX catalogues we compare our new dataset against; see Section 2.4.1 for further discussion). For the quality flag cut (step 3), we exclude sources with the summary flag set to $\geq$1 (*i.e.* the "clean" criterion defined by the

Swift team). When filtering out sources consistent with being the host galaxy nuclei (step 4), we also find $R_{\rm min,excl} = 9''$, similar to our analysis of 4XMM. Finally, when identifying likely matches with known foreground stars/background quasars (step 5), we use a matching radius of $10''$ for the *Swift* data, again corresponding to the typical 3σ positional accuracy for sources in 2SXPS (Evans et al. 2020b).

2.3.2.3 CSC2

Similar to 2SXPS, the main table of the CSC2 catalogue (Evans et al. 2020a) is formatted such that every row entry represents a unique X-ray source, with the observation-by-observation detection information presented in a separate table, and similar to 4XMM both point-like and extended sources are included. We therefore use the primary source table when performing the initial position match with our galaxy catalogue (step 1), such that we are again using the best-fit position determined from all of the available observations of a given source, but we then compile the observation-by-observation information for each matched source from the secondary table so that we can be sure to account for the peak flux seen by *Chandra* for each source in our analysis. Sources listed as being extended are discarded. When computing detection luminosities (step 2), we use the broadband CSC2 fluxes, *i.e.* 'broad' fluxes for the ACIS detectors (Garmire et al. 2003b), spanning 0.5–8.0 keV, or 'wide' fluxes for the HRC (Zombeck et al. 1995), spanning 0.2–10.0 keV. Where possible we again use fluxes derived assuming a powerlaw spectral form (as with 2SXPS, fluxes for a variety of spectral models are provided, see the CSC2 documentation for details). Here the catalogued powerlaw fluxes we use are computed assuming $\Gamma = 2$ and the appropriate Galactic column. However, if this powerlaw flux is not available then we use the raw aperture flux instead. For the quality flag cut, we only consider sources which are flagged as 'true' detections in the primary source table (*i.e.* sources flagged as 'marginal' detections are excluded), and we also exclude source detections at the observation level for which the 'streak' flag is set.

In addition to the standard filtering steps outlined above, one further issue that is of relevance for the observation-by-observation *Chandra* data is the fact that the

Chandra PSF degrades rapidly with off-axis angle (in a relative sense, much more severely than is the case for either *XMM-Newton* or *Swift*). As such, the typical extraction radii used in CSC2 also increase with increasing off-axis angle; for example, sources with off-axis angles of $\sim 8'$ often have extraction radii of $\sim$9–10$''$, significantly larger than the on-axis PSF. Unfortunately, for point sources that are either in crowded regions or are embedded in extended regions of diffuse emission, this can result in spurious fluxes for any significantly off-axis observations, as these off-axis detections can occasionally be blends of multiple point sources, and/or include significant diffuse flux not actually associated with the point source in question. This is particularly an issue for observations of nearby giant elliptical galaxies; *Chandra* has undertaken significant programs tiling a number of these galaxies (*e.g.* M87) resulting in a combination of on- and off-axis observations of the same crowded fields. As such, there are a number of sources in these galaxies which have very modest luminosities when viewed on-axis ($L_{\rm X} < 10^{38}\,{\rm erg\ s^{-1}}$) but which all appear to share the same ULX-level off-axis detection. Although some ULXs can be highly variable, as noted above, in many of these cases the ULX-level detections are unfortunately spurious. We therefore manually inspect cases where the only ULX-level detection is taken significantly off-axis, and there is also an on-axis observation that shows the source to have a significantly lower luminosity. Where these are clearly cases relating to source confusion, we exclude these sources from our analysis. We also exclude cases in which the size of the aperture increases to the point where it covers the nominal position of the galaxy centre. In cases where the higher flux could plausibly be due to variability (*i.e.* the on-axis observations show no evidence for large numbers of sources or diffuse emission whose integrated flux could explain that seen in the off-axis observation) we retain these detections, but stress that they should be considered high-priority for further (triggered) follow-up to confirm their nature. We also retain cases in which the aperture marginally overlaps with the edge of the nuclear exclusion zone (but not the nominal nuclear position).

When filtering out sources consistent with being the host galaxy nuclei (step 4), we find $R_{\rm min,excl} = 6.1''$ for CSC2, smaller than the equivalent value for both 4XMM and 2SXPS. Although in a qualitative sense this is not surprising, given the superior

imaging capabilities, it is still worth noting that this value is still significantly larger than the *Chandra* point spread function. This likely reflects the fact that for more complex galaxy morphologies it can be difficult to accurately identify the position of the true galaxy centre. Finally, when identifying likely matches with known foreground stars/background quasars (step 5), we use a matching radius of $3''$.

2.3.3 Merging and Further Filtering

Once all of the individual catalogues of ULX candidates from each of the 4XMM-DR10, CSC2 and 2SXPS archives have been produced, we merge them all into a final 'master' ULX catalogue. To do so, we sequentially match our individual *XMM-Newton*, *Swift* and *Chandra* catalogues of ULX candidates by position. We begin by matching the *XMM-Newton* and *Swift* catalogues. As *Swift* is typically the limiting factor regarding position uncertainties, we match the two within a radius of $10''$, corresponding to the typical 3σ 2SXPS position uncertainty. There are three main outcomes from this initial match: sources with only *XMM-Newton* data, sources with only *Swift* data, and matched sources with both. Each of these lists are then matched with the *Chandra* catalogue. For the sources with only *Swift* data, we again use a matching radius of $10''$ here, and for the sources with only *XMM-Newton* data we use a matching radius of $5''$ (again, the typical 3σ 4XMM-DR10 position error, as *XMM-Newton* is the limiting factor regarding position uncertainties here). For sources with both *XMM-Newton* and *Swift* data, we assume the *XMM-Newton* position to be more accurate, and so use this to match to the *Chandra* catalogue, again using a matching radius of $5''$.

At each of these matching stages, there is the possibility that there are multiple matches for the same source. This is particularly the case when matching either the *XMM-Newton* or the *Swift* data with *Chandra*, given the potential for source confusion and the superior imaging capabilities of the latter; a famous example is the case of NGC 2276, in which a source perceived to be an extremely luminous ULX by *XMM-Newton* is actually resolved into three distinct point sources by *Chandra* (Sutton et al. 2012). In that case, all of the resolved sources are themselves ULXs, but it is also possible that a source that appears as a ULX to *XMM-Newton* or

Swift will actually be resolved into multiple sub-ULX sources (this is conceptually similar to the issue regarding the degradation of the off-axis *Chandra* PSF discussed in Section 2.3.2.3). In addition to matching them against our *Chandra* catalogue of ULX candidates, we therefore also match our *XMM-Newton* and *Swift* ULX candidates against the set of *Chandra* sources that did not make our luminosity cut, and again manually inspect all cases of multiple matches in order to identify sources that only appear to be ULXs because of a detection that is actually likely the blend of several point sources, artificially inflating its apparent flux. As before, these sources are removed from our analysis. We note, however, that we still retain cases where *e.g. Chandra* resolves an *XMM-Newton* detection into two discrete sources, but that the *XMM-Newton* data imply that at least one of these must have varied into the ULX regime (for example, a scenario in which *Chandra* sees two sources at $L_{\rm X} \sim 10^{38}\,{\rm erg\ s^{-1}}$, but the *XMM-Newton*/*Swift* detection that is consistent with both of these sources implies $L_{\rm X} \sim 2 \times 10^{39}\,{\rm erg\ s^{-1}}$, meaning that at least one of these sources must have been in the ULX regime during the *XMM-Newton*/*Swift* observation). In these cases, we add a flag to the final version of the master catalogue noting that this issue exists (a separate flag is added for each of the matched catalogue pairs, see Table 2.1 for the definitions of the different values these flags can take).

On occasion, where there are multiple matches it is possible to determine with reasonable confidence which of the resolved sources the unresolved detection is actually associated with (for example, cases where *Chandra* sees two sources, one with $L_{\rm X} \sim 10^{38}\,{\rm erg\ s^{-1}}$and one with $L_{\rm X} \sim 10^{40}\,{\rm erg\ s^{-1}}$ and *XMM-Newton*/*Swift* sees one source that also has $L_{\rm X} \sim 10^{40}\,{\rm erg\ s^{-1}}$, or alternatively cases in which the position of the first *Chandra* source is in outstanding agreement with the position of the *XMM-Newton*/*Swift* detection, while the second *Chandra* source is right at the edge of the 3σ uncertainty range). In these cases, we make a judgement call ourselves and assign the unresolved detection to the resolved source we feel is most appropriate. Where we feel unable to make a judgement, but there are multiple ULX candidates among the resolved sources (similar to the case of NGC 2276 highlighted above), we we retain all of the potential resolved matches within the master catalogue. Both

Table 2.1: Definitions for the flags detailing the decision taken for any complex matches between the individual ULX catalogues

Value	Description
NULL	No match between the catalogues
0	Unique match between ULX candidates
1	Formally more than one potential match between ULX candidates, but one is clearly preferred and assumed to be the correct match; only this match is reported
2	Formally more than one potential match between ULX candidates, and it is unclear which is the correct association; all potential matches are given
3	ULX detection consistent with several lower luminosity sources seen by the other mission in question, but their combined flux is not sufficient to explain that seen of the ULX detection, so the source is still retained

of these scenarios are also indicated by the matching flags highlighted above (again, see Table 2.1).

Having merged the *XMM-Newton*, *Swift* and *Chandra* data as best we can, we now address the presence of one more class of known contaminants, X-ray transients associated with one-off explosive events (*i.e.* supernovae). Although certainly not all do, these events can reach ULX luminosities, and would then be selected by our process (given our interest in genuinely transient ULXs) even though they are clearly not accretion-powered X-ray binaries. This is particularly relevant here given our use of *Swift* data, since one of *Swift*'s main focuses is rapid follow-up of transient events. We therefore correlate our master catalogue with the positions of known supernovae recorded in the Open Supernova Catalogue (Guillochon et al. 2017; note

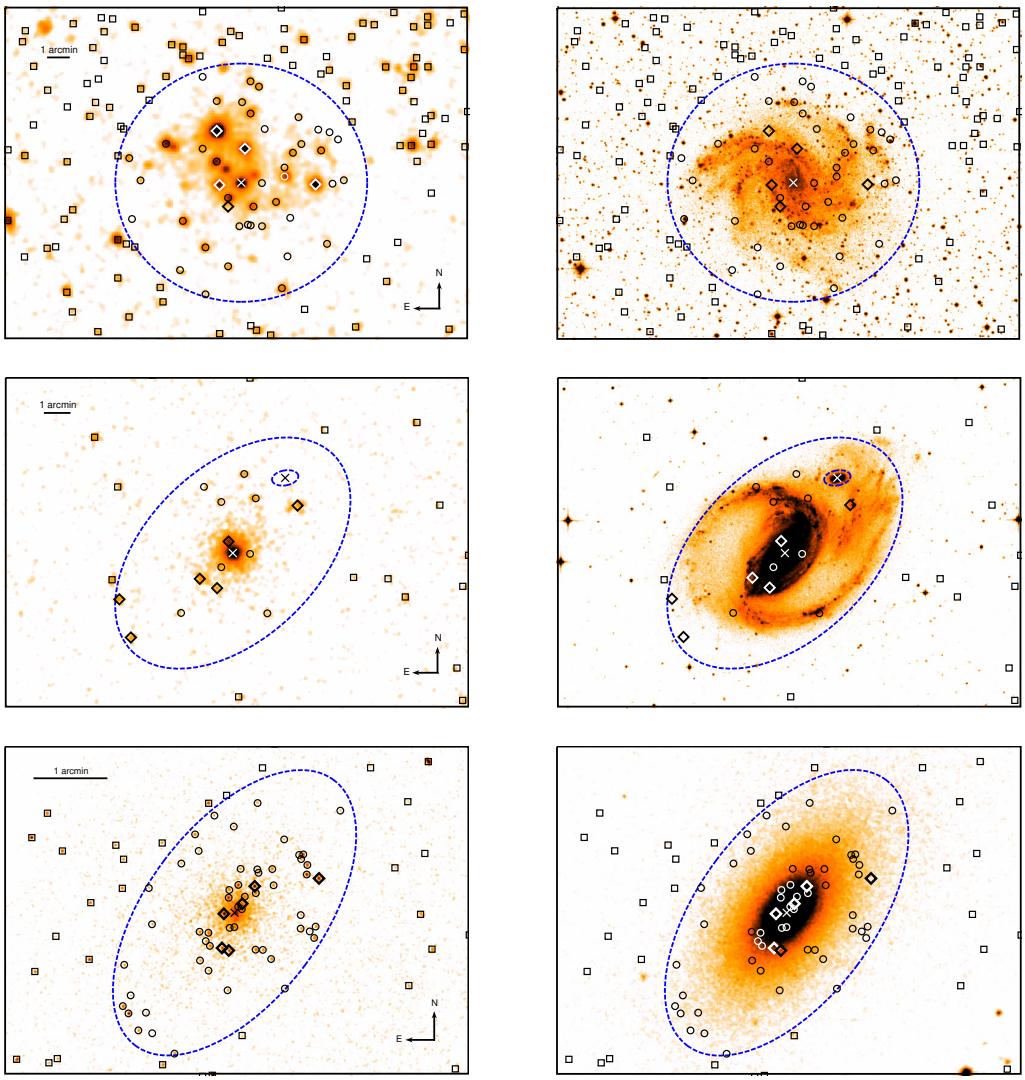

Figure 2.2: X-ray (*left*) and accompanying optical (*right*) images for three example galaxies that demonstrate some of the main stages of our source selection. For the X-ray images, from top to bottom, we show an *XMM-Newton* EPIC image of NGC6946 (OBSID 0691570101), the integrated *Swift* XRT image of NGC1097 (generated with the standard online XRT pipeline; Evans et al. 2009) and a *Chandra* ACIS image of NGC720 (stack ID acisfJ0153056m134345). All are smoothed with a Gaussian of width 3 pixels. The optical images are from the Digitized Sky Survey. In all panels, the D_{25} extent of the galaxy in question is indicated with the blue dashed ellipse, and the nuclear position with a cross (note that in the case of NGC1097, the small companion galaxy NGC1097A is also shown). 'Field' sources (*i.e.* outside of the D_{25} extent) are shown with squares, point sources within the D_{25} extent that do not qualify as ULX candidates with circles, and finally sources selected as ULX candidates are shown with diamonds, respectively; all markers are shown in either black or white simply so that they can most easily be seen against the background images, there is no further significance to the choice of colour. The *XMM-Newton* and *Chandra* images represent the deepest observation/stack of NGC6946 and NGC720 that are included in 4XMM-DR10 and CSC2, respectively. However, owing to the variable nature of the ULX population (see *e.g.* Earnshaw et al. 2019a for NGC6946 in particular), not all sources identified as ULX candidates are necessarily visible in these X-ray images.

that this includes both supernovae that have occurred since *XMM-Newton*, *Chandra* and *Swift* have been observing and more historic supernovae). To do so, we prioritise X-ray source positions from *Chandra*, *XMM-Newton* and *Swift* in that order (*i.e.* in cases where a source is detected by all three observatories, we use the *Chandra* position for this match), and perform the match using search radii of $3''$, $5''$ and $10''$ for *Chandra*, *XMM-Newton* and *Swift* positions, respectively. However, in order to determine whether the X-ray source is really associated with the transient in question we also examine the relative timing of the event and the first detection of the X-ray source (hence our decision to only apply this filter to the merged dataset, where we can most robustly determine when the source was first detected). X-ray sources that are positionally coincident with supernovae, but which were detected as ULXs significantly before the event occurred are deemed to be unrelated to the supernova and retained in our sample. However, sources positionally coincident with known transients that have only been detected after the event occurred are assumed to be associated with the supernova, and so are excluded from our final sample.

We also match our remaining sample against both the NED and SIMBAD databases in order to identify and remove any further non-ULX contaminants that have been identified in the literature (uncatalogued AGN, stars, supernovae). We adopt the same spatial matching procedure as for the Open Supernova Catalogue, prioritising *Chandra*, *XMM-Newton* and *Swift* positions in that order and using matching radii of $3''$, $5''$ and $10''$. For any further supernovae identified, we also again consider the date of the first X-ray detection when deciding whether the X-ray source should be removed. We then remove any remaining sources obviously associated with the host-galaxy AGN that have been missed by our nuclear cut (*e.g.* sources with $L_{\rm X} \geq 10^{42}\,{\rm erg\ s^{-1}}$ that lie just outside our nuclear exclusion radii or, in the case of Centaurus A, are located in the X-ray emission from the AGN jet; Hardcastle et al. 2007) as well as a number of sources for which we are aware of follow-up studies that have previously found the ULX candidate to be an uncatalogued background quasar/foreground star (Dadina et al. 2013; Guo et al. 2016; Heida et al. 2013; Sutton et al. 2015).

Finally, after all of the above steps, we find that the remaining sample contains a

number of highly clustered sources which only appear in 2SXPS and actually seem to be associated with the bright diffuse emission known to be present in the M82 galaxy (*e.g.* Griffiths et al. 2000; Lopez et al. 2020), even though 2SXPS is intended to be a dedicated point source catalogue. This is likely related to the typical snapsnot nature of *Swift* XRT observations; with such short exposures random Poisson fluctuations from the diffuse emission may more easily be mistaken as point sources. 2SXPS notes all of the potential aliases for each entry, and many of these M82 sources are listed as potentially being aliased with each other. We therefore also manually inspect X-ray images – both the images integrated over the duration of the *Swift* mission and specifically taken from the observation corresponding to the reported best detection for the XRT, and, where available, any CSC2 *Chandra* images as well – for all of the 2SXPS sources which have not also been identified as a ULX candidate in either of our 4XMM-DR10 or CSC2 subsamples and are listed as having other potential 2SXPS aliases. Any sources which we judge to be likely associated with diffuse emission (similar to the M82 case) are removed from the final sample. During this process, if a source is aliased with another genuine point source (as opposed to being part of a cluster of sources associated with extended emission), we also make a judgement over whether these are likely the same source, and retain only one entry in these cases.

2.4 The Final Sample

Our final sample of ULX candidates consists of 1843 individual sources residing in 951 host galaxies. The catalogue will be made available to the public, and will be comprised of four tables. The first is a 'master' list formatted to have one row entry per source, summarising some key information and detailing which combination of *XMM-Newton*, *Swift* and *Chandra* have reported the source as a ULX. We stress that we are focused only on the detections of these sources that meet the ULX luminosity threshold here (*i.e.* $L_{\rm X} \geq 10^{39}\,{\rm erg\ s^{-1}}$); if an *XMM-Newton* ULX candidate does not have a *Chandra* counterpart reported, for example, this does not necessarily mean that *Chandra* has not detected that source, only that *Chandra* has not seen it at

Table 2.2: The final sample of ULX candidates compiled from the 4XMM-DR10, 2SXPS and CSC2 catalogues

	4XMM-DR10	2SXPS	CSC2	Combined Sample
Number of ULX Candidates	641	501	1031	1843
(with multiple ULX detections in the parent catalogue)	177	291	246	702
(seen as a ULX by multiple observatories)	241	173	209	293
(HLX candidates)	22	36	17	71
Host Galaxies	403	269	548	951
(average distance, Mpc)	62.3 ± 3.5	34.8 ± 2.7	83.8 ± 3.8	74.7 ± 2.7
(containing multiple ULX candidates)	130	89	190	333

a flux that would correspond to the ULX regime. The other three tables provide the full details of the 4XMM-DR10, 2SXPS and CSC2 entries for the ULX-level detections of these sources. These follow the formats of the data used to compile these subsamples of ULX candidates in the first place (i.e. the *XMM-Newton* and *Chandra* tables have one row entry per observation of a ULX candidate, while the *Swift* table just has one row entry per ULX candidate).

Some statistics for the full sample and the individual 4XMM-DR10, 2SXPS and CSC2 sub-samples are given in Table 2.2, and we show examples of our source selection in Figure 2.2 for each of the *XMM-Newton*, *Swift* and *Chandra* observatories. By number, the CSC2 component contributes the most sources to our final sample, followed by 4XMM-DR10 and then 2SXPS. The latter still makes a very significant contribution though. There is obviously notable overlap between the individual subsamples (*i.e.* some sources are detected as ULXs by multiple missions), as also detailed in Table 2.2 and in the master table provided. Of our 1843 individual sources, 50 are detected at ULX luminosities in all three of our contributing source catalogues.

As expected, given the known connection between ULXs and recent star formation (Lehmer et al. 2019; Mineo et al. 2012; Swartz et al. 2009), the majority of our ULX host galaxies with morphology information available are spiral galaxies ($\sim$60%, using the T-type ranges defined above). We also plot the distribution of host galaxy distances in Figure 2.3 for the full sample and each of the individual catalogue subsamples. There is significant overlap in the individual distributions, but typical host galaxy distances are lowest for the 2SXPS subsample, and largest for the CSC2 subsample, as the latter has the best sensitivity to faint point sources among the X-ray catalogues considered owing to both the low background and superior imaging capabilities of *Chandra*. This allows *Chandra* to more easily detect ULX candidates out to larger distances than either *XMM-Newton* or *Swift*, and thus the CSC2 subsample ends up making the largest contribution to our final sample.

Of our 951 host galaxies, 333 are found to host multiple ULX candidates. As our primary interest is focused on individual sources, and our sample selection is highly non-uniform, we do not make any attempt to correct for (in)completeness in any

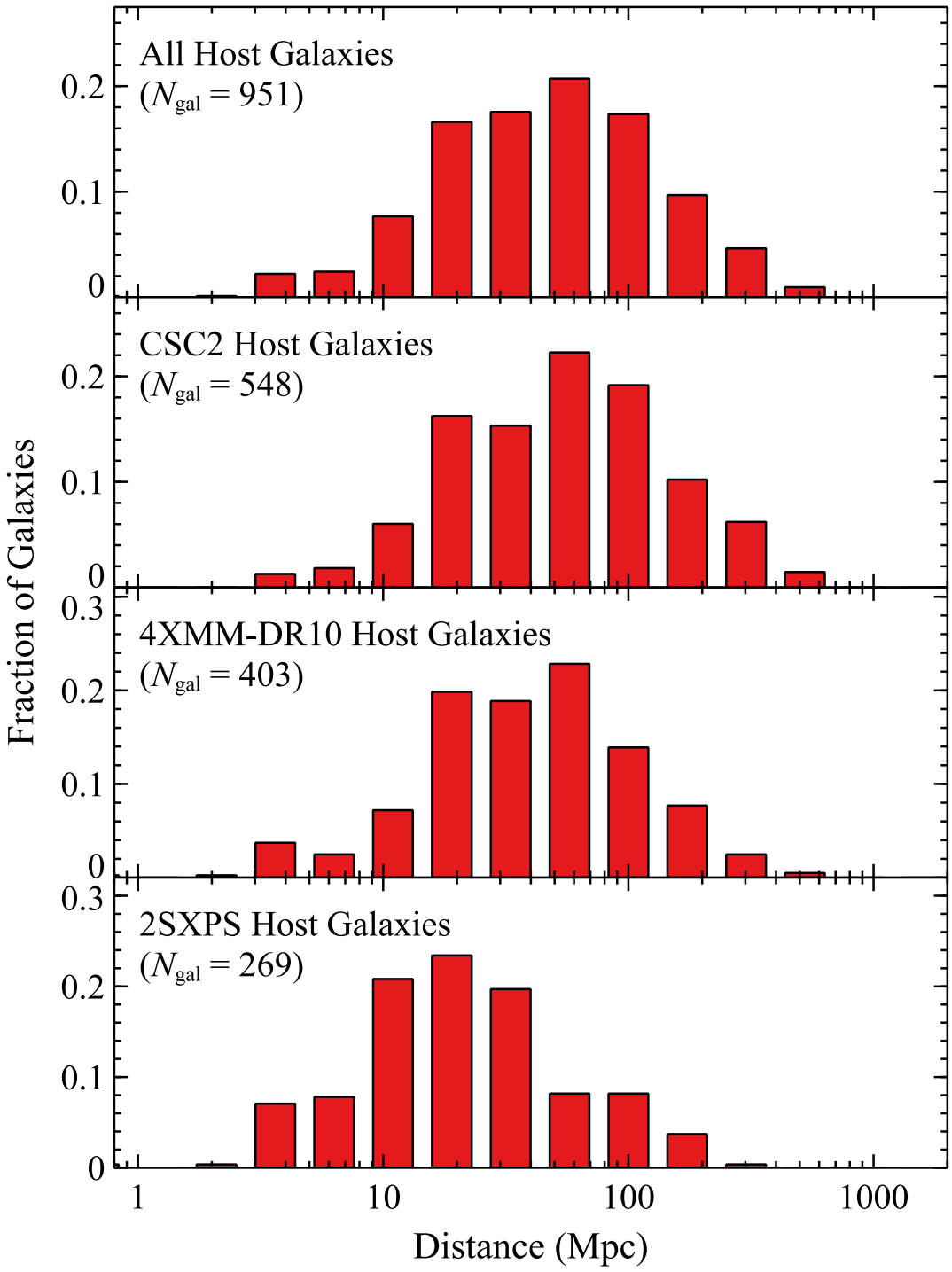

Figure 2.3: Distance distributions for ULX host galaxies, showing the full multi-mission sample (top), and the CSC2, 4XMM-DR10 and 2SXPS subsets, respectively (lower panels).

galaxies observed with insufficient depth to reach luminosities of 10^{39} erg s^{-1}, so this should likely be considered a lower limit for ULX multiplicity in these hosts. The most extreme example is NGC 2207 – one half of an interacting galaxy pair (the other being IC 2163; Eskridge et al. 2002) – which appears to host an astonishing 34 ULX candidates, the majority of which (31) are contributed by the CSC2 catalogue. This is notably larger than the 21 ULXs reported to reside in NGC 2207/IC 2163 by Mineo et al. (2013), likely due to additional *Chandra* observations being included in CSC2 and our explicit consideration of long-term variability in selecting our ULX sample. Owing to the interacting nature of these galaxies, it is not surprising that there should be a large number of ULXs. It is nevertheless worth noting that there seems to be some disagreement over the distance to NGC 2207 in the literature. The distance we have adopted here is $D = 36.4$ Mpc, which is based on the recession velocity reported in HyperLEDA. This distance is very similar to that reported based on the supernova SN1975A which occurred in NGC 2207 ($D = 39.6$ Mpc; Arnett 1982), which is adopted by Mineo et al. (2013). However, the more recent estimates from the Tully-Fisher method typically seem to imply a distance of $D \sim 17$ Mpc (Russell 2002; Theureau et al. 2007). Should this be correct, only 7 of our sources in NGC 2207 would still be considered ULXs. However, our assumption is that the supernova-based distance is the most reliable here, and so our luminosity estimates should be reasonable.

We also note that among the 1843 ULX candidates, our catalogue contains 71 'hyperluminous' X-ray source (HLX) candidates.[3] These are the most extreme members of the ULX population, exhibiting luminosities of $L_{\rm X} \geq 10^{41}$ erg s^{-1}. Owing to their astonishing luminosities, such sources are often considered the best candidates for IMBH accretors. Indeed, two of the sources discussed as the leading IMBH candidates in the literature, M82 X-1 and ESO 243-49 HLX-1, are found among this population. However, it is also worth noting that one of the known ULX pulsars,

[3]Note that for in order for sources detected in 2SXPS to be considered good HLX candidates we apply a similar criterion to our initial source selection procedure, such that if the peak luminosity is not well constrained (average fractional uncertainty of >40%) then the source has to either have a better-constrained average luminosity that is also in the HLX regime, or at least two separate XRT observations that place it in the HLX regime.

NGC 5907 ULX, also reaches luminosities of $L_{\rm X} \sim 10^{41}\,{\rm erg\ s^{-1}}$ (Fürst et al. 2017; Israel et al. 2017a), despite being powered by a neutron star. Nevertheless, these sources are still of particular interest, and our new HLX candidates will be discussed in more detail in Chapter 3.

2.4.1 Comparison with Previous ULX Catalogues

The first major effort to search for ULXs among any of the X-ray source catalogues considered here was presented by Kovlakas et al. (2020), who also searched CSC2 for ULX candidates. Although both the approach taken and the input galaxy sample used are quite similar in both cases, there are also a couple of notable differences. First and foremost, we have considered the *Chandra* data down to the observation-by-observation level, in order to select sources based on their peak flux and specifically include transient ULXs in our sample, while Kovlakas et al. (2020) base their luminosity selection on the flux recorded in the longest uninterrupted segment of *Chandra* data (which is not necessarily the peak flux exhibited by the source). Second, we have taken a much more conservative approach to excluding potential nuclear sources associated with our host galaxies. Kovlakas et al. (2020) flag a source as 'nuclear' if it is within 3″ of the nominal galaxy centre, while we both consider the position error on the X-ray detection and utilize a much larger minimum exclusion radius (6.1″). This is based on our empirical assessment of the separation between the nominal centre of the host galaxies and sources that we consider likely to be their AGN (those that appear to have $L_{\rm X} \geq 10^{42}\,{\rm erg\ s^{-1}}$). Our more conservative approach does mean that our catalogue is likely cleaner with regards to any remaining contamination from AGN in our host galaxies, but this will come at the cost of excluding a larger number of *bona fide* ULXs from our sample, particularly given that the spatial density of ULXs is seen to increase towards the galaxy centres (Kovlakas et al. 2020; Swartz et al. 2011; Wang et al. 2016). Nevertheless, this is a more appropriate approach given that our primary motivation is to find individual sources that are of interest for follow-up studies; detailed follow-up of ULXs within a few arcseconds of the nuclear position will not realistically be feasible for the majority of our current and planned X-ray facilities if the nuclear black

hole is even reasonably active. Despite these differences, though, there is naturally a fairly significant degree of overlap (754 sources) between our sample and sources that would qualify as ULXs in Kovlakas et al. (2020).

More recently, Inoue et al. (2021) have also searched for CSC2 for ULX candidates. However, a major difference between these works is that Inoue et al. (2021) have used a much smaller catalogue of input galaxies than that used here, derived by combining IRAS galaxies with the CNG catalogue. Furthermore, while they do consider the observation-by-observation data provided in CSC2, they use the flux from the longest individual observation when computing luminosities, which again is not necessarily the peak flux exhibited by the sources in question (which is what we are interested in here), and we have again been more conservative in our treatment of nuclear sources. Although their work primarily focuses on CSC2, the final catalogue does also include sources selected from 4XMM-DR9 and 2SXPS, and so is therefore conceptually similar to our multi-mission approach. There is not a lot of specific detail provided for these latter analyses, unfortunately, but the approach is stated to be broadly similar to that used for CSC2, and so similar differences between the two works are presumably present here too. In addition, another key difference with regard to the 2SXPS analysis is that they appear to have only made use of the average fluxes from *Swift*, while we have considered the peak flux (where this is considered reliable). Furthermore, we have used an even more recent release of the 4XMM survey here. Nevertheless, despite these differences, there is again some notable overlap of 357 sources in total (251, 107 and 149 from *Chandra*, *XMM-Newton* and *Swift*, respectively).

Finally, Barrows et al. (2019) also utilize CSC2, but only search specifically for HLXs within the SDSS-DR7 galaxy sample. However, the spatial offsets relative to the central galaxy positions would result in the majority of their HLX candidates being considered as nuclear sources with our more empirical approach to this stage of the catalogue production. Only one of our sources is also present in the Barrows et al. (2019) catalogue, 2CXO J155910.3+204619, and we have assigned this to a different (and closer) host galaxy, giving it a much more modest luminosity of $L_{\rm X} \sim 2.5 \times 10^{39}\,{\rm erg\ s^{-1}}$. As such, our sample of HLX candidates differs entirely to that

presented by Barrows et al. (2019).

In addition to these more recent works, we also match our new catalogue against a series of other archival ULX catalogues, which have been derived using previous generations of X-ray surveys. In these cases we match by position, as they are not drawn from any of the exact X-ray catalogues used here (and thus do not have identical naming conventions). Similar to our final matching against the NED and SIMBAD for remaining contaminants, we split our ULX catalogue into sources where the best position comes from *Chandra*, from *XMM-Newton* and from *Swift*, and then individually match these sub-sections against each of the archival ULX catalogues in turn. The matching radius used for each comparison depends on the origins of the data being compared, and always corresponds to the larger of the typical positional uncertainties associated with the two input tables. As before, positions from *Chandra*, *XMM-Newton* and *Swift* are considered to have typical uncertainties of $3''$, $5''$ and $10''$, respectively, and *ROSAT* positions are considered to have a typical uncertainty of $20''$. For example, when comparing the subset of our catalogue with *Chandra* positions against another catalogue derived from *Chandra* data, we would use a matching radius of $3''$, but comparing the same subset against a catalogue derived from *ROSAT* observations, we would use a matching radius of $20''$ instead. For this analysis, we simply note all potential matches. The catalogues we match against are listed in Table 2.3.

Based on all of these matches, we find that 689 of the ULX candidates presented here are completely new, *i.e.* do not seem to appear in any of the other ULX catalogues considered, and 1318 have only recently been catalogued as a ULX, *i.e.* they only appear in catalogues based on the latest generation of X-ray source catalogues (this work, Barrows et al. 2019, Kovlakas et al. 2020 and Inoue et al. 2021). Of these 'new' and 'recent' ULX candidates, 48 and 59, respectively, are HLX candidates. We stress that even if a source is considered 'new' in this respect, this does not necessarily mean the sources are completely unknown, only that it has not been formally catalogued as a ULX previously. For example, NGC 300 ULX1 is considered 'new' here, even though this source is one of the few known ULX pulsars (Carpano et al. 2018), and as such has received significant individual attention (Heida et al. 2019;

Kosec et al. 2018b; Vasilopoulos et al. 2018, 2019; Walton et al. 2018a).

2.4.2 Estimation of Unknown Contaminants

Although we have taken significant measures to try and remove known contaminants, these processes can never be perfect, and so we stress that there will still be a significant contribution of sources that are not actually ULXs in our final sample of ULX candidates. By far the majority of these will be foreground/background sources that coincidentally appear to be associated with the host galaxies in question in projection, but have just not been formally identified/catalogued as such in the databases we have utilized (and thus have not been removed by our effort to identify and exclude these sources). Although we cannot remove these sources, it is still important to quantify their likely contribution.

In order to do so, we broadly follow the approach taken in Walton et al. (2011b), and subsequently Sutton et al. (2012) and Earnshaw et al. (2019b). This involves a calculation of the total expected number of sources that would be resolved from the cosmic X-ray background (CXB) given our selection criterion, the sensitivity of the observations from which the 4XMM, 2SXPS and CSC2 X-ray catalogues have been generated, and the full set of galaxies in our catalogue that have been covered by the observations that contribute to these X-ray catalogues (not just those galaxies that have ULX detections). These estimates are then compared to the number of sources remaining in our catalogue, after accounting for the number of identified foreground/background sources that have already been filtered out, in order to estimate the remaining fractional contribution from these contaminants.

In order to estimate the total expected number of contaminants, we make use of empirically determined forms of the $N(>S)$ curves which quantify the number of sources per square degree (N) resolved from the CXB as a function of flux sensitivity (S). These are combined with observational sensitivity maps in order to estimate the number of background sources each galaxy in our input sample that has been observed should contribute. Sensitivity maps for the observations from which the 4XMM and CSC2 catalogues are compiled are provided as part of these data releases, but are not available for the 2SXPS catalogue at the time of writing. We therefore

Table 2.3: Details of the archival ULX catalogues against which our new archive is compared

Catalogue	Primary Source & Notes
Colbert and Ptak (2002)	*ROSAT*
Swartz et al. (2004)	*Chandra*
Liu and Bregman (2005)	*ROSAT*
Liu and Mirabel (2005)	Literature (incl. *ROSAT*, so positions treated as having *ROSAT* accuracy)
Liu (2011)	*Chandra*
Swartz et al. (2011)	*Chandra*
Walton et al. (2011b)	*XMM-Newton* (specifically 2XMM)
Gong et al. (2016)	*Chandra* (only $L_{\rm X} \geq 3 \times 10^{40}\,{\rm erg\ s^{-1}}$)
Earnshaw et al. (2019b)	*XMM-Newton* (specifically 3XMM-DR4)
Barrows et al. (2019)	*Chandra* (specifically CSC2 HLXs)
Kovlakas et al. (2020)	*Chandra* (specifically CSC2)
Inoue et al. (2021)	Mainly *Chandra* (specifically CSC2), but also includes *XMM-Newton* and *Swift* (specifically 4XMM-DR9 and 2SXPS)

focus our calculations on the 4XMM and CSC2 data, performing this calculation for each dataset separately; as will be clear below, the expected level of contamination for these datasets are very similar, and so we still expect these results to hold overall.

For CSC2, since the initial source detection is performed using 'stacks' of observations (a stack is defined as a group of observations for which the aimpoints are all within 1 arcminute; see the CSC2 documentation), we use the sensitivity maps generated for these stacks in our analysis. These are provided for all of the energy bands considered in the CSC2 catalogue. However, as noted by Walton et al. (2011b), owing to absorption in the apparent host galaxies (which lie between us and any background AGN) these calculations are most robust at higher energies, and so we limit ourselves to the hard band (2–7 keV) ACIS maps that correspond to the 'true' detection threshold to match our data selection (the HRC makes a negligible overall contribution here). We also make use of the $N(>S)$ curves recently published by Masini et al. (2020), who present an expression for the same 2–7 keV band.

There are two limiting fluxes to consider here. The first is set by our selection of sources that appear to have $L_{\rm X} \geq 10^{39}$ erg s^{-1}. For each galaxy we work out the hard band flux that would correspond to a broadband luminosity of 10^{39} erg s^{-1}, $S_{\rm ulx}$, based on the distance to the galaxy and the fraction of the broadband flux that would appear in the hard band. We use a coarse representation of the average spectral shape for ULXs below 10 keV (*e.g.* Gladstone et al. 2009; Pintore et al. 2017; Stobbart et al. 2006): an absorbed powerlaw spectrum with $\langle n_{\rm H} \rangle = 3 \times 10^{21}$ cm^{-2} and $\langle \Gamma \rangle = 2.1$. The second flux is the limiting sensitivity of the stack in question, $S_{\rm obs}$, provided by the sensitivity maps. The relevant limiting sensitivity for use with the $N(>S)$ curve is then the larger of these two values, such that if an observation is sensitive enough to detect sources at lower luminosities, these are not included in our estimated number of contaminants. For each of the galaxies covered by CSC2 we use the $N(>S)$ curve and the appropriate limiting sensitivity to compute maps of the number of expected background sources per pixel, and integrate these over the area of the galaxy covered by each relevant *Chandra* stack (excluding the typical area excised around the central galaxy location by our nuclear cut). For each of

the galaxies covered by CSC2 data (again, not just those with ULX detections), we perform this calculation for every available stack. We then select the stack that would give the largest number of contaminants, and sum these values over all of the galaxies covered by CSC2 stacks to compute the total number of expected contaminants prior to the removal of any known foreground/background sources. From this, we compute the remaining fractional contamination among the CSC2 ULX candidates by comparing the expected number of remaining contaminants to the number of ULX candidates detected in the hard band for self-consistency (*i.e.* excluding sources that only have upper limits).

For 4XMM, the sensitivity maps are only provided for the full band (0.2–12.0 keV) and are based on the combined sensitivity for all of the EPIC detectors (see Section 9 in Webb et al. 2020). However, as stated above, it is preferable to work in the hard band here. Furthermore, suitable $N(>S)$ curves are not currently available for the full *XMM-Newton* bandpass; aside from work focusing specifically on *Chandra*, $N(>S)$ curves are determined almost exclusively for the 0.5–2.0 and 2–10 keV bands. It is therefore necessary to correct the results from the available broadband maps to one of these bands, and we again choose the harder band, but this is not a trivial process. To do so, we also make use of the hard band (2–12 keV) sensitivity maps computed as part of the Earnshaw et al. (2019b) ULX catalogue for the majority of observations that make up 4XMM-DR10 (specifically those that make up 3XMM-DR4). However, these are computed using a different approach (see Carrera et al. 2007 and Mateos et al. 2008), consider each of the EPIC detectors separately, and adopt a different detection threshold (the hard band maps are computed for a $\sim 4\sigma$ detection in a single detector, while the broadband maps are computed for a $\sim 3\sigma$ detection combining all the EPIC detectors), further complicating the situation.

For each galaxy covered by these earlier observations, we therefore process the available hard band sensitivity maps for each of the detectors in a similar manner as above, using the appropriate $N(>S)$ curve published by Cappelluti et al. (2009) but only considering for the limiting observational sensitivity ($S_{\rm obs}$) for the time being, and note the results for the detector that predicts the largest number of contaminants. We also process the broadband maps for the same observations by

computing the fraction of the broadband flux in both the softer (0.5-2.0 keV) and harder (2–10 keV) bands using the spectral form assumed in their generation (an absorbed powerlaw with $n_{\rm H} = 1.7 \times 10^{20}$ cm^{-2} and $\Gamma = 1.42$, typical for CXB sources), processing these updated maps in turn using the relevant $N(>S)$ curves, again only considering $S_{\rm obs}$, and averaging the final results to obtain an estimate for the number of contaminating sources the broadband maps would imply. For each galaxy covered by these earlier observations, we then compare the results from the broadband and the hard band maps to compute an empirical correction for the former; we find this correction to be a factor of 9. We then process the full set of 4XMM-DR10 broadband sensitivity maps using this correction to produce maps of the expected number of hard band CXB sources. At this point, we also consider the number of contaminants implied by the second limiting sensitivity, $S_{\rm ulx}$, and update the maps accordingly. Similar to before, we then integrate these maps over the galaxy area covered by every observation of that galaxy (again excluding the typical area around the central position excised by our nuclear cut, and again considering all galaxies covered by 4XMM-DR10) and pick the observation that gives the largest number of hard-band contaminants for each galaxy. We then sum these values to compute the total number of expected contaminants prior to the removal of any known foreground/background sources, and finally compute the remaining fractional contamination among the 4XMM ULX candidates (comparing the expected number of remaining contaminants against the number of ULX candidates that are detected at the 4σ level in any of the EPIC detectors for self-consistency).

Based on these approaches, and the numbers of known foreground/background contaminants already removed, we estimate fractional contaminations of $(23 \pm 2)\%$, and $(18 \pm 3)\%$ for our CSC2 and 4XMM-DR10 ULX candidates, respectively (quoted uncertainties are due to counting statistics, and are 1σ). These values are sufficiently similar that, even though the relevant sensitivity maps are not yet available for 2SXPS, we still expect that an overall fractional contamination of $\sim$20% is relevant for the whole catalogue.

2.5 NGC 3044 ULX1 – A New Extreme ULX

The non-uniform selection means the full ULX sample presented here is not necessarily well suited for detailed statistical studies of the ULX population similar to those presented by Kovlakas et al. (2020) and Inoue et al. (2021). Indeed, our intention in compiling this sample is to facilitate follow-up studies of interesting individual sources. As such, in order to highlight the potential of our catalogue, we instead present a case study of a new extreme ULX candidate with $L_{\rm X,peak} \sim 10^{40}\,{\rm erg\ s^{-1}}$ in the edge-on spiral galaxy NGC 3044 detected by both *Swift* and *XMM-Newton* (see Figure 2.4). Although we have found several new HLX candidates in our analysis, we highlight this new source in particular both because its luminosity is still very extreme, but also because it already has high signal-to-noise (S/N) *XMM-Newton* data (several thousand counts) available in the archive; as noted above, our new HLX candidates will instead be studied independently in Chapter 3. Hereafter we refer to this source as NGC 3044 ULX1 for simplicity, as it is the brightest ULX candidate in NGC 3044, but its catalogued 4XMM-DR10 and 2SXPS IAU names are 4XMM J095343.8+013416 and 2SXPS J095343.7+013417, respectively. Throughout this analysis, we assume a distance of $D = 20.6\,{\rm Mpc}$ to NGC 3044 (Tully et al. 2016).

2.5.1 Observations and Data Reduction

NGC 3044 has been observed on four occasions by *XMM-Newton*, and on five occasions by *Swift*. A log of these observations is given in Table 2.4. We primarily focus on the *XMM-Newton* observations here, but also process the *Swift* observations to provide further information on the long-term variability.

The *XMM-Newton* data for each observation are reduced following standard procedures using the *XMM-Newton* Science Analysis System (SAS v19.1.0). All of the *XMM-Newton* observations were taken in full frame mode. Raw observation files for the EPIC-pn and EPIC-MOS detectors are cleaned using EPCHAIN and EMCHAIN, respectively. In order to facilitate pulsation searches, the cleaned EPIC-pn event files are corrected to the solar barycentre using the DE200 solar ephemeris, as this

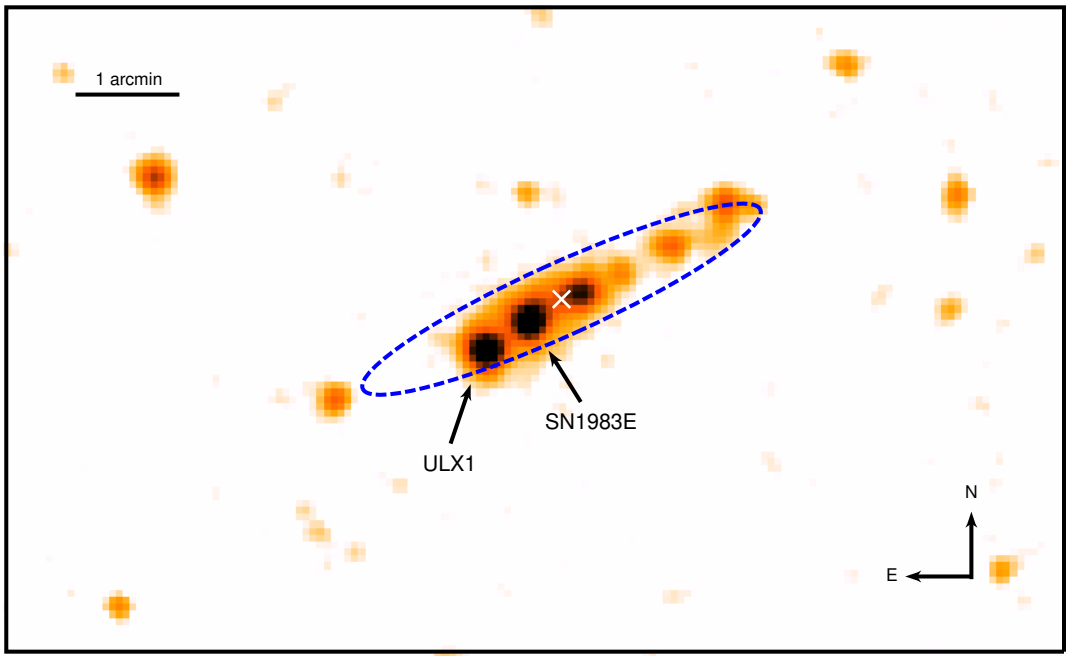

Figure 2.4: *XMM-Newton* image of NGC3044 from OBSID 0782650101. As with Figure 2.2, the D_{25} extent of NGC3044 is shown with the blue dashed ellipse, and the nuclear position with a white cross. The positions of the brightest ULX candidate in NGC3044, which we refer to as ULX1, and the nearby supernova 1983E are indicated.

has the best time resolution of the *XMM-Newton* detectors (73.4 ms in full frame mode). Source products are extracted from the cleaned event files with XMMSELECT. Given the relative proximity of supernova SN1983E (separated by $\sim$35″; see Figure 2.4), we use circular source regions of radius 15–20″, with the larger region size used for the higher flux observations (see below). Background is estimated from a larger region of blank sky on the same detector as ULX1. All of the observations suffer from periods of enhanced background to some degree, and for each observation we determine the background threshold that maximises the source S/N over the full *XMM-Newton* band considered in our more detailed analysis (0.3–10.0 keV) following the method outlined in Piconcelli et al. (2004). Only single and double patterned events are considered for EPIC-pn (PATTERN ≤ 4) and single to quadruple patterned events for EPIC-MOS (PATTERN ≤ 12), as recommended, and all of the necessary instrumental response files were generated using ARFGEN and RMFGEN. After performing the reduction separately for the two EPIC-MOS units, we combine their individual spectra using ADDASCASPEC.

Table 2.4: Details of the X-ray observations of NGC3044 ULX1 considered in this work.

Mission	OBSID	Start Date	Good Exposure (ks)[a]
XMM-Newton	0070940101	2001-11-24	6/8
XMM-Newton	0070940401	2002-05-10	9/21
XMM-Newton	0720252401	2013-05-06	9/11[b]
Swift	00092188001	2015-04-17	1
Swift	00092188002	2015-04-19	1
Swift	00092188003	2015-06-23	2
Swift	00092188004	2015-06-24	2
Swift	00092188005	2015-06-25	2
XMM-Newton	0782650101	2016-12-07	80/93

[a] *XMM-Newton* exposures are listed for the EPIC-pn/MOS detectors, after filtering for background flaring (see Section 2.5.1).
[b] ULX1 falls on a dead chip for the MOS1 detector in this observation.

2.5.2 Spectral Analysis

Based on the 4XMM-DR10 data, the first two *XMM-Newton* observations (2001 and 2002) both caught NGC 3044 ULX1 in a lower flux state, while the latter two (2013 and 2016) caught the source in a higher flux state. We therefore combine the *XMM-Newton* spectra from these pairs of observations using ADDASCASPEC to provide the highest S/N data possible for these two flux regimes. These spectra are shown in Figure 2.5.

We initially begin by fitting the high-flux data with a simple absorbed powerlaw model. We use XSPEC for our spectral analysis (Arnaud 1996), and allow for both the Galactic absorption column of $N_{\rm H,Gal} = 2.33 \times 10^{20}$ cm^{-2} (HI4PI Collaboration et al. 2016) and further absorption at the redshift of NGC 3044 ($z = 0.00430$) that is free to vary in all our models. Both absorbers are modelled using TBABS, and we adopt solar abundances from Wilms et al. (2000a) and absorption cross-sections from Verner et al. (1996). We also allow for cross-normalisation constants to float between the data from the pn and MOS detectors to account for residual calibration differences; these factors are always within a few per cent of unity. Finally, the higher flux data are grouped to a minimum of 25 counts per bin to facilitate the use of χ^2 minimisation. The absorbed powerlaw model returns a fairly steep continuum, with $n_{\rm H,high} = (2.1 \pm 0.2) \times 10^{21}$ cm^{-2} and $\Gamma_{\rm high} = 2.41 \pm 0.07$ (uncertainties on the spectral parameters are quoted at the 90% level). Unsurprisingly, the lower flux data have a much lower S/N (in addition to the lower flux, these data have a much lower combined exposure). We therefore group these data to just 1 count per bin, and fit them with the same model using the Cash statistic (Cash 1979). Here we find $n_{\rm H,low} = 1.1^{+0.8}_{-0.7} \times 10^{21}$ cm^{-2} and $\Gamma_{\rm low} = 2.3 \pm 0.4$. Within the limitations of the available data, there is therefore little evidence for spectral variability, although the parameter constraints are not particularly tight for the lower flux data.

Although the absorbed powerlaw model captures the overall shape of the spectrum in the 0.3-10.0 keV band fairly well, the high-flux data have sufficient S/N that systematic residuals to this simple model can be seen (see Figure 2.6), implying that a more complex continuum model is required. Indeed, the quality of fit provided by the absorbed powerlaw model for the high flux data is $\chi^2 = 353$ for 285 degrees of

Table 2.5: Key parameters obtained for the various continuum model fits to the high-flux data available for NGC3044 ULX1

Model Component	Parameter	Continuum Model		
		POWERLAW	DISKBB+POWERLAW	DISKBB+DISKPBB
TBABS	$N_{\rm H}$ [10^{21} cm^{-2}]	2.1 ± 0.2	$3.5^{+0.7}_{-0.6}$	3.0 ± 0.6
DISKBB	$T_{\rm in}$ [keV]	–	0.16 ± 0.02	0.19 ± 0.03
	Norm	–	37^{+80}_{-25}	13^{+26}_{-7}
POWERLAW	Γ	2.41 ± 0.07	2.2 ± 0.1	–
	Norm [10^{-5}]	6.1 ± 0.3	$5.0^{+0.6}_{-0.5}$	–
DISKPBB	$T_{\rm in}$ [keV]	–	–	$1.7^{+0.7}_{-0.4}$
	p	–	–	$0.56^{+0.15}_{-0.05}$
	Norm [10^{-4}]	–	–	$3.6^{+5.7}_{-0.5}$
χ^2/DoF		353/285	284/283	273/282

freedom (DoF), which is not formally an acceptable fit. This residual structure is fairly typical for extreme ULXs when fit with a single powerlaw model (*e.g.* Gladstone et al. 2009; Mukherjee et al. 2015; Stobbart et al. 2006), and indicates the need for distinct continuum components above and below ∼1–2 keV. We therefore fit the high-flux data with a few more complex models often used to describe ULX spectra. First, we fit a model consisting of a lower energy accretion disc component, and a higher energy powerlaw continuum. We use the DISKBB model (Mitsuda et al. 1984) for the former, which implicitly assumes a thin disc profile (Shakura and Sunyaev 1973), such that the model broadly represents the classic disc–corona geometry seen in sub-Eddington X-ray binaries. This provides a significant improvement to the simpler powerlaw fit, with χ^2/DoF = 284/283. The best-fit parameters are given in Table 2.5.

There is still a mild hint of curvature in the spectrum at higher energies though

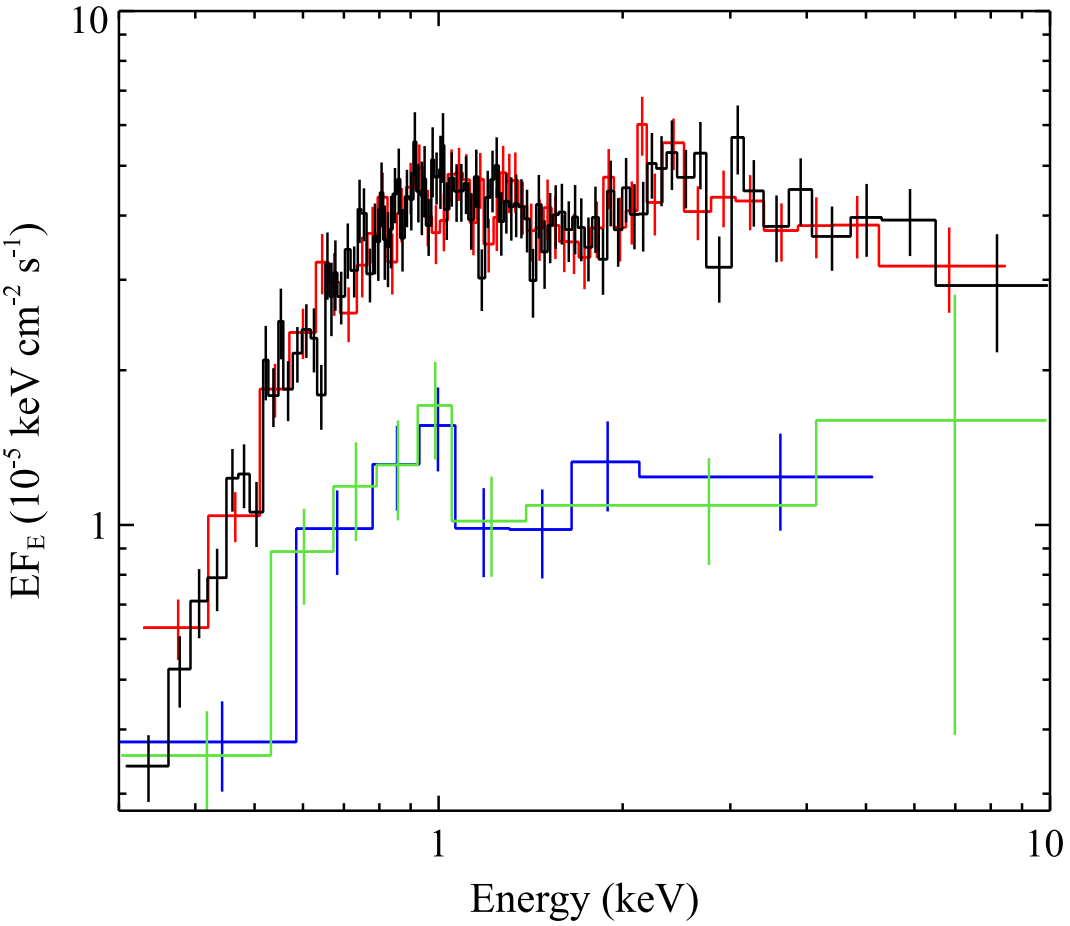

Figure 2.5: The *XMM-Newton* spectra of NGC3044 ULX1 from the high- and low-flux states seen in the available data, unfolded through a model that is constant with energy. The EPIC-pn data are shown in black and green, and the EPIC-MOS data are shown in red and blue. The data have been rebinned for visual clarity.

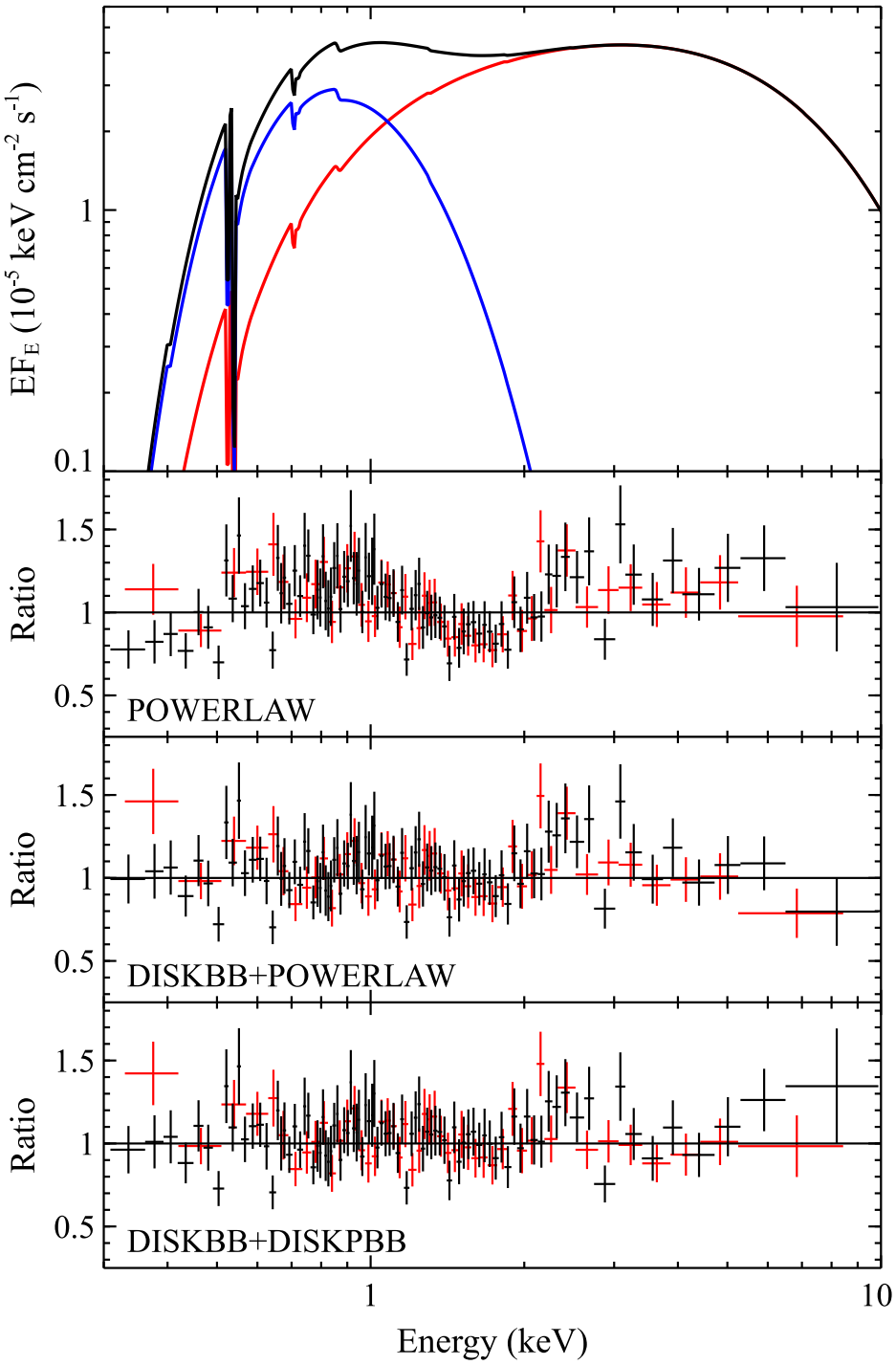

Figure 2.6: *Top panel:* The relative contributions of the best-fit DISKBB+DISKPBB model to the high-flux *XMM-Newton* data for NGC3044 ULX1. The total model is shown in black, the DISKBB component in blue and the DISKPBB component in red, respectively. *Lower panels:* The data/model ratio for a simple absorbed power-law continuum model, a DISKBB+POWERLAW continuum and the DISKBB+DISKPBB models, respectively. For the ratio panels, the colours have the same meanings as in Figure 2.5, and the data have again been rebinned for visual purposes.

($E > 2\,\mathrm{keV}$; Figure 2.6). This is seen in the majority of high S/N ULX spectra, initially implied by *XMM-Newton* (*e.g.* Gladstone et al. 2009; Walton et al. 2011a) and then unambiguously confirmed by the higher energy coverage provided by *NuSTAR* (*e.g.* Bachetti et al. 2013; Rana et al. 2015; Walton et al. 2014). These broadband observations find that ULX spectra are primarily described by two thermal components below 10 keV. We therefore also fit a second model that is often considered for ULXs, combining two accretion disc components.[4] Specifically, for the higher energy emission we replace the powerlaw component with a DISKPBB model (Mineshige et al. 1994). This allows for the radial temperature index (p) to be an additional free parameter, such that the model can mimic a thick, advection-dominated super-Eddington accretion disc (which would be expected to have $p < 0.75$ instead of the $p = 0.75$ appropriate for thin accretion discs; Abramowicz et al. 1988). The DISKBB+DISKPBB does provide a moderate additional improvement in fit over the DISKBB and powerlaw combination, with $\chi^2/\mathrm{DoF} = 273/282$ (*i.e.* an improvement of $\Delta\chi^2 = 11$ for one extra free parameter). As our best-fit model, we show the relative contributions of the different model components in Figure 2.6, and the parameter constraints are also given in Table 2.5.

The best-fit spectral form for NGC 3044 ULX1 differs somewhat from that used to compute the fluxes in 4XMM-DR10, so we also re-calculate the observed 0.3–10 keV fluxes for the individual *XMM-Newton* observations using the spectral models for the high- and low-flux states discussed above. To further examine the long-term behaviour of the source we also consider the *Swift* data at this stage. These observations can themselves be split into two main groups, taken in April and June 2015. We process the combined data from these two sets of observations, compute the average count rates for each of the two groups using the same 20″ regions as for the *XMM-Newton* data (correcting appropriately for the point spread function), and convert these to fluxes using the spectral shape implied by the simple powerlaw fits to the *XMM-Newton* data. The long term lightcurve combining the *XMM-Newton*

[4]The best *NuSTAR* data available for ULXs shows that a third continuum component is typically required above ∼10 keV to model the broadband spectra (*e.g.* Walton et al. 2018b). However, without coverage of these energies we cannot say anything about the presence of this component here, and so restrict ourselves to a simpler two-component model for the data below 10 keV.

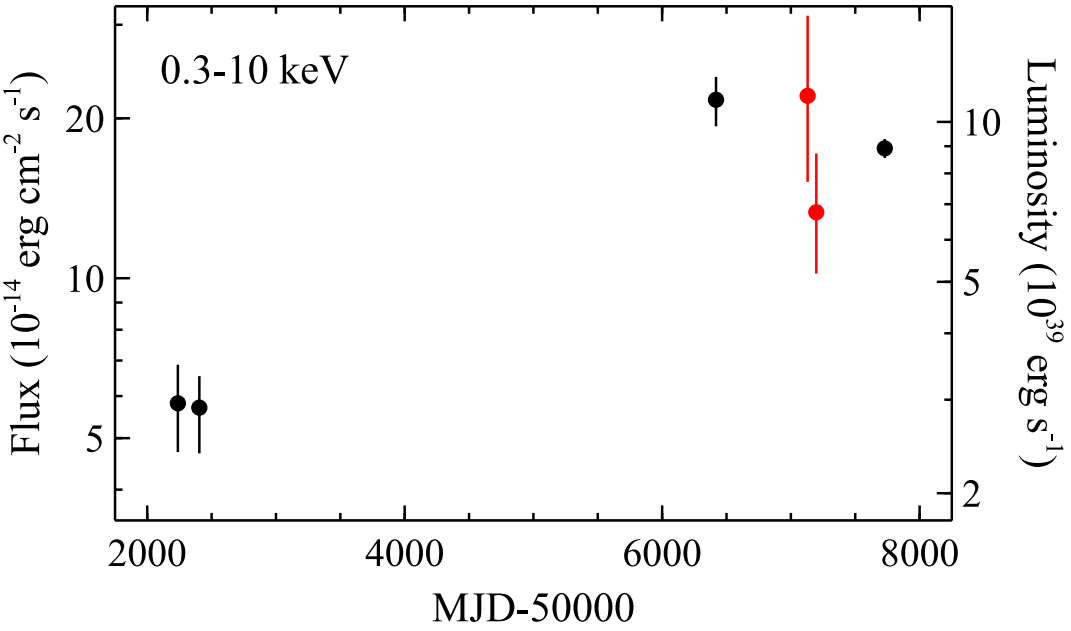

Figure 2.7: Longtime lightcurve for NGC3044 ULX1 based on the available X-ray data. *XMM-Newton* data are shown in black, and *Swift* in red. Note that the sets of *Swift* observations taken in April and in June have been combined together here (see Section 2.5.2).

and *Swift* data is shown in Figure 2.7. The coverage is admittedly sparse, but the *Swift* fluxes are consistent with the more recent *XMM-Newton* measurements, and so it appears as though the higher flux state persisted throughout 2013–2016. We also still find the peak luminosity of the source to be $L_{\rm X,peak} \sim 10^{40}\,{\rm erg\ s^{-1}}$, confirming the extreme luminosity implied by our analysis of 4XMM-DR10.

2.5.3 Timing Analysis

The longest of the available *XMM-Newton* observations of NGC 3044 ULX1, OBSID 0782650101, returns a total of ∼5000 net source counts with the EPIC-pn detector, roughly comparable to the quality of data used to detect X-ray pulsations for some of the known ULX pulsars (*e.g.* Israel et al. 2017a; Rodríguez Castillo et al. 2020). We therefore also perform a search for pulsations on this dataset. We focus on the data from the EPIC-pn detector here as this has both the highest count rate and the best timing resolution of the EPIC detectors (73.4 ms in the full-frame mode used for this observation).

For this analysis we use the pulsar timing tools included in the HENDRICS package

(Bachetti 2018). Since the pulse period can evolve rapidly in ULX pulsars, either due to the secular spin-up driven by the extreme accretion (Carpano et al. 2018; Fürst et al. 2016; Israel et al. 2017a; Vasilopoulos et al. 2018) or orbital motion of the neutron star (Bachetti et al. 2014; Fürst et al. 2021, 2018; Israel et al. 2017a), we perform an 'accelerated' pulsation search, which considers both the frequency of the pulsations (f) and its first derivative ($\dot{f}$) when searching for any signals. Specifically, we use the HENZSEARCH script, which performs the Z_n^2 search originally outlined in Buccheri et al. (1983), and allow for $n = 2$ harmonics in our search (*i.e.* we use the Z_2^2 statistic). Based on the properties of the known ULX pulsars, we focus on the frequency range of 0.01–6.75 Hz, and the "fast" search option utilized allows for $\dot{f}$ values in the range $\pm 10^{-8}$ Hz s^{-1}. Unfortunately we did not find any promising pulsation candidates in this observation.

In the absence of a robust pulsation detection, we estimate an upper limit on the pulsed fraction any undetected signal could have following the method used in Walton et al. (2021). In short, we use the HENZN2VSPF script, which simulates datasets using the same GTIs and total number of events as the real data, then uses rejection sampling to modulate the events with an increasingly strong pulsed signal (assuming a sinusoidal pulse profile, which is appropriate for ULX pulsars), and finally calculates the Z_2^2 for each pulsed fraction to see how strongly such pulsations would have been detected. We simulate 100 datasets in order to determine the pulsed fraction at which the Z_2^2 statistic reaches $\sim$40. This threshold roughly corresponds to a 3σ detection, and thus indicates the equivalent upper limit on the pulsed fraction that could still be present in the real data. We find an upper limit on the pulsed fraction of $\sim$22% when considering the full *XMM-Newton* bandpass.

2.5.4 The Nature of NGC 3044 ULX1

NGC 3044 ULX1 is a new extreme ULX discovered in our analysis that already has high S/N data available in the archive. Although it has always been in the ULX regime whenever observed with our current X-ray facilities (considering *XMM-Newton* and *Swift* in combination, we have observations from 6 different epochs), sometime between 2002 and 2013 it seemed to jump up by a factor of $\sim$3–4 in

luminosity from $L_{\rm X} \sim 3 \times 10^{39}\,{\rm erg\ s^{-1}}$ to $L_{\rm X} \sim 10^{40}\,{\rm erg\ s^{-1}}$, where it seems to have remained since (see Figure 2.7).

The 0.3–10.0 keV X-ray spectrum observed during this high-flux period is very similar to other extreme ULXs: the flux below 10 keV is dominated by two continuum components that primarily contribute above and below ∼1–2 keV and, although it is not a strong statistical detection, there is a hint of spectral curvature in the higher energy component. We note in particular that, although there is no higher energy coverage available here, the spectrum of NGC 3044 ULX1 is highly reminiscent of that seen from Holmberg II X-1 – another extreme ULX with $L_{\rm X,peak} \sim 10^{40}\,{\rm erg\ s^{-1}}$ – during the broadband observations performed with *XMM-Newton*, *Suzaku* and *NuSTAR* in 2013 (Walton et al. 2015). As noted previously, this was part of a series of broadband observations of ULXs (*e.g.* Bachetti et al. 2013; Mukherjee et al. 2015; Rana et al. 2015; Walton et al. 2014) that robustly confirmed earlier indications from *XMM-Newton* (*e.g.* Gladstone et al. 2009; Stobbart et al. 2006; Walton et al. 2011a) that the high-energy spectra of ULXs are distinct from those seen from sub-Eddington black holes. While the spectra from these systems are typically dominated by Comptonisation in an optically-thin 'corona' above ∼2 keV (*e.g.* Haardt and Maraschi 1991), the spectra of ULXs instead seem to be dominated by two thermal components below 10 keV, before falling away steeply at higher energies. Indeed, the best-fitting model for the high-flux *XMM-Newton* spectra from NGC 3044 ULX1 consists of two thermal accretion disc components.

The distinct broadband spectra of ULXs, along with the detection of X-ray pulsations (Bachetti et al. 2014; Carpano et al. 2018; Fürst et al. 2016; Israel et al. 2017a,b; Rodríguez Castillo et al. 2020; Sathyaprakash et al. 2019b) and extreme outflows (Kosec et al. 2018b; Pinto et al. 2017, 2016, 2020; Walton et al. 2016b) from a growing number of these systems have, together, helped clearly establish that the majority of the ULX population is dominated by super-Eddington accretors. In this context, the two continuum components seen in ULXs below 10 keV likely represent the complex thermal emisson from a hot, super-Eddington accretion disc (and potentially its associated outflow; *e.g.* Middleton et al. 2015; Poutanen et al. 2007). Given its similarity to other, better studied ULXs that are now well accepted

to be super-Eddington accretors, NGC 3044 ULX1 is therefore likely another super-Eddington system. As discussed above, these sources are of particular interest, as they may provide a local observational window into the conditions required to rapidly grow SMBHs in the early universe (*e.g.* Bañados et al. 2018).

We have searched for X-ray pulsations from NGC 3044 ULX1, which would unambiguously identify the accretor as another neutron star and confirm its nature as a highly super-Eddington system. We focused on the 2016 data, which by far have the best S/N among the available observations, and searched for pulsations over the 0.01–6.75 Hz frequency range based on the properties of the known ULX pulsars, but unfortunately we did not find a robust detection of any such variations. However, even though the available data has quite high S/N, we can only place an upper limit of ∼20% on the pulsed fraction of any pulsations present during this observation. Although pulsations of the strength seen in NGC 300 ULX1 can therefore be firmly excluded (pulsed fraction of ∼60% below 10 keV; Carpano et al. 2018), other known ULX pulsars exhibit pulsed fractions that are lower than this limit in the *XMM-Newton* bandpass (*e.g.* Rodríguez Castillo et al. 2020; Sathyaprakash et al. 2019b). Furthermore, even in ULXs that are known to be pulsars the pulsations can be transient, and are not always observed even when the data should have sufficient S/N to see them (*e.g.* Bachetti et al. 2020; Israel et al. 2017a). As such, even though we have not seen any clear evidence for X-ray pulsations from NGC 3044 ULX1, we cannot exclude the possibility that this is another neutron star ULX.

Although the comparison with other ULXs is quite compelling, obtaining higher energy data would be of particular use in order to more robustly confirm NGC 3044 ULX1 as another super-Eddington accretor. In the known ULX pulsars the pulsed fraction is seen to increase with energy, perhaps because non-pulsed components from the accretion flow make a more significant contribution below ∼10 keV (*e.g.* Walton et al. 2018b). Higher energy coverage would therefore help to mitigate against these issues in terms of further pulsation searches, and would also allow us to extend the continuum spectroscopy above 10 keV, and further confirm that the broadband spectrum of NGC 3044 ULX1 is similar to other ULXs. Unfortunately, given both the fairly low peak flux from NGC 3044 ULX1 ($\sim 2 \times 10^{-13}$ erg cm^{-2} s^{-1}

in the 0.3–10 keV band; see Figure 2.7) and the fairly close proximity of SN1983E (see Figure 2.4), meaningful observations of NGC 3044 ULX1 with *NuSTAR* would likely be very challenging. This may, instead, be a suitable target for a facility like the *High Energy X-ray Probe* (*HEX-P*; Madsen et al. 2018), which would have both superior sensitivity and imaging capabilities to *NuSTAR*.

2.6 Summary and Outlook

We have compiled a new catalogue of ULX candidates, combining the latest data releases from each of the *XMM-Newton*, *Swift* and *Chandra* observatories (the 4XMM-DR10, 2SXPS and CSC2 source catalogues, respectively). Our new catalogue contains 1843 sources residing in 951 different host galaxies, making it the largest ULX catalogue compiled to date. Of these, 689 sources are catalogued as ULX candidates for the first time. Our sample also contains 71 HLX candidates, of which 48 are new catalogue entries. We have made significant efforts to clean the catalogue of known non-ULX contaminants (e.g. foreground stars, background AGN, supernovae), and estimate that the remaining contribution of unknown contaminants is ∼20%. Our primary motivation here is to unearth new sources of interest for detailed follow-up studies, and among this new catalogue we have already found one new extreme ULX candidate with high S/N data in the archive: NGC 3044 ULX1. This shows a factor of at least ∼4 variability on long timescales, based on the available *XMM-Newton* and *Swift* data, with a peak luminosity of $L_{\rm X,peak} \sim 10^{40}\,{\rm erg\ s^{-1}}$ to date. The *XMM-Newton* spectrum of the source while at this peak flux is reminiscent of other extreme ULXs (and Holmberg II X-1 in particular), and is best-fit by a model combining two thermal accretion disc components. This likely indicates that NGC 3044 ULX1 is another member of the ULX population accreting at super-Eddington rates.

We anticipate this new catalogue will be a valuable resource for planning further observational campaigns, both with our current X-ray imaging facilities (*XMM-Newton*, *Chandra*, *Swift*, *NuSTAR*) and with upcoming missions such as *XRISM* and, in particular, *Athena*. Our new catalogue should also help to facilitate further

studies of ULXs at longer wavelengths, particularly in the era of the new optical, NIR and radio facilities due to come online (the thirty-metre class ground-based observatories, *JWST*, the SKA). Such work will be vital for determining the contribution of ULX pulsars to the broader ULX population, their accretion physics, the prevalence of extreme outflows among the ULX population and the impact of the winds launched by super-Eddington accretors, and for the hunt for the first dynamically confirmed black hole ULX. Further iterations of the *XMM-Newton*, *Swift* and *Chandra* serendipitous surveys, combined with the upcoming results from *eROSITA* (Predehl and eROSITA Consortium 2021), will also allow us to continue expanding this ULX sample in the future.

2.7 Epilogue

Around the time at which the results of this chapter were formally published, Bernadich et al. (2022) also published a ULX catalogue built from an earlier *XMM-Newton* data release to the one used in this chapter. Shortly after, an alternative multi-mission catalogue using data from across *Swift*, *XMM-Newton* and *Chandra* was published by Tranin et al. (2024). Here we explore our work in the context of these other, published ULX catalogues.

2.7.1 Bernadich et al. 2022

Bernadich et al. (2022) used the Fourth *XMM-Newton* Serendipitous Source Catalog, Ninth Data Release, (4XMM-DR9, Webb et al. 2020) as the basis for their ULX catalogue. This is the release prior to 4XMM-DR10 that was used in our multi-mission catalogue. The catalogue construction methods used are similar to those of our catalogue, broadly following the processes set out by Walton et al. (2011b) and Earnshaw et al. (2019b).

Bernadich et al. (2022) use the stacked version of 4XMM-DR9 combined with the Heraklion Extragalactic CATaloguE (HECATE, Kovlakas et al. 2021). From the overlapping observations, extra source variability parameters that are not included in the bare 4XMM-DR9 are computed into this stacked version of 4XMM-DR9.

However, this does still lose some of the observation-by-observation level information available in this chapter. The final catalogue contains 779 ULX candidates whereas our complete catalogue contains 1843 ULX candidates. This discrepancy is to be expected given the multi-mission nature of our catalogue as using the data from a greater number of soft, X-ray telescopes gives us more spatial and temporal coverage. However, when we break down our own catalogue into its constituents (as described in Table 2.2) our *XMM-Newton* component gives 641 ULX candidates, which makes for a better comparison with Bernadich et al. (2022) and a comparison of our catalogue and both Bernadich et al. (2022) and Tranin et al. (2024) can be found in Table 2.6.

Sources are correlated with galaxies when they overlap within the isophotal ellipses defined by HECATE within their positional uncertainty. Bernadich et al. (2022) flag central sources as any source whose position overlapped with a circle of radius 3" around the host galaxy centre within three times their uncertainty. This is a much more lenient cut than the conservative $R_{\mathrm{min,excl}} = 9''$ used in the *XMM* portion of our catalogue. They inspect candidates assigned to multiple host galaxies and ensure that any entries of a flagged central source are marked across any optically coincident galaxies. They adopt the method of flagging sources, as opposed to our work where poor ULX candidates (those excluded by nucleus proximity, matched with a background QSO etc.) are removed from the catalogue and piped away to separate, respective tables. The result is that the final Bernadich et al. (2022) catalogue contains all of their 4XMM-DR9 sources within a HECATE D_{25} ellipse and we are only ultimately concerned with those flagged as $ULXCand = 1$.

Potential foreground stellar objects are identified by matching against *Gaia* DR2 (Gaia Collaboration 2018) and Tycho2 (Høg et al. 2000), with a positional tolerance of three times the positional uncertainty required on both sides of the cross-match. Bernadich et al. (2022) then make use of additional optical information, taking optical fluxes F_{V} from *Gaia* DR2, beyond the positional information solely used to remove foreground object matches in our catalogue. They look to generate X-ray to bolometric flux ratios for their candidates, but in the absence of a measure of bolometric flux, F_{BOL}, Bernadich et al. (2022) instead approximate it as the optical

flux of the star, $F_{\rm V}$. They determine $log(F_{\rm X}/F_{\rm V})$ (with $F_{\rm X}$ taken in the 0.2-12 keV band) using the following from Maccacaro et al. (1988):

$$log(F_{\rm X}/F_{\rm V}) = log(F_{\rm X}) + \frac{m_V}{2.5} + 5.37$$

X-ray binaries and ULX candidates typically have X-ray/optical flux ratios, $log(F_{\rm X}/F_{\rm V}) \geq 0$ (Lewin and van der Klis 2006), so any candidate with a flux ratio above 0 is retained. A value of $log(F_{\rm X}/F_{\rm BOL}) < -2.2$ is highly likely to be a foreground star and so anything below this is flagged as such. For those candidates with $0 > log(F_{\rm X}/F_{\rm V}) >$ -2.2, Bernadich et al. (2022) nominally flag them as stars, however, each source is manually inspected to determine whether the optical flux is instead associated with host galaxy material and thus the source can be kept as a candidate. This is necessary given bright regions of galaxies (which can host ULXs) will dilute the X-ray/optical flux ratio.

One issue we ourselves identified with cross-matching against data releases from *Gaia* was that the sheer scope of the survey meant that a simple positional cross-match resulted in all ULX candidates being assigned a counterpart from *Gaia*. Removing ULX candidates as foreground stars based only on an existing match in *Gaia* DR2 would drastically and incorrectly reduce the catalogue size. Bernadich et al. (2022) have mitigated this by using the optical magnitudes and flux ratios, but make no further use of other information available in *Gaia* DR2 such as proper motions that would clearly identify objects as foreground Galactic.

Bernadich et al. (2022) eliminate background QSOs in a similar method to our own (albeit by cross-matching against SDSS-DR14 instead of GaiaunWISE) and similarly cross-referencing against the SIMBAD database for keywords such as "Star" or the "*" symbol, "AGN", "AGN Candidate", "QSO", "QSO Candidate" or "SN" for flagging. There is no mention of using the temporal information, as we did, to confirm or deny matches with main type = SN in SIMBAD. Their subsequent analysis of their bright luminous ULX candidates, classified as having $L_{\rm X} > 5 \times 10^{40}$ erg s^{-1} and their HLX candidates goes beyond the scope of what was covered in this chapter since, at the time of publication, it had been left to a subsequent work which we shall cover in Chapter 3.

When assessing the residual contamination, Bernadich et al. (2022) observe the number of objects in each group (AGN, QSO, stellar object etc.) that would have been classified as ULX candidates if it were not for their association. In total, they would constitute 11.5% of the quality ULX candidates. They then determine whether this method has overshot or has been insufficient, by comparing the number of expected background sources to the identified ones. It is concluded that the filtering pipeline does a good job of identifying most of the background contaminants, but also that ∼2% of sources may still be unidentified background sources, including ∼15 ULX candidates. This suggests an estimate for the unknown contamination fraction well below that which has been found previously in archival ULX catalogues and this work. However, it relies on a much simpler sensitivity estimate which likely leads to a severe underestimation of the background.

2.7.2 Tranin et al. 2024

Tranin et al. (2024) and our catalogue are multi-mission ULX catalogues, both using information from *Swift*, *XMM-Newton* and *Chandra*. Previous ULX catalogues, including the recent Bernadich et al. (2022), have focused on a single X-ray observatory. As such, Tranin et al. (2024) and our complete catalogue are more justifiably compared numerically, although they differ somewhat in their construction.

More recent ULX catalogues make use of ever larger galaxy catalogues to be more complete. Some examples include HyperLEDA with 965,795 galaxies (Makarov et al. 2014) which was used in building our catalogue; or HECATE with 204,733 galaxies within 200 Mpc (Kovlakas et al. 2021) used by Kovlakas et al. (2020) and Bernadich et al. (2022). Tranin et al. (2024) used a recent compilation of galaxy catalogues, GLADE (Galaxy List for the Advanced Detector Era, Dálya et al. 2018). GLADE contains more than 270,000 entries at D <200 Mpc, ∼30% more than HECATE for the same distance range. However, unlike the other galaxy catalogues, GLADE does not contain any information on the galaxy morphology. To get a more complete census of spiral and elliptical galaxies, they cross-correlate GLADE with the catalogue of galaxy morphologies inferred by machine learning on *PanSTARRS* images (Goddard and Shamir 2020). As a result, Tranin et al. (2024) obtain morphologies

for $\sim$1 million galaxies.

This galaxy sample was matched against CSC2.0, 2SXPS and a later *XMM-Newton* data release than ours, 4XMM-DR11. When matching X-ray sources onto the footprints of the galaxy sample, Tranin et al. (2024) make use of the Holmberg diameter $D_{\rm Holm} = 1.26 \times D_{25}$, defining it as the major axis of each galaxy. In our catalogue we make use of the Holmberg radius $R_{\rm Holm} = (1.26 \pm 0.02) R_{D_{25}}$ information within CNG only in order to normalise it back to the D_{25} definition. The result is that the galaxies in Tranin et al. (2024) have a larger footprint for matching when compared to our catalogue. While this does result in more matches and thus retains more ULX candidates moving forward into later analysis, increasing the foreground galaxy footprint increases the false ULX detection likelihood due to higher background contamination. In addition, Tranin et al. (2024) also consider a much less conservative exclusion radius for the galaxy centres, $d > 3(POSERR + 0.5)$ for all three catalogues.

Using the large existing datasets for both AGN and stars is one of the most common methods of filtering out these types of contaminants (e.g. Kovlakas et al. 2020; Walton et al. 2022). The alternate option, applied in Bernadich et al. (2022), is to remove all sources that are too bright in the optical to be a ULX. In contrast, Tranin et al. (2024) make use of their own automated probabilistic classification of X-ray sources. The classification is based on three classes: AGN, X-ray binaries and soft sources; with the former corresponding to background contaminants and most sources located in galaxy centres, while the latter are a miscellaneous class containing stars, supernovae and supernova remnants, which are both *in-situ* within the host galaxies and foreground contaminants. To assign each source to a given class the X-ray data is complemented with information on their optical and infrared counterparts from large ground-based surveys; galaxies hosting the source; X-ray variability ratio between multi-instrument observations; and source identification given by external catalogues. The Tranin et al. (2024) classifier is very efficient at retrieving AGN, and retrieves more than 80% of X-ray binaries. It is stated that false positive rates are also low ($\leq$15%) and can be further decreased by applying a probability threshold on the class under consideration.

Table 2.6: Details of the Bernadich et al. (2022) and Tranin et al. (2024) ULX catalogues compared to our work.

Catalogue[+]	ULX Candidates Total	Host Galaxies	HLXs	Avg. Distance [Mpc]	Contaminant Fraction*
Walton et al. (2022)	1843	951	71	74.7	20%
Tranin et al. (2024)	1901	1303	191	75.0	2%
Walton et al. (2022)	641	403	22	62.3	18%
Tranin et al. (2024)	667	599	115	73.3	2%
Bernadich et al. (2022)	779	517	30	37.0	2%

[+] The upper portion of the table corresponds to a comparison of the full, 3-mission catalogues described here in Chapter 2 and by Tranin et al. (2024). The lower portion only compares the contributions from *XMM-Newton* and is listed for better comparison with Bernadich et al. (2022).
* These contamination values are quoted directly from their respective works but do not correspond to the same calculation and are unsuitable for comparison.

The large number of ULX candidates found by Tranin et al. (2024) is partly explained by the choice of nuclear exclusion radius and using the host galaxy Holmberg radius, as above. However, the catalogue is not only presented as the largest ULX catalogue to date, but also the cleanest. Some contaminants will remain in their sample after the filtering process described above. To remove them, Tranin et al. (2024) match their sample with Simbad (3 arcsec) and exclude objects of types AGN or stellar objects. They find that 75% of these objects were already successfully identified by their classification. They also visually inspect all ULX candidates with an optical counterpart. There are 327 sources across *XMM-Newton*, *Swift* and *Chandra* that are discarded in this process and this reduces their remaining contaminant fraction down to about 2%. This is significantly lower than was found in previous catalogues (Earnshaw et al. 2019b ∼24%; Walton et al. 2011b ∼24%; Walton et al. 2022 ∼20%) and is established solely on their own classification algorithm (Tranin et al. 2022).

2.7.3 Conclusions

Table 2.6 shows an overview of the contents of each catalogue, while a direct comparison of the level to which their contents overlap can be found in Table 2.7. A visual comparison of the three catalogues is shown in Fig 2.8. In the case of these two relatively nearby galaxies, NGC 4258 (7.3 Mpc) and NGC 6946 (7.7 Mpc) both chosen for illustrative purposes, we identify more ULX candidates in our catalogue than Bernadich et al. (2022) or Tranin et al. (2024). Given our use of data from 3 different missions and the size of the overall catalogue, it would be expected that our total number of candidates in these two galaxies would be greater than that found by Bernadich et al. (2022). In this case, even considering only data taken from *XMM-Newton*, we identify an additional ULX candidate in NGC 6946. However, the Tranin et al. (2024) multi-mission catalogue is larger and this is likely to do with more distant galaxies, see Fig 2.9. More distant galaxies subtend smaller angles on the sky and so the larger galaxy footprint (defined by Holmberg radius over the D_{25}) and less conservative nuclear exclusion used by Tranin et al. (2024) will allow for a greater ULX candidate contribution from those galaxies. However,

for closer galaxies, our larger number of sources are largely *Swift* ULX candidates. *Swift* has extensive (albeit shallower) coverage and so our greater temporal coverage by considering luminosities at the per observation level reveals a greater number of ULX candidates in these galaxies.

The Bernadich et al. (2022) catalogue and this work represent the latest and largest ULX candidate catalogues assembled in the way established by Walton et al. (2011b) and Earnshaw et al. (2019a). The work in this chapter, published in Walton et al. (2022), is the largest catalogue of ULX candidates assembled in this way and is the only one which uses data from across three independent X-ray missions. While our catalogue uses a later edition of data from *XMM-Newton* than Bernadich et al. (2022) (4XMM-DR10 instead of 4XMM-DR9), the *XMM-Newton* portion of our catalogue contains fewer ULX candidates, in part due to our use of less lenient constraints for cross-matching and nuclear exclusion. The assembly of the Tranin et al. (2024) catalogue represents an alternate and novel statistical method for finding ULX candidates. The Tranin et al. (2024) catalogue compares closely to our own since it also uses data from across *Chandra*, *Swift* and *XMM-Newton*. However, they end with a larger final sample, partly due to using host galaxy footprints defined by the larger Holmberg radius over the D_{25} during cross-matching and a more lenient nuclear exclusion. This sample of ULX candidates, the largest to date, also only has a residual 2% unknown contaminant fraction provided their object classification algorithmn works as successfully as they claim.

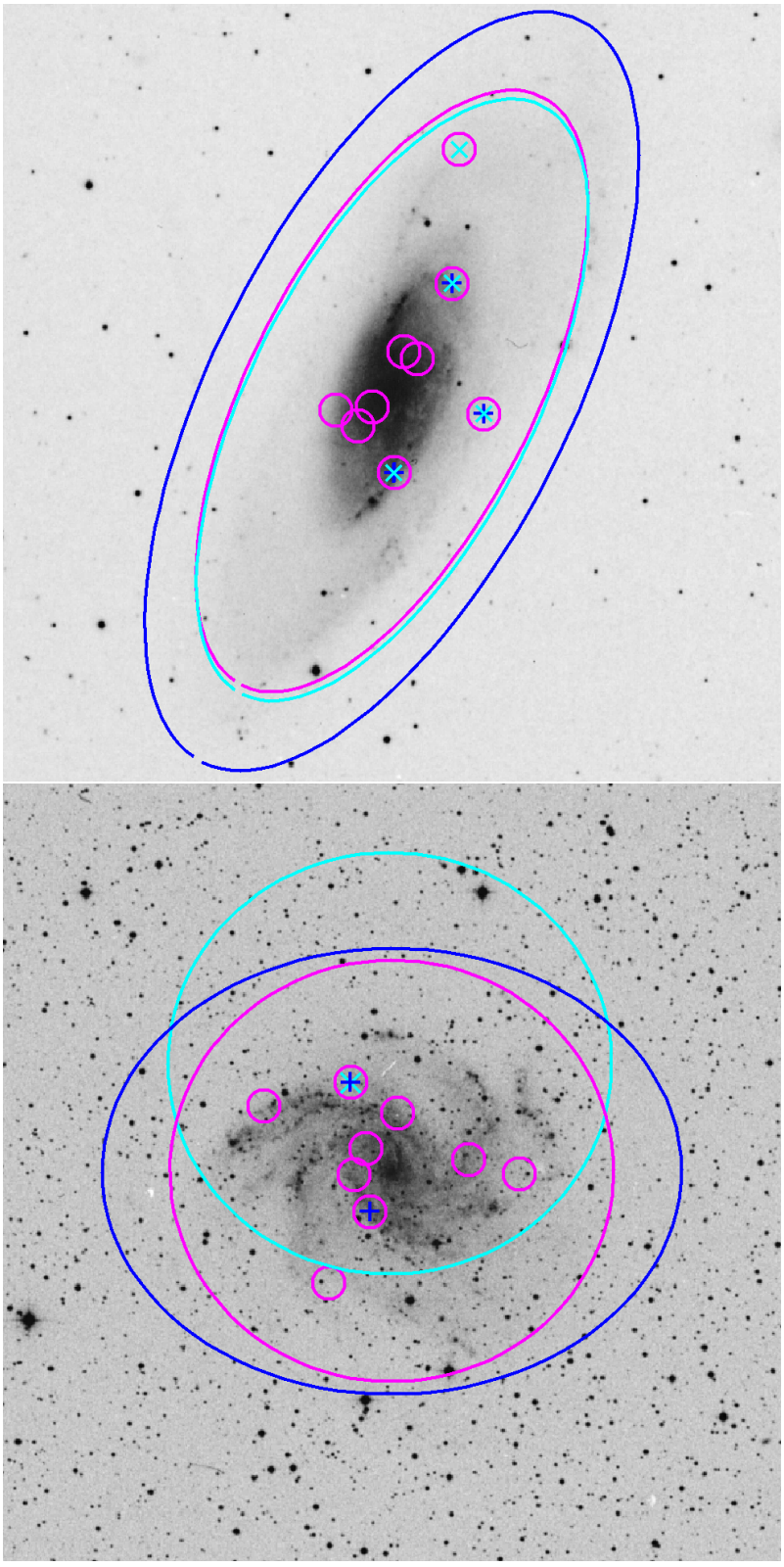

Figure 2.8: ULX candidate positions from Walton et al. (2022) (magenta circle), Bernadich et al. (2022) (cyan cross 'x') and Tranin et al. (2024) (dark blue cross '+') catalogues overlaid on optical images of NGC4258 (top) and NGC6946 (bottom). The corresponding coloured ellipses represent the footprint of the galaxy used by each catalogue. We suspect the Bernadich et al. (2022) NGC6946 footprint is due to a numerical error in the host galaxy RA and Dec.

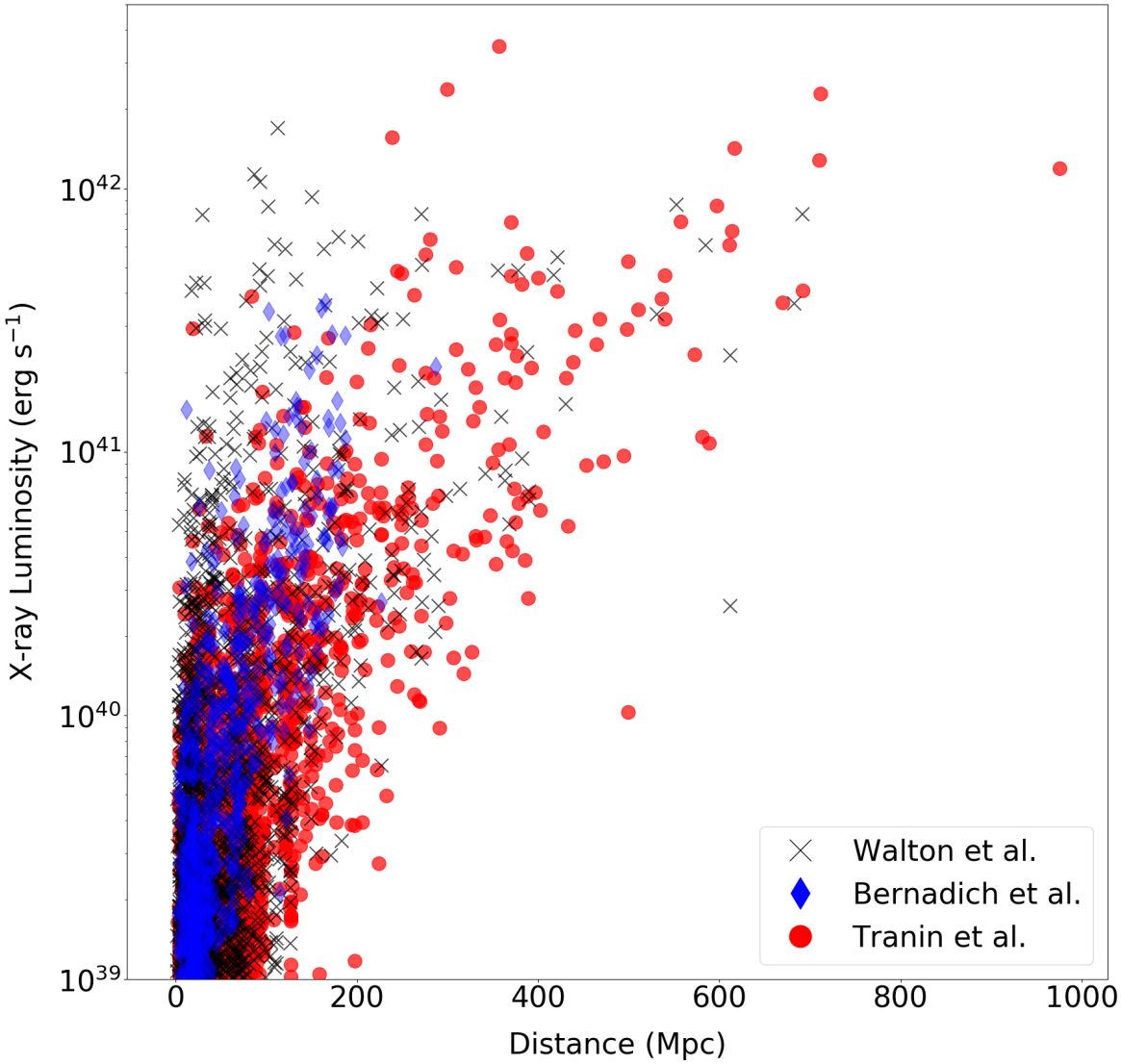

Figure 2.9: Visual comparison between the average X-ray luminosity and distance for the ULX candidates of the different catalogues; Walton et al. (2022) (black 'x'), Bernadich et al. (2022) (blue diamond) and Tranin et al. (2024) (red circle).

Table 2.7: Table showing the level of statistical overlap between the three catalogues; Walton et al. (2022), Bernadich et al. (2022) and Tranin et al. (2024).

	Unique			W v B	W v T	B v T	All
	W*	B	T				
	807	257	871	143	651	136	242

* Where W, B and T represent the Walton et al. (2022), Bernadich et al. (2022) and Tranin et al. (2024) catalogues respectively. The remaining columns then show the number of sources common to both catalogues, for example W v B is the number of sources found both in Walton et al. (2022) and Bernadich et al. (2022) but not in Tranin et al. (2024). The 'All' column denotes sources common to all three catalogues.

Combine the extremes, and you will have the true center.

- Karl Wilhelm Friedrich Schlegel

CHAPTER 3

Hyperluminous X-ray Sources

In this chapter we examine the hyperluminous X-ray source (HLX) population of the Walton et al. (2022) multi-mission catalogue of ULXs presented in Chapter 2. The catalogue contains 71 hyperluminous X-ray source (HLX) candidates; these are the most extreme members of the ULX population with luminosities above 10^{41} erg s^{-1}. These sources are often considered the best candidates for possessing IMBH accretors and include the archetypal IMBH candidate ESO 243-49 HLX-1. However, the most luminous of the known pulsating ULXs (PULXs), NGC 5907 ULX, is also a HLX at its brightest. We demonstrate that these two objects occupy distinct areas of the hardness-intensity parameter space, and use this to contextualise the results from our study of the 20 best HLX candidates in the Walton et al. (2022) catalogue.

3.1 Introduction

Hyperluminous X-ray sources (HLXs) are a sub-population of the wider ULX class, defined as having $L_{\rm X} \geq 10^{41}$ erg s^{-1} (Gao et al. 2003). As a sub-class of ULXs, HLXs are also found in external galaxies and are disassociated from the host nucleus (to discount accreting SMBHs). At their defined luminosities, HLXs can include accret-

ing binary systems where the degenerate compact object is violating its Eddington limit by several orders of magnitude (with $L_{\rm X}/L_{\rm Edd} \sim 500$ for NGC 5907 ULX; Israel et al. 2017a). Studying HLXs, the very brightest (and by extent most extreme) sources amongst the wider ULX population, allows us to understand just how extreme super-Eddington accretion can become. We only know of a small number of HLXs and the sub-class constitutes only a few percent of the wider ULX population (Kaaret et al. 2017). A few 10s of HLXs have been identified compared to the ∼2000 ULX candidates in the most recent ULX catalogues from Walton et al. (2022) and Tranin et al. (2024). Some of these HLX candidates were then found to be background AGN or QSOs during deeper studies (Barrows et al. 2024; Earnshaw et al. 2019a; Sutton et al. 2015), further diminishing the already small sample.

Just as with ULXs, one way to attempt to increase our understanding of HLXs is to widen the pool of known sources by constructing new HLX catalogues. In some cases this can be done from scratch where the catalogue is built up as described in chapter 2, with the exception of applying a $L_{\rm X} \geq 10^{41}\,{\rm erg\,s^{-1}}$ luminosity cut instead (see Barrows et al. 2019; Zolotukhin et al. 2016 for examples). Another method is to build a catalogue of ULXs and then identify the HLX sub-population within your sample, effectively establishing a sub-catalogue of HLXs as is the case here from Walton et al. (2022) or as done by Tranin et al. (2024).

Both PULXs and good IMBH candidates are rare. However, it is clear that the ULX population is heterogeneous to some degree, and strong candidates for both IMBHs and PULXs have been identified. For PULXs, these include M82 X-2 (Bachetti et al., 2014), NGC 7793 P13 (Fürst et al., 2016; Israel et al., 2017b), NGC 300 ULX-1 (Carpano et al., 2018), NGC 1313 X-2 (Sathyaprakash et al., 2019b) and M51 ULX-7 (Rodríguez Castillo et al., 2020); IMBH candidates include M82 X-1 (Feng and Kaaret, 2010; Pasham et al., 2014) and NGC 2276–3c (Mezcua et al., 2015). In principle, reaching HLX luminosities ($L_{\rm X} \geq 10^{41}\,{\rm erg\,s^{-1}}$) is more readily explained for an IMBH, which could remain sub-Eddington. However, for a PULX (which must have a NS accretor) to reach these X-ray luminosities requires violating the Eddington limit by at least two orders of magnitude. The detection of the source ESO 243-49 HLX-1, which is a very strong candidate for hosting an IMBH, with

a multitude of supporting evidence short of a dynamical mass measurement (Davis et al. 2011; Farrell et al. 2014, 2009; Godet et al. 2014; Webb et al. 2014), confirms HLXs can be IMBHs. However, NGC 5907 ULX, a source which has been detected with a peak X-ray luminosity in the HLX regime and has coherent pulsations (Israel et al. 2017a), shows that at least the lowest luminosity HLXs could also be NS ULXs.

The general properties of ESO 243-49 HLX-1 align with those observed in sub-Eddington BH binaries, albeit scaled up, as expected of an IMBH candidate. The source is characteristically soft at high luminosities, with a strong disc component dominating a thermal state with temperatures of $< 0.26\,\mathrm{keV}$ and spectra not well constrained by a simple absorbed powerlaw (Servillat et al. 2011; Webb et al. 2012). Critically, ESO 243-49 HLX-1 has been observed to undergo spectral state transitions similar to those observed in BH binaries. The *Swift* monitoring by Servillat et al. (2011) revealed that at low luminosities the spectrum is dominated by a hard power law with a photon index in the range $1.4-2.1$, consistent with a hard state. Two fast rise and exponential decay type outbursts separated by just over a year were also observed in the *Swift* XRT data with a $\sim 40\times$ increase in the count rate. Webb et al. (2012) report the detection of transient radio emission at the location of ESO 243-49 HLX-1, which is consistent with a discrete jet ejection event (for more on the radio properties see Cseh et al. 2015). Previously, ESO 243-49 HLX-1 has gone through long periods of quiescence and Lasota et al. (2011) proposed that it may be a binary system with an eccentric orbit. The outburst observed at the beginning of 2015 occurred ∼460 days after the prior outburst (Kong et al. 2015) and ESO 243-49 HLX-1 then returned to an apparent state of quiescence for more than 800 days until observed in a high X-ray flux state by *Swift* in 2017 (Yan and Yu 2017). The source has now been in a prolonged, low state since it was last seen in outburst in 2019 (Lin et al. 2020). This has led to the suggestion that the ESO 243-49 HLX-1 accreting system is actually an extremely long-lived tidal disruption event of a companion star that orbits the IMBH on a highly elliptical orbit. The recent quiescence may be due to the star being ejected from the system, ending the previously observed X-ray flaring and radio jets (Webb et al. 2023).

NGC 5907 ULX is a very different source. As one of the few ULXs with confirmed detections of coherent pulsations, the accreting, degenerate, compact object in the binary system is a NS. Israel et al. (2017a) observed a spin period evolving from 1.43 seconds in 2003 to 1.13 seconds in 2014 and an isotropic peak luminosity of ∼1000 times the Eddington limit for a NS at 17.1 Mpc. While standard accretion models cannot account for reaching these luminosities, even under the assumption of beamed emission, the existence of a strong magnetic field can help explain its properties. In contrast to ESO 243-49 HLX-1, NGC 5907 ULX is characterised by a much harder spectrum with a hard power-law tail at energies above 10 keV (Fürst et al. 2017). Below 10 keV the X-ray spectra are well represented by accretion disc models, but is lacking emission in the soft X-ray regime (Sutton et al. 2013a). This cool disc-like component, thought to be explained by radiatively-driven ULX winds (Kajava and Poutanen 2009; Middleton et al. 2011), may be hidden as a result of the high column density along the line-of-sight to the source. NGC 5907 is an edge-on galaxy and so the soft X-ray component is likely more heavily absorbed by material in the host galaxy.

NGC 5907 ULX is known for its fast spin-up during the on-state (Fürst et al. 2023) and long-term *Swift* monitoring by Walton et al. (2016a) revealed the detection of a ∼78 day period in the X-ray light curve. Fürst et al. (2023) found that the source was in an off- or low-state between mid-2017 to mid-2020. During this state, the pulse period monitoring showed that the source had spun down considerably. This spin-down is likely due to the propeller effect, a phenomenon in accreting NS systems whereby accretion is halted due to an interaction between the rotating magnetic field and the accreting matter.

This chapter is structured as follows: in Section 3.2 we filter our initial 71 HLXs to remove likely AGN contaminants, and in Section 3.3 we discuss our treatment and processing of the X-ray data from each of the three missions. Section 3.4 presents our model-independent pilot analysis of the *Swift* portion of our 38 good HLX candidates and we highlight the different methods we use to obtain spectral information, colours and resultant behaviour we observe in Section 3.5. Finally, we discuss our findings in the context of the wider field in Section 3.6.

3.2 HLX Sample Cleaning

In Chapter 2 we relied on a long-established series of steps to both select candidate ULXs, and to clean the sample of host galaxy AGN and foreground/background contaminants, detailed in Section 2.3 (see also Earnshaw et al. 2019b; Walton et al. 2011b). In particular, we took a conservative stance in terms of nuclear exclusion radii, excising regions around the host galaxy nuclei based on an empirical selection of a region that covers 99% of all objects at AGN-like luminosity ($> 10^{42}$ erg s^{-1}), which allows for poor nuclear positioning and/or offset supermassive black holes in the host galaxies. This results in exclusion radii of 9" for *XMM-Newton* and *Swift* data, and 6" arcseconds for *Chandra*. A similarly conservative stance was taken when excluding other contaminants, with any detected object in the Tycho2 stellar catalogue (Høg et al. 2000), or in the GaiaunWISE or Véron AGN/QSO catalogues (Shu et al. 2019; Véron-Cetty and Véron 2010) within a radius of 3"/5"/10" of the position of a ULX candidate from CSC2.0, 4XMM-DR10 or 2SXPS removed respectively. The same radii were used for final exclusions against supernovae (where the X-ray source was detected after the detonation), and any other contaminants identified in the NED[1] or Simbad[2] databases, or in the literature.

This methodology, while largely successful, is not necessarily complete - for example, individual contaminants can slip through if not explicitly in the catalogues utilised (cf. Roberts et al. 2023). Indeed, it leaves a residual contamination fraction that can be estimated by considering the sensitivity of the observations contributing to the serendipitous survey data, and log$N$-log$S$ curves derived from surveys. We calculated this to be at the $\sim$ 20% level for our candidate ULXs with *XMM-Newton* and *Chandra* detections[3]. Here we repeat the calculation, but using the much higher luminosity threshold for HLXs. We find that the contamination fraction rises to $\sim$ 30% for 4XMM-DR10 ULX candidates (an expectation of 4.4 hard band contaminants, after Walton et al. (2022) removed 6 objects as identified con-

[1] `https://ned.ipac.caltech.edu/`

[2] `http://simbad.cds.unistra.fr/simbad/`

[3] This is fairly typical for ULX surveys, although Tranin et al. (2024) and Bernadich et al. (2022) claim far lower contamination ($\sim$ 2%) with the former using X-ray and multi-wavelength data to statistically classify sources

taminants, compared to 14 hard band detections) and is much higher still for CSC2.0 sources at $\sim 60\%$ (12.5 expected hard band detections after known contaminants removed, compared to 20 actual hard band detections), with the latter most likely a result of Chandra's greater sensitivity to low fluxes, and greater spatial resolving power particularly when observing more distant ($d > 100$ Mpc) galaxies.

Given these potential high levels of contamination, we undertook further analysis to produce a cleaner sample of HLXs. As our sample constituted 71 candidate HLXs, this was a manageable number for a by-eye analysis of multi-wavelength counterparts using Aladin-lite[4]. We searched the positions of the HLX candidates in the variety of optical, IR and UV catalogues available on that platform and judged objects based on whether they had no discernable counterpart, or lay directly coincident with structure in the host galaxy (both acceptable); or whether they had a point-like or extended counterpart that did not appear (either through position, or distinct colours) to be directly associated with the host galaxy (rejected). The latter criteria is designed specifically to remove background AGN; however it will in many cases also encompass the nuclei of neighbouring galaxies and/or satellite dwarf galaxies, particularly for objects beyond ~ 100 Mpc distance. We note that removing such objects is a distinct difference between this analysis and the work of Tranin et al. (2024) and Barrows et al. (2024), as they explicitly include HLXs associated with candidate dwarf galaxy nuclei in their sample. A total of 23 candidates are removed by this step, with those objects removed listed in Table 3.1.

For the remaining HLX candidates, the X-ray data corresponding to their Walton et al. (2022) catalogue entry was examined for anomalies. In particular, we looked for detections that were from a single mission, that were low significance, that were made solely in one *XMM-Newton* detector and/or energy band, or that were from a single blind detection in *Swift* data. We also looked for questionable detections due to the presence of other bright objects and/or strong diffuse emission. From this, a total of 10 more HLX candidates (3 from 4XMM-DR10, 7 from 2SXPS) were rejected; they are also listed in Table 3.1, and some examples of rejected objects

[4] `http://aladin.cds.unistra.fr/AladinLite/`

(alongside those we kept) are shown in Fig. 3.1.

This combination of visual checks reduces our HLX candidate sample by close to a factor 2, down to 38 HLX candidates. We note that although we do not consider the objects in Table 3.1 any further in this chapter, we have not conclusively rejected any of them as HLXs. Instead, given our suspicions on their possibly spurious nature, we focus our analysis in the remainder of this chapter on the 38 objects for which no strong reason to doubt their validity as HLXs exists at this point (although we revisit this in Section 3.5.2).

3.3 Data Selection and Reduction

In the remainder of this chapter we focus our analysis on the available X-ray data for the retained HLX candidates. In particular, we focus on the same three missions as Walton et al. (2022). Data for each source was obtained on a rolling basis between the dates August 2022 to November 2023. We summarise the extent of data for each source in Table 3.2 where the total number of observations, and the integrated good exposure time, per observatory per HLX candidate are shown. In total, we used data from 895 observations (79/42/774 from *XMM-Newton*/*Chandra*/*Swift*, respectively), totalling 4268 ks of exposure (1653/1345/1270).

We limited our analysis to the 0.3-10 keV band common to the three missions (accepting that the response of *Chandra* ACIS-S in particular is relatively limited at either end of this range, and indeed has become increasingly degraded over the lifetime of the detector at its soft end). All spectra were extracted in this range, and images used to provide aperture photometry were created in either the full 0.3-10 keV range or in two sub-bands, split at 2 keV, where a colour was derived. More details of the reduction of the data, specific to each mission, are provided below.

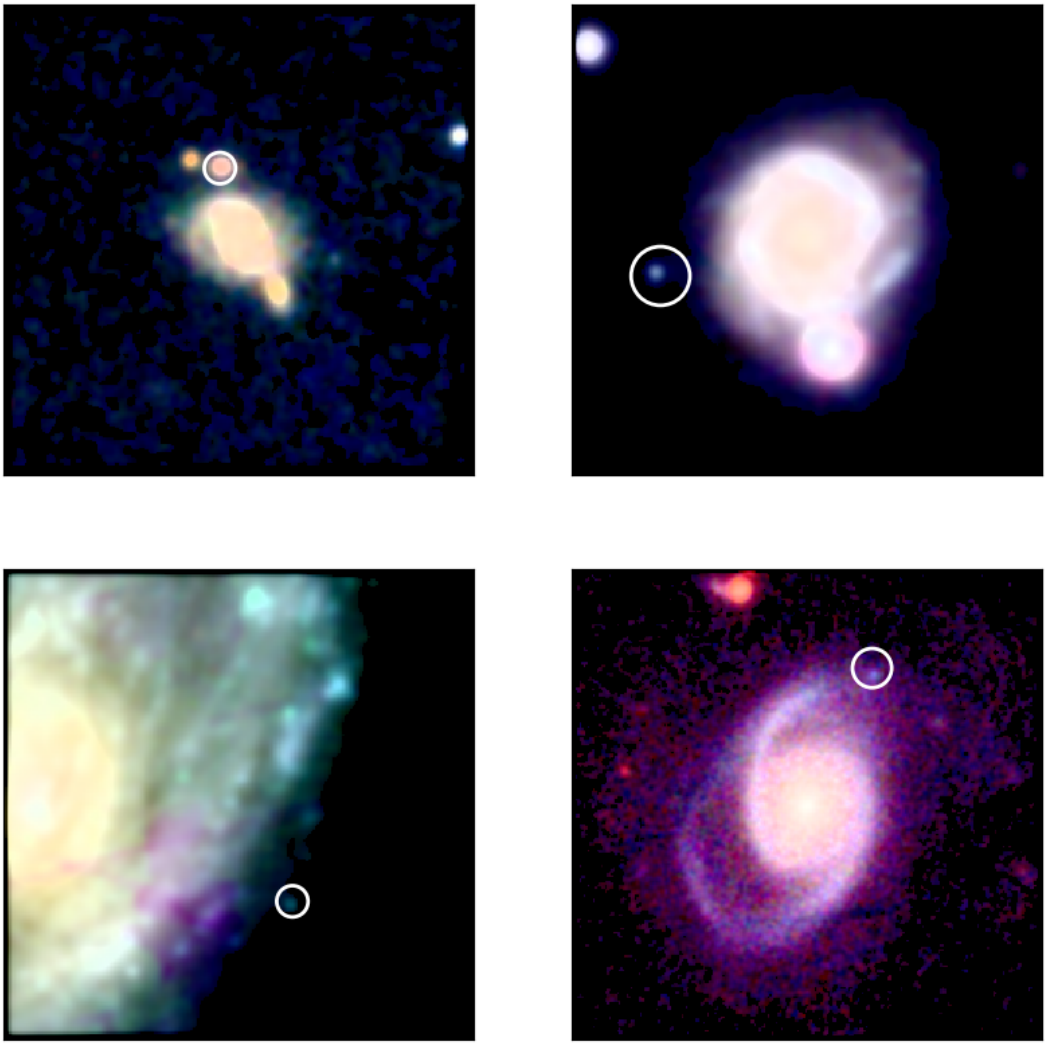

Figure 3.1: 3-colour Pan-STARRs images of the fields containing 4 HLX candidates. Each panel is 1 arcminute across, with the position of the HLX candidate highlighted by a 3, 5 or 10-arcsecond radius circle corresponding to the best available HLX position from *Chandra*, *XMM-Newton* or *Swift* respectively. The colours are taken from the g (blue), r (green) and i (red) filters, displayed on a logarithmic scale, with each panel scaled separately for display purposes. The HLX candidates are (from top left, clockwise: 2CXO J113128.9-020817, 2SXPS J095605.2+102950, 4XMM J103956.7-083446, 2CXO J011942.7+032422. The top two panels show HLX candidates rejected as likely AGN contaminants from neighbouring galaxies or background AGN; the bottom two panels show objects retained as more likely associated with structure in the host galaxies (which, for the case of 2CXO J011942.7+032422 in NGC 470, is confirmed spectroscopically by Gutiérrez and Moon 2014).

Table 3.1: Walton et al. (2022) HLX candidates associated with a counterpart or having spurious X-ray data quality. These candidates are not brought forward for analysis as part of our 'good' HLX candidates.

Source	Counterpart	Poor X-ray Quality	Comment
2CXO J004150.7-091824	✓		Ultraviolet excess source (UvES) and Candidate QSO in NED.
2CXO J020937.6+354727	✓		Blue optical counterpart in PanSTARRS/DR1.
2CXO J101525.0-053352	✓		Blue optical counterpart in PanSTARRS/DR1.
2CXO J113128.9-020817	✓		Red optical counterpart in PanSTARRS/DR1. Also detected in UV.
2CXO J120009.9+032204	✓		Faint, blue optical counterpart in PanSTARRS/DR1.
2CXO J125723.7-302303	✓		Blue optical counterpart in PanSTARRS/DR1. Also detected in UV.
2CXO J224906.5-642043	✓		Faint, red optical counterpart in DSS2. Also detected in UV.
2CXO J224956.5-642548	✓		Blue optical counterpart in DSS2.
4XMM J032954.8-284623		✓	Source is the result of a single false EPIC-pn detection.
4XMM J115150.0-284806		✓	Source is compromised by an EPIC-pn readout artefact.
4XMM J122556.7+310122	✓		Blue and red optical counterparts within 5" in PanSTARRS/DR1.
4XMM J130021.9+264725		✓	HLX candidate is result of an EPIC-pn hot pixel.
4XMM J134114.5+302230	✓		Red optical counterpart in PanSTARRS/DR1. Matched with distant NED galaxy.
4XMM J152109.8+303429	✓		Red optical counterpart in PanSTARRS/DR1. NED entry for IR, UV and Radio.
4XMM J173303.3+434535	✓		Red optical point source in PanSTARRS/DR1 and NED IR source.
4XMM J200238.9-555409	✓		Blue optical counterpart in DSS2.
2SXPS J010726.9+322458		✓	Source is not fully resolved and is likely hot gas in the host galaxy.
2SXPS J054746.6-195132	✓		Blue optical counterpart in PanSTARRS/DR1.
2SXPS J062226.1-645600	✓		Red optical counterpart in DSS2. Also detected in UV and IR.
2SXPS J072625.9-355359		✓	Single *Swift* detection is not spatially resolved from AGN.
2SXPS J091948.8+334450	✓		Red optical counterpart in PanSTARRS/DR1.
2SXPS J095605.2+102950	✓		Blue optical counterpart in PanSTARRS/DR1.
2SXPS J104153.9+004800	✓		Red optical counterpart in PanSTARRS/DR1. Negative redshift galaxy in NED.
2SXPS J104358.5+702216		✓	Only ever detected in the soft (0.3-1 keV) band at low S/N.
2SXPS J105359.4+164855	✓		Blue and green optical counterparts in PanSTARRS/DR1.
2SXPS J112827.9+583355		✓	X-ray detected only in the medium (1-2 keV) band with low S/N (< 2)
2SXPS J120124.1+615405		✓	Stack only detection. Majority of counts in a single, short exposure and < 1 keV.
2SXPS J120153.6-185234		✓	Diffuse X-ray emission in crowded region at the centre of the Antennae galaxies.
2SXPS J143452.1+542902	✓		Faint, blue optical counterpart in PanSTARRS/DR1.
2SXPS J150111.1+014233		✓	Soft source at edge of FoV. Barely detected.
2SXPS J150112.4+014255	✓		Matched to a non-host galaxy in NED within the exclusion radius.
2SXPS J212729.2-600102	✓		Red optical counterpart in DSS2. Also observed in IR.
2SXPS J213458.4-244146	✓		Blue optical counterpart in PanSTARRS/DR1.

Table 3.2: The remaining 37 'good' HLX candidates from Walton et al. (2022) following sifting for multiwavelength counterparts or poor X-ray quality.

				Swift			*XMM-Newton*			*Chandra*		
Source	Host	Distance [a]	$N_{H,gal}$ [b]	Obs[c]	Det	Exp	Obs	Det	Exp	Obs	Det	Exp
2CXO J001143.2-285548	PGC087431	267.7	0.15	-			1	0	9.4	1	1	19.9
2SXPS J003404.0-094222	NGC0151	60.0	0.30	18	1	41.5	-			1	0	4.9
2CXO J005501.4-351909	ESO351-021	250.4	0.26	-			1	0	7.0	1	1	39.5
2SXPS J005950.5-073455	NGC0337	19.2	0.93	27	3	48.9	-			1	1	3.1
2SXPS J010952.1-455524	IC1633	92.9	0.21	401	2	398.2	2	0	70.3	1	0	24.8
2SXPS J010957.0-455500	IC1633	92.9	0.21	401	2	398.2	2	0	70.3	1	0	24.8
4XMM J011046.1-454529	PGC073734	149.3	0.22	2	0	6.6	3	1	39.8	-		
4XMM J011906.5-342230	PGC663162	355.1	0.26	-			34	2	500.4	-		
2SXPS J011942.7+032423	NGC0470	40.0	0.35	25	19	40.1	3	3	111.0	1	1	28.1
2SXPS J021218.5-020805	UGC01697	162.9	0.26	3	1	58.1	-			-		
2CXO J024228.5-000202	PGC3112720	691.2	0.32	20	0	39.7	2	2	67.2	3	1	60.1
2SXPS J032206.2-152338	NGC1309	31.2	0.43	23	1	44.6	-			-		
2SXPS J032240.5-371135	NGC1316	17.5	0.26	20	1	64.0	-			5	0	255.2
2CXO J043338.4-131612	PGC015524	150.7	0.63	-			6	0	184.3	3	3	104.0
4XMM J050107.9-384321	PGC146838	226.7	0.21	-			1	1	7.8	-		
2SXPS J053246.8-140437	NGC1954	66.7	1.30	18	7	64.9	-			-		
2CXO J055107.0-570640	PGC393843	266.9	0.80	-			-			2	2	36.1
4XMM J061410.3-332954	ESO365-001	164.4	0.41	3	2	13.9	2	2	17.0	-		
2SXPS J061617.5-212222	NGC2207	36.4	1.24	53	1	111.1	1	0	46.4	4	0	62.4
2SXPS J061619.3-212219	NGC2207	36.4	1.24	53	3	111.1	1	0	46.4	4	0	62.4
2SXPS J064706.9+741404	NGC2256	77.2	1.01	2	1	2.0	-			-		
2SXPS J074512.3-712410	NGC2466	73.0	1.74	17	4	36.4	-			-		
2CXO J103619.8-273939	PGC141471	430.1	0.59	2	0	12.1	1	0	32.1	1	1	31.9
4XMM J103956.7-083446	PGC083292	271.6	0.35	-			3	2	9.3	-		
2SXPS J111416.1+481833	NGC3583	30.5	0.15				1	1		1	1	
2SXPS J120155.4-185213	NGC4038	22.1	0.37	91	2	191.1	-			-		
4XMM J125708.6-044144	PGC1054690	203.3	0.17	-			1	1	94.3	-		
4XMM J140147.7-113438	PGC094246	292.4	0.62	-			1	1	16.4	1	1	58.8
2CXO J151011.0+333358	PGC2034704	530.9	0.16	4	0	4.0	2	0	18.5	6	1	255.7
2CXO J153240.3+324228	SDSSJ153238+324242	611.8	0.24	-			2	0	71.4	1	1	97.0
4XMM J160211.8+155437	PGC2790838	140.6	0.36	-			2	0	16.2	1	1	17.9
4XMM J163818.7-642201	ESO101-004	215.7	1.67	-			2	0	11.6	3	2	72.9
2CXO J185712.5-782830	PGC140831	181.6	1.32	5	0	9.6	-			1	1	5.0
2SXPS J204443.5-684540	NGC6943	36.0	0.37	15	1	12.6	-			-		
4XMM J210536.0-522300	PGC128847	155.0	0.29	-			1	1	38.6	-		
2SXPS J230451.5+121825	NGC7479	36.8	0.79	25	16	70.6	3	2	112.0	2	2	34.9
4XMM J235700.5-344118	ESO349-009	182.8	0.13	-			4	0	171.7	2	2	132.8

[a] Distance to the host galaxy (and therefore the source) in units of Mpc. [b] Galactic absorption given in units of 10^{21} cm^{-2}.
[c] Number of observations, detections and total exposure (in ks; sum of GTIs after flare filtering in *XMM-Newton*) for each candidate from each individual mission.

3.3.1 *Swift*

We extracted data products for each HLX candidate that had been detected by *Swift* XRT directly from the 2SXPS interface[5]. In doing this we ensured that data were obtained at the observation level, and recorded as count rates (with an associated 1σ error) where the detection significance was at or above the 3σ level, or as a 3σ upper limit where the significance was lower. We also extracted count rates in three bands – soft, medium and hard – from 2SXPS (see Evans et al. 2020b), and combined the data from the soft and medium bands such that we had count rates in the 0.3-2 and 2-10 keV bands that we used to calculate a hardness ratio. We also obtained stacked *Swift* XRT spectra directly from the same 2SXPS interface, along with appropriate background data and response matrix (*.rmf) and ancillary response (*.arf) files.

In addition, we searched the *Swift* data archive[6] for observations covering the positions of HLX candidates that were detected by either *XMM-Newton* or *Chandra* but not by *Swift*. Where such data was identified we obtained the data products at the observation level from the archive and created 0.3-10 keV images. We then used a 35 arcsecond radius circular aperture placed at the best position of the HLX candidate (favouring *Chandra* positions over *XMM-Newton* where both detected the HLX candidate) and extracted raw counts. These were background-subtracted using an adjacent, source-free circular aperture of radius 70 arcseconds, and a 3σ upper limit on the count rate was calculated for each observation.

3.3.2 *XMM-Newton*

Observation data files (ODFs) were obtained from the *XMM-Newton* Science Archive (XSA)[7] for all observations containing the position of a HLX candidate within the field of view. The data were reduced using the *XMM-Newton* Science Analysis Software (SAS) v.18.0.0. Calibrated EPIC event lists were generated following the procedure laid out in the relevant EPIC reprocessing thread[8]. These were cleaned

[5] https://www.swift.ac.uk/2SXPS/
[6] https://www.swift.ac.uk/swift_live/index.php
[7] http://nxsa.esac.esa.int/nxsa-web/
[8] https://www.cosmos.esa.int/web/xmm-newton/sas-thread-epic-reprocessing

for periods of high background, using the standard method of creating good time interval files based on periods where the 10-12 keV background light curve does not exceed rates of 0.4 count s^{-1} in the pn, or 0.35 count s^{-1} in either MOS.

Images were created from the cleaned event lists, selecting only events with low numerical pattern values ($\leq$ 4 for the pn, and $\leq$ 12 for each MOS) and the scientific flags XMMEA_EP and XMMEA_EM for pn and MOS respectively, in the 0.3-10, 0.3-2 and 2-10 keV bands. Aperture photometry was performed in each image at the position of each HLX candidate in each observation, regardless of whether it was detected or not. We used an aperture of radius 20 arcseconds on-axis, which transitioned to a larger 30 arcsecond radius aperture beyond 9 arcminutes off-axis to account for point spread function degradation[9]. A source-free background region of twice the radius, placed on the same chip at a similar off-axis angle and (for the pn) a similar distance from the readout nodes, was used to background-correct the measured count rates. For simplicity when converting to fluxes (see later), aperture photometry was taken solely from the pn unless the aperture was impacted by detector structure (i.e. chip gaps) or other factors that might contaminate the aperture (e.g. readout streaks). In these cases MOS data was used preferentially, with the MOS2 detector chosen unless that also presented issues with the source data. In only 9 of the 79 *XMM-Newton* observations of our HLX candidates was the pn sufficiently impacted such that data taken from MOS2 (5 observations) or MOS1 (4 observations) was used instead. There was a single observation of HLX candidate 2CXO J153240.3+324228 in which all three were unusable.

Where sufficient counts were available in an observation, we also extracted spectra in all three detectors, alongside other files relevant to their analysis (i.e. background spectra, response matrix and ancillary response files) using the same apertures as above. Before analysis, spectra were binned to a minimum of 25 counts per bin, with bins chosen such that the spectral resolution of the EPIC detectors is not over-sampled (the criterion "oversample=3" in the SAS tool SPECGROUP).

[9] https://xmm-tools.cosmos.esa.int/external/xmm_user_support/documentation/uhb/effareaoffaxis.html

3.3.3 *Chandra*

Given that the ACIS detectors do not fill the entire field-of-view of the High Resolution Mirror Assembly, we assessed the coverage of the HLX candidates by *Chandra* using the *Chandra* footprint server[10]. Where the position of any candidate lay within an ACIS detector all corresponding observations were downloaded from the *Chandra* data archive[11]. We used CIAO v.4.12 to reprocess all the data to create new level 2 events files prior to analysis. Images were again created in the 0.3-10, 0.3-2 and 2-10 keV bands and aperture photometry extracted at the position of each HLX candidate. We used a 3 arcsecond radius circular aperture to extract data from on-axis observations, with larger radii used off-axis. Our selection for the aperture evolution is determined from empirical analysis of how the semi-major axis of the elliptical PSF 90% Enclosed Counts Fraction aperture (**mjr_axis_aper90_b**) varies with off-axis angle (**theta**) in CSC2.0. We find that a circular aperture of 5 arcseconds is more suitable beyond 5 arcminutes, 7 arcseconds beyond 7 arcminutes and finally 10 arcseconds out at off-axis angles beyond 10 arcminutes (only applicable at the extremeties of ACIS). A source-free, circular background aperture of 7 arcsecond radius was used for on-axis HLX candidates, increasing to 10/14/20 arcseconds off-axis at 5/7/10 arcminutes respectively. Finally, source and background spectra were extracted from the same apertures using the CIAO task SPECEXTRACT, which also provided the response matrix and ancillary response files.

3.4 Model-independent pilot analysis

The majority of the HLX candidates detections are not photon-rich, which limits our ability to perform more complex spectral and temporal analyses on the data. Instead, for most sources, we must look for another way to study and contextualise their X-ray emission. One simple diagnostic tool used widely for X-ray binaries in general (e.g. Homan and Belloni 2005; Remillard and McClintock 2006) and for ULXs in some instances (e.g. Gúrpide et al. 2021; Servillat et al. 2011; Sutton

[10] `https://cxcfps.cfa.harvard.edu/cda/footprint/cdaview.html`
[11] `https://cxc.cfa.harvard.edu/cda/`

et al. 2013b) is the colour-intensity diagram. Here, we examine its use for our HLX candidate sample using our numerous *Swift* observation-level detections.

A colour-intensity diagram is often used to study the behaviour of individual objects. When used for populations, extra information can be useful to contextualise the data. Here, we attempt to do this by comparing the *Swift* data to two famous, and physically very different objects that both peak in luminosity in the HLX regime. These are the most luminous of the pulsating ULXs, NGC 5907 ULX (Israel et al. 2017a), and the good IMBH candidate ESO 243-49 HLX-1 (Farrell et al. 2009), see also Section 3.1. Crucially, both are very well-studied by *Swift* and so we are able to represent the parameter space they occupy in a colour-intensity diagram using contours. They can therefore be used as yardsticks for comparison with the other HLX candidates to search for similar behaviour. NGC 5907 ULX is actually one of the HLXs in our sample (detected as 2SXPS 151558.7+561810, with further detections in 4XMM-DR10 and CSC2.0 but not as a HLX), whereas ESO 243-49 HLX-1 was not catalogued as a ULX by W22 as it lies outside the D_{25} elliptical isophote of its associated galaxy. Given how well studied NGC 5907 ULX is we only use it as a benchmark HLX for the remainder of this work; we extract the data for ESO 243-49 HLX-1 similarly to the other objects (as described above in Section 3.3).

Our pilot *Swift* XRT colour-intensity diagram is shown in Fig. 3.2. The colours are calculated as the hardness ratio $(H - S)/(H + S)$, where H is the counts in the 2-10 keV band, S is the counts in the 0.3-2 keV band, and the associated error is calculated as per Park et al. (2006). To enable us to directly compare the properties of the HLX candidates during their *Swift* detections, we account for them all being at different distances by normalising their count rates to the equivalent count rate for a HLX candidate at 10 Mpc. We note that this does not involve any assumptions about the spectral form of the HLXs in the 0.3-10 keV *Swift* bandpass, and so this can be considered a simple, model-independent comparison of the data. Fig. 3.2 shows two key things. First, that NGC 5907 ULX and ESO 243-49 HLX-1 are a good choice as comparators given that their detections sit in distinct regions of parameter space. Second, the subset of the 37 'good' HLX candidates detected by

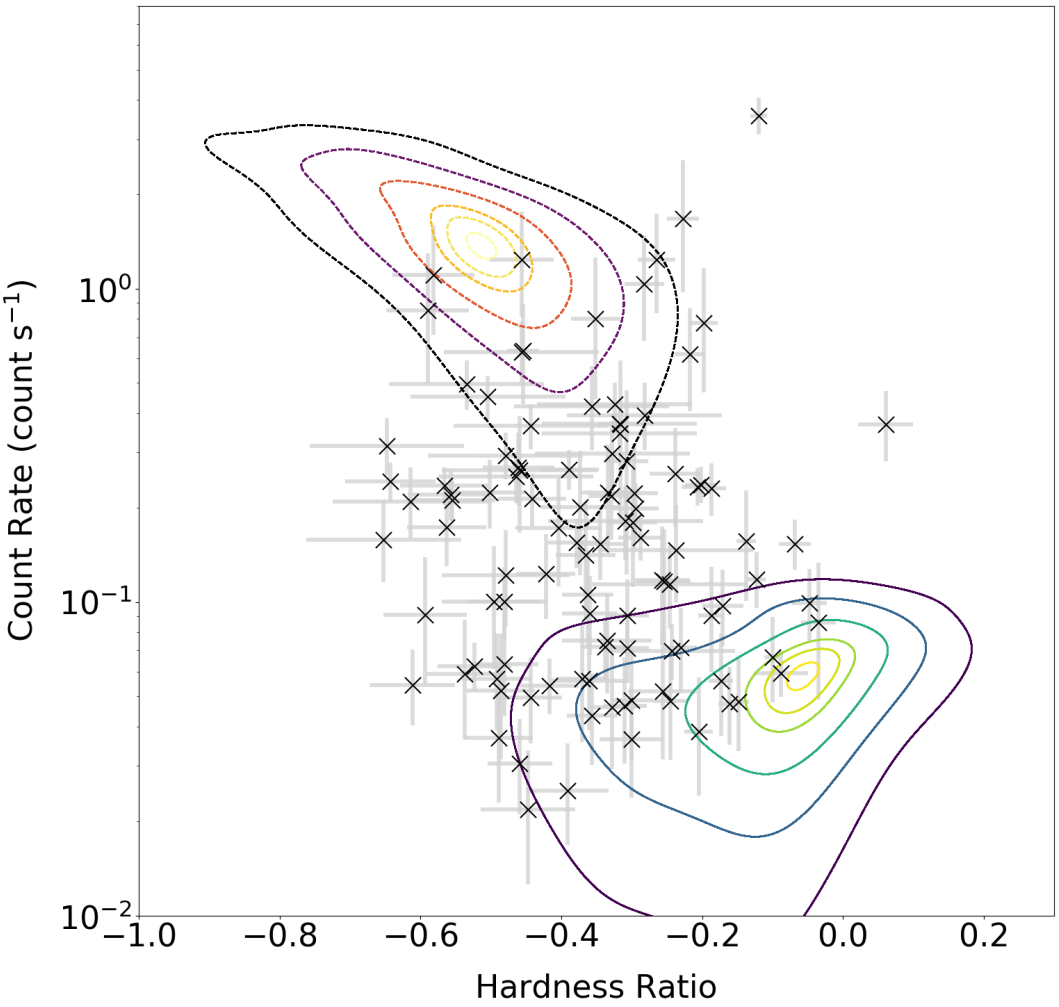

Figure 3.2: Colour-intensity diagram for the observation-level *Swift* detections of good HLX candidates. The hardness ratios are between the 2-10 and 0.3-2 keV regimes (details are in the text), and the count rates are all scaled to an equivalent distance of 10 Mpc. The candidate HLX data is compared to the parameter space occupied by *Swift* detections of two very different but relatively well-understood HLXs. The parameter space for NGC 5907 ULX, a PULX, is in the lower right of the colour-intensity diagram and its contours (solid lines, blue/green colours) encompass 1, 5, 10, 25, 50 and 75% of all observations. Similarly, the parameter space for the good IMBH candidate ESO 243-49 HLX-1 is towards the top left, with contours (dashed lines, red colours) plotted at the same levels of encapsulation.

Swift clearly cover a large range of parameter space, with some overlapping the regions occupied by either benchmark object, and some sat in between. This is therefore very encouraging in that we might be able to identify possible look-alikes for either NGC 5907 ULX, which would present as possible PULX candidates; or for ESO 243-49 HLX-1, which similarly might be IMBHs. We therefore concentrate in the next section of the work on expanding these comparisons to include both *XMM-Newton* and *Chandra* data, and to encompass both spectral information (in the cases where sufficient counts are available) and light curves for the HLX candidates.

3.5 Results

Given the differences in effective areas and responses between different combinations of detectors and missions, we cannot directly compare data based on their count rates in specific energy bands. Instead, if we want to directly compare the sources we must remove the imprint of the detectors, which we can do if we convert the count rate data into band-limited source fluxes. These fluxes can then be used to provide both luminosity and hardness information for the individual observations, from which light curves and colour-intensity (or, in this case, hardness-luminosity) diagrams can be parsed. However, to convert from count rate to flux we also need to understand the underlying spectra of the sources. We begin this section by addressing that problem.

3.5.1 Understanding the source spectra

3.5.1.1 X-ray spectroscopy

The best way of recovering the underlying source spectrum, for those datasets with sufficient counts, is spectral fitting. Hence, we initially identified a total of five datasets with at least 300 background-subtracted counts in one detector as those suitable for spectral fitting. However, after an inspection of our initial fits this threshold was dropped slightly to 275 counts, which included two further objects, noting that no further datasets had more than $\sim$ 200 counts so this presented a natural break in the data.

All our spectra were binned to at least 25 counts per bin, background-subtracted using data from the apertures described in Sec 3.3, and fitted in XSPEC v.12.12[12] using the χ^2 statistic. We report the results of fitting two simple models, an absorbed power-law continuum and an absorbed multi-colour disc blackbody spectrum, in Tables 3.3 and 3.4. The foreground absorption columns were found using the UK *Swift* science data centre NHTOT online tool[13], which obtains n_H values from Willingale et al. (2013), and the relative elemental abundances in the ISM were set to the values of Wilms et al. (2000b). Fluxes for each spectrum were recovered using the CFLUX multiplicative model, and are shown as the observed flux. All errors to the fits are quoted at the 90% level.

For comparison we also included an aggregate spectrum of all *Swift* datasets for our two archetypal sources, ESO 243-49 HLX-1 and NGC 5907 ULX in Tables 3.3 and 3.4. These two objects have been observed hundreds of times by *Swift* (along with a multitude of observations with *XMM-Newton* and *Chandra*). Instead of fitting the spectra from each observation individually, we decide an aggregate spectrum gives the best overview in defining the properties of the archetype. Even using an aggregate spectrum from across many observations, we can still see a substantial difference between ESO 243-49 HLX-1 and NGC 5907 ULX. Looking at the simple powerlaw fit in Tab. 3.3, NGC 5907 ULX is better characterised by an absorbed powerlaw ($\chi^2 = 173.0$ for 171 degrees of freedom) than ESO 243-49 HLX-1 - for which the fit is not well constrained ($\chi^2 = 226.0$ for 121 degrees of freedom).

For our 6 HLX candidates, the majority of the extracted spectra are well fit by either (or both) of the simple models. For example, both 2CXO J043338.4-131612 in PGC015524 and 2SXPS J111416.1+481833 in NGC 3583 are better fit by an absorbed multi-colour disc blackbody spectrum, while 2CXO J011942.7+032422 in NGC 470 follows an absorbed power-law continuum. In fact, our candidate in NGC 470 follows a powerlaw and remains the same within errors across the four different spectra obtained from *XMM-Newton* or *Chandra*.

[12]Part of the HEASOFT package available from `https://heasarc.gsfc.nasa.giv/docs/software/heasoft`.

[13]`https://www.swift.ac.uk/analysis/nhtot/`

Table 3.3: Details of the *Swift*, *Chandra* and *XMM-Newton* HLX candidate powerlaw spectral fits.

HLX	Host	$N_{\rm H,gal}$ [a]	n_H [a]	Γ	χ^2	DoF	Flux [b]	Instrument
NGC 5907 PULX [c]	NGC 5907	0.13	$1.01^{+0.12}_{-0.11}$	$1.55^{+0.090}_{-0.086}$	173.0	171	13.0	*Swift*
HLX1 [d]	ESO 243-49	0.19	$0.134^{+0.017}_{-0.016}$	$3.92^{+0.12}_{-0.12}$	226.0	121	3.58	*Swift*
2CXO J005501.4-351909	ESO 351-021	0.26	$10.2^{+7.2}_{-6.0}$	$1.98^{+0.73}_{-0.64}$	4.7	7	0.89	*Chandra*
4XMM J011942.7+032422	NGC 0470	0.35	$1.29^{+0.78}_{-0.69}$	$1.70^{+0.22}_{-0.20}$	17.7	21	9.13	*XMM-Newton*
4XMM J011942.7+032422	NGC 0470	0.35	$0.83^{+0.40}_{-0.36}$	$1.75^{+0.14}_{-0.13}$	47.5	42	1.37	*XMM-Newton*
4XMM J011942.7+032422	NGC 0470	0.35	$1.0^{+0.3}_{-0.2}$	$1.79^{+0.11}_{-0.10}$	50.2	61	1.50	*XMM-Newton*
2CXO J011942.7+032422	NGC 0470	0.35	<2.0	$1.70^{+0.23}_{-0.21}$	24.1	21	2.21	*Chandra*
2CXO J043338.4-131612	PGC015524	0.63	$1.7^{+1.2}_{-1.0}$	$1.91^{+0.29}_{-0.26}$	24.0	36	0.77	*Chandra*
4XMM J061410.3-332954	ESO 365-001	0.41	<0.9	$3.12^{+0.57}_{-0.27}$	9.13	12	0.78	*XMM-Newton*
2SXPS J111416.1+481833	NGC 3583	0.15	$1.0^{+0.4}_{-0.3}$	$1.68^{+0.11}_{-0.10}$	41.7	53	6.16	*Swift*
2SXPS J111416.1+481833	NGC 3583	0.15	$1.0^{+0.2}_{-0.1}$	$1.87^{+0.07}_{-0.06}$	83.9	77	6.56	*XMM-Newton*
4XMM J210536.0-522300	PGC128847	0.29	$1.2^{+1.1}_{-0.7}$	$2.20^{+0.50}_{-0.30}$	27.4	24	0.45	*XMM-Newton*

[a] Both Galactic and intrinsic absorption are given in units of 10^{21} cm^{-2}. $N_{\rm H,gal}$ values are fixed to determined value and are not fitted.
[b] Absorbed flux from spectral fit in units of 10^{-13} erg cm^{-2} s^{-1}. [c,d] We fit to the aggregate spectra containing all *Swift* observations of each of our two archetypal sources.

Table 3.4: Details of the *Swift*, *Chandra* and *XMM-Newton* HLX candidate disc blackbody spectral fits.

HLX	Host	$N_{\rm H,gal}$ [a]	$n_{\rm H}$ [a]	$T_{\rm in}$ [keV]	χ^2	DoF	Flux [b]	Instrument
NGC 5907 PULX [c]	NGC 5907	0.13	$6.21^{+0.69}_{-0.63}$	$2.18^{+0.17}_{-0.15}$	160.0	171	11.8	*Swift*
HLX1 [d]	ESO 243-49	0.19	<0.08	$0.25^{+0.02}_{-0.01}$	394.5	121	3.42	*Swift*
2CXO J005501.4-351909	ESO 351-021	0.26	$5.5^{+4.7}_{-4.0}$	$1.27^{+0.86}_{-0.37}$	5.7	7	0.68	*Chandra*
4XMM J011942.7+032422	NGC 0470	0.35	<0.3	$1.24^{+0.17}_{-0.15}$	14.7	21	7.12	*XMM-Newton*
4XMM J011942.7+032422	NGC 0470	0.35	<0.06	$1.20^{+0.15}_{-0.13}$	100.0	42	1.14	*XMM-Newton*
4XMM J011942.7+032422	NGC 0470	0.35	<0.04	$1.19^{+0.11}_{-0.10}$	150.2	61	1.31	*XMM-Newton*
2CXO J011942.7+032422	NGC 0470	0.35	<0.2	$1.30^{+0.21}_{-0.17}$	44.3	21	2.06	*Chandra*
2CXO J043338.4-131612	PGC015524	0.63	<0.5	$1.12^{+0.19}_{-0.16}$	27.6	36	0.62	*Chandra*
4XMM J061410.3-332954	ESO 365-001	0.41	<0.82	$0.24^{+0.03}_{-0.02}$	28.7	12	0.60	*XMM-Newton*
2SXPS J111416.1+481833	NGC 3583	0.15	<0.09	$1.37^{+0.12}_{-0.11}$	54.3	53	5.09	*Swift*
2SXPS J111416.1+481833	NGC 3583	0.15	<0.01	$1.09^{+0.06}_{-0.05}$	265.2	77	5.33	*XMM-Newton*
4XMM J210536.0-522300	PGC128847	0.29	<0.4	$0.7^{+0.2}_{-0.2}$	29.3	24	0.34	*XMM-Newton*

[a] Both Galactic and intrinsic absorption are given in units of 10^{21} cm^{-2}. $N_{\rm H,gal}$ values are fixed to determined value and are not fitted.
[b] Absorbed flux from spectral fit in units of 10^{-13} erg cm^{-2} s^{-1}. [c,d] We fit to the aggregate spectra containing all *Swift* observations of each of our two archetypal sources.

However, some of our candidates are not well characterised by either of these simple models. Sources 4XMM J061410.3-332954 and 2CXO J005501.4-351909 were the two candidates with fewer than 300 background-subtracted counts in one detector, for which we lowered the threshold; the low count statistics do result in the fits being relatively poorly constrained.

3.5.1.2 Recovering approximate spectra by other means

Given the quality of the data available across our sample, it is not feasible to extract and fit a spectrum in the case of each individual source. For the majority of our HLX candidates there are insufficient counts in any individual detection to constrain a spectral fit. But, even in these cases, it was still necessary to extract what spectral information we could, so hardness ratios (i.e. X-ray colours) were used to provide approximate spectral shapes. To determine the X-ray colour of any detection we first determine two hardness ratios corresponding to that detection (labelled as HR1 and HR2). These hardness ratios are determined by measuring source counts in the three bands originally defined within 2SXPS (section 3.3): soft (S: 0.3-1 keV), medium (M: 1-2 keV) and hard (H: 2-10 keV). HR1 is given by $(M-S)/(M+S)$ and HR2 is given by $(H-M)/(H+M)$. Thus we generate a colour-colour plot for these sources (HR2 vs HR1) and overlay grids marked out by a range of spectral forms for each given detector.

In this work we have 5 unique detector responses to consider and take into account, the *Swift* XRT, *XMM-Newton* EPIC-pn, *XMM-Newton* EPIC-MOS, *Chandra* ACIS-S and *Chandra* ACIS-I. For each of these we determine values of HR1 and HR2 for a total of 25 distinct absorbed powerlaw spectral forms. We take Γ values of (1, 1.5, 2, 3, 4) and intrinsic n_H values of (0.5, 1, 2, 3, 5) $\times 10^{21}$ cm^{-2}. These 25 'nodes' generate a grid across our colour-colour plot which we then use to determine an X-ray spectrum for each detection corresponding to its nearest node. For points outside the grid, on any side, we also match to the nearest node. Conversion from count rate to flux was then applied at the per observation level, where each detection was converted using the spectral form it was assigned. In observations where the source was not detected, with only an upper limit, we lack the colour information

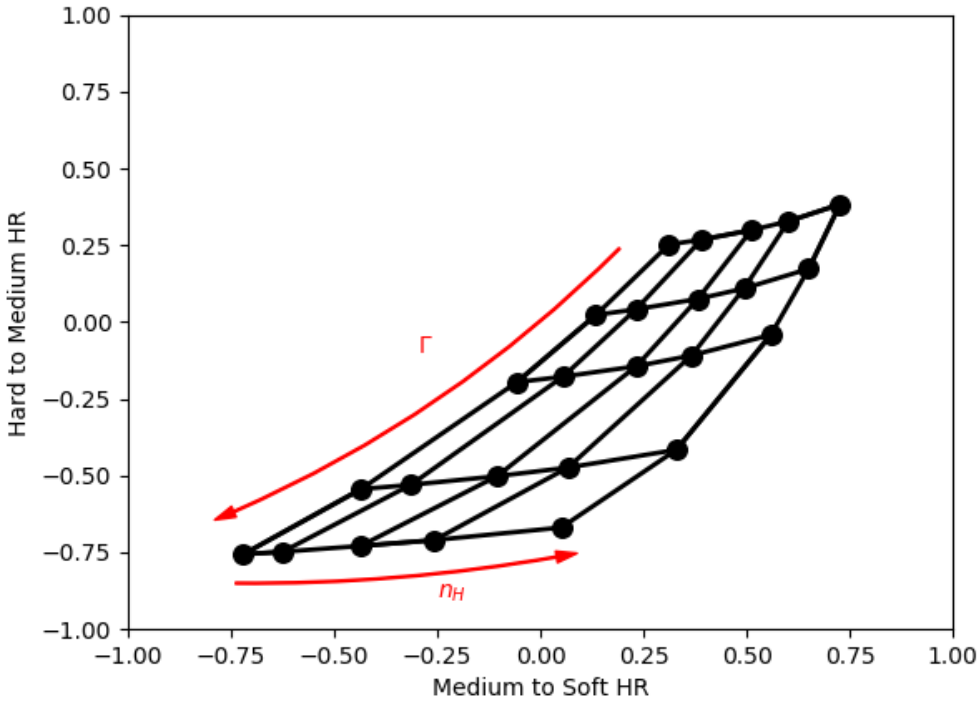

Figure 3.3: Colour-colour plot containing the grid used to determine spectral form for any *Swift* XRT detections among our HLX candidates. The red arrows indicate the directions of increasing values of Γ and n_H. We take Γ values = 1, 1.5, 2, 3, 4 from top to bottom and intrinsic n_H values = 0.5, 1, 2, 3, 5 $\times 10^{21}$ cm^{-2} from left to right.

necessary to apply the grid method directly to each upper limit. Instead, upper limits on the long-term light curves are converted from count rate to flux based on the source's average spectrum, as determined from its detections. Examples of the *Swift* and *XMM-Newton* grids can be found in Figs. 3.3 and 3.4.

However, *Chandra* presented an additional complication. Due to degradation over time, the ACIS instrument responses have changed significantly across 26 *Chandra* observation cycles. When assigning a spectrum to a given *Chandra* detection there is an additional temporal component that must be accounted for, since a given spectrum will shift on the colour-colour plot as the response changes, which can be seen in Figs. 3.5 and 3.6. To save having to generate a new grid for each distinct *Chandra* cycle (both for ACIS-S and ACIS-I respectively) we instead select 5 cycles distributed across the lifetime of *Chandra* - cycles 3, 8, 13, 18 and 23. Any detections from intermediate cycles are then compared against both of the corresponding grids either side and a weighted, mean average value for Γ and n_H are calculated according to the following weightings depending on the observation dates compared to the chosen cycles: 80/20, 60/40, 40/60 and 20/80. For example, a *Chandra* detection observed during cycle 6 will have a 40/60 weighted spectrum taken from the cycle 3 and cycle 8 grids respectively.

This information (alongside galaxy distances adopted in W22) was then used to convert count rates from each observation to luminosities, which were used to determine long-term light curves for each HLX. As count rates above and below 2 keV were also determined for each observation, we were also able to produce hardness-luminosity (equivalent to colour-intensity) plots for each HLX.

3.5.2 Behavioural Analysis

The above analysis allowed us to plot HLX candidate data on a long-term light curve and colour-intensity diagram. In our hardness-intensity diagrams, the soft and medium bands are combined and compared against the hard band, generating a single hardness ratio with a break at 2 keV. To better understand the hardness-intensity plots, we again place our HLXs in the context of the confirmed PULX, NGC 5907 ULX, and the strong IMBH candidate, ESO 243-49 HLX-1. All available

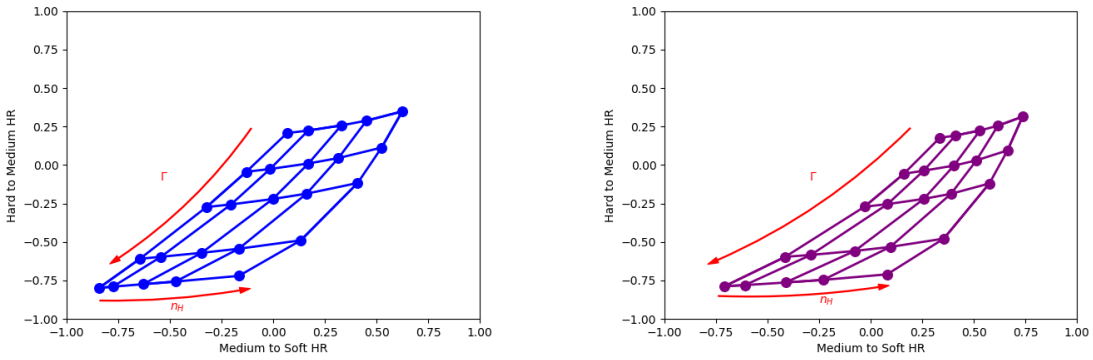

Figure 3.4: Colour-colour plots containing the grids used to determine spectral form for any *XMM-Newton* EPIC-pn (left, blue) or EPIC-MOS (right, purple) detections among our HLX candidates. The red arrows indicate the directions of increasing values of Γ and n_H. We take Γ values = 1, 1.5, 2, 3, 4 from top to bottom and intrinsic n_H values = 0.5, 1, 2, 3, 5 $\times 10^{21}$ cm^{-2} from left to right.

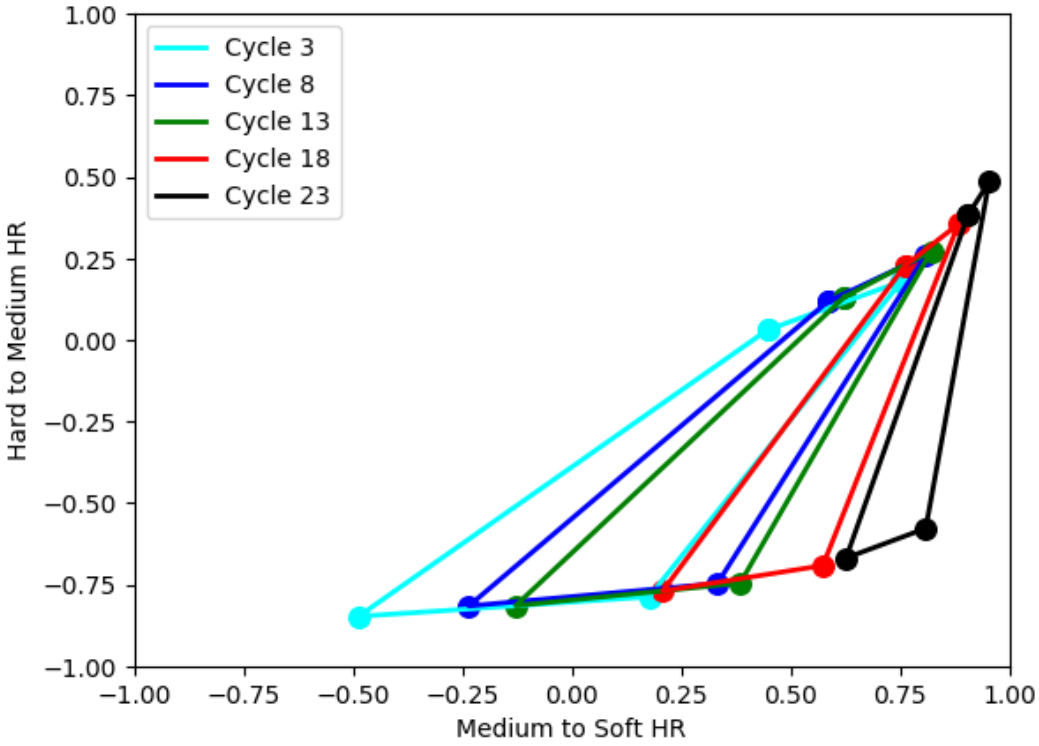

Figure 3.5: Evolution of the *Chandra* ACIS-I instrument response across our 5 selected cycles. The quadrilaterals each represent the approximate outline of the corresponding grid. The four corners starting from top left and moving clockwise correspond to the spectra $\Gamma = 1, n_H = 5 \times 10^{20}$ cm^{-2}; $\Gamma = 1, n_H = 5 \times 10^{21}$ cm^{-2}; $\Gamma = 4, n_H = 5 \times 10^{21}$ cm^{-2} and $\Gamma = 4, n_H = 5 \times 10^{20}$ cm^{-2}.

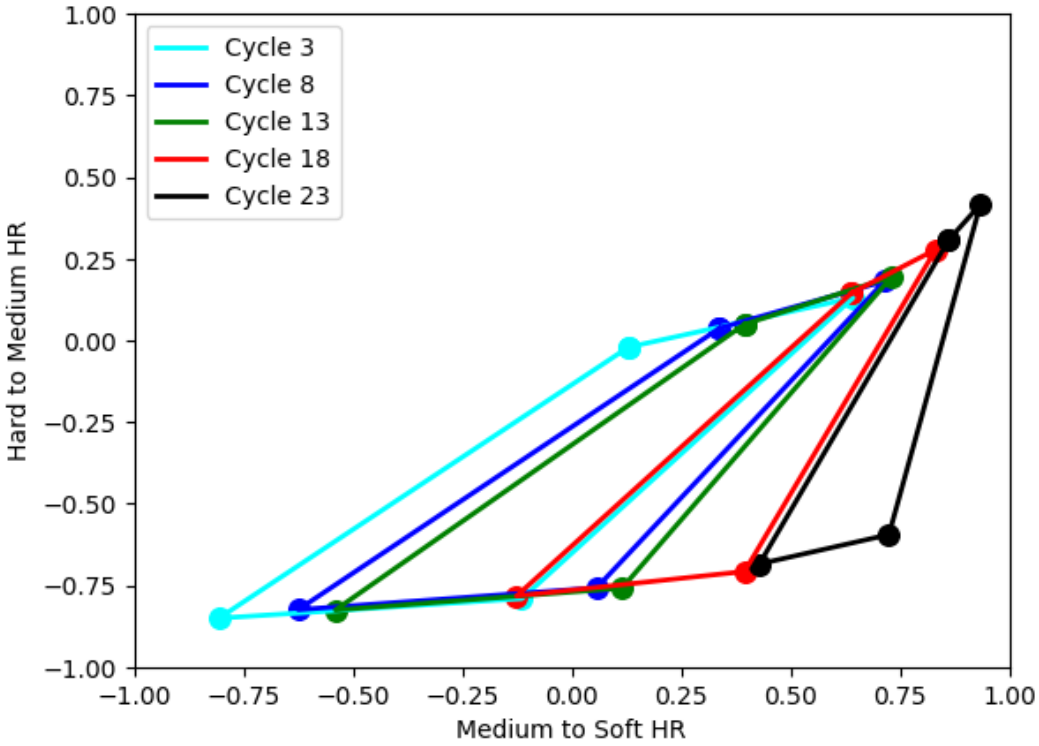

Figure 3.6: Evolution of the *Chandra* ACIS-S instrument response across our 5 selected cycles. The quadrilaterals each represent the approximate outline of the corresponding grid. The four corners starting from top left and moving clockwise correspond to the spectra $\Gamma = 1, n_H = 5 \times 10^{20}\,\mathrm{cm}^{-2}$; $\Gamma = 1, n_H = 5 \times 10^{21}\,\mathrm{cm}^{-2}$; $\Gamma = 4, n_H = 5 \times 10^{21}\,\mathrm{cm}^{-2}$ and $\Gamma = 4, n_H = 5 \times 10^{20}\,\mathrm{cm}^{-2}$.

Swift data for these two sources was converted to fluxes using our aggregate spectral fits (see Tab. 3.3) and then plotted as contours on our HLX hardness-intensity diagrams, with contours representing 1, 5, 10, 25, 50 and 75% of all observation data encapsulated.

3.5.2.1 *Swift* stacks

However, once the long-term light curves and colour-intensity plots were derived for our HLX candidates, two issues arose. The first problem was revealed for a handful of our *Swift* HLX candidates. For these sources, count rate values associated with the *Swift* stacks were appearing as data points in our ULX catalogue. However, the treatment of our ULX catalogue (Walton et al. 2022) and the HLX candidate sample has always been carried out at the per-observation level. While *Swift* stack data can be used to obtain averaged spectral information about a source (where counts are sufficient), they cannot be plotted on a long-term light curve given they span multiple observations. More significantly, these sources were either not detected at 3σ significance in any of the individual observations or were substantially less luminous in any observation than their peak $L_{\rm X}$, which invariably corresponded to the *Swift* stack. In the case of this handful of candidates, the *Swift* correction factor - a correction constant for vignetting, bad columns, pile-up and the finite radius over which counts were extracted - was significantly inflated for the stack compared to the rest of the sample. Table 3.5 shows the 4 *Swift* sources among our HLX candidate sample where this is an issue. We tabulate the over-inflated correction factor and the new peak X-ray luminosity, $L_{\rm X,\ peak}$ found at the per-observation level (thus disregarding the dubious stack values).

The exact cause of this disruption to the *Swift* pipeline functionality varies between the candidates. For example, the two HLX candidates 2SXPS J120155.4-185213 and 2SXPS J120153.6-185234, found in the Antennae galaxies (NGC 4038), suffer due to being present in a crowded field. The pipeline struggles due to source confusion and the decomposition of the data into discrete sources. On the other hand, a closer inspection of 2SXPS J061617.5-212222 reveals diffuse emission with a small hole at the centre; as the pipeline is trained on point sources it mistakenly

Table 3.5: Walton et al. (2022) HLX candidates associated with having spurious X-ray data quality due to *Swift* pipeline. These candidates are not brought forward for analysis as part of our 'good' HLX candidates.

Source	Host	*Swift* stack correction factor
2SXPS J010952.1-455524	IC1633	36.88
2SXPS J032206.2-152338	NGC1309	41.99
2SXPS J032240.5-371135	NGC1316	103.47
2SXPS J061617.5-212222	NGC2207	7.02
2SXPS J120155.4-185213	NGC4038	7.50

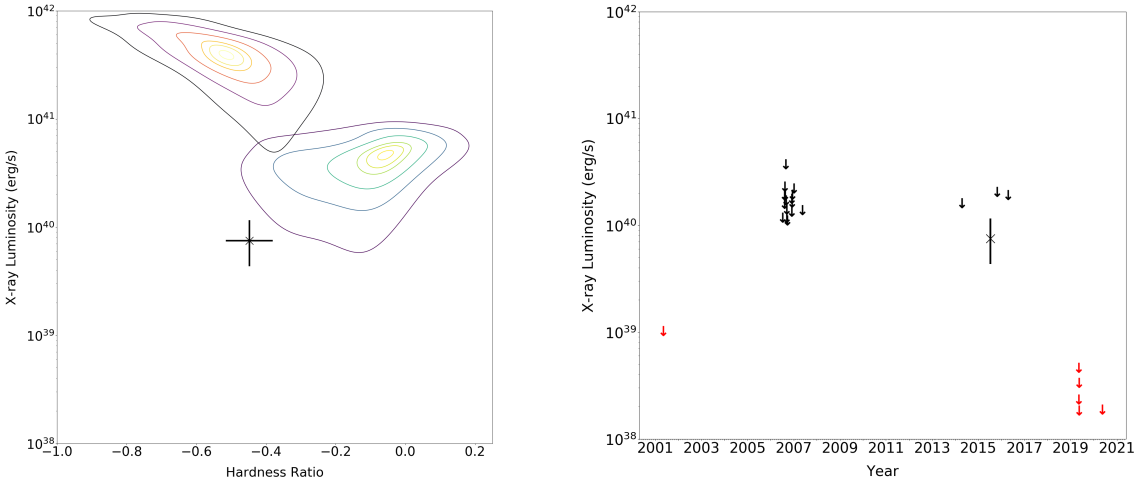

Figure 3.7: 2SXPS J032240.5-371135 in NGC1316 has a hugely inflated *Swift* correction factor on the stack. *Swift* detections and upper limits (ULs) are in black. ULs from the *Chandra* observations are plotted in red.

determines this source is extremely piled up.

3.5.2.2 No longer a HLX

From decisions on spectral shape, bandpass and aperture photometry, 12 candidates no longer have any observations in which they are detected above the $L_{\rm X} = 10^{41}\,{\rm erg\,s^{-1}}$ threshold.

With our HLX analysis, to make for an accurate comparison, we consider the *Swift* energy bandpass of 0.3-10 keV across all three missions. This extrapolates data beyond the energy range over which *Chandra* is sensitive (∼0.5-8 keV), but is narrower than the 0.2-12 keV bandpass used for 4XMM-DR10 and so our catalogue in Chapter 2. This means marginal cases where our HLX candidates have *XMM-Newton* data just below the $L_{\rm X} = 10^{41}\,{\rm erg\,s^{-1}}$ threshold, may be shown to be HLXs when the energy bandpass is not truncated. However, we find no such marginal

Table 3.6: Walton et al. (2022) HLX candidates which were no longer found to peak above the HLX L_X threshold following our spectral conversion. These candidates are not brought forward for analysis as part of our 'best' HLX candidates and a new peak L_X is listed.

Source	Host	New Peak L_X
2SXPS J003404.0-094222	NGC0151	7.7 $\times 10^{40}$
2SXPS J005950.5-073455	NGC0337	9.1 $\times 10^{40}$
2SXPS J010957.0-455500	IC1633	3.5 $\times 10^{40}$
4XMM J011046.1-454529	PGC073734	8.1 $\times 10^{40}$
4XMM J011906.5-342230	PGC663162	5.0 $\times 10^{40}$
2SXPS J061619.3-212219	NGC2207	5.6 $\times 10^{40}$
4XMM J125708.6-044144	PGC1054690	4.8 $\times 10^{40}$
4XMM J160211.8+155437	PGC2790838	9.2 $\times 10^{40}$
4XMM J163818.7-642201	ESO101-004	4.0 $\times 10^{40}$
2SXPS J204443.5-684540	NGC6943	6.1 $\times 10^{40}$
2SXPS J230451.5+121825	NGC7479	7.5 $\times 10^{40}$
4XMM J235700.5-344118	ESO349-009	4.2 $\times 10^{40}$

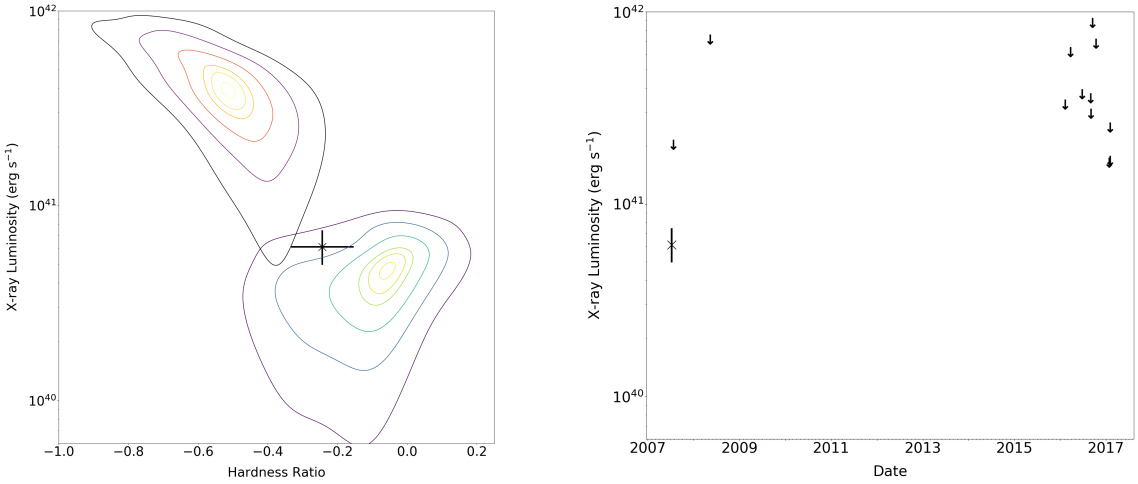

Figure 3.8: 2SXPS J204443.5-684540 in NGC6943, with only *Swift* data, is found to no longer be a HLX candidate following spectral conversion.

cases.

An example of one such (former) HLX candidate can be found in Fig. 3.8. The candidate, 2SXPS J204443.5-684540, only has data taken from *Swift*, having never been observed by *XMM-Newton* or *Chandra* (see Table 3.2). The single *Swift* detection has only 30 counts and since we cannot extract and fit a spectrum with so few counts, we apply the grid method. We find a spectrum characterised by $\Gamma = 1$ and an intrinsic absorption $n_H = 2 \times 10^{21}$ cm^{-2}. When converting the count rate into a flux via this spectrum, we find a new peak X-ray luminosity of 6.1×10^{40} erg s^{-1}. All such sources, which are found to still be ULXs (and are not excluded from the

Walton et al. (2022) catalogue), but no longer have any detection above the HLX luminosity threshold are shown in Tab. 3.6. With these sources no longer being HLXs, we do not bring them forward for any further discussion or analysis as part of our final 'good' sample of HLXs.

3.5.2.3 'Good' HLX Candidates

We present the hardness-intensity plots and long-term light curves for our remaining 20 'good' HLX candidates in Figure 3.9.

Figure 3.9: The remaining 20 'good' HLX candidates. *Swift* detections and errors are in black, *XMM-Newton* is in blue and *Chandra* in red. Upper limits in any detector are indicated by a downward arrow of the corresponding colour. In the two cases where a source has only a single observation, we do not plot the long-term light curve.

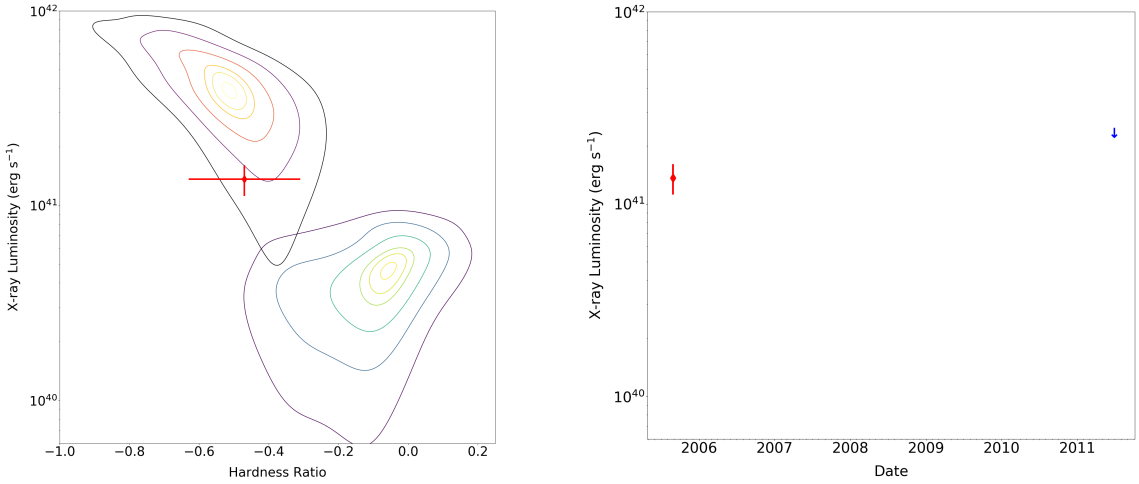

2CXO J001143.2-285548 in PGC087431

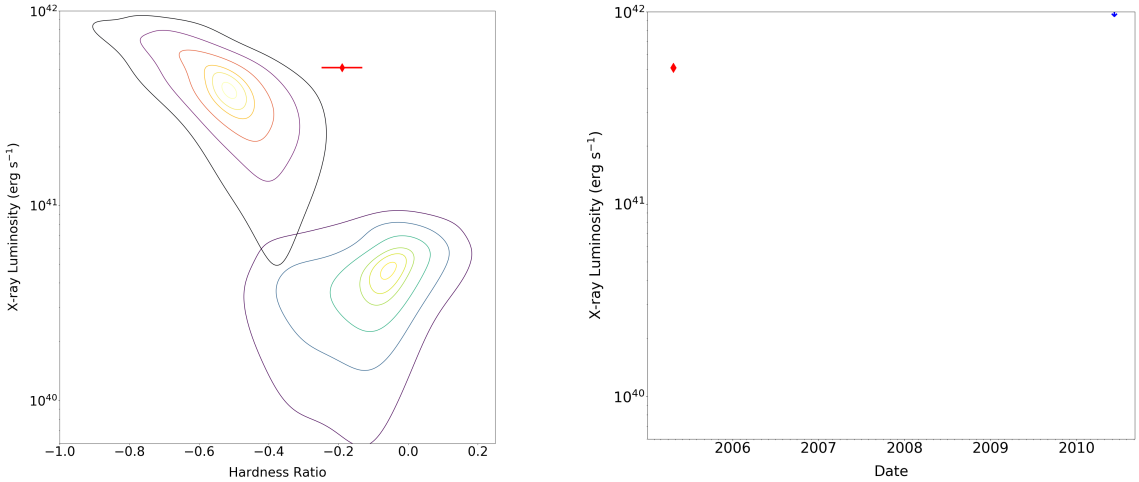

2CXO J005501.4-351909 in ESO351-021

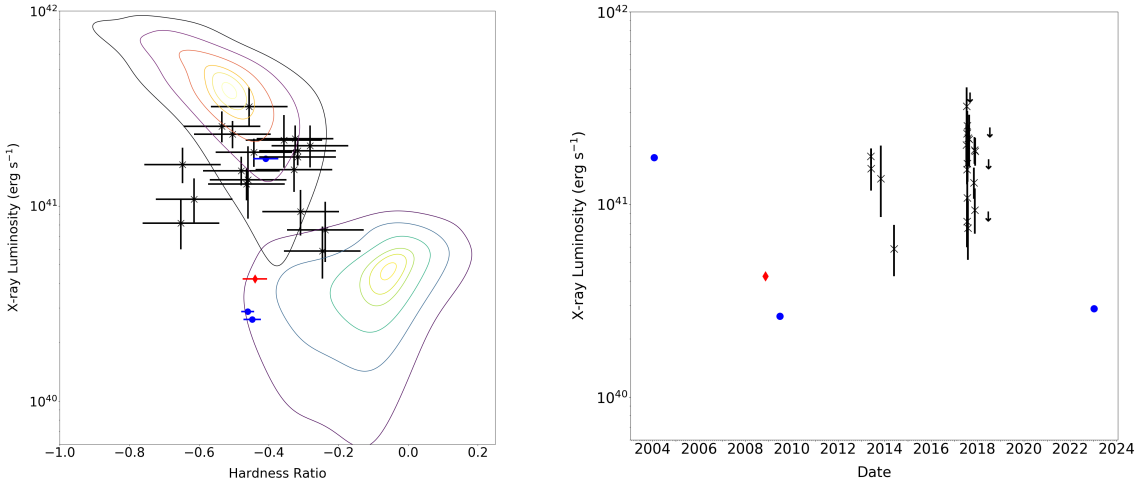

2SXPS J011942.7+032423 in NGC0470

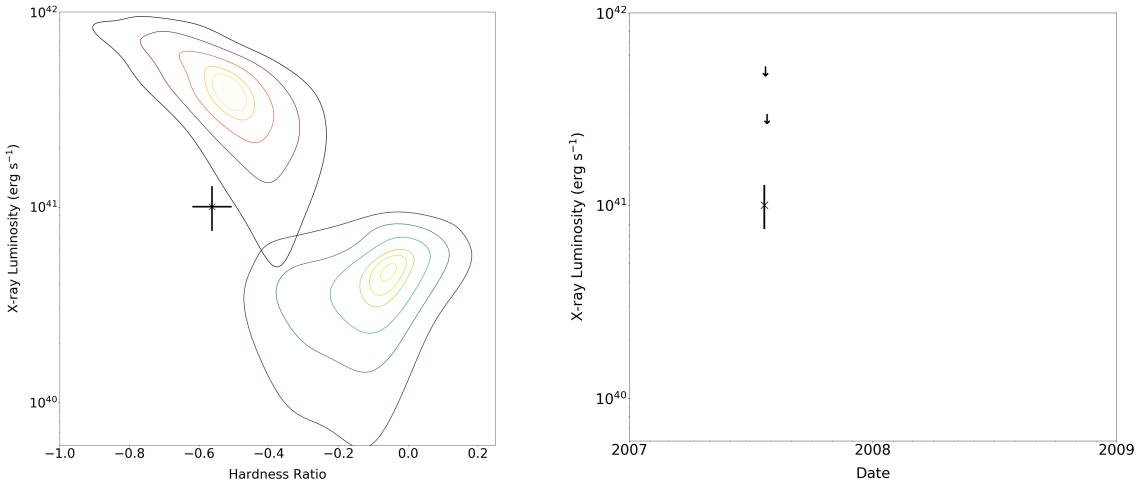

2SXPS J021218.5-020805 in UGC01697

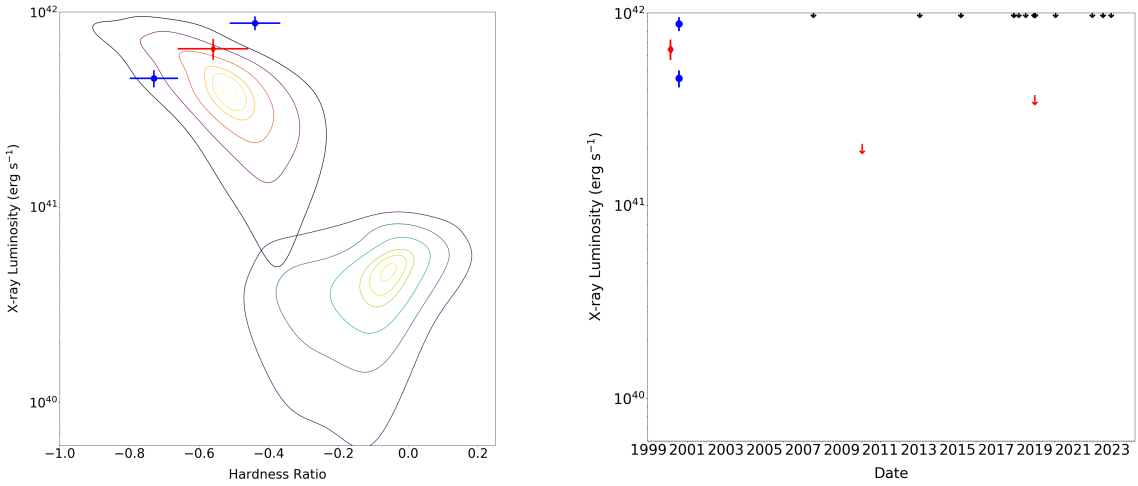

2CXO J024228.5-000202 in PGC3112720

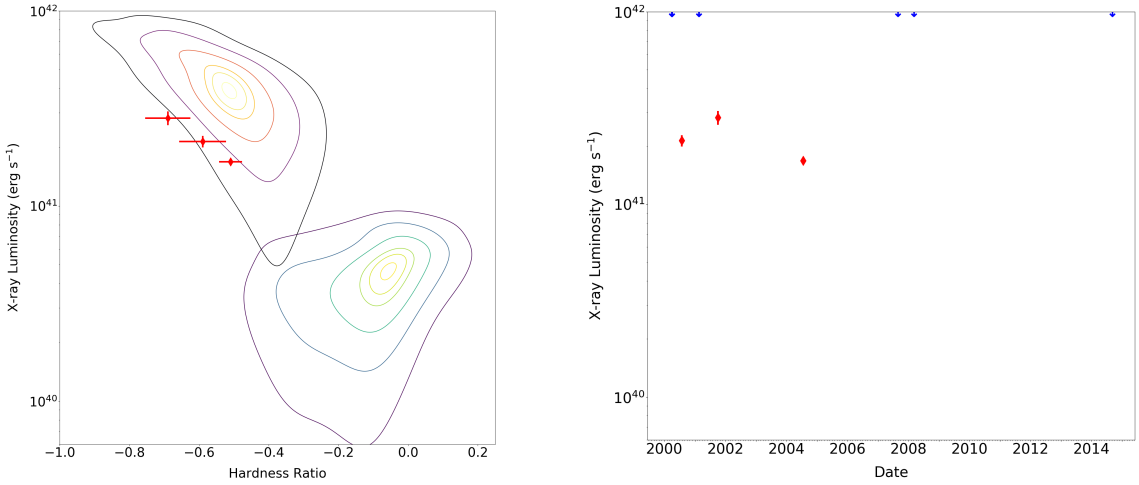

2CXO J043338.4-131612 in PGC015524

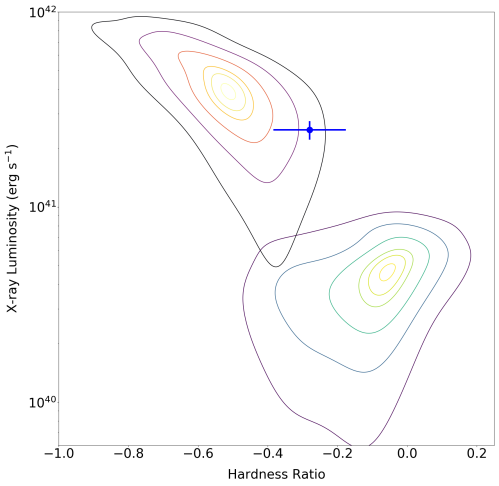

4XMM J050107.9-384321 in PGC146838

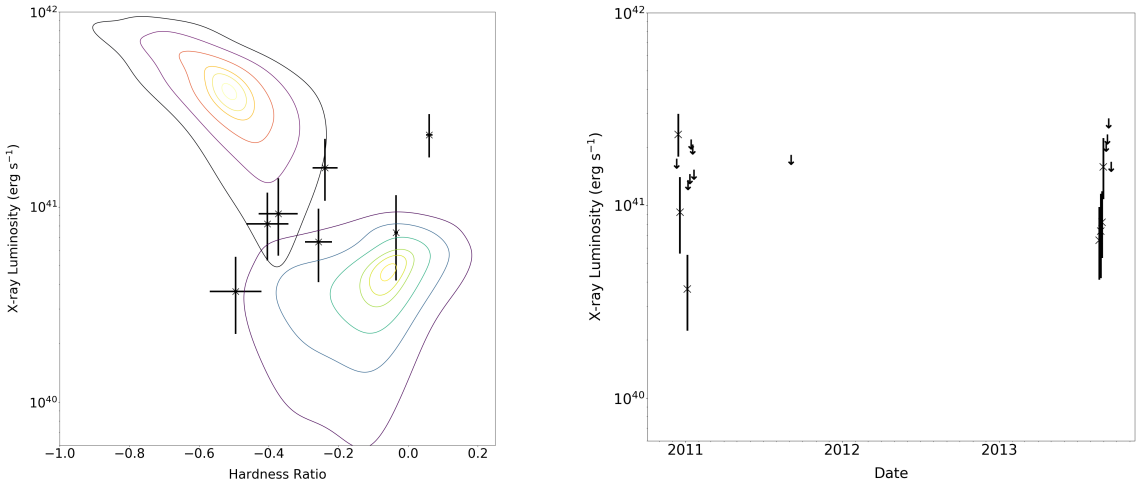

2SXPS J053246.8-140437 in NGC1954

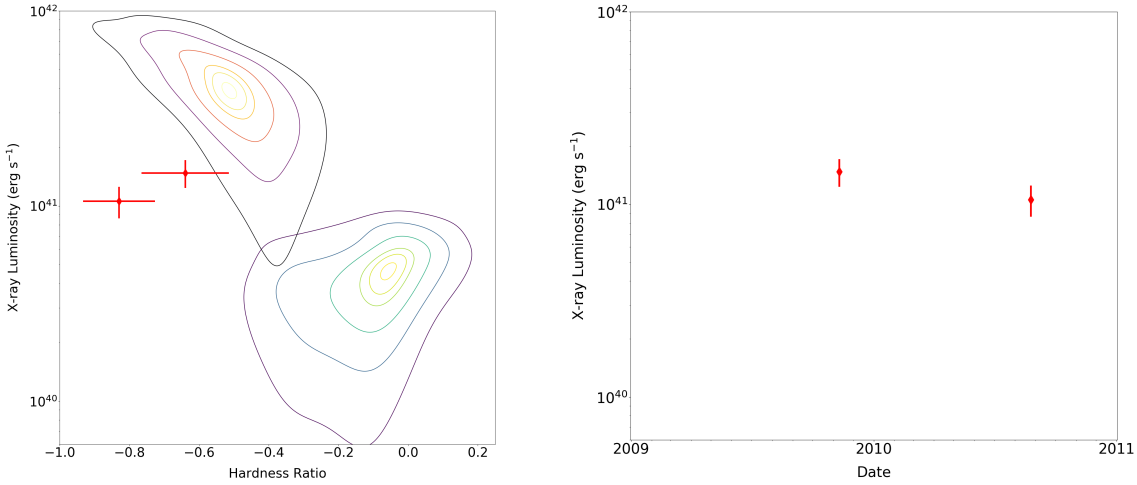

2CXO J055107.0-570640 in PGC393843

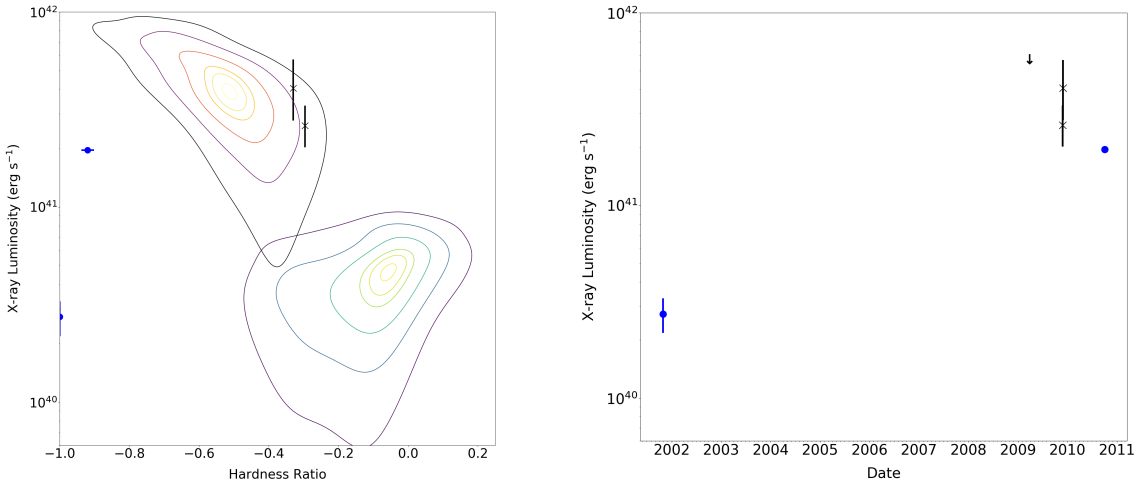

4XMM J061410.3-332954 in ESO365-001

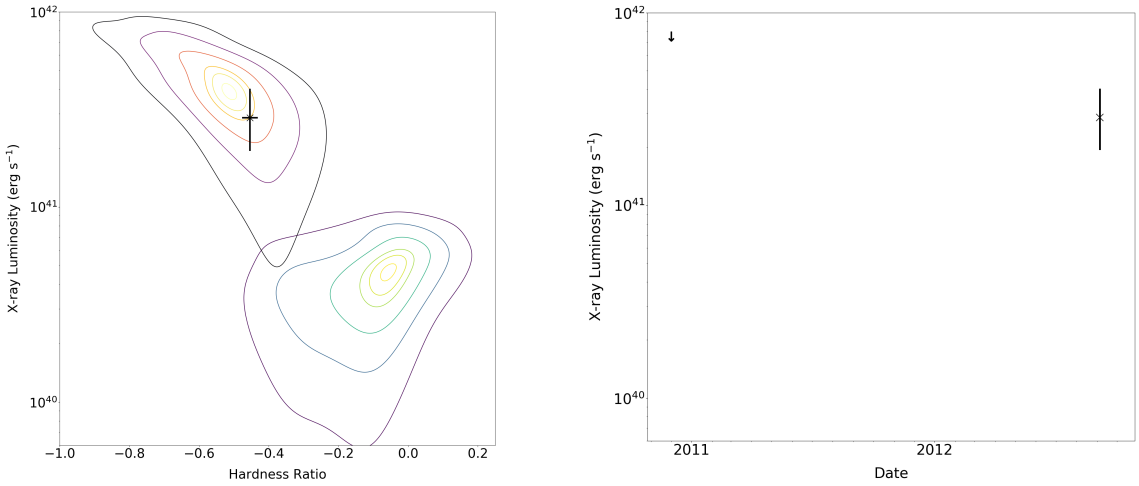

2SXPS J064706.9+741404 in NGC2256

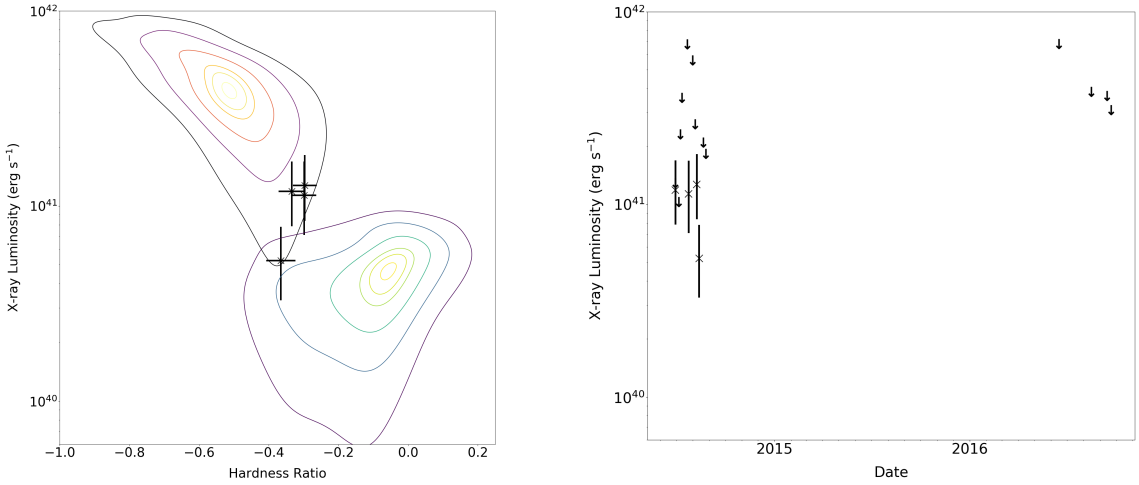

2SXPS J074512.3-712410 in NGC2466

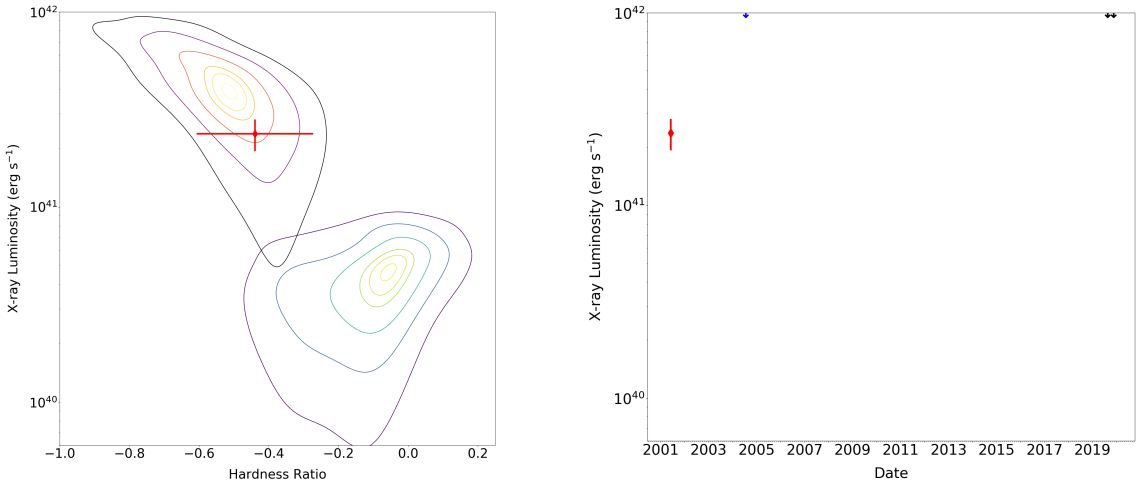

2CXO J103619.8-273939 in PGC141471

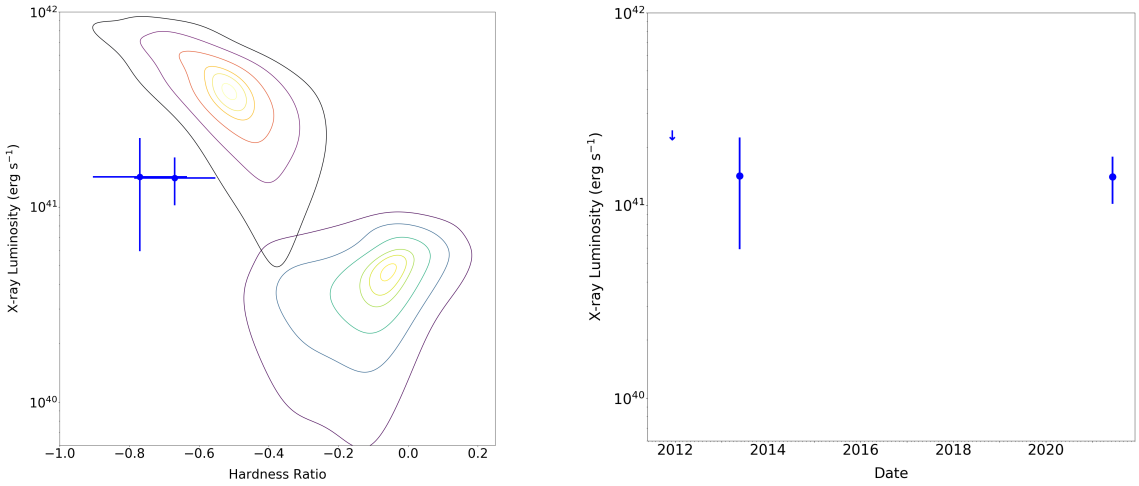

4XMM J103956.7-083446 in PGC083292

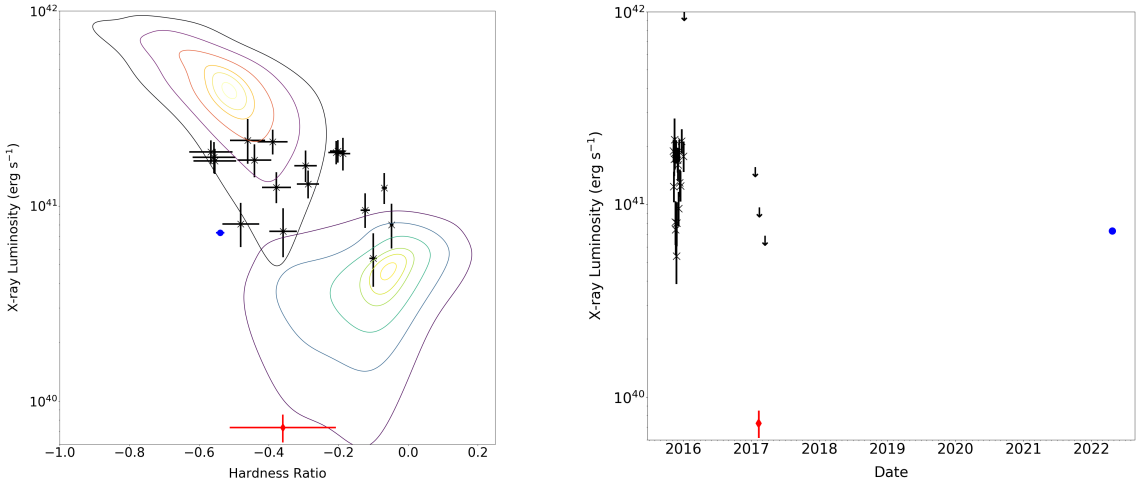

2SXPS J111416.1+481833 in NGC3583

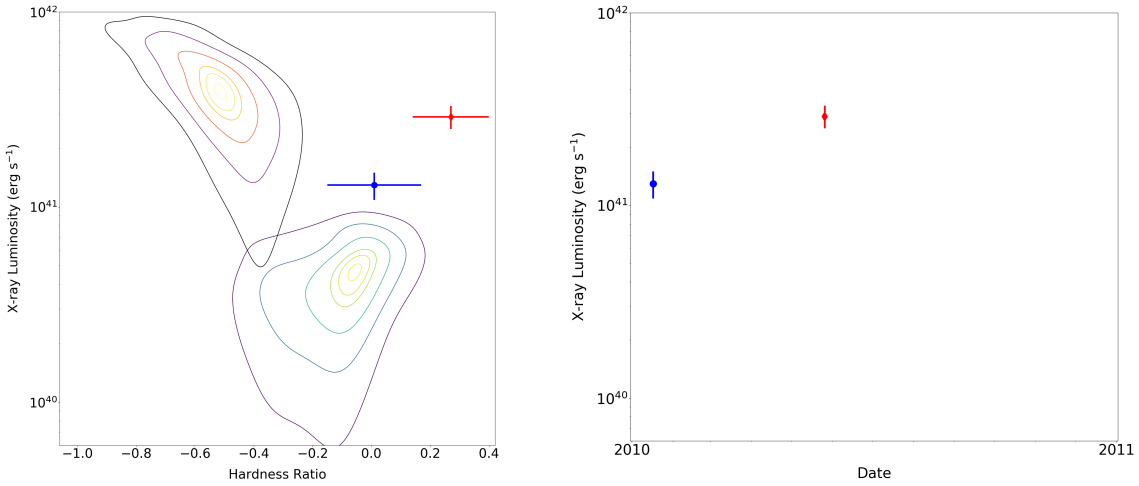

4XMM J140147.7-113438 in PGC094246

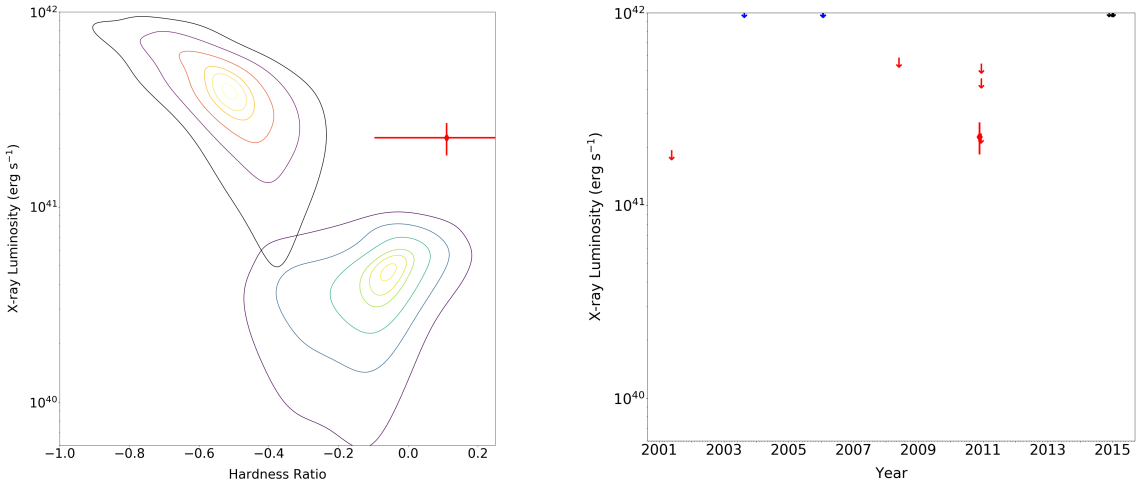

2CXO J151011.0+333358 in PGC2034704

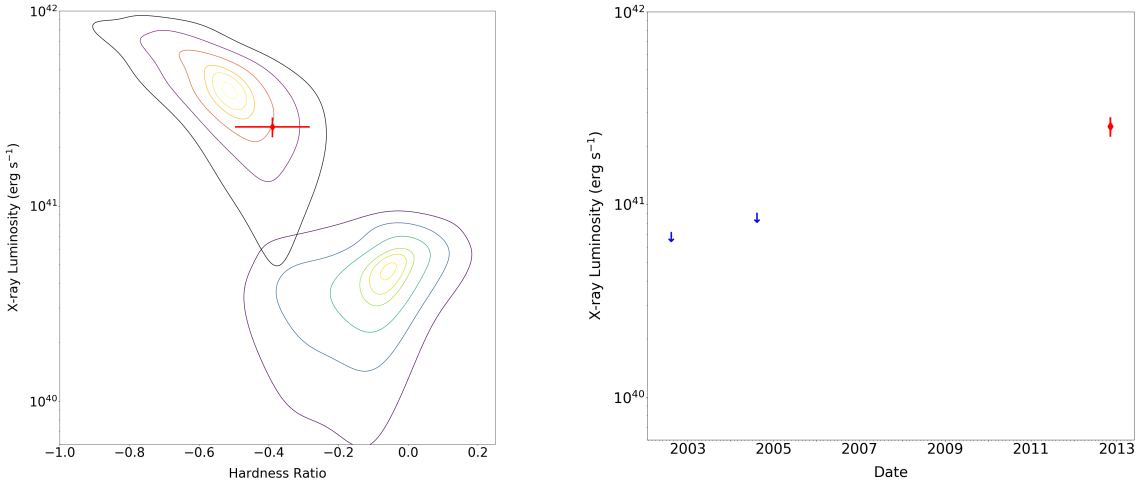

2CXO J153240.3+324228 in SDSSJ153238.30+324242.1

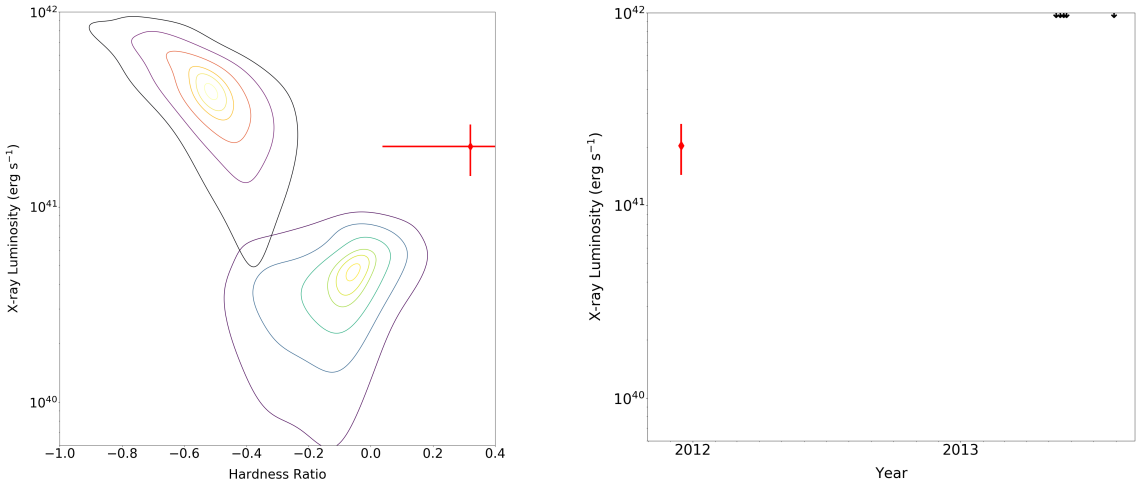

2CXO J185712.5-782830 in PGC140831

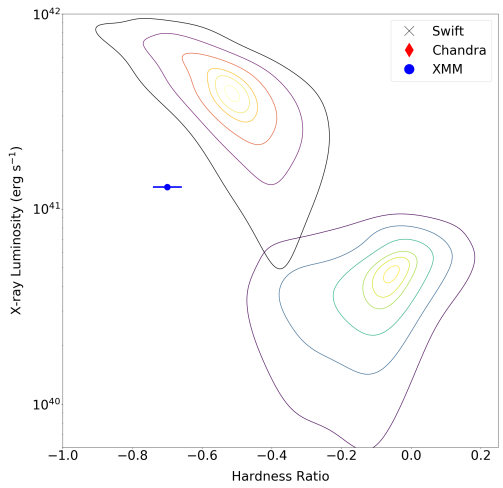

4XMM J210536.0-522300 in PGC128847

3.6 Discussion

We have analysed data from the 20 'best' HLX candidates from W22 and begin our discussion with the 6 HLX candidates with sufficient counts to extract spectra. Among these 6 HLX candidates, although for the majority the simple absorbed powerlaw offers a better fit to our spectra than the disc blackbody model, the observed differences are marginal. However, two *Chandra* candidates, 2CXO J043338.4-131612 in PGC015524 and 2CXO J005501.4-351909 in ESO 351-021 and one spectrum from a *Swift* candidate, 2SXPS J111416.1+481833 in NGC 3583 are better fit by a disc blackbody. We observe a $\Delta\chi^2$ difference in the disc blackbody compared to a powerlaw of 3.6, 1.0 and 12.6 for the same degrees of freedom respectively. 2CXO J005501.4-351909 and 2CXO J043338.4-131612 are characterised by inner disc temperatures of $T_{\rm in}$ =$1.27^{+0.86}_{-0.37}$ and $1.12^{+0.19}_{-0.16}$ keV respectively, consistent with ULXs (King et al. 2023). However, even in the improved disc blackbody case, both *Chandra* spectra are overfitting the data, while the *Swift* candidate is discussed below. The intrinsic absorption parameter is not well constrained in almost all of the disc blackbody fits, with 2CXO J005501.4-351909 in ESO 351-021 being the only exception. This source appears heavily absorbed with $n_{\rm H} = 10.2^{+7.2}_{-6.0}$ and $n_{\rm H} = 5.5^{+4.7}_{-4.0} \times 10^{21}$ cm^{-2} which are greater or equivalent to the values we observe in NGC 5907 ULX, an edge-on, host galaxy case.

In the majority of our sources listed in Tables. 3.3 and 3.4, we observe Γ values between 1.7 and 2.0 when fit with a simple absorbed powerlaw model. These measures of the photon index are well within and central to the typical range found for ULX spectra ($\Gamma \sim 1.5-3$; Kaaret et al. 2017). Two of the sources, while still within this range, are fit with softer spectra with higher photon index values in their powerlaw and both having inner disc temperatures $T_{\rm in} < 1$ keV. HLX candidate 4XMM J210536.0-522300 in host galaxy PGC128847 is quite soft, having a $\Gamma = 2.20^{+0.50}_{-0.30}$ and is better characterised by the soft powerlaw ($\chi^2 = 27.4$) than a disc blackbody ($\chi^2 = 29.3$) for 24 degrees of freedom. The source in ESO 365-001, 4XMM J061410.3-332954, is our softest source for which we extract a full spectrum (outside of our aggregate *Swift* spectrum for potential archetype - ESO 243-49 HLX-1). We find $\Gamma = 3.12^{+0.57}_{-0.27}$ and while 4XMM J061410.3-332954 is marginally better characterised by

the powerlaw fit, the data is being overfitted (reduced $\chi^2 < 1$).

Among the 20 best HLX candidates in our sample, the candidates in NGC 470 and NGC 3583 are the only sources that have multiple observations with sufficient data to take a spectrum. Source 4XMM J011942.7+032422 in NGC 470 was first observed in early 2004 and was discovered to be a HLX during that observation of the NGC 474 elliptical galaxy. It was then targeted for observations with *Chandra* and *XMM-Newton* in 2008 and 2009 respectively, but was found to have dipped below the HLX threshold (as can be seen in the long-term light curve, Fig. 3.9). A recent targeted observation with *XMM-Newton* in 2023 found this candidate outside the HLX regime, but short exposure observations with *Swift* taken in the epoch between suggest the candidate in NGC 470 has returned to HLX luminosities. Across the four spectra obtained from *XMM-Newton* or *Chandra* (which are all better fit by a powerlaw), we only observe a maximum spectral difference in the photon index $\Delta\Gamma = 0.1$ in candidate 4XMM J011942.7+032422, even with the luminosity varying by a factor $\sim$7.

HLX candidate 2SXPS J111416.1+481833 in NGC 3583 is one of the few cases better fit by a disc blackbody. The *Swift* spectra in Tables. 3.3 and 3.4 are fit to the *Swift* stack, entirely composed of data from 3σ *Swift* detections in late 2015 and early 2016. However, with the source then unobserved by our 3 missions for $\sim$5 years, the first observation with *XMM-Newton* in 2022 had sufficient data for a spectrum. The second spectrum is not only better characterised by a powerlaw ($\chi^2 = 83.9$ for 77 DoF), but the disc blackbody fit is so poor as to be outright rejected ($\chi^2 = 265.2$ for 77 DoF). Unlike 4XMM J011942.7+032422 which appears to remain spectrally consistent, 2SXPS J111416.1+481833 exhibits some spectral variability.

We have compared all 20 'best' HLX candidates to two potential archetypes of the class, NGC 5907 ULX and ESO 243-49 HLX-1, allowing us to contextualise the members of our sample for which data is limited. When looking at the hardness-intensity diagrams (HIDs) and long-term light curves presented in Fig. 3.9, we identify 4 rough categories to sort our candidates based on the position of detections in hardness-intensity space. The first two categories are for sources that strongly resemble one archetype or the other, which we label 5907-like for candidates with

behaviour matching NGC 5907 ULX and HLX1-like for sources like ESO 243-49 HLX-1. A significant population of our candidates are found to overlap with both 5907 and HLX1, or show no strong affinity to either within the maximal 75% *Swift* data contours. We define these as 'intermediate' and 'distinct' candidates respectively.

Several candidates exhibit a resemblance to ESO 243-49 HLX-1. Given that 2SXPS J064706.9+741404, 2CXO J103619.8-273939 and 2CXO J153240.3+324228 have detections within the 25% encapsulation contour, we classify these candidates as HLX1-like. However, these three sources each have only a single 3σ detection, so we make such a classification under the caveat that more observations are needed to draw any final conclusions about these candidates. 2CXO J024228.5-000202 in PGC3112720 is an extremely bright HLX candidate with a softness similar to ESO 243-49 HLX-1. However, while we do class this particular source as HLX1-like, the spectral evolutionary track in hardness-intensity space goes perpendicular to that of its corresponding archetype. As can be seen from the *Swift* data contours, ESO 243-49 HLX-1 undergoes a softening of its spectrum at higher luminosities. But studies into X-ray binaries have revealed a variety of HID shapes are possible for different candidates corresponding to the inclination of the system relative to the observer (Muñoz-Darias et al. 2013). The source 2CXO J024228.5-000202 appears to become spectrally harder at greater luminosities and the long-term light curve shows a *Chandra* detection in the middle of the suggested evolutionary track followed by a peak $L_{\rm X}$ some months later in the *XMM-Newton* observation, before dropping back to the lower, softer state over a time period of the order of days. 2CXO J043338.4-131612 in PGC015524 we also define to be HLX1-like and is our candidate with the strongest resemblance to ESO 243-49 HLX-1. 2CXO J043338.4-131612 occupies the same part of hardness-intensity space as defined by the contours of its potential archetype and follows the same spectral evolutionary track. As we have already discussed, 2CXO J043338.4-131612 is also one of the few HLX candidates for which we have an extracted spectrum better fit by a disc blackbody model than a powerlaw, which also aligns with ESO 243-49 HLX-1 behaviour (Servillat et al. 2011;Webb et al. 2012). However, the differences between the two fits for 2CXO J043338.4-

131612 are marginal and we note that the source is not very soft ($\Gamma \sim 2.0$) making it harder than the archetype. This is also reflected in the hardness-intensity diagram with all three *Chandra* detections skewed to the hard side of the ESO 243-49 HLX-1 parameter space.

We only characterise a single candidate as 5907-like, 2SXPS J053246.8-140437 in NGC 1954. This source overlaps with NGC 5907 ULX in hardness-intensity parameter space below the HLX threshold luminosity and its peak X-ray luminosity occurs in its hardest observed state, aligning with the spectral evolutionary track of NGC 5907 ULX (albeit extrapolated to a higher luminosity). We also note the rapid changes in flux on the long-term light curve which are reminiscent of NGC 5907 ULX (Walton et al. 2016a), although both archetypes exhibit fairly rapid changes, with ESO 243-49 HLX-1 typically having a sharp rise into an exponential decay (Kong et al. 2015).

We identify 8 'distinct' candidates; 2CXO J005501.4-351909, 2SXPS J021218.5-020805, 2CXO J055107.0-570640, 4XMM J103956.7-083446, 4XMM J140147.7-113438, 2CXO J151011.0+333358, 2CXO J185712.5-782830 and 4XMM J210536.0-522300. All of these candidates do not have any detections on their hardness-intensity plots which are coincident with the 75% *Swift* data encapsulated contour of either archetype. Due to their lack of association with either NGC 5907 ULX or ESO 243-49 HLX-1 and with 5 of these sources having only a single 3σ detection, these members of our sample are difficult to contextualise. The HLX candidates in this category are particularly hard or soft and so do not align with our archetypes, which are already significantly, spectrally hard and soft respectively amongst the wider ULX and HLX classes. Among our remaining HLX candidates, some of these harder sources are the most likely to still be background AGN interlopers, given their great distances and high luminosities. However, the softer sources in this category, may represent hyperluminous members of the supersoft ULX sub-class where most of the flux is emitted below 1 keV (Kaaret et al. 2017; Liu and Di Stefano 2008). But, for an X-ray spectrum dominated by low energy photons to be this luminous would be unusual, most supersoft ULXs have observed luminosities around or below $10^{39}\,\mathrm{erg\,s^{-1}}$ (Urquhart and Soria 2016).

The remaining 6 HLXs then fall into our 'intermediate' category, sat in the middle of the hardness-intensity parameter space or uniformly spread across it. Intermediate sources can have different observations within the smaller contours of both archetypes, such as the case for 2SXPS J111416.1+481833. Other intermediate sources solely occupy the specific region of parameter space where the two archetypes overlap, e.g. 2SXPS J074512.3-712410. That we find the majority of our sources to be either occupying the intermediate or distinct parts of the hardness-intensity parameter space suggests that the range of behaviour of HLXs goes well beyond that seen for ESO 243-49 HLX-1 and NGC 5907 ULX, potentially indicative of a heterogeneous source class composed of both IMBHs and the peak of the X-ray binary population.

3.7 Conclusion

The 71 HLX candidates presented as part of a new catalogue of ULXs, published under Walton et al. (2022) and discussed in Chapter 2, have been stringently filtered down to the 20 'best' HLX candidates.

Ten of our candidates were removed during an initial pass over the X-ray data, where it was deemed that the supposed source was the result of a readout artefact or a nearby bright object. A total of 23 candidates were removed due to being positionally coincident with point-like or extended multiwavelength counterparts outside of the host galaxy. There are 5 *Swift* HLX candidates found to have spurious X-ray data associated *Swift* pipeline functionality, specifically its treatment of the stacked 2SXPS data where correction factors have become inflated. The exact cause varies between these sources, but in each case the result has been a falsified, highly luminous entry in our ULX catalogue. We then found 12 candidates to no longer be at HLX luminosities after a spectral conversion of their measured count rates in to the *Swift* bandpass (0.3-10 keV).

We compared our 20 best candidates to two well-known HLXs; NGC 5907 ULX and ESO 243-49 HLX-1. This allows us to better understand the sources in our remaining sample through comparison, even with limited data, and explore whether

these two well-studied HLXs represent archetypes of the wider HLX class. While some sources do show an affiliation towards HLX1-like behaviour (albeit within their limited data), a significant portion of our candidates are found to either be intermediary or distinct from the two regions of parameter space defined by NGC 5907 ULX and ESO 243-49 HLX-1. This seems to suggest that these two well-known HLXs are not the only archetypes of the HLX class, but may represent the extremeties of a heterogeneous class - with the majority of other candidates falling somewhere in between.

These 20 HLX candidates represent good targets for further observations both with the current and future X-ray observatories. In particular, 2SXPS J011942.7+032423 in NGC0470 is already a coveted source for targeted observations, but hasn't been caught at HLX luminosities by a deep observation with *XMM-Newton* or *Chandra* since first observed in 2004. Further observations of our best HLX1-like candidate, 2CXO J043338.4-131612 in PGC015524, and our only 5907-like candidate, 2SXPS J053246.8-140437 in NGC 1954 will shed more light on their exact nature. However, it is clear from Tables. 3.3 and 3.4 in Section 3.5 we require sources that exhibit fluxes of the order of NGC 5907 ULX and ESO 243-49 HLX-1 ($\sim 10^{-12}\,\mathrm{erg\,cm^{-2}\,s^{-1}}$ to have sufficient X-ray data taken in follow-up observations and make a meaningful analysis.

It's the little details that are vital.
Little things make big things happen.

- John Wooden

CHAPTER 4

A targeted study of eRASS1 J060547.1-330413

We perform targeted analysis on an individual ULX candidate, eRASS1 J060547.1-330413, a source in our ULX catalogue in Chapter 2 and which also appears in each all-sky survey conducted by *eROSITA*. Two spectra for our candidate, taken from successfully proposed *XMM-Newton* and *Chandra* observations, are extracted and fit with four different models. To determine whether the target can be identified as a PULX, we carry out an accelerated pulsation search. However, the *XMM-Newton* observation that was proposed to provide sufficient data in order to do this is severely impacted by flaring. We use the method defined by Piconcelli et al. (2004) to try and mitigate the impact of this. There is no significant evidence for spectral variability and we are unable to detect coherent pulsations. We search for multiwavelength counterparts to the ULX candidate in the available *HST* data and find clear evidence of extended structure visible in the optical, which is suitable for follow-up.

4.1 Introduction

One key reason for compiling catalogues of astronomical sources is to add members to, and increase the populations of, individual sub-classes. Having assembled a catalogue of ULXs in chapter 2 and explored the HLX sub-class in chapter 3, in this chapter we explore proprietary data we obtained for an extreme ULX (eULX) identified in our catalogue and the novel *eROSITA* data. eULXs represent a sub-class between the ULX and HLX boundaries and were initially defined by Sutton et al. (2011) as sources with $L_{\rm X} \geq 5 \times 10^{40}\,{\rm erg\,s^{-1}}$. Over time the definition has now more generally shifted to $L_{\rm X} \geq 1 \times 10^{40}\,{\rm erg\,s^{-1}}$ (Roberts et al. 2023).

4.1.1 Target Selection

The intrinsic pulsations in PULXs are not easy to detect as simple periodograms can be insufficient for pulsation detections given that the secular and orbital variations decohere the pulsation signal, so an accelerated pulsation search is necessary. This can only be carried out with sufficient data, typically requiring $>10^4$ counts, and so is only currently plausible for the brightest ULXs.

We are involved in building a ULX catalogue from eRASS1 - 4 (the catalogue of sources composed from the first 4 passes over the western hemisphere of the sky), using the techniques established in Chapter 2. The first of these eROSITA ULX catalogues, assembled from eRASS1 data, to be published by Weber et al. is currently in preparation, and we anticipate using the extensive sky coverage of eRASS to hunt for new PULX targets. With this in mind, we took an initial sift through the population for good pulsation-detection candidates (with data from Weber and Wilms, priv. comm), using the following criteria; an observed luminosity placing the candidate in the 10^{40} - $10^{41}\,{\rm erg\,s^{-1}}$ eULX regime, a high flux of $>10^{-12}\,{\rm erg\,cm^{-2}\,s^{-1}}$ in the 0.2-5 keV eROSITA bandpass, only sources that have not been well-observed by *XMM-Newton* previously and nearby targets ($d < 10\,{\rm Mpc}$). Our flux criterion optimised the chance of obtaining high quality data from the sources and the distance cap minimises the potential for background interlopers and source confusion within the host galaxies.

Table 4.1: Details of the selected target eULX eRASS1 J060547.1-330413

RA & Dec (J2000)	Host Galaxy	d[1]	L_X (0.2-5 keV)[2]
$060547.1 - 330413$	ESO 364-029	9.0	$(2.2 \pm 0.4) \times 10^{40}$

[1] Distance in Mpc.
[2] Observed luminosity in the eROSITA bandpass ($\mathrm{erg\,s^{-1}}$), as inferred from eRASS1.

From this we were left with a single target, which we henceforth refer to as J0605. Details of our target are shown in Table 4.1. The location of this eULX had never previously been observed by *XMM-Newton* or *Chandra*. It has been covered by *Swift* in seven short observations, totalling ∼18 ks of exposure.

4.2 Data Reduction

We present the analysis of our proprietary *XMM-Newton* and *Chandra* observations, the first taken of the source by these observatories, in this chapter. A summary of the observation details of all data used is given in Table 4.2.

4.2.1 *Chandra*

We used CIAO v.4.12 to reprocess the data and create new level 2 events files prior to analysis. We used a 3 arcsecond radius circular aperture to extract data from our on-axis observation, and a nearby source-free background aperture of 7 arcsecond radius. Source and background spectra were extracted using the CIAO task SPECEXTRACT, which also provided the response matrix and ancillary response files.

4.2.2 *Swift*

We extracted data products from the *Swift* data archive for all observations covering the position of J0605 at the observation level. We then used a 35 arcsecond radius circular aperture placed at the best known position of J0605 and extracted raw counts from the event file. These were background-subtracted using an adja-

Table 4.2: Details of the observations of J0605 used in this chapter.

Mission	OBSID	Start Date	Good Exposure (ks)[a]
Swift	00038767001	2010-01-05	1.5
Swift	00048470001	2013-07-26	1.7
HST	13442	2013-11-17	1.1
Swift	00084263001	2014-07-21	0.5
Swift	00084263002	2014-07-25	8.8
Swift	00084263003	2014-07-27	5.2
Swift	07018787001	2019-05-11	0.1
Swift	07018831001	2019-05-11	0.1
XMM-Newton	0902090101	2022-10-18	18.1/16.7
Chandra	26678	2023-05-25	9.8

[a] *XMM-Newton* exposures are listed for the EPIC-pn/MOS detectors, after filtering for background flaring (see Section 4.3).

cent, source-free circular aperture of radius 70 arcseconds, and a count rate (with appropriate errors) determined for each observation.

4.2.3 *eROSITA*

We utilise data taken from early, private versions of the eRASS1 ULX catalogue (and subsequent eRASS2 to eRASS4 data available at time of writing) provided as part of collaboration on a ULX catalogue (Weber and Wilms priv. comm.). We took fluxes in the 0.2-5 keV *eROSITA* bandpass, which we convert to the *Swift* bandpass (0.3-10 keV) and use respective eRASS timings across each of the 4 eRASS cycles in order to supplement the long term source lightcurve.

4.2.4 *XMM-Newton*

We reduced our *XMM-Newton* data with the Science Analysis System (SAS v18.0.0, CALDB available in March, 2020). We generated calibrated and concatenated EPIC event lists using epproc and emproc following the SAS EPIC reprocessing thread. We defined a circular aperture of 20 arcsecond radius centred on J0605 as our source region for aperture photometry, flare filtering and spectral extraction. Typically, the next step would be to flare filter all *XMM-Newton* data for high particle background in accordance with the SAS EPIC filter background analysis thread, as is also described in previous chapters, see sections 2.3.2.1 and 3.3.2.

The successful proposal for the first *XMM-Newton* observation of J0605 called for a 30 ks exposure. This was determined to be a sufficient exposure to obtain a detailed characterisation of the source's X-ray emission, allowing for an accelerated search for pulsations with $\geq 10^4$ EPIC-pn counts from J0605. However, while our *XMM-Newton* observation was scheduled and taken across a 30 ks duration, the latter portion of the observation was badly impacted by background particle flaring. After taking measures to partly mitigate the flaring using the method outlined in Section 4.3, we retain $\sim$60% of the observation for analysis (as shown in Table 4.2).

4.3 Application of the Piconcelli Flare Filtering Method

The impact which low or moderate background flaring has had on an observation can be limited by following certain, post-observation processing steps. However, with the latter half of our observation severely impacted, we lose out on the high quality data in that portion of exposure and therefore that share of X-ray photon counts from the source, J0605. This impacts our likelihood of detecting pulsations in the source for the reasons discussed prior. But with the aim to still obtain as much information as possible about this object, we relax the typical constraints for flare filtering an observation by *XMM-Newton*. Instead, we search for the ideal analysis parameters via an empirical method.

To this end we implement the method first defined in the appendix of Piconcelli et al. (2004) where the flare filtering is performed based on the signal-to-noise ratio as opposed to the standard method of rejecting periods with count rates above the threshold cutoff at energies $\geq 10\,\mathrm{keV}$. The premise is to filter out just those time intervals for which the background count rate is so high that the SNR of the source does not significantly improve (or even worsens) by including such time intervals in the analysis. We focus our efforts on the EPIC-pn in order to define our overall criteria across EPIC-pn, MOS1 and MOS2 since this has the greatest amount of data and energy sensitivity. We extract EPIC-pn source and background lightcurves in the 0.3-10 keV energy range and the data points are sorted for increasing values of the count rate (CR) of the background region. The cumulative signal-to-noise ($\mathrm{SNR_{Cum}}$) distribution function is then calculated. Piconcelli et al. (2004) then describe how the $\mathrm{SNR_{Cum}}$ as a function of increasing background CR builds up to a peak after which it flattens or even decreases and use the point at which it overturns as the threshold used to reject the high background periods. However, as can be seen in Figure 4.1 in our case the distribution never overturns, possibly due to the difference in flux between our ULX, J0605, and the much brighter target analysed by Piconcelli et al. (2004), MKN 304. Instead, we identify 3 different regions in the curve, the initial climb, the shoulder and the plateau which correspond to $\mathrm{SNR_{Cum}}$

values of $\approx$ 6, 7 and 8 respectively in the EPIC-pn. We extract a background-corrected spectrum in each of the 3 cases and examine the fits of several spectral models to search for improvements at higher $\mathrm{SNR_{Cum}}$ values. The raw spectra in each case is plotted in Figure 4.2 and we find no improvement in the $\mathrm{SNR_{Cum}} = 7$ shoulder case or the plateau $\mathrm{SNR_{Cum}} = 8$ case, noting the reduced data quality in high energy bins. Thus we adopt the $\mathrm{SNR_{Cum}}$ value which corresponds to the end of the initial climb, which is 6, 4 and 4 for EPIC-pn, MOS1 and MOS2 respectively. Reading off from Figure 4.1 this gives cutoff values of 0.05, 0.02 and 0.02 count $\mathrm{s^{-1}}$ respectively for inside the background region to define our GTIs.

We cross-check our EPIC-pn final cleaned sample against the standard method of flare filtering and do not find as significant an improvement as in the Piconcelli et al. (2004) case. However, we still observe a marginal improvement in the total exposure and SNR we retain in the observation and so we elect to use the data cleaned by the Piconcelli et al. (2004) method going forward.

4.4 Spectral Analysis

4.4.1 *XMM-Newton*

We initially began by fitting the data with a simple absorbed powerlaw model. It can be the case for extreme ULXs to exhibit residual structure beyond such a simplified model (*e.g.* Gladstone et al. 2009; Mukherjee et al. 2015; Stobbart et al. 2006), but the model provides a crucial baseline. We then subsequently fit the data with more complex models often used to describe ULX spectra, see Table 4.3 for a full description. Analysing with XSPEC version 12.12 (Arnaud 1996) we allow for both the Galactic absorption column along the line of sight ($n_{\mathrm{H}} = 2.84 \times 10^{20}$ atoms $\mathrm{cm^{-2}}$; Willingale et al. 2013) and a further, intrinsic absorption at the distance of ESO 364-029 that is free to vary in all our models. In all fitted spectra, both the absorbers are modelled using TBABS and we use abundances set from Wilms et al. (2000b). In the case of *XMM-Newton* we also allow for multiplicative constants to scale between the data from the different EPIC camera detectors, since they have slight calibration differences. Between the spectra from different detectors,

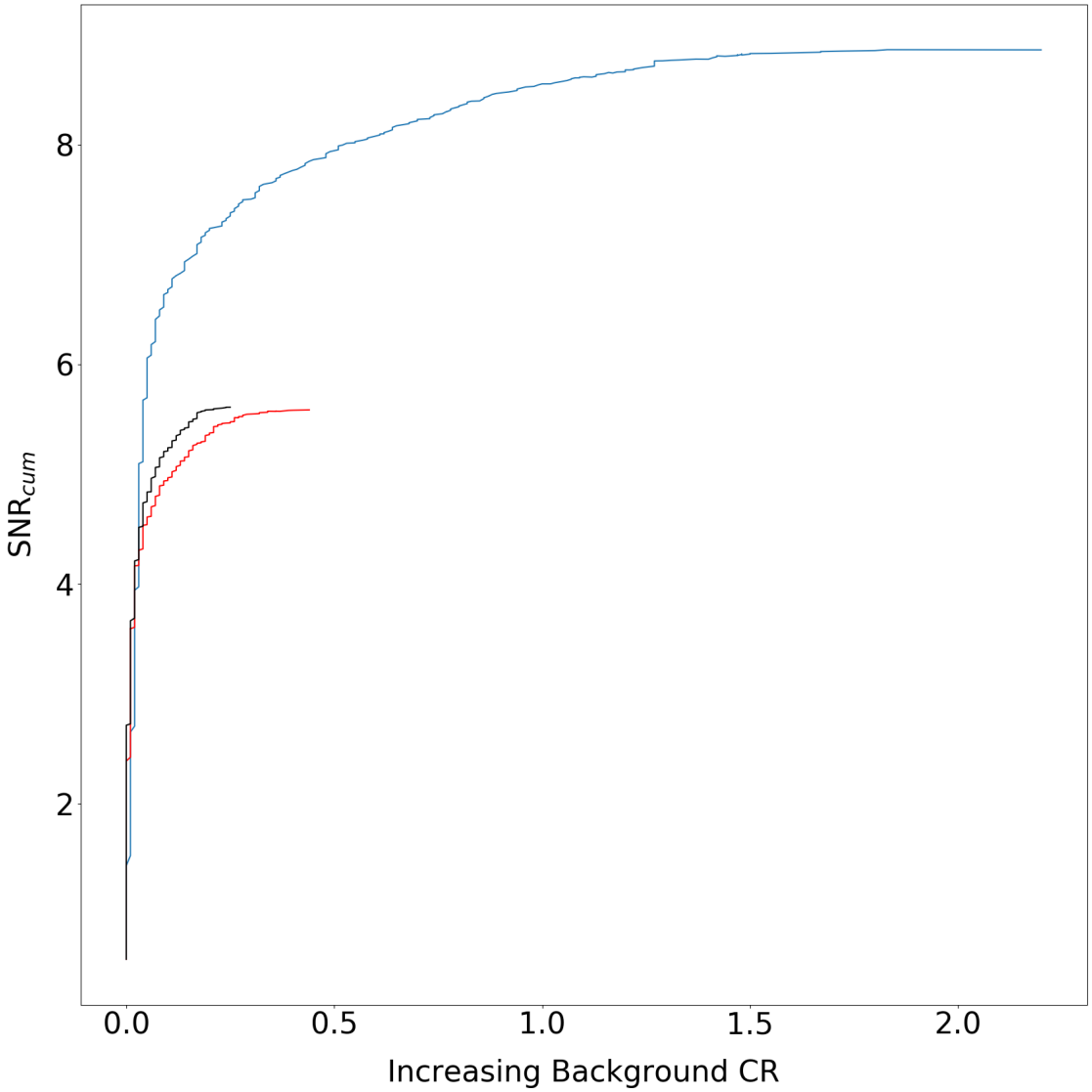

Figure 4.1: The cumulative SNR as a function of increasing CR in the background aperture for our *XMM-Newton* observation. The three different curves represent EPIC-pn (cyan), MOS1 (red) and MOS2 (black).

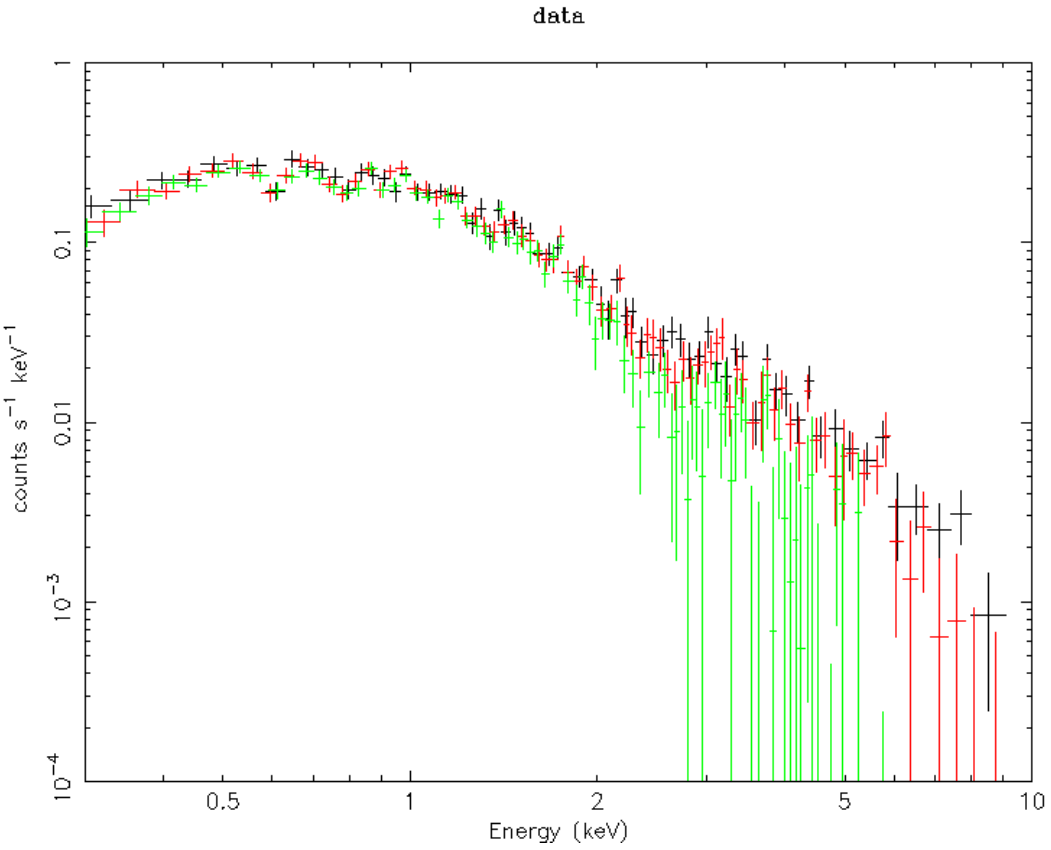

Figure 4.2: The raw EPIC-pn spectra from our *XMM-Newton* observation when cleaned based on SNR_{Cum} values of 6 (black), 7 (red) and 8 (green).

Table 4.3: Results of different spectral models as fit to the *XMM-Newton* spectra.

Spectral Model	$n_{\rm H}$ (10^{20} cm^{-2})	Γ/kT (keV)	p	χ^2	DoF
tbabs*tbabs*po	$3.92\pm^{1.60}_{1.52}$	$1.87\pm^{0.06}_{0.06}$		159.37	182
tbabs*tbabs*diskbb	< 0.08	$0.92\pm^{0.05}_{0.05}$		525.53	182
tbabs*tbabs*diskpbb	$3.82\pm^{1.63}_{1.55}$	< 4.94	$0.52\pm^{0.01}_{0.01}$	157.73	181
tbabs*tbabs*(diskbb+diskbb)	< 2.65	$0.34\pm^{0.03}_{0.05}$ / $1.97\pm^{1.63}_{0.40}$		152.78	180

the EPIC-pn multiplicative constant was set and held at unity while EMOS1 and EMOS2 are free to vary. We found these constants to be consistent within 10% across all our fits. The *XMM-Newton* spectrum, as shown in Figure 4.1, fit with the absorbed powerlaw model, returns an absorption $n_{\rm H} = (3.92\pm^{1.60}_{1.52}) \times 10^{20}$ cm^{-2} and $\Gamma = 1.87\pm^{0.06}_{0.06}$ (uncertainties on the spectral parameters are quoted at the 90% level).

Next, we fit another simplistic model, the DISKBB model (Mitsuda et al. 1984) which implicitly assumes a thin disc profile (Shakura and Sunyaev 1973). This model broadly represents the classic disc geometry seen in sub-Eddington X-ray binaries. We measure an inner disc temperature (kT) of $0.92\pm^{0.05}_{0.05}$ keV, however, when determining the 90% errors, the fit does not require a significant, intrinsic absorption parameter so we can only quote an upper limit, $n_{\rm H} < 0.08 \times 10^{20}$ cm^{-2}. In this case, when fitting the DISKBB model to J0605, we find that the fit is not only poorly constrained but is outright rejected with a $\chi^2 = 525.53$ for 182 degrees of freedom.

We then fit two more complicated spectral models. The first is the DISKPBB model (Mineshige et al. 1994), this builds on the DISKBB model by allowing for the additional free parameter p, a radial temperature index. This allows the model to reflect a thick, advection-dominated, super-Eddington accretion disc. A value of the $p = 0.75$ is appropriate for thin accretion discs Abramowicz et al. 1988, whereas our observed value of 0.5 ± 0.01 is indicative of a thick, advection-dominated super-Eddington accretion disc ($p < 0.75$). Our absorption in the DISKPBB fit is close to that found in the absorbed powerlaw case, $n_{\rm H} = 3.82\pm^{1.63}_{1.55} \times 10^{20}$ cm^{-2}. However, unable to place strong constraints on disc temperature.

The second case is a double disc blackbody model combined as TBABS*TBABS* (DISKBB+DISKBB). The intrinsic absorption is not well constrained, $n_{\rm H} < 2.65 \times$

Table 4.4: Results of different spectral models as fit to our *Chandra* spectrum.

Spectral Model	$n_{\rm H}$ (10^{20} cm^{-2})	Γ/kT (keV)	p	χ^2	DoF
tbabs*tbabs*po	< 0.46	$1.58\pm^{0.24}_{0.22}$		19.37	36
tbabs*tbabs*diskbb	< 0.07	$1.84\pm^{0.27}_{0.21}$		25.15	36
tbabs*tbabs*diskpbb	< 0.40	< 2.24	$0.59\pm^{0.08}_{0.06}$	19.12	35
tbabs*tbabs*(diskbb+diskbb)	< 0.85	$0.61\pm^{0.53}_{0.37}$ / $2.83\pm^{0.71}_{1.11}$		19.15	34

10^{20} cm^{-2}. Since the model is composed of two blackbody disc components we obtain two values, one corresponding to the inner accretion flow and the other a source of X-ray emission further out, $T_1 = 0.34\pm^{0.03}_{0.05}$ and $T_2 = 1.97\pm^{1.63}_{0.40}$.

4.4.2 *Chandra*

For our single *Chandra* observation we extract a background-corrected spectrum of J0605 using the CIAO task SPECEXTRACT in accordance with the online data analysis thread for extracting spectra and responses for pointlike sources in *Chandra*. Using XSPEC we fit our obtained spectrum with the same four spectral models used against our *XMM-Newton* data; an absorbed powerlaw, DISKBB, DISKPBB and the double disc component model. The powerlaw and DISKBB fits are presented with the *Chandra* spectrum and unfolded spectrum in Fig. 4.4 and the results of all fits are shown in Table 4.4.

The *Chandra* observation is best fit by a DISKBB, in contrast to our *XMM-Newton* spectra where this model was rejected and the spectrum is harder in the *Chandra* case based on the powerlaw. We do not observe any significant improvement over the simple powerlaw or DISKBB fits when using more complicated models. The radial temperature index in the DISKPBB model fit, with a value of $0.59\pm^{0.08}_{0.06}$, is indicative of a thick disc as with *XMM-Newton*. However, in the case of *Chandra*, we are unable to place strong constraints on the absorption or disc temperature.

With the reduced χ^2 values of all our fits being less than unity, it is clear that our models overfit this particular spectrum. The poor constraints on the intrinsic absorption parameter (the second TBABS value which is free to vary), are a result of continued degradation and lack of spectral sensitivity at low energies exhibited by *Chandra*. The progressive impact of degrading ACIS-S and ACIS-I detectors across

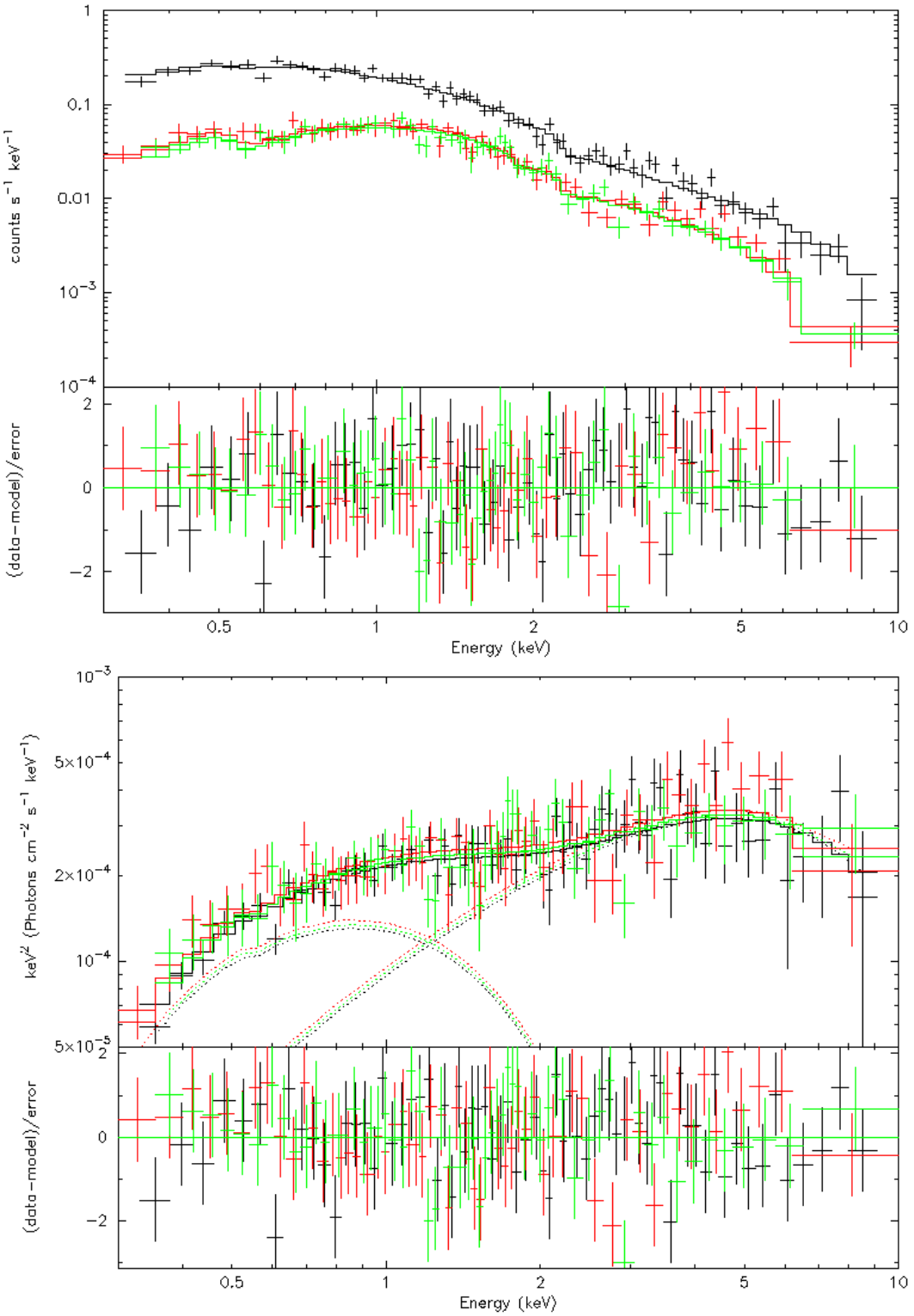

Figure 4.3: Spectra (top) and unfolded spectra (bottom) from the EPIC-pn (black), MOS1 (green) and MOS2 (red) detectors for our *XMM-Newton* observation of J0605-3304. All three spectra have been plotted in each case and then simultaneously fit with an absorbed powerlaw model (top) and a double disc blackbody model (bottom). The lower panel in each plot corresponds to the $\Delta\chi$ residuals between the fit and the data.

the *Chandra* cycles is discussed further in Chapter 3. The poor sensitivity at low energies leads to reduced information in the low energy end of the spectrum shown in Fig. 4.4, which means it is difficult to constrain the turnover due to absorption at lower energies and thus a greater uncertainty in the $n_{\rm H}$ parameter.

4.4.3 Evidence for Spectral Variability

One method for searching for spectral variability in a source with multiple spectra from different observations is to simultaneously fit all the spectra. We fit the simple absorbed powerlaw model, across our 5 input spectra (*XMM-Newton* MOS and pn, *Chandra* and stacked *Swift* spectra) and froze the fit parameters to match our best fit for the absorbed powerlaw to our *XMM-Newton* data. The result was a good fit, with $\chi^2 = 262.21$ for 244 degrees of freedom. This suggested that the spectra taken from the different instruments during separate observation times are significantly similar in both physical (and non-physical) parameters (or properties). We then observed the change in reduced χ^2 when we thawed normalisation, a non-physical parameter, on the *Swift* and *Chandra* spectra only. We found the new $\chi^2 = 250.97$ for 242 degrees of freedom, which shows an improvement over the fully frozen case, but only corresponds to a $\Delta\chi^2 = 5.62$ per additional degree of freedom. As this represents a marginal change, we also inspected the impact on the fit by allowing physical parameters to change. First, returning back to the fully frozen case beforehand, we varied the intrinsic absorption parameter ($n_{\rm H}$) for *Chandra* and *Swift*. The new fit was characterised by $\chi^2 = 257.11$ for 242 degrees of freedom, a $\Delta\chi^2 = 2.55$ per additional degree of freedom, which corresponds to an even lesser change than the normalisation. While this could suggest that the absorption is largely consistent between the spectra, it is more likely the result of $n_{\rm H}$ being poorly constrained in the *Chandra* spectrum and the parameter value having little effect on the final fit (see Table 4.4). Having returned to the fully frozen spectral fit, we thawed the photon index Γ of *Swift* and *Chandra*. The parameters of the resultant spectral fit did show a significant change in this case, $\chi^2 = 209.99$ for 242 degrees of freedom, which corresponds to a $\Delta\chi^2 = 26.11$ per additional degree of freedom. By comparing the powerlaw fits in Tables 4.3 and 4.4 (although the *Chandra* spectrum is better

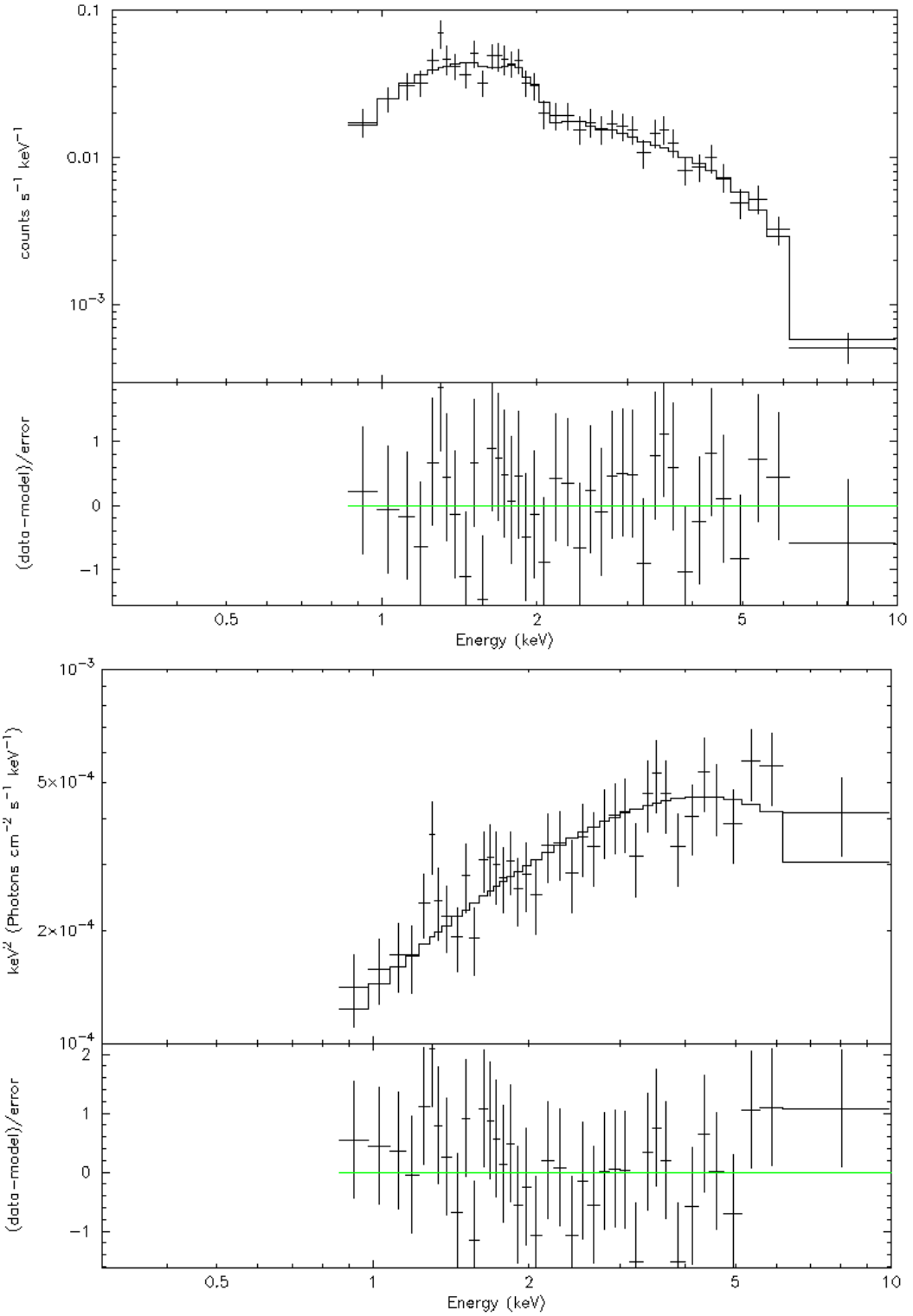

Figure 4.4: Spectrum (top) and unfolded spectrum (bottom) from the ACIS-S detector for our *Chandra* observation of J0605-3304, fit with an absorbed powerlaw model and a DISKBB model respectively. The lower panel in each plot corresponds to the $\Delta\chi$ residuals between the fit and the data.

characterised by a disc blackbody) the *Chandra* observation is spectrally harder but consistent within errors, $\Gamma = 1.87\pm^{0.06}_{0.06}$ for *XMM-Newton* and $\Gamma = 1.58\pm^{0.24}_{0.22}$ for *Chandra*. This is also reflected in our combined fit with the photon index free to vary, with Γ values of $1.61\pm^{0.06}_{0.05}$ and $1.60\pm^{0.10}_{0.09}$ for *Chandra* and *Swift* respectively. Considering the time at which our targeted observations with *XMM-Newton* and *Chandra* were taken, this gives evidence for intrinsic spectral variability in the source on $\sim$7 month timescales.

4.5 Temporal Analysis

We have 13 total X-ray observations of J0605 to date (see Table 4.2). In this section we search the data for any evidence of long or short term temporal variability, by plotting the source flux across all observations in a long term lightcurve and carrying out a pulsation search on our longest exposure observation by *XMM-Newton*. Performing an accelerated pulsation search to hunt for a statistically significant pulsation signal is currently the best method of determining if the J0605 compact accretor is a neutron star.

4.5.1 Long term Lightcurve

With J0605 having been observed by *Swift* across 7 observations totaling $\sim$18 ks, *eROSITA* during eRASS1:4 and *XMM-Newton* and *Chandra* during targeted observations, we combine all the data from our suite of modern, soft X-ray observatories into a single long term light curve for J0605, shown in Fig. 4.5. The four *eROSITA* data points correspond to the source flux detected and measured from eRASS 1:4 respectively. As in Chapter 3, we convert the fluxes from each mission into a common energy band, for which we select the *Swift* 0.3-10 keV energy bandpass. To do this we just assume a simple, absorbed powerlaw spectrum and take our parameter values from the best fit to the *XMM-Newton* spectra.

The results in Fig. 4.5 show J0605 exhibits some moderate long term variability. Earlier *Swift* observations, prior to 2015, caught J0605 in a period of relative quiescence below the eULX threshold of $L_{\rm X} > 10^{40}$ erg s^{-1}. The luminosity then peaked

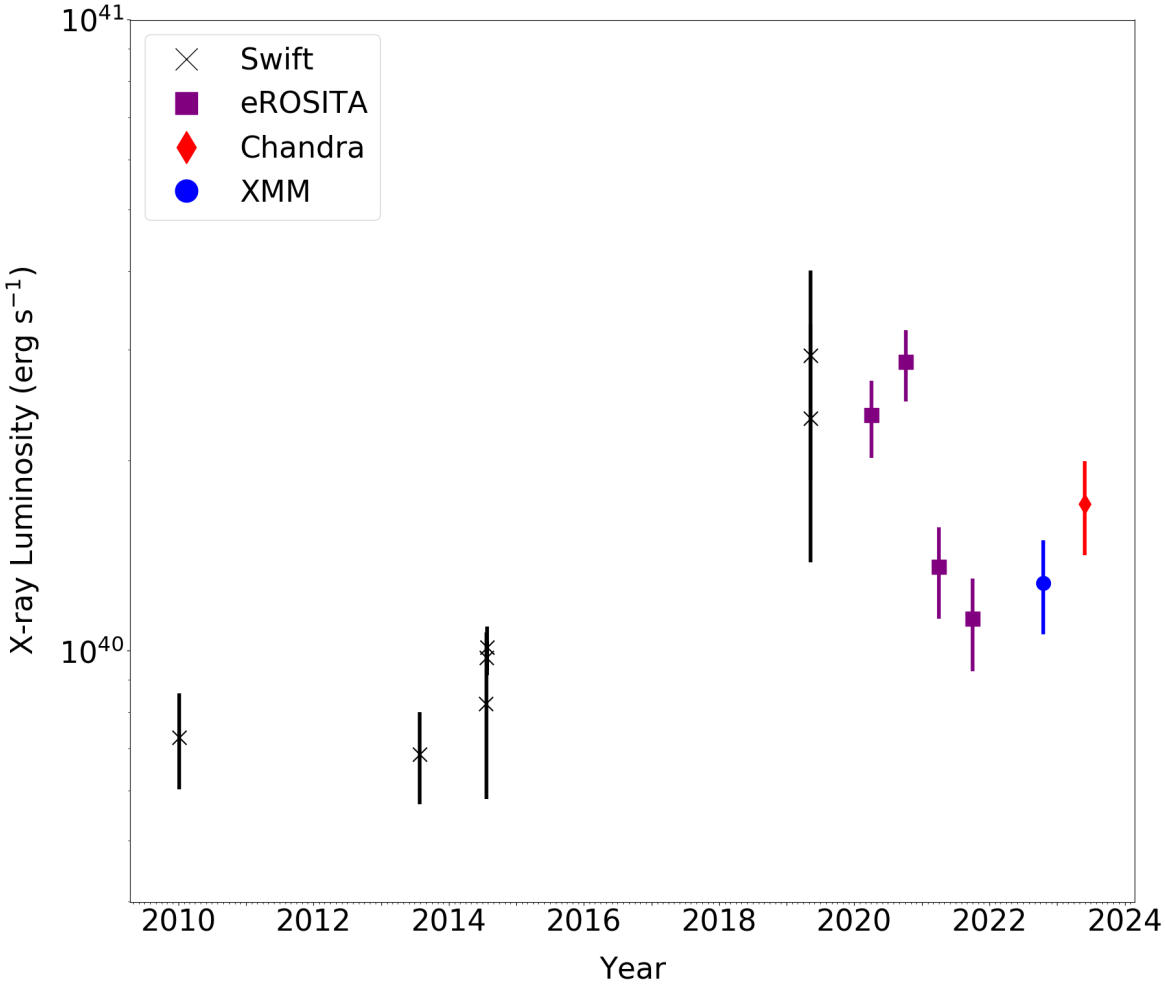

Figure 4.5: Long term lightcurve for J0605 in the 0.3-10 keV energy range based on the available X-ray data. Our *XMM-Newton* observation data is shown in blue, all available *Swift* data in black, *eROSITA* in purple and *Chandra* in red. Note that the all-sky scans, each taken over 6 months, from *eROSITA* have been combined together into individual data points to represent eRASS1:4 inclusive.

around 2020 with the last *Swift* observations and the first *eROSITA* observations during eRASS1 and eRASS2, before declining during later eRASS coverage back down below the eULX threshold. Our latest, targeted observations with *XMM-Newton* and *Chandra* suggest a bounce back as the luminosity climbs once more. However, the light curve is sparsely sampled with no information of the order ∼day to week timescales.

4.5.2 Pulsation Searches

Unlike the rest of our post-analysis products, the details in this section are applied to our raw data file prior to the flare cleaning via the Piconcelli method (Piconcelli et al. 2004). To search for short term temporal variability we use the pulsar timing tools included in the HENDRICS package (Bachetti 2018) which works directly from our initial observation data. Primarily we save our raw event files into the HENDRICS format and generate a lightcurve for our source region in the 0.3 to 10 keV energy range. We perform an accelerated pulsation search using the HENACCELSEARCH script. This script is the HENDRICS implementation of the Ransom et al. (2002) accelerated search where, starting from a single FFT, it is convolved with responses corresponding to different values of spin-up or spin-down. This technique is extremely efficient and often used to find binary pulsars, but is less sensitive than the focused Z search. However, the Z search requires prerequisite knowledge about the pulsations. Unfortunately we did not find any promising pulsation candidates in this observation, with no statistically significant detection recorded. Without a robust pulsation detection, HENACCELSEARCH returns an upper limit on the pulsed fraction of $\sim$20% for the frequency range, 0.01–5.00 Hz, over which we focused our pulsation search.

4.6 Multiwavelength Observations

The position of J0605 is covered by a single *HST* observation taken using the Wide Field Camera (WFC) in both the F606W and F814W filters (further details in Table 4.2). We extract the *HST* data directly from the archive and a resultant image giving an enhanced view of the source position is shown in Fig. 4.6. To associate any visible features with our X-ray source, we check the astrometry of the *Chandra* data, following the online data analysis thread for correcting absolute *Chandra* astrometry[1].

We run source detection across our *Chandra* image using WAVDETECT and match

[1] `https://cxc.cfa.harvard.edu/ciao/threads/reproject_aspect/`

this against the positions from *Gaia* DR2 of the same field. The positions corresponding to data from the *Gaia* DR2 catalogue are mapped over our two *HST* images to confirm alignment with optical sources and check the astrometry. However, *Chandra* and *HST* have different fields of view, meaning our *HST* coverage only covers a small portion of the ACIS-S3 chip. While we found significant agreement between *Gaia* DR2 and sources in *HST*, we found no overlap with our *Chandra* source detections within the *HST* FoV. Without some form of match between our X-ray and a multiwavelength dataset, we could not hope to correct the *Chandra* astrometry. We expanded our search to the field covered by the entirety of the *Chandra* ACIS instrument and found 3 matches with *Gaia* DR2 sources. We determined the astrometric offsets (ΔRA and ΔDec) between our source detections in *Chandra* from WAVDETECT and *Gaia* DR2 across these 3 matches. We then calculated the mean average ΔRA and ΔDec and use these to correct our *Chandra* astrometry. We find a mean average $\Delta\text{RA} = +1.01 \pm 0.59$ arcseconds and mean average $\Delta\text{Dec} = -0.57 \pm 0.17$ arcseconds for *Chandra* against *Gaia* DR2 and therefore invert these and apply them to our *Chandra* position in order to correct it. We consider the *Gaia* astrometric error to be negligible. Given the accepted 1σ accuracy in *Chandra* position as 0.1 arcseconds, the positional error radius of J0605 was derived as 1.02 arcseconds at 90% confidence level by combining all the errors in quadrature.

Within the colour composite *HST* image in Fig. 4.6, we observe some extended structure at the apparent position of the source. The structure is clearly visible using the F606W filter, but cannot be seen in the image taken with the F814W filter. Given that the F606W traces Hα where F814W does not, this could be evidence of a ULX bubble nebula.

4.7 Discussion

Our findings have shown that J0605 remains a compelling ULX candidate. We observe some spectral variability, primarily in the slope of the powerlaw, between our proposed *XMM-Newton*, *Chandra* and the stacked, archival *Swift* data. Our *Chandra* spectrum is better fit by an absorbed DISKBB while the same model is

Figure 4.6: *Above:* Colour composite image from the archival *HST* data using the F606W and F814W filters represented in blue and red respectively. The image is focused on the apparent position of the source J0605. *Below:* The same colour composite image as above, however, the overplotted magenta circle represents the positional uncertainty (1.02 arcseconds) following *Chandra* astrometric correction and error calculation.

outright rejected in the case of the *XMM-Newton* observation taken ∼7 months prior, further indicating the changes in spectral form of J0605. Both AGN than ULXs can show this level of spectral variability over longer timescales and when fitting an absorbed powerlaw J0605 is characterised by a hard Γ value (Γ ∼ 1.58 - 1.87) which is within the scope of those values for AGN. However, these fit parameters do also align with other ULXs, specifically the harder members of ULX population.

Our studies on the temporal variability of J0605 reveal little variation, as shown by the long term lightcurve in Fig. 4.5. Both ULXs and AGN can be observed to exhibit only small variability on long timescales, but it is uncommon in PULXs as the NS accretor's magnetic field can result in phenomena such as the propeller effect (Fürst et al. 2023; Tsygankov et al. 2016). However, it should be noted that a sparse sampling of the long term temporal behaviour in known PULX NGC 1313 X-2 would reveal similar variability (amplitude ∼2) to J0605 (Sathyaprakash et al. 2019b).

Having carried out an accelerated pulsation search, we do not detect coherent pulsations indicative of a NS accretor and identifying J0605 as a confirmed PULX. As was the case with NGC 3044 ULX1 at the end of Chapter 2, with clean, high S/N data we can still estimate an upper limit on the pulsed fraction. Our implementation of the methods from Piconcelli et al. (2004) have proven effective in reducing the data lost to the flaring and helped maximise the S/N, so we do estimate an upper limit on the pulsed fraction for J0605, found to be ∼20% in the 0.01–5.00 Hz frequency range. This can then rule out the existence of strong pulsations, like those in the PULX - NGC 300 ULX1 (Carpano et al. 2018) but cannot completely rule out weak or transient pulsations, such as those in NGC 1313 X-2 (Sathyaprakash et al. 2019b). Therefore we cannot rule out J0605 as a PULX candidate.

We identify an extended structure coincident with J0605 in an archival *HST* observation. ULX 'bubbles', large, ∼100 pc ionised nebulae, have been observed around some, but not all, ULXs. It is not yet clear why only a sub-sample of ULXs are found embedded in these structures (Pakull and Mirioni 2003). We propose that the observed structure may be a newly observed ULX 'bubble' associated with our novel ULX candidate, J0605. Some individual ULX bubbles have been studied

extensively (Moon et al. 2011) and these nebulae are a product of mechanical work from the ULX caused by outflows from the accretion mechanism and so their study allows us to estimate how long the ULX has been active. In this regard, the J0605 'bubble' is smaller compared with some of the better studied cases, being only ∼1 arcseconds across at a supposed distance of 9 Mpc corresponds to a physical size of ∼45 pc. This is closer in size to the small ULX bubbles in NGC 6946 X-1 (20×34 pc; Abolmasov et al. 2007) or Ho II X-1 (45 pc; Kaaret et al. 2004) as opposed to the ∼400 pc bubble observed in association with Holmberg IX X-1 (Sathyaprakash et al. 2019a). This may be a result of the surrounding medium being denser in ESO 364-029 (J0605's host) than Ho IX, as the bubble is driven out into the surrounding medium it will not expand as far in the J0605 case for the same amount of work done.

The apparent coincidence with the position of J0605 and this optical structure in the host galaxy casts further doubt on the candidate resulting from a background AGN. We consider the possibility that J0605 is an X-ray bright supernova remnant, given it has an optical nebula and - unlike many ULXs - appears to be invariable over long timescales. Although our X-ray detection in *Chandra* is point-like and does not exhibit any elongation, there is no strong evidence for a corresponding X-ray bubble, a supernova that recently occurred would also appear X-ray point-like (Immler et al. 2007). These types of young supernovae can be highly X-ray luminous and also exhibit hard spectra similar to that found in J0605 (Katsuda et al. 2014; Pooley et al. 2007). While the observed optical structure in J0605 does resemble other, observed ULX bubble nebulae these sort of structural features have been observed around supernovae (Immler et al. 2008). Fig. 4.7 shows a comparison between the archival *HST* observation of the J0605 position and a well known supernova in the Large Magellanic Cloud (LMC), SN 1987a. Despite the similarities, we have no prior record of a supernova at the position of J0605.

Figure 4.7: *Above:* Optical shells from SN 1987a in the LMC as observed in March 1988 by the *European Southern Observatory*. Two concentric circles are visible at 33 and 55 arcsecond radii corresponding to ∼16 pc and ∼26 pc across (Arnett et al. 1989). *Below:* Optical structure observed around the position of J0605 with *HST* (F606W filter).

4.8 Conclusion

The ULX candidate eRASS1 J060547.1-330413 (J0605) remains a promising, novel ULX candidate. The data quality from our successful proposal for observing time with *XMM-Newton* suffers from flaring which impacted ∼40% of the observation. We determined the method outlined by Piconcelli et al. (2004) was the most effective technique in retaining the maximum amount of usable data from the observation for analysis. We also have a targeted observation taken by *Chandra* for which we check the astrometry against *Gaia* so as to accurately constrain the eULX candidate position and associate with multiwavelength data from an archival *HST* observation.

J0605 exhibits some marginal spectral variability, being better characterised by a DISKBB fit that was rejected in an observation 7 months prior. Examining the absorbed powerlaw fits through simultaneous fitting reveals a variation in the photon index, Γ, between our *XMM-Newton* and *Chandra* observations and the *Swift* stack spectrum, with the *XMM-Newton* spectrum found to be softer. We observe no significant long term variability beyond a maximum amplitude of the order $\sim 2\times$ in luminosity, which is within reason for both ULXs and AGN. It is less common for PULXs to exhibit so little variation over long timescales due to interactions between the magnetic field and accretion mechanism. Although, other PULXs such as PULX NGC 1313 X-2 would show temporal variation of this type if the data were as sparse as J0605.

We were unable to detect coherent pulsations via pulsation searches, but due to the data limitations we cannot completely rule out the candidate as a PULX or the existence of pulsations. We detect a 20% upper limit on the pulsed fraction between 0.01–5.00 Hz which rules out strong pulsations in J0605, but we cannot confirm the absence of weak or tranisent pulsations.

We do identify an extended structure within the optical *HST* data at the periphery of the position of J0605. This suggests the possible existence of a ULX 'bubble nebula' around J0605, similar to those which have already been observed around some other ULXs. The structure also resembles that found with supernovae and the hard X-ray spectrum and compact X-ray detection are largely consistent with a young supernova. However, there is no current record of a supernova at the

position of J0605. Further follow-up is necessary to confirm the eULX candidate or supernova, with the possibility that J0605 presents a newly discovered ULX bubble nebula.

Deep in the human unconscious is a pervasive need for a logical universe that makes sense.
But the real universe is always one step beyond logic.

- Frank Herbert

CHAPTER 5

Conclusions and further work

With this work we aimed to create a multi-mission catalogue of ULXs that could be used to explore sub-populations of the ULX class, such as HLXs and eULXs. We also used the catalogue as a means to locate and identify individual sources of particular interest that are suitable for follow-up study. The thesis takes on something of an inverted pyramid structure (wide view at the top and narrow at the bottom) where we constructed a new, large catalogue of ULX candidates, then focused on a small, extreme sub-sample and finally looked at an individual eULX. Here we summarise the results of this work, briefly discuss the future of the ULX field and suggest next steps for this work going forward.

5.1 Conclusions

In Chapter 2 we created a new catalogue of ULX candidates containing 1843 sources residing in 951 different host galaxies. This was the largest catalogue of ULX candidates ever compiled at the time of publication. We revealed 689 new ULX candidates published in the catalogue and our sample also contained 71 HLX candidates, with a detailed analysis of this sub-population given in Chapter 3. Unlike previ-

ously published ULX catalogues, we used the latest data releases from three different, currently operating X-ray observatories; *XMM-Newton*, *Swift* and *Chandra* (the 4XMM-DR10, 2SXPS and CSC2 source catalogues, respectively). While this does introduce some non-uniformity to the catalogue, it maximises our X-ray sky and temporal coverage allowing us to identify the greatest number of ULX candidates. Our catalogue was cleaned based on similar methods to the previous *XMM-Newton* ULX catalogues from Walton et al. (2011b) and Earnshaw et al. (2019b). We also followed the approach taken in these works (and additionally Sutton et al. 2012) to estimate the remaining contribution of unknown contaminants. The residual unknown contamination fraction is estimated at $\sim$20% which is consistent with the values found for previous ULX catalogues (e.g. Earnshaw et al. 2019b; Walton et al. 2011b).

Subsequent ULX catalogues from Bernadich et al. (2022) and Tranin et al. (2024), to which we also compared our work, have quoted contamination estimates of $\sim$2%. While our final ULX count is lower, both in the *XMM-Newton* case for Bernadich et al. (2022) and overall compared to Tranin et al. (2024), our candidates are more likely to be reliable due to our use of stricter constraints for cross-matching, nuclear exclusion and host galaxy footprint. The assembly of the Tranin et al. (2024) catalogue follows a similar thread, but the cleaning is performed by their own developed, statistical classification of sources (Tranin et al. 2022). The quoted residual 2% unknown contaminant fraction depends on their object classification algorithmn having worked as successfully as they claim. Bernadich et al. (2022) rely on a much simpler sensitivity estimate, which potentially leads to a big underestimate of the background.

To demonstrate the capabilities of our new catalogue, which is already unveiling new sources of interest, we presented the first-look at a new ULX candidate found in NGC 3044. NGC 3044 ULX1 is a new extreme ULX candidate with high S/N data from both *Swift* and *XMM-Newton* in our catalogue. This source was observed with a current peak luminosity of $L_{\rm X,peak} \sim 10^{40}\,{\rm erg\ s^{-1}}$ by both *XMM-Newton* and *Swift* in 2013. The *XMM-Newton* spectrum revealed a best-fit model using two combined thermal accretion disc components at this peak flux, particularly reminiscent

of the previously studied ULX candidate Holmberg II X-1. We have searched for X-ray pulsations from NGC 3044 ULX1, but found no robust detection of any such variations. However, we do not rule out the possibility that it is a neutron star ULX, given the weaker pulsations detected in other sources (*e.g.* Rodríguez Castillo et al. 2020; Sathyaprakash et al. 2019b) and the transient nature of the pulsations in known PULXs (*e.g.* Bachetti et al. 2020; Israel et al. 2017a). NGC 3044 ULX1 lacks high energy X-ray coverage, which could help in further pulsation searches given the greater contribution from other components of the accretion flow below $\sim$10 keV in masking the pulsations. This makes NGC 3044 ULX1 a suitable target for a follow-up observing proposal with *NuSTAR* or the upcoming *High Energy X-ray Probe* (*HEX-P*; Madsen et al. 2018), which would have both superior sensitivity and imaging capabilities to *NuSTAR*.

We honed in on the HLX sub-class in Chapter 3, defined as those ULX candidates with $L_{\rm X,peak} > 10^{41}$ erg s^{-1}, of which there were 71 HLX candidates in our new catalogue from Chapter 2. This was reduced first down to 37 'good' candidates and finally our 20 'best' HLX candidates. The initial pass over the X-ray data to search for sources that were solely the result of defects, such as readout artefacts, removed 10 candidates. A further 23 candidates were found to be positionally coincident with point-like or extended multiwavelength counterparts outside of the host galaxy. The remaining 37 candidates, with one having been separated from the sample as a potential archetype and well-studied HLX, were brought forward to be analysed in greater detail. This revealed an issue in the functionality of the *Swift* data pipeline that had caused 2SXPS data stacks to be become falsely inflated. The exact origin depends on the source, but 5 *Swift* HLXs are found to be spurious. We then found 12 candidates to no longer be at HLX luminosities after a spectral conversion of their measured count rates in the 0.3-10 keV energy range.

We plotted long-term light curves and hardness-intensity plots for our remaining 20 best candidates. To better understand the sources in our remaining sample, many of which have only limited data, we compare to two well-known HLXs; NGC 5907 ULX (Israel et al. 2017a) and ESO 243-49 HLX-1 (Farrell et al. 2009). This allowed us to better understand the sources through context and explore whether these two

well-studied HLXs represent archetypes of the wider HLX class. We characterised only a single candidate as 5907-like and five other sources as HLX1-like, the remaining 14 candidates appear to either overlap with the hardness-intensity parameter space carved out by both our two archetypes or be entirely separate from it. This suggests that these two well-known HLXs are not archetypes of the HLX class. However, it may indicate that they are instead the extremeties of a heterogeneous class - with the majority of other candidates falling somewhere in between. All 20 of the best HLX candidates from the Walton et al. (2022) catalogue in Chapter 2 represent good targets for further observations both with the current and future X-ray observatories. However, we can identify 3 especially interesting sources among the final sample. The HLX candidate in NGC 470 is already a coveted source for targeted observations, unobserved at HLX luminosities by *XMM-Newton* or *Chandra* since first observed in 2004. With further observations of our best HLX1-like candidate in PGC015524, and our only 5907-like candidate in NGC 1954 we can shed more light on their exact nature.

In Chapter 4 we performed targeted analysis on an individual eULX candidate, labelled J0605, from our ULX catalogue which also appears in each all-sky survey conducted by *eROSITA*. Having obtained observing time with *XMM-Newton* and *Chandra* with successful proposals, we explored the X-ray, temporal and spectral properties of J0605. Approximately 40% of the *XMM-Newton* observation is affected by significant flaring and we take measures to mitigate the impact on our data analysis, determining that the method outlined by Piconcelli et al. (2004) was the most effective technique. The two spectra for our candidate, taken from *XMM-Newton* and *Chandra*, are extracted and fit with four different models. The *XMM-Newton* spectrum is well characterised by an absorbed powerlaw while the DISKBB fit is outright rejected. However, our *Chandra* observation $\sim$7 months later is best characterised by the DISKBB model. We perform a simultaneous fit of the absorbed powerlaw which reveals a variation in the photon index, Γ, between our *XMM-Newton* and *Chandra* observations and the *Swift* stack spectrum giving further evidence to J0605 exhibiting some marginal spectral variability.

We observe no significant long term variability in the X-ray luminosity of J0605.

Our latest, targeted observations with *XMM-Newton* and *Chandra* suggest a climb in luminosity after the apparent dip during the last two observations with *eROSITA*, however, the light curve is sparsely sampled with no information of the order ∼day to week timescales. On shorter timescales, we were unable to detect coherent pulsations with an accelerated pulsation search, we find a 20% upper limit on the pulsed fraction between 0.01–5.00 Hz which rules out strong pulsations in J0605, but we cannot confirm the absence of weak or tranisent pulsations.

We check the *Chandra* astrometry against *Gaia* so as to accurately constrain the eULX candidate position and associate it with any visible features within multi-wavelength data from an archival *HST* observation. There is an extended structure within the host galaxy at the position of J0605 which may be a ULX 'bubble nebula' surrounding the eULX candidate, similar to those which have already been observed around some other ULXs (Moon et al. 2011; Pakull and Mirioni 2002). The observed structure is however also reminiscent of a supernova remnant (Arnett et al. 1989; Immler et al. 2008), it is not uncommon for the two phenomena to be difficult to distinguish, with the hard X-ray spectrum and compact X-ray detection largely consistent with a young supernova (Immler et al. 2007; Katsuda et al. 2014; Pooley et al. 2007). However, with no current record of a supernova at that position, the ULX candidate eRASS1 J060547.1-330413 (J0605) remains a novel eULX candidate and possible PULX with an observed bubble nebula.

5.2 Future Work

With Chapters 3 and 4 we have already shown just some of the science, both through exploration of sub-populations and individual target analysis, that can stem from the new, large catalogue of ULX candidates presented in Chapter 2. We have largely covered the different types of publication that exist in the ULX field at this time; the publication of newer (and ever larger) catalogues, population studies (though these can extend beyond what we covered in our own work in Chapter 3 to explore the host galaxies statistics too) and finally individual ULX candidate studies.

It is clear that the best way of identifying ULX candidate as having a NS or BH

accretor, and thus determining the exact contribution of each type of compact object to the wider population, is searching for coherent pulsations. To have sufficient data quality in order do this requires ∼10,000 counts, but with constraints on exposure time and the limiting fluxes of the current suite of X-ray missions observations like this (and appropriate sources to target) are difficult to obtain. We have published a catalogue of 1843 sources, however, as can be seen from the HLX sub-class as an example, many lack data of the quality necessary to search for pulsations. Nevertheless, the future of the field is promising with the next generation of X-ray missions already under development.

As was already discussed during Chapter 2 in the context of NGC 3044 ULX1, below 10 keV the components of the accretion flow have a greater contribution which masks the coherent pulsations during timing analysis, making them more difficult to detect. Many sources lack observation coverage at these energies. By observing more ULX candidates above 10 keV we have an increased chance of identifying PULXs. The upcoming, proposed *HEX-P* probe (Madsen et al. 2018) will provide further coverage at this energy range (∼2-200 keV), consolidating that of *NuSTAR* (3-79 keV), but with greater imaging capabilities and superior sensitivity. *HEX-P* will be $\sim 40\times$ more sensitive than previous missions in the 10–80 keV band, and more than $100\times$ more sensitive in the 80–200 keV band (Madsen et al. 2019).

The exact scope of the *Athena* mission has changed substantially over recent years, but its launch will still offer a great improvement on observations of the X-ray sky (Nandra et al. 2013). Early simulations for *Athena* suggest it will have the requisite sensitivity to detect weak pulsations, like those that could exist in eULX candidate J0605 in Chapter 4, to a higher significance than current missions such as *XMM-Newton*. By discovering many more PULXs, due to the ability to find those that are weakly pulsating, *Athena* will be crucial in understanding the exact make-up of the heterogeneous ULX population and determining what fraction of ULXs contain NS or BH accretors.

The field of ULXs, like much of modern science and astronomy, is evolving rapidly. Once thought to be a rare population solely composed of IMBHs it is now seen as a heterogeneous class containing super-Eddington accretion and pul-

sating neutron stars with some IMBH candidates still remaining. The work in this thesis is only a part of what can be done with a large, clean catalogue of ULXs and we hope it provides further opportunities for the field to continue to grow.

Bibliography

Abbott, B. P., Abbott, R., Abbott, T. D., Abernathy, M. R., LIGO Scientific Collaboration, and Virgo Collaboration (2016). Observation of Gravitational Waves from a Binary Black Hole Merger. , 116(6):061102. 1.3.2

Abbott, R., Abbott, T. D., Abraham, S., Acernese, F., LIGO Scientific Collaboration, and Virgo Collaboration (2020). GW190521: A Binary Black Hole Merger with a Total Mass of 150 $M_{\odot}$. , 125(10):101102. 1.3.2, 1, 1.4.2

Abolmasov, P., Fabrika, S., Sholukhova, O., and Afanasiev, V. (2007). Spectroscopy of optical counterparts of ultraluminous X-ray sources. *Astrophysical Bulletin*, 62(1):36–51. 4.7

Abramowicz, M. A., Czerny, B., Lasota, J. P., and Szuszkiewicz, E. (1988). Slim Accretion Disks. *ApJ*, 332:646. 1.4.2, 2.5.2, 4.4.1

Alcock, C., Farhi, E., and Olinto, A. (1986). Strange Stars. *ApJ*, 310:261. 1.3.2

Almheiri, A., Marolf, D., Polchinski, J., and Sully, J. (2013). Black holes: complementarity or firewalls? *Journal of High Energy Physics*, 2013:62. 1.3.2

Arcodia, R., Merloni, A., Buchner, J., Baldini, P., Ponti, G., Rau, A., Liu, Z., Nandra, K., and Salvato, M. (2024). Cosmic hide and seek: the volumetric rate of X-ray quasi-periodic eruptions. *arXiv e-prints*, page arXiv:2403.17059. 1.2.4

Arnaud, K. A. (1996). XSPEC: The First Ten Years. In Jacoby, G. H. and Barnes, J., editors, *Astronomical Data Analysis Software and Systems V*, volume 101 of *Astronomical Society of the Pacific Conference Series*, page 17. 2.5.2, 4.4.1

Arnett, W. D. (1982). The cosmic distance scale - Methods for determining the distance to supernovae. *ApJ*, 254:1–7. 2.4

Arnett, W. D., Bahcall, J. N., Kirshner, R. P., and Woosley, S. E. (1989). Supernova 1987A. *ARA&A*, 27:629–700. 4.7, 5.1

Avakyan, A., Neumann, M., Zainab, A., Doroshenko, V., Wilms, J., and Santangelo, A. (2023). XRBcats: Galactic low-mass X-ray binary catalogue. *A&A*, 675:A199. 1.3.3

Bañados, E., Venemans, B. P., Mazzucchelli, C., Farina, E. P., Walter, F., Wang, F., Decarli, R., Stern, D., Fan, X., Davies, F. B., Hennawi, J. F., Simcoe, R. A., Turner, M. L., Rix, H.-W., Yang, J., Kelson, D. D., Rudie, G. C., and Winters, J. M. (2018). An 800-million-solar-mass black hole in a significantly neutral Universe at a redshift of 7.5. *Nat*, 553(7689):473–476. 1.4.2, 2.5.4

Bachetti, M. (2018). HENDRICS: High ENergy Data Reduction Interface from the Command Shell. Astrophysics Source Code Library, record ascl:1805.019. 2.5.3, 4.5.2

Bachetti, M., Harrison, F. A., Walton, D. J., Grefenstette, B. W., Chakrabarty, D., Fürst, F., Barret, D., Beloborodov, A., Boggs, S. E., Christensen, F. E., Craig, W. W., Fabian, A. C., Hailey, C. J., Hornschemeier, A., Kaspi, V., Kulkarni, S. R., Maccarone, T., Miller, J. M., Rana, V., Stern, D., Tendulkar, S. P., Tomsick, J., Webb, N. A., and Zhang, W. W. (2014). An ultraluminous X-ray source powered by an accreting neutron star. *Nat*, 514(7521):202–204. 1.4.2, 1.14, 2.5.3, 2.5.4, 3.1

Bachetti, M., Maccarone, T. J., Brightman, M., Brumback, M. C., Fürst, F., Harrison, F. A., Heida, M., Israel, G. L., Middleton, M. J., Tomsick, J. A., Webb, N. A., and Walton, D. J. (2020). All at Once: Transient Pulsations, Spin-down, and a Glitch from the Pulsating Ultraluminous X-Ray Source M82 X-2. *ApJ*, 891(1):44. 2.5.4, 5.1

Bachetti, M., Rana, V., Walton, D. J., Barret, D., Harrison, F. A., Boggs, S. E., Christensen, F. E., Craig, W. W., Fabian, A. C., Fürst, F., Grefenstette, B. W., Hailey, C. J., Hornschemeier, A., Madsen, K. K., Miller, J. M., Ptak, A. F., Stern, D., Webb, N. A., and Zhang, W. W. (2013). The Ultraluminous X-Ray Sources NGC 1313 X-1 and X-2: A Broadband Study with NuSTAR and XMM-Newton. *ApJ*, 778(2):163. 1.4.2, 2.5.2, 2.5.4

Bahar, Y. E., Bulbul, E., Ghirardini, V., Sanders, J. S., and eROSITA Consortium (2024). The SRG/eROSITA All-Sky Survey: Constraints on AGN Feedback in Galaxy Groups. *arXiv e-prints*, page arXiv:2401.17276. 1.2.4

Barrows, R. S., Mezcua, M., and Comerford, J. M. (2019). A Catalog of Hyperluminous X-Ray Sources and Intermediate-mass Black Hole Candidates out to High Redshifts. *ApJ*, 882(2):181. 2.4.1, 2.3, 3.1

Barrows, R. S., Mezcua, M., Comerford, J. M., and Stern, D. (2024). Merger-driven Growth of Intermediate-mass Black Holes: Constraints from Hubble Space Telescope Imaging of Hyper-luminous X-Ray Sources. *ApJ*, 964(2):187. 3.1, 3.2

Bekenstein, J. D. (1972). Black holes and the second law. *Nuovo Cimento Lettere*, 4:737–740. 1.3.2

Belczynski, K., Bulik, T., Fryer, C. L., Ruiter, A., Valsecchi, F., Vink, J. S., and Hurley, J. R. (2010). On the Maximum Mass of Stellar Black Holes. *ApJ*, 714(2):1217–1226. 1.3.2

Bernadich, M. C. i., Schwope, A. D., Kovlakas, K., Zezas, A., and Traulsen, I. (2022). An expanded ultraluminous X-ray source catalogue. *A&A*, 659:A188. (document), 1.5, 2, 2.7, 2.7.1, 2.7.2, 2.6, 2.7.3, 2.8, 2.9, 2.7, 3, 5.1

Bradt, H. V. D., Ohashi, T., and Pounds, K. A. (1992). X-ray astronomy missions. *ARA&A*, 30:391–427. 1.1

Brightman, M., Earnshaw, H., Fürst, F., Harrison, F. A., Heida, M., Israel, G., Pike, S., Stern, D., and Walton, D. J. (2020a). Swift Monitoring of M51: A 38 day Superorbital Period for the Pulsar ULX7 and a New Transient Ultraluminous X-Ray Source. *ApJ*, 895(2):127. 2.3.1

Brightman, M., Walton, D. J., Xu, Y., Earnshaw, H. P., Harrison, F. A., Stern, D., and Barret, D. (2020b). Spectral Evolution of the Ultraluminous X-Ray Sources M82 X-1 and X-2. *ApJ*, 889(1):71. 1.4.2

Buccheri, R., Bennett, K., Bignami, G. F., Bloemen, J. B. G. M., Boriakoff, V., Caraveo, P. A., Hermsen, W., Kanbach, G., Manchester, R. N., Masnou, J. L., Mayer-Hasselwander, H. A., Özel, M. E., Paul, J. A., Sacco, B., Scarsi, L., and Strong, A. W. (1983). Search for pulsed γ-ray emission from radio pulsars in the COS-B data. *A&A*, 128:245–251. 2.5.3

Burrows, D. N., Hill, J. E., Nousek, J. A., Kennea, J. A., Wells, A., Osborne, J. P., Abbey, A. F., Beardmore, A., Mukerjee, K., Short, A. D. T., Chincarini, G., Campana, S., Citterio, O., Moretti, A., Pagani, C., Tagliaferri, G., Giommi, P., Capalbi, M., Tamburelli, F., Angelini, L., Cusumano, G., Bräuninger, H. W., Burkert, W., and Hartner, G. D. (2005). The Swift X-Ray Telescope. , 120(3-4):165–195. 1.2.3, 2.3.2.2

Cappelluti, N., Brusa, M., Hasinger, G., Comastri, A., Zamorani, G., Finoguenov, A., Gilli, R., Puccetti, S., Miyaji, T., Salvato, M., Vignali, C., Aldcroft, T., Böhringer, H., Brunner, H., Civano, F., Elvis, M., Fiore, F., Fruscione, A., Griffiths, R. E., Guzzo, L., Iovino, A., Koekemoer, A. M., Mainieri, V., Scoville, N. Z., Shopbell, P., Silverman, J., and Urry, C. M. (2009). The XMM-Newton wide-field survey in the COSMOS field. The point-like X-ray source catalogue. *A&A*, 497(2):635–648. 2.4.2

Carpano, S., Haberl, F., Maitra, C., and Vasilopoulos, G. (2018). Discovery of pulsations from NGC 300 ULX1 and its fast period evolution. *Monthly Notices of the RAS*, 476(1):L45–L49. 1.4.2, 2.4.1, 2.5.3, 2.5.4, 3.1, 4.7

Carrera, F. J., Ebrero, J., Mateos, S., Ceballos, M. T., Corral, A., Barcons, X., Page, M. J., Rosen, S. R., Watson, M. G., Tedds, J. A., Della Ceca, R., Maccacaro, T., Brunner, H., Freyberg, M., Lamer, G., Bauer, F. E., and Ueda, Y. (2007). The XMM-Newton serendipitous survey. III. The AXIS X-ray source counts and angular clustering. *A&A*, 469(1):27–46. 2.4.2

Cash, W. (1979). Parameter estimation in astronomy through application of the likelihood ratio. *ApJ*, 228:939–947. 2.5.2

Charles, P. A. and Coe, M. J. (2006). Optical, ultraviolet and infrared observations of X-ray binaries. In *Compact stellar X-ray sources*, volume 39, pages 215–265. 1.3.2

Colbert, E. J. M. and Mushotzky, R. F. (1999). The Nature of Accreting Black Holes in Nearby Galaxy Nuclei. *ApJ*, 519(1):89–107. 1.1, 1.4.2

Colbert, E. J. M. and Ptak, A. F. (2002). A Catalog of Candidate Intermediate-Luminosity X-Ray Objects. *ApJS*, 143(1):25–45. 1.1, 2.1, 2.3

Cseh, D., Webb, N. A., Godet, O., Barret, D., Corbel, S., Coriat, M., Falcke, H., Farrell, S. A., Körding, E., Lenc, E., and Wrobel, J. M. (2015). On the radio properties of the intermediate-mass black hole candidate ESO 243-49 HLX-1. *MNRAS*, 446(4):3268–3276. 3.1

Dadina, M., Masetti, N., Cappi, M., Malaguti, G., Miniutti, G., Ponti, G., Gandhi, P., and De Marco, B. (2013). Ultraluminous X-ray source XMMUJ132218.3-164247 is in fact a type I Quasar. *A&A*, 559:A86. 2.3.3

Dall'Osso, S., Giacomazzo, B., Perna, R., and Stella, L. (2015). Gravitational Waves from Massive Magnetars Formed in Binary Neutron Star Mergers. *ApJ*, 798(1):25. 1.4.2

Dálya, G., Galgóczi, G., Dobos, L., Frei, Z., Heng, I. S., Macas, R., Messenger, C., Raffai, P., and de Souza, R. S. (2018). GLADE: A galaxy catalogue for multimessenger searches in the advanced gravitational-wave detector era. *MNRAS*, 479(2):2374–2381. 2.7.2

Davis, S. W., Narayan, R., Zhu, Y., Barret, D., Farrell, S. A., Godet, O., Servillat, M., and Webb, N. A. (2011). The Cool Accretion Disk in ESO 243-49 HLX-1: Further Evidence of an Intermediate-mass Black Hole. *ApJ*, 734(2):111. 3.1

Done, C., Gierliński, M., and Kubota, A. (2007). Modelling the behaviour of accretion flows in X-ray binaries. Everything you always wanted to know about accretion but were afraid to ask. , 15(1):1–66. 1.3.3

Drake, J. J., Marshall, H. L., Dreizler, S., Freeman, P. E., Fruscione, A., Juda, M., Kashyap, V., Nicastro, F., Pease, D. O., Wargelin, B. J., and Werner, K. (2002). Is RX J1856.5-3754 a Quark Star? *ApJ*, 572(2):996–1001. 1.3.2

Earnshaw, H. P., Grefenstette, B. W., Brightman, M., Walton, D. J., Barret, D., Fürst, F., Harrison, F. A., Heida, M., Pike, S. N., Stern, D., and Webb, N. A. (2019a). A Broadband Look at the Old and New ULXs of NGC 6946. *ApJ*, 881(1):38. 2.3.1, 2.2, 2.7.3, 3.1

Earnshaw, H. P., Heida, M., Brightman, M., Fürst, F., Harrison, F. A., Jaodand, A., Middleton, M. J., Roberts, T. P., Sathyaprakash, R., Stern, D., and Walton, D. J. (2020). The (Re)appearance of NGC 925 ULX-3, a New Transient ULX. *ApJ*, 891(2):153. 2.3.1

Earnshaw, H. P., Roberts, T. P., Middleton, M. J., Walton, D. J., and Mateos, S. (2019b). A new, clean catalogue of extragalactic non-nuclear X-ray sources in nearby galaxies. *MNRAS*, 483(4):5554–5573. 2.1, 2.2, 2.3.1, 2.3.2.1, 2.4.2, 2.3, 2.7.1, 2.7.2, 3.2, 5.1

Earnshaw, H. P., Roberts, T. P., and Sathyaprakash, R. (2018). Searching for propeller-phase ULXs in the XMM-Newton Serendipitous Source Catalogue. *MNRAS*, 476(3):4272–4277. 2.3.1

Esin, A. A., McClintock, J. E., and Narayan, R. (1997). Advection-Dominated Accretion and the Spectral States of Black Hole X-Ray Binaries: Application to Nova Muscae 1991. *ApJ*, 489(2):865–889. 1.3.3

Eskridge, P. B., Frogel, J. A., Pogge, R. W., Quillen, A. C., Berlind, A. A., Davies, R. L., DePoy, D. L., Gilbert, K. M., Houdashelt, M. L., Kuchinski, L. E., Ramírez, S. V., Sellgren, K., Stutz, A., Terndrup, D. M., and Tiede, G. P. (2002). Near-Infrared and Optical Morphology of Spiral Galaxies. *ApJS*, 143(1):73–111. 2.4

Evans, I. N., Primini, F. A., Miller, J. B., Evans, J. D., Allen, C. E., Anderson, C. S., Becker, G., Budynkiewicz, J. A., Burke, D., Chen, J. C., Civano, F., D'Abrusco, R., Doe, S. M., Fabbiano, G., Martinez Galarza, J., Gibbs, D. G., I., Glotfelty, K. J., Graessle, D. E., Grier, J. D., J., Hain, R. M., Hall, D. M., Harbo, P. N., Houck, J. C., Lauer, J. L., Laurino, O., Lee, N. P., McCollough, M. L., McDowell, J. C., McLaughlin, W., Morgan, D. L., Mossman, A. E., Nguyen, D. T., Nichols, J. S., Nowak, M. A., Paxson, C., Perdikeas, M., Plummer, D. A., Rots, A. H., Siemiginowska, A. L., Sundheim, B. A., Thong, S., Tibbetts, M. S., Van Stone, D. W., Winkelman, S. L., and Zografou, P. (2020a). The Chandra Source Catalog — A Billion X-ray Photons. In *American Astronomical Society Meeting Abstracts #235*, volume 235 of *American Astronomical Society Meeting Abstracts*, page 154.05. 2.1, 2.3.2.3

Evans, P. A., Beardmore, A. P., Page, K. L., Osborne, J. P., O'Brien, P. T., Willingale, R., Starling, R. L. C., Burrows, D. N., Godet, O., Vetere, L., Racusin, J., Goad, M. R., Wiersema, K., Angelini, L., Capalbi, M., Chincarini, G., Gehrels, N., Kennea, J. A., Margutti, R., Morris, D. C., Mountford, C. J., Pagani, C., Perri, M., Romano, P., and Tanvir, N. (2009). Methods and results of an automatic analysis of a complete sample of Swift-XRT observations of GRBs. *MNRAS*, 397(3):1177–1201. 2.2

Evans, P. A., Page, K. L., Osborne, J. P., Beardmore, A. P., Willingale, R., Burrows, D. N., Kennea, J. A., Perri, M., Capalbi, M., Tagliaferri, G., and Cenko, S. B. (2020b). 2SXPS: An Improved and Expanded Swift X-Ray Telescope Point-source Catalog. *Astrophysical Journal, Supplement*, 247(2):54. 2.1, 2.3.2.2, 3.3.1

Event Horizon Telescope Collaboration (2019). First M87 Event Horizon Telescope Results. I. The Shadow of the Supermassive Black Hole. *ApJ*, 875(1):L1. 1.3.2, 1.7

Farrell, S. A., Servillat, M., Gladstone, J. C., Webb, N. A., Soria, R., Maccarone, T. J., Wiersema, K., Hau, G. K. T., Pforr, J., Hakala, P. J., Knigge, C., Barret,

D., Maraston, C., and Kong, A. K. H. (2014). Combined analysis of Hubble and VLT photometry of the intermediate mass black hole ESO 243-49 HLX-1. *MNRAS*, 437(2):1208–1215. 3.1

Farrell, S. A., Webb, N. A., Barret, D., Godet, O., and Rodrigues, J. M. (2009). An intermediate-mass black hole of over 500 solar masses in the galaxy ESO243-49. *Nat*, 460(7251):73–75. 1.4.2, 2.3.1, 3.1, 3.4, 5.1

Feng, H. and Kaaret, P. (2010). Identification of the X-ray Thermal Dominant State in an Ultraluminous X-ray Source in M82. *ApJ*, 712(2):L169–L173. 1.4.2, 3.1

Forman, W., Jones, C., Cominsky, L., Julien, P., Murray, S., Peters, G., Tananbaum, H., and Giacconi, R. (1978). The fourth Uhuru catalog of X-ray sources. *ApJS*, 38:357–412. 1.1

Fürst, F., Walton, D. J., Harrison, F. A., Stern, D., Barret, D., Brightman, M., Fabian, A. C., Grefenstette, B., Madsen, K. K., Middleton, M. J., Miller, J. M., Pottschmidt, K., Ptak, A., Rana, V., and Webb, N. (2016). Discovery of Coherent Pulsations from the Ultraluminous X-Ray Source NGC 7793 P13. *Astrophysical Journal, Letters*, 831(2):L14. 1.4.2, 2.5.3, 2.5.4, 3.1

Fürst, F., Walton, D. J., Heida, M., Bachetti, M., Pinto, C., Middleton, M. J., Brightman, M., Earnshaw, H. P., Barret, D., Fabian, A. C., Kretschmar, P., Pottschmidt, K., Ptak, A., Roberts, T., Stern, D., Webb, N., and Wilms, J. (2021). Long-term pulse period evolution of the ultra-luminous X-ray pulsar NGC 7793 P13. *A&A*, 651:A75. 2.5.3

Fürst, F., Walton, D. J., Heida, M., Harrison, F. A., Barret, D., Brightman, M., Fabian, A. C., Middleton, M. J., Pinto, C., Rana, V., Tramper, F., Webb, N., and Kretschmar, P. (2018). A tale of two periods: determination of the orbital ephemeris of the super-Eddington pulsar NGC 7793 P13. *A&A*, 616:A186. 2.5.3

Fürst, F., Walton, D. J., Israel, G. L., Bachetti, M., Barret, D., Brightman, M., Earnshaw, H. P., Fabian, A., Heida, M., Imbrogno, M., Middleton, M. J., Pinto, C., Salvaterra, R., Roberts, T. P., Rodríguez Castillo, G. A., and Webb, N. (2023). Probing the nature of the low state in the extreme ultraluminous X-ray pulsar NGC 5907 ULX1. *A&A*, 672:A140. 3.1, 4.7

Fürst, F., Walton, D. J., Stern, D., Bachetti, M., Barret, D., Brightman, M., Harrison, F. A., and Rana, V. (2017). Spectral Changes in the Hyperluminous Pulsar in NGC 5907 as a Function of Super-orbital Phase. *ApJ*, 834(1):77. 2.4, 3.1

Gaia Collaboration (2018). Gaia Data Release 2. Summary of the contents and survey properties. *A&A*, 616:A1. 2.7.1

Gao, Y., Wang, Q. D., Appleton, P. N., and Lucas, R. A. (2003). Nonnuclear Hyper/Ultraluminous X-Ray Sources in the Starbursting Cartwheel Ring Galaxy. *ApJ*, 596(2):L171–L174. 3.1

Garmire, G. P., Bautz, M. W., Ford, P. G., Nousek, J. A., and Ricker, George R., J. (2003a). Advanced CCD imaging spectrometer (ACIS) instrument on the Chandra X-ray Observatory. In Truemper, J. E. and Tananbaum, H. D., editors, *X-Ray and Gamma-Ray Telescopes and Instruments for Astronomy.*, volume 4851 of *Society of Photo-Optical Instrumentation Engineers (SPIE) Conference Series*, pages 28–44. 1.2.1

Garmire, G. P., Bautz, M. W., Ford, P. G., Nousek, J. A., and Ricker, George R., J. (2003b). Advanced CCD imaging spectrometer (ACIS) instrument on the Chandra X-ray Observatory. In Truemper, J. E. and Tananbaum, H. D., editors, *X-Ray and Gamma-Ray Telescopes and Instruments for Astronomy.*, volume 4851 of *Society of Photo-Optical Instrumentation Engineers (SPIE) Conference Series*, pages 28–44. 2.3.2.3

Gatuzz, E., Wilms, J., Hämmerich, S., and Arcodia, R. (2024a). Probing the physical properties of the intergalactic medium using SRG/eROSITA spectra from blazars. *A&A*, 683:A213. 1.2.4

Gatuzz, E., Wilms, J., Zainab, A., Freund, S., Schneider, P. C., Robrade, J., Czesla, S., García, J. A., and Kallmanınst, T. R. (2024b). SRG/eROSITA 3D mapping of the ISM using X-ray absorption spectroscopy. *arXiv e-prints*, page arXiv:2401.17284. 1.2.4

Gehrels, N. (1986). Confidence Limits for Small Numbers of Events in Astrophysical Data. *ApJ*, 303:336. 2.3.2.2

Gehrels, N., Chincarini, G., Giommi, P., Mason, K. O., Nousek, J. A., Wells, A. A., White, N. E., Barthelmy, S. D., Burrows, D. N., Cominsky, L. R., Hurley, K. C., Marshall, F. E., Mészáros, P., Roming, P. W. A., Angelini, L., Barbier, L. M., Belloni, T., Campana, S., Caraveo, P. A., Chester, M. M., Citterio, O., Cline, T. L., Cropper, M. S., Cummings, J. R., Dean, A. J., Feigelson, E. D., Fenimore, E. E., Frail, D. A., Fruchter, A. S., Garmire, G. P., Gendreau, K., Ghisellini, G., Greiner, J., Hill, J. E., Hunsberger, S. D., Krimm, H. A., Kulkarni, S. R., Kumar, P., Lebrun, F., Lloyd-Ronning, N. M., Markwardt, C. B., Mattson, B. J., Mushotzky, R. F., Norris, J. P., Osborne, J., Paczynski, B., Palmer, D. M., Park, H. S., Parsons, A. M., Paul, J., Rees, M. J., Reynolds, C. S., Rhoads, J. E., Sasseen, T. P., Schaefer, B. E., Short, A. T., Smale, A. P., Smith, I. A., Stella, L., Tagliaferri, G., Takahashi, T., Tashiro, M., Townsley, L. K., Tueller, J., Turner, M. J. L., Vietri, M., Voges, W., Ward, M. J., Willingale, R., Zerbi, F. M., and Zhang, W. W. (2004). The Swift Gamma-Ray Burst Mission. *ApJ*, 611(2):1005–1020. 1.2, 1.2.3, 2.1

Ghez, A. M., Salim, S., Hornstein, S. D., Tanner, A., Lu, J. R., Morris, M., Becklin, E. E., and Duchêne, G. (2005). Stellar Orbits around the Galactic Center Black Hole. *ApJ*, 620(2):744–757. 1.3.2

Ghosh, H., Mathur, S., Fiore, F., and Ferrarese, L. (2008). Low-Level Nuclear Activity in Nearby Spiral Galaxies. *ApJ*, 687(1):216–229. 2.3.1

Giacconi, R. (2003). Nobel Lecture: The dawn of x-ray astronomy. *Reviews of Modern Physics*, 75(3):995–1010. 1.1

Giacconi, R., Branduardi, G., Briel, U., Epstein, A., Fabricant, D., Feigelson, E., Forman, W., Gorenstein, P., Grindlay, J., Gursky, H., Harnden, F. R., Henry, J. P., Jones, C., Kellogg, E., Koch, D., Murray, S., Schreier, E., Seward, F., Tananbaum, H., Topka, K., Van Speybroeck, L., Holt, S. S., Becker, R. H., Boldt, E. A., Serlemitsos, P. J., Clark, G., Canizares, C., Markert, T., Novick, R., Helfand, D., and Long, K. (1979). The Einstein (HEAO 2) X-ray Observatory. *ApJ*, 230:540–550. 1.1

Giacconi, R., Gursky, H., Paolini, F. R., and Rossi, B. B. (1962). Evidence for x Rays From Sources Outside the Solar System. , 9(11):439–443. 1.1

Giacconi, R., Kellogg, E., Gorenstein, P., Gursky, H., and Tananbaum, H. (1971). An X-Ray Scan of the Galactic Plane from UHURU. *ApJ*, 165:L27. 1.1, 1.3.2

Gierliński, M. and Done, C. (2002). A comment on the colour-colour diagrams of low-mass X-ray binaries. *MNRAS*, 331(4):L47–L50. 1.3.3

Gladstone, J. C., Copperwheat, C., Heinke, C. O., Roberts, T. P., Cartwright, T. F., Levan, A. J., and Goad, M. R. (2013). Optical Counterparts of the Nearest Ultraluminous X-Ray Sources. *ApJS*, 206(2):14. 1.4.3

Gladstone, J. C., Roberts, T. P., and Done, C. (2009). The ultraluminous state. *MNRAS*, 397(4):1836–1851. 1.4.2, 2.4.2, 2.5.2, 2.5.2, 2.5.4, 4.4.1

Goddard, H. and Shamir, L. (2020). A Catalog of Broad Morphology of Pan-STARRS Galaxies Based on Deep Learning. *ApJS*, 251(2):28. 2.7.2

Godet, O., Lombardi, J. C., Antonini, F., Barret, D., Webb, N. A., Vingless, J., and Thomas, M. (2014). Implications of the Delayed 2013 Outburst of ESO 243-49 HLX-1. *ApJ*, 793(2):105. 3.1

Gong, H., Liu, J., and Maccarone, T. (2016). An Extreme Luminous X-ray Source Catalog Based on Chandra ACIS Observations. *ApJS*, 222(1):12. 2.1, 2.3

Goodwin, A. J., Anderson, G. E., Miller-Jones, J. C. A., Malyali, A., Grotova, I., Homan, D., Kawka, A., Krumpe, M., Liu, Z., and Rau, A. (2024). A radio flare associated with the nuclear transient eRASSt J234403-352640: an outflow launched by a potential tidal disruption event. *MNRAS*, 528(4):7123–7136. 1.2.4

Grandis, S., Ghirardini, V., Bocquet, S., Garrel, C., and eROSITA Consortium (2024). The SRG/eROSITA All-Sky Survey: Dark Energy Survey Year 3 Weak Gravitational Lensing by eRASS1 selected Galaxy Clusters. *arXiv e-prints*, page arXiv:2402.08455. 1.2.4

Griffiths, R. E., Ptak, A., Feigelson, E. D., Garmire, G., Townsley, L., Brandt, W. N., Sambruna, R., and Bregman, J. N. (2000). Hot Plasma and Black Hole Binaries in Starburst Galaxy M82. *Science*, 290(5495):1325–1328. 2.3.3

Guillochon, J., Parrent, J., Kelley, L. Z., and Margutti, R. (2017). An Open Catalog for Supernova Data. *ApJ*, 835(1):64. 2.3.3

Guo, J.-C., Liu, J.-F., Wang, S., Wu, Y., and Qin, Y.-X. (2016). An active M star with X-ray double flares disguised as an ultra-luminous X-ray source. *Research in Astronomy and Astrophysics*, 16(2):34. 2.3.3

Gúrpide, A., Godet, O., Koliopanos, F., Webb, N., and Olive, J. F. (2021). Long-term X-ray spectral evolution of ultraluminous X-ray sources: implications on the accretion flow geometry and the nature of the accretor. *A&A*, 649:A104. 3.4

Gutiérrez, C. M. and Moon, D.-S. (2014). Optical Study of the Hyper-luminous X-Ray Source 2XMM J011942.7+032421. *ApJ*, 797(1):L7. 3.1

Haardt, F. and Maraschi, L. (1991). A Two-Phase Model for the X-Ray Emission from Seyfert Galaxies. *ApJ*, 380:L51. 2.5.4

Haensel, P., Zdunik, J. L., and Schaefer, R. (1986). Strange quark stars. *A&A*, 160(1):121–128. 1.3.2

Hardcastle, M. J., Kraft, R. P., Sivakoff, G. R., Goodger, J. L., Croston, J. H., Jordán, A., Evans, D. A., Worrall, D. M., Birkinshaw, M., Raychaudhury, S., Brassington, N. J., Forman, W. R., Harris, W. E., Jones, C., Juett, A. M., Murray, S. S., Nulsen, P. E. J., Sarazin, C. L., and Woodley, K. A. (2007). New Results on Particle Acceleration in the Centaurus A Jet and Counterjet from a Deep Chandra Observation. *ApJ*, 670(2):L81–L84. 2.3.3

Harrison, F. A., Craig, W. W., Christensen, F. E., Hailey, C. J., Zhang, W. W., Boggs, S. E., Stern, D., Cook, W. R., Forster, K., Giommi, P., Grefenstette, B. W., Kim, Y., Kitaguchi, T., Koglin, J. E., Madsen, K. K., Mao, P. H., Miyasaka, H., Mori, K., Perri, M., Pivovaroff, M. J., Puccetti, S., Rana, V. R., Westergaard, N. J., Willis, J., Zoglauer, A., An, H., Bachetti, M., Barrière, N. M., Bellm, E. C., Bhalerao, V., Brejnholt, N. F., Fuerst, F., Liebe, C. C., Markwardt, C. B., Nynka, M., Vogel, J. K., Walton, D. J., Wik, D. R., Alexander, D. M., Cominsky, L. R., Hornschemeier, A. E., Hornstrup, A., Kaspi, V. M., Madejski, G. M., Matt, G., Molendi, S., Smith, D. M., Tomsick, J. A., Ajello, M., Ballantyne, D. R., Baloković, M., Barret, D., Bauer, F. E., Blandford, R. D., Brandt, W. N., Brenneman, L. W., Chiang, J., Chakrabarty, D., Chenevez, J., Comastri, A., Dufour, F., Elvis, M., Fabian, A. C., Farrah, D., Fryer, C. L., Gotthelf, E. V., Grindlay, J. E., Helfand, D. J., Krivonos, R., Meier, D. L., Miller, J. M., Natalucci, L., Ogle, P., Ofek, E. O., Ptak, A., Reynolds, S. P., Rigby, J. R., Tagliaferri, G., Thorsett, S. E., Treister, E., and Urry, C. M. (2013). The Nuclear Spectroscopic Telescope Array (NuSTAR) High-energy X-Ray Mission. *ApJ*, 770(2):103. 1.2, 1.4.2

Hasinger, G. and van der Klis, M. (1989). Two patterns of correlated X-ray timing and spectral behaviour in low-mass X-ray binaries. *A&A*, 225:79–96. 1.3.3, 1.10

Heger, A., Fryer, C. L., Woosley, S. E., Langer, N., and Hartmann, D. H. (2003). How Massive Single Stars End Their Life. *ApJ*, 591(1):288–300. 1.3.2

Heida, M., Jonker, P. G., Torres, M. A. P., Kool, E., Servillat, M., Roberts, T. P., Groot, P. J., Walton, D. J., Moon, D. S., and Harrison, F. A. (2014). Near-infrared counterparts of ultraluminous X-ray sources. *MNRAS*, 442(2):1054–1067. 1.4.3

Heida, M., Jonker, P. G., Torres, M. A. P., Roberts, T. P., Miniutti, G., Fabian, A. C., and Ratti, E. M. (2013). VLT/FORS2 observations of four high-luminosity ULX candidates. *MNRAS*, 433(1):681–687. 2.3.3

Heida, M., Lau, R. M., Davies, B., Brightman, M., Fürst, F., Grefenstette, B. W., Kennea, J. A., Tramper, F., Walton, D. J., and Harrison, F. A. (2019). Discovery of a Red Supergiant Donor Star in SN2010da/NGC 300 ULX-1. *ApJ*, 883(2):L34. 2.4.1

Hewish, A., Bell, S. J., Pilkington, J. D. H., Scott, P. F., and Collins, R. A. (1968). Observation of a Rapidly Pulsating Radio Source. *Nat*, 217(5130):709–713. 1.3.2

HI4PI Collaboration, Ben Bekhti, N., Flöer, L., Keller, R., Kerp, J., Lenz, D., Winkel, B., Bailin, J., Calabretta, M. R., Dedes, L., Ford, H. A., Gibson, B. K., Haud, U., Janowiecki, S., Kalberla, P. M. W., Lockman, F. J., McClure-Griffiths, N. M., Murphy, T., Nakanishi, H., Pisano, D. J., and Staveley-Smith, L. (2016). HI4PI: A full-sky H I survey based on EBHIS and GASS. *A&A*, 594:A116. 2.5.2

Høg, E., Fabricius, C., Makarov, V. V., Urban, S., Corbin, T., Wycoff, G., Bastian, U., Schwekendiek, P., and Wicenec, A. (2000). The Tycho-2 catalogue of the 2.5 million brightest stars. *A&A*, 355:L27–L30. 2.3.1, 2.7.1, 3.2

Holt, S. S. (1993). High energy spectroscopy with the AXAF. *A&AS*, 97(1):367–369. 1.2.1

Homan, J. and Belloni, T. (2005). The Evolution of Black Hole States. , 300(1-3):107–117. 3.4

Immler, S., Brown, P. J., Milne, P., Dessart, L., Mazzali, P. A., Landsman, W., Gehrels, N., Petre, R., Burrows, D. N., Nousek, J. A., Chevalier, R. A., Williams, C. L., Koss, M., Stockdale, C. J., Kelley, M. T., Weiler, K. W., Holland, S. T., Pian, E., Roming, P. W. A., Pooley, D., Nomoto, K., Greiner, J., Campana, S., and Soderberg, A. M. (2007). X-Ray, UV, and Optical Observations of Supernova 2006bp with Swift: Detection of Early X-Ray Emission. *ApJ*, 664(1):435–442. 4.7, 5.1

Immler, S., Modjaz, M., Landsman, W., Bufano, F., Brown, P. J., Milne, P., Dessart, L., Holland, S. T., Koss, M., Pooley, D., Kirshner, R. P., Filippenko, A. V., Panagia, N., Chevalier, R. A., Mazzali, P. A., Gehrels, N., Petre, R., Burrows, D. N., Nousek, J. A., Roming, P. W. A., Pian, E., Soderberg, A. M., and Greiner, J. (2008). Swift and Chandra Detections of Supernova 2006jc: Evidence for Interaction of the Supernova Shock with a Circumstellar Shell. *ApJ*, 674(2):L85. 4.7, 5.1

Inoue, Y., Tanaka, Y. T., and Isobe, N. (2016). Binary black hole merger rates inferred from luminosity function of ultra-luminous X-ray sources. *MNRAS*, 461(4):4329–4334. 1.4.2

Inoue, Y., Yabe, K., and Ueda, Y. (2021). A fundamental plane in X-ray binary activity of external galaxies. *PASJ*, 73(5):1315–1332. 2.4.1, 2.3, 2.5

Israel, G. L., Belfiore, A., Stella, L., Esposito, P., Casella, P., De Luca, A., Marelli, M., Papitto, A., Perri, M., Puccetti, S., Castillo, G. A. R., Salvetti, D., Tiengo, A., Zampieri, L., D'Agostino, D., Greiner, J., Haberl, F., Novara, G., Salvaterra, R., Turolla, R., Watson, M., Wilms, J., and Wolter, A. (2017a). An accreting pulsar with extreme properties drives an ultraluminous x-ray source in NGC 5907. *Science*, 355(6327):817–819. 1.4.2, 2.4, 2.5.3, 2.5.4, 3.1, 3.4, 5.1

Israel, G. L., Papitto, A., Esposito, P., Stella, L., Zampieri, L., Belfiore, A., Rodríguez Castillo, G. A., De Luca, A., Tiengo, A., Haberl, F., Greiner, J., Salvaterra, R., Sandrelli, S., and Lisini, G. (2017b). Discovery of a 0.42-s pulsar in the ultraluminous X-ray source NGC 7793 P13. *Monthly Notices of the RAS*, 466(1):L48–L52. 1.4.2, 2.5.4, 3.1

Jansen, F., Lumb, D., Altieri, B., Clavel, J., Ehle, M., Erd, C., Gabriel, C., Guainazzi, M., Gondoin, P., Much, R., Munoz, R., Santos, M., Schartel, N., Texier, D., and Vacanti, G. (2001). XMM-Newton observatory. I. The spacecraft and operations. *A&A*, 365:L1–L6. 1.2, 1.2.2, 1.4.2, 2.1

Jerius, D., Donnelly, R. H., Tibbetts, M. S., Edgar, R. J., Gaetz, T. J., Schwartz, D. A., Van Speybroeck, L. P., and Zhao, P. (2000). Orbital measurement and verification of the Chandra X-ray Observatory's PSF. In Truemper, J. E. and Aschenbach, B., editors, *X-Ray Optics, Instruments, and Missions III*, volume 4012 of *Society of Photo-Optical Instrumentation Engineers (SPIE) Conference Series*, pages 17–27. 1.2.1

Kaaret, P., Feng, H., and Roberts, T. P. (2017). Ultraluminous X-Ray Sources. *ARA&A*, 55(1):303–341. 1, 1.4.2, 1.13, 1.4.3, 3.1, 3.6

Kaaret, P., Ward, M. J., and Zezas, A. (2004). High-resolution imaging of the HeII λ4686 emission line nebula associated with the ultraluminous X-ray source in Holmberg II. *MNRAS*, 351(3):L83–L88. 4.7

Kajava, J. J. E. and Poutanen, J. (2009). Spectral variability of ultraluminous X-ray sources. *MNRAS*, 398(3):1450–1460. 3.1

Kaplan, D. L., Frail, D. A., Gaensler, B. M., Gotthelf, E. V., Kulkarni, S. R., Slane, P. O., and Nechita, A. (2004). An X-Ray Search for Compact Central Sources in Supernova Remnants. I. SNRS G093.3+6.9, G315.4-2.3, G084.2+0.8, and G127.1+0.5. *ApJS*, 153(1):269–315. 1.3.2

Karachentsev, I. D., Kaisina, E. I., and Makarov, D. I. (2018). Morphological properties of galaxies in different Local Volume environments. *MNRAS*, 479(3):4136–4152. 2.2

Katsuda, S., Maeda, K., Nozawa, T., Pooley, D., and Immler, S. (2014). SN 2005ip: A Luminous Type IIn Supernova Emerging from a Dense Circumstellar Medium as Revealed by X-Ray Observations. *ApJ*, 780(2):184. 4.7, 5.1

Kerr, R. P. (1963). Gravitational Field of a Spinning Mass as an Example of Algebraically Special Metrics. , 11(5):237–238. 1.3.2

Kettner, C., Weber, F., Weigel, M. K., and Glendenning, N. K. (1995). Structure and stability of strange and charm stars at finite temperatures. , 51(4):1440–1457. 1.3.2

King, A., Lasota, J.-P., and Middleton, M. (2023). Ultraluminous X-ray sources. , 96:101672. 1, 3.6

King, A. R., Davies, M. B., Ward, M. J., Fabbiano, G., and Elvis, M. (2001). Ultraluminous X-Ray Sources in External Galaxies. *ApJ*, 552(2):L109–L112. 1.4.2

Koliopanos, F., Vasilopoulos, G., Godet, O., Bachetti, M., Webb, N. A., and Barret, D. (2017). ULX spectra revisited: Accreting, highly magnetized neutron stars as the engines of ultraluminous X-ray sources. *A&A*, 608:A47. 1.4.2

Kong, A. K. H., Soria, R., and Farrell, S. (2015). New X-ray Outburst of ESO 243-49 HLX-1. *The Astronomer's Telegram*, 6916:1. 3.1, 3.6

Kosec, P., Pinto, C., Fabian, A. C., and Walton, D. J. (2018a). Searching for outflows in ultraluminous X-ray sources through high-resolution X-ray spectroscopy. *MNRAS*, 473(4):5680–5697. 1.4.2

Kosec, P., Pinto, C., Walton, D. J., Fabian, A. C., Bachetti, M., Brightman, M., Fürst, F., and Grefenstette, B. W. (2018b). Evidence for a variable Ultrafast Outflow in the newly discovered Ultraluminous Pulsar NGC 300 ULX-1. *MNRAS*, 479(3):3978–3986. 1.4.2, 2.4.1, 2.5.4

Kovlakas, K., Zezas, A., Andrews, J. J., Basu-Zych, A., Fragos, T., Hornschemeier, A., Kouroumpatzakis, K., Lehmer, B., and Ptak, A. (2021). The Heraklion Extragalactic Catalogue (HECATE): a value-added galaxy catalogue for multimessenger astrophysics. *MNRAS*, 506(2):1896–1915. 2.7.1, 2.7.2

Kovlakas, K., Zezas, A., Andrews, J. J., Basu-Zych, A., Fragos, T., Hornschemeier, A., Lehmer, B., and Ptak, A. (2020). A census of ultraluminous X-ray sources in the local Universe. *MNRAS*, 498(4):4790–4810. 2.1, 2.4.1, 2.3, 2.5, 2.7.2

Lasota, J. P., Alexander, T., Dubus, G., Barret, D., Farrell, S. A., Gehrels, N., Godet, O., and Webb, N. A. (2011). The Origin of Variability of the Intermediate-mass Black-hole ULX System HLX-1 in ESO 243-49. *ApJ*, 735(2):89. 3.1

Lehmer, B. D., Eufrasio, R. T., Tzanavaris, P., Basu-Zych, A., Fragos, T., Prestwich, A., Yukita, M., Zezas, A., Hornschemeier, A. E., and Ptak, A. (2019). X-Ray Binary Luminosity Function Scaling Relations for Local Galaxies Based on Subgalactic Modeling. *ApJS*, 243(1):3. 2.4

Lewin, W. H. G. and van der Klis, M. (2006). *Compact Stellar X-ray Sources*, volume 39. 1.8, 1.9, 2.7.1

Lin, L. C.-C., Hu, C.-P., Li, K.-L., Takata, J., Yen, D. C.-C., Kwak, K., Kim, Y.-M., and Kong, A. K. H. (2020). Investigation of X-ray timing and spectral properties of ESO 243-49 HLX-1 with long-term Swift monitoring. *MNRAS*, 491(4):5682–5692. 3.1

Linares, M. (2009). *Accretion states and thermonuclear bursts in neutron star X-ray binaries*. PhD thesis, University of Amsterdam, Anton Pannekoek Institute for Astronomy. 1.3.3

Liu, B. F. and Qiao, E. (2022). Accretion around black holes: The geometry and spectra. *iScience*, 25(1):103544. 1.3.1

Liu, J. (2011). Chandra ACIS Survey of X-ray Point Sources in 383 Nearby Galaxies. I. The Source Catalog. *ApJS*, 192(1):10. 2.1, 2.3

Liu, J. and Di Stefano, R. (2008). An Ultraluminous Supersoft X-Ray Source in M81: An Intermediate-Mass Black Hole? *ApJ*, 674(2):L73. 3.6

Liu, J.-F. and Bregman, J. N. (2005). Ultraluminous X-Ray Sources in Nearby Galaxies from ROSAT High Resolution Imager Observations I. Data Analysis. *ApJS*, 157(1):59–125. 1.1, 2.1, 2.3

Liu, Q. Z. and Mirabel, I. F. (2005). A catalogue of ultraluminous X-ray sources in external galaxies. *A&A*, 429:1125–1129. 2.3

Locatelli, N., Ponti, G., Zheng, X., Merloni, A., Becker, W., Comparat, J., Dennerl, K., Freyberg, M. J., Sasaki, M., and Yeung, M. C. H. (2024). The warm-hot circumgalactic medium of the Milky Way as seen by eROSITA. *A&A*, 681:A78. 1.2.4

López, K. M., Jonker, P. G., Heida, M., Torres, M. A. P., Roberts, T. P., Walton, D. J., Moon, D. S., and Harrison, F. A. (2019). Discovery and analysis of a ULX nebula in NGC 3521. *MNRAS*, 489(1):1249–1264. 1.4.3

Lopez, L. A., Mathur, S., Nguyen, D. D., Thompson, T. A., and Olivier, G. M. (2020). Temperature and Metallicity Gradients in the Hot Gas Outflows of M82. *ApJ*, 904(2):152. 1.4.3, 2.3.3

Maccacaro, T., Gioia, I. M., Wolter, A., Zamorani, G., and Stocke, J. T. (1988). The X-Ray Spectra of the Extragalactic Sources in the Einstein Extended Medium-Sensitivity Survey. *ApJ*, 326:680. 2.7.1

MacKenzie, A. D. A., Roberts, T. P., and Walton, D. J. (2023). The hyperluminous X-ray source population. *Astronomische Nachrichten*, 344(4):e20230028. (document)

Madsen, K., Hickox, R., Bachetti, M., Stern, D., Gellert, N. C., García, J., Kara, E., Brandt, W. N., Krawczynski, H., Lohfink, A., Brenneman, L., Christensen, F., Middleton, M., Hornstrup, A., Matt, G., Jaodand, A., Lansbury, G., Ricci, C., Fuerst, F., Ballantyne, D., Walton, D., Fabian, A., Della Monica Ferreira, D.,

Pottschmidt, K., Miller, J. M., Windt, D. L., Baloković, M., Kamraj, N., Wilms, J., Heida, M., Alexander, D., Boorman, P., Wik, D., Vogel, J., Earnshaw, H., Descalle, M.-A., Civano, F., Fornasini, F., Grindlay, J., Zhang, W., Hornschemeier, A., and Craig, W. (2019). HEX-P: The High-Energy X-ray Probe. In *Bulletin of the American Astronomical Society*, volume 51, page 166. 5.2

Madsen, K. K., Harrison, F., Broadway, D., Christensen, F. E., Descalle, M., Ferreira, D., Grefenstette, B., Gurgew, D., Hornschemeier, A., Miyasaka, H., Okajima, T., Pike, S., Pivovaroff, M., Saha, T., Stern, D., Vogel, J., Windt, D., and Zhang, W. (2018). Optical instrument design of the high-energy x-ray probe (HEX-P). In den Herder, J.-W. A., Nikzad, S., and Nakazawa, K., editors, *Space Telescopes and Instrumentation 2018: Ultraviolet to Gamma Ray*, volume 10699 of *Society of Photo-Optical Instrumentation Engineers (SPIE) Conference Series*, page 106996M. 2.5.4, 5.1, 5.2

Maitra, C., Haberl, F., Vasilopoulos, G., Rau, A., Schwope, A., Friedrich, S., Buckley, D. A. H., Valdes, F., Lang, D., and Macfarlane, S. A. (2024). eRASSU J060839.5-704014: A double degenerate ultra-compact binary in the direction of the LMC. *A&A*, 683:A21. 1.2.4

Makarov, D., Prugniel, P., Terekhova, N., Courtois, H., and Vauglin, I. (2014). HyperLEDA. III. The catalogue of extragalactic distances. *A&A*, 570:A13. 2.2, 2.7.2

Masini, A., Hickox, R. C., Carroll, C. M., Aird, J., Alexander, D. M., Assef, R. J., Bower, R., Brodwin, M., Brown, M. J. I., Chatterjee, S., Chen, C.-T. J., Dey, A., DiPompeo, M. A., Duncan, K. J., Eisenhardt, P. R. M., Forman, W. R., Gonzalez, A. H., Goulding, A. D., Hainline, K. N., Jannuzi, B. T., Jones, C., Kochanek, C. S., Kraft, R., Lee, K.-S., Miller, E. D., Mullaney, J., Myers, A. D., Ptak, A., Stanford, A., Stern, D., Vikhlinin, A., Wake, D. A., and Murray, S. S. (2020). The Chandra Deep Wide-field Survey: A New Chandra Legacy Survey in the Boötes Field. I. X-Ray Point Source Catalog, Number Counts, and Multiwavelength Counterparts. *ApJS*, 251(1):2. 2.4.2

Mateos, S., Warwick, R. S., Carrera, F. J., Stewart, G. C., Ebrero, J., Della Ceca, R., Caccianiga, A., Gilli, R., Page, M. J., Treister, E., Tedds, J. A., Watson, M. G., Lamer, G., Saxton, R. D., Brunner, H., and Page, C. G. (2008). High precision X-ray log N - log S distributions: implications for the obscured AGN population. *A&A*, 492(1):51–69. 2.4.2

Merloni, A., Lamer, G., Liu, T., Ramos-Ceja, M. E., and eROSITA Consortium (2024). The SRG/eROSITA all-sky survey. First X-ray catalogues and data release of the western Galactic hemisphere. *A&A*, 682:A34. 1.2.4

Mezcua, M. (2017). Observational evidence for intermediate-mass black holes. *International Journal of Modern Physics D*, 26(11):1730021. 1

Mezcua, M., Roberts, T. P., Lobanov, A. P., and Sutton, A. D. (2015). The powerful jet of an off-nuclear intermediate-mass black hole in the spiral galaxy NGC 2276. *MNRAS*, 448(2):1893–1899. 1.4.2, 3.1

Middleton, M. J., Heil, L., Pintore, F., Walton, D. J., and Roberts, T. P. (2015). A spectral-timing model for ULXs in the supercritical regime. *MNRAS*, 447(4):3243–3263. 1.4.2, 2.5.4

Middleton, M. J., Miller-Jones, J. C. A., Markoff, S., Fender, R., Henze, M., Hurley-Walker, N., Scaife, A. M. M., Roberts, T. P., Walton, D., Carpenter, J., Macquart, J.-P., Bower, G. C., Gurwell, M., Pietsch, W., Haberl, F., Harris, J., Daniel, M., Miah, J., Done, C., Morgan, J. S., Dickinson, H., Charles, P., Burwitz, V., Della Valle, M., Freyberg, M., Greiner, J., Hernanz, M., Hartmann, D. H., Hatzidimitriou, D., Riffeser, A., Sala, G., Seitz, S., Reig, P., Rau, A., Orio, M., Titterington, D., and Grainge, K. (2013). Bright radio emission from an ultraluminous stellar-mass microquasar in M 31. *Nat*, 493(7431):187–190. 2.3.1

Middleton, M. J., Roberts, T. P., Done, C., and Jackson, F. E. (2011). Challenging times: a re-analysis of NGC 5408 X-1. *MNRAS*, 411(1):644–652. 3.1

Middleton, M. J., Sutton, A. D., Roberts, T. P., Jackson, F. E., and Done, C. (2012). The missing link: a low-mass X-ray binary in M31 seen as an ultraluminous X-ray source. *MNRAS*, 420(4):2969–2977. 2.3.1

Migliazzo, J. M., Gaensler, B. M., Backer, D. C., Stappers, B. W., van der Swaluw, E., and Strom, R. G. (2002). Proper-Motion Measurements of Pulsar B1951+32 in the Supernova Remnant CTB 80. *ApJ*, 567(2):L141–L144. 1.3.2

Miller, J. M., Fabian, A. C., and Miller, M. C. (2004). A Comparison of Intermediate-Mass Black Hole Candidate Ultraluminous X-Ray Sources and Stellar-Mass Black Holes. *ApJ*, 614(2):L117–L120. 1.4.2

Mineo, S., Gilfanov, M., and Sunyaev, R. (2012). X-ray emission from star-forming galaxies - I. High-mass X-ray binaries. *MNRAS*, 419(3):2095–2115. 2.4

Mineo, S., Rappaport, S., Steinhorn, B., Levine, A., Gilfanov, M., and Pooley, D. (2013). Spatially Resolved Star Formation Image and the Ultraluminous X-Ray Source Population in NGC 2207/IC 2163. *ApJ*, 771(2):133. 2.4

Mineshige, S., Hirano, A., Kitamoto, S., Yamada, T. T., and Fukue, J. (1994). Time-dependent Disk Accretion in X-Ray Nova MUSCAE 1991. *ApJ*, 426:308. 2.5.2, 4.4.1

Misner, C. W., Thorne, K. S., and Wheeler, J. A. (1973). *Gravitation*. 1.3.2

Mitsuda, K., Inoue, H., Koyama, K., Makishima, K., Matsuoka, M., Ogawara, Y., Shibazaki, N., Suzuki, K., Tanaka, Y., and Hirano, T. (1984). Energy spectra of low-mass binary X-ray sources observed from Tenma. *PASJ*, 36:741–759. 2.5.2, 4.4.1

Mondal, S., Belczyński, K., Wiktorowicz, G., Lasota, J.-P., and King, A. R. (2020). The connection between merging double compact objects and the ultraluminous X-ray sources. *MNRAS*, 491(2):2747–2759. 1.4.2

Moon, D.-S., Harrison, F. A., Cenko, S. B., and Shariff, J. A. (2011). Large Highly Ionized Nebulae Around Ultra-luminous X-ray Sources. *ApJ*, 731(2):L32. 4.7, 5.1

Moran, E. C., Shahinyan, K., Sugarman, H. R., Vélez, D. O., and Eracleous, M. (2014). Black Holes At the Centers of Nearby Dwarf Galaxies. *AJ*, 148(6):136. 1

Motch, C., Pakull, M. W., Grisé, F., and Soria, R. (2011). The supergiant optical counterpart of ULX P13 in NGC 7793. *Astronomische Nachrichten*, 332(4):367. 1.4.3

Muñoz-Darias, T., Coriat, M., Plant, D. S., Ponti, G., Fender, R. P., and Dunn, R. J. H. (2013). Inclination and relativistic effects in the outburst evolution of black hole transients. *MNRAS*, 432(2):1330–1337. 3.6

Muñoz-Darias, T., Fender, R. P., Motta, S. E., and Belloni, T. M. (2014). Black hole-like hysteresis and accretion states in neutron star low-mass X-ray binaries. *MNRAS*, 443(4):3270–3283. 1.3.3

Mukai, K. (2017). X-Ray Emissions from Accreting White Dwarfs: A Review. *PASP*, 129(976):062001. 1.3.2

Mukherjee, E. S., Walton, D. J., Bachetti, M., Harrison, F. A., Barret, D., Bellm, E., Boggs, S. E., Christensen, F. E., Craig, W. W., Fabian, A. C., Fuerst, F., Grefenstette, B. W., Hailey, C. J., Madsen, K. K., Middleton, M. J., Miller, J. M., Rana, V., Stern, D., and Zhang, W. (2015). A Hard X-Ray Study of the Ultra-luminous X-Ray Source NGC 5204 X-1 with NuSTAR and XMM-Newton. *ApJ*, 808(1):64. 1.4.2, 2.5.2, 2.5.4, 4.4.1

Mushtukov, A. A., Suleimanov, V. F., Tsygankov, S. S., and Poutanen, J. (2015). On the maximum accretion luminosity of magnetized neutron stars: connecting X-ray pulsars and ultraluminous X-ray sources. *MNRAS*, 454(3):2539–2548. 1.4.2

Nandra, K., Barret, D., Barcons, X., Fabian, A., and Athena Collaboration (2013). The Hot and Energetic Universe: A White Paper presenting the science theme motivating the Athena+ mission. *arXiv e-prints*, page arXiv:1306.2307. 2.1, 5.2

Neumann, M., Avakyan, A., Doroshenko, V., and Santangelo, A. (2023). XRBcats: Galactic High Mass X-ray Binary Catalogue. *A&A*, 677:A134. 1.3.3

Ostriker, J. P. and Gunn, J. E. (1969). On the Nature of Pulsars. I. Theory. *ApJ*, 157:1395. 1.3.2

Pakull, M. W., Grisé, F., and Motch, C. (2006). Ultraluminous X-ray Sources: Bubbles and Optical Counterparts. In Meurs, E. J. A. and Fabbiano, G., editors, *Populations of High Energy Sources in Galaxies*, volume 230, pages 293–297. 1.4.3

Pakull, M. W. and Mirioni, L. (2002). Optical Counterparts of Ultraluminous X-Ray Sources. *arXiv e-prints*, pages astro–ph/0202488. 1.4.3, 5.1

Pakull, M. W. and Mirioni, L. (2003). Bubble Nebulae around Ultraluminous X-Ray Sources. In Arthur, J. and Henney, W. J., editors, *Revista Mexicana de Astronomia y Astrofisica Conference Series*, volume 15 of *Revista Mexicana de Astronomia y Astrofisica Conference Series*, pages 197–199. 4.7

Park, T., Kashyap, V. L., Siemiginowska, A., van Dyk, D. A., Zezas, A., Heinke, C., and Wargelin, B. J. (2006). Bayesian Estimation of Hardness Ratios: Modeling and Computations. *ApJ*, 652(1):610–628. 3.4

Pasham, D. R., Strohmayer, T. E., and Mushotzky, R. F. (2014). A 400-solar-mass black hole in the galaxy M82. *Nat*, 513(7516):74–76. 1.4.2, 3.1

Pedersen, O. (1993). *Early Physics and Astronomy*. 1.1

Piconcelli, E., Jimenez-Bailón, E., Guainazzi, M., Schartel, N., Rodríguez-Pascual, P. M., and Santos-Lleó, M. (2004). Evidence for a multizone warm absorber in the XMM-Newton spectrum of Markarian 304. *MNRAS*, 351(1):161–168. 2.5.1, 4, 4.3, 4.3, 4.5.2, 4.7, 4.8, 5.1

Pinto, C., Alston, W., Soria, R., Middleton, M. J., Walton, D. J., Sutton, A. D., Fabian, A. C., Earnshaw, H., Urquhart, R., Kara, E., and Roberts, T. P. (2017). From ultraluminous X-ray sources to ultraluminous supersoft sources: NGC 55 ULX, the missing link. *MNRAS*, 468(3):2865–2883. 1.4.2, 2.5.4

Pinto, C., Middleton, M. J., and Fabian, A. C. (2016). Resolved atomic lines reveal outflows in two ultraluminous X-ray sources. *Nat*, 533(7601):64–67. 1.4.2, 1.16, 2.5.4

Pinto, C., Walton, D. J., Kara, E., Parker, M. L., Soria, R., Kosec, P., Middleton, M. J., Alston, W. N., Fabian, A. C., Guainazzi, M., Roberts, T. P., Fuerst, F., Earnshaw, H. P., Sathyaprakash, R., and Barret, D. (2020). XMM-Newton campaign on ultraluminous X-ray source NGC 1313 X-1: wind versus state variability. *MNRAS*, 492(4):4646–4665. 1.4.2, 2.5.4

Pintore, F., Belfiore, A., Novara, G., Salvaterra, R., Marelli, M., De Luca, A., Rigoselli, M., Israel, G., Rodriguez, G., Mereghetti, S., Wolter, A., Walton, D. J., Fuerst, F., Ambrosi, E., Zampieri, L., Tiengo, A., and Salvaggio, C. (2018). A new ultraluminous X-ray source in the galaxy NGC 5907. *MNRAS*, 477(1):L90–L95. 2.3.1

Pintore, F., Marelli, M., Salvaterra, R., Israel, G. L., Rodríguez Castillo, G. A., Esposito, P., Belfiore, A., De Luca, A., Wolter, A., Mereghetti, S., Stella, L., Rigoselli, M., Earnshaw, H. P., Pinto, C., Roberts, T. P., Walton, D. J., Bernardini, F., Haberl, F., Salvaggio, C., Tiengo, A., Zampieri, L., Bachetti, M., Brightman, M., Casella, P., D'Agostino, D., Dall'Osso, S., Fürst, F., Harrison, F. A., Mapelli, M., Papitto, A., and Middleton, M. (2020). The Ultraluminous X-Ray Sources Population of the Galaxy NGC 7456. *ApJ*, 890(2):166. 2.3.1

Pintore, F., Zampieri, L., Stella, L., Wolter, A., Mereghetti, S., and Israel, G. L. (2017). Pulsator-like Spectra from Ultraluminous X-Ray Sources and the Search for More Ultraluminous Pulsars. *ApJ*, 836(1):113. 1.4.2, 2.4.2

Plucinsky, P. P., Bogdan, A., Marshall, H. L., and Tice, N. W. (2018). The complicated evolution of the ACIS contamination layer over the mission life of the Chandra X-ray Observatory. In den Herder, J.-W. A., Nikzad, S., and Nakazawa, K., editors, *Space Telescopes and Instrumentation 2018: Ultraviolet to Gamma Ray*, volume 10699 of *Society of Photo-Optical Instrumentation Engineers (SPIE) Conference Series*, page 106996B. 2.3.1

Pons, J. A., Walter, F. M., Lattimer, J. M., Prakash, M., Neuhäuser, R., and An, P. (2002). Toward a Mass and Radius Determination of the Nearby Isolated Neutron Star RX J185635-3754. *ApJ*, 564(2):981–1006. 1.3.2

Pooley, D., Immler, S., and Filippenko, A. V. (2007). Chandra Observation of SN 2005kd: Very Luminous and Hard X-ray Emission. *The Astronomer's Telegram*, 1023:1. 4.7, 5.1

Pounds, K. (2020). X-ray UK. *Astronomy and Geophysics*, 61(1):1.32–1.37. 1.2

Poutanen, J., Krolik, J. H., and Ryde, F. (1997). The nature of spectral transitions in accreting black holes: the case of CYG X-1. *MNRAS*, 292(1):L21–L25. 1.3.3

Poutanen, J., Lipunova, G., Fabrika, S., Butkevich, A. G., and Abolmasov, P. (2007). Supercritically accreting stellar mass black holes as ultraluminous X-ray sources. *MNRAS*, 377(3):1187–1194. 1.4.2, 1.4.2, 2.5.4

Predehl, P. and eROSITA Consortium (2021). The eROSITA X-ray telescope on SRG. *A&A*, 647:A1. 1.2, 1.2.4, 2.6

Rana, V., Harrison, F. A., Bachetti, M., Walton, D. J., Furst, F., Barret, D., Miller, J. M., Fabian, A. C., Boggs, S. E., Christensen, F. C., Craig, W. W., Grefenstette, B. W., Hailey, C. J., Madsen, K. K., Ptak, A. F., Stern, D., Webb, N. A., and Zhang, W. W. (2015). The Broadband XMM-Newton and NuSTAR X-Ray Spectra of Two Ultraluminous X-Ray Sources in the Galaxy IC 342. *ApJ*, 799(2):121. 1.4.2, 2.5.2, 2.5.4

Ransom, S. M., Eikenberry, S. S., and Middleditch, J. (2002). Fourier Techniques for Very Long Astrophysical Time-Series Analysis. *AJ*, 124(3):1788–1809. 4.5.2

Remillard, R. A. and McClintock, J. E. (2006). X-Ray Properties of Black-Hole Binaries. *ARA&A*, 44(1):49–92. 1.3.3, 3.4

Roberts, T. P., Gladstone, J. C., Goulding, A. D., Swinbank, A. M., Ward, M. J., Goad, M. R., and Levan, A. J. (2011). (No) dynamical constraints on the mass of the black hole in two ULXs. *Astronomische Nachrichten*, 332(4):398. 1.4.3

Roberts, T. P., Goad, M. R., Ward, M. J., and Warwick, R. S. (2003). The unusual supernova remnant surrounding the ultraluminous X-ray source IC 342 X-1. *MNRAS*, 342(3):709–714. 1.4.3

Roberts, T. P., Walton, D. J., Mackenzie, A. D. A., Heida, M., and Scaringi, S. (2023). Digging a little deeper: characterizing three new extreme ULX candidates. *MNRAS*, 525(3):3330–3343. (document), 3.2, 4.1

Roberts, T. P. and Warwick, R. S. (2000). A ROSAT High Resolution Imager survey of bright nearby galaxies. *MNRAS*, 315(1):98–114. 1.1, 2.1

Rodríguez Castillo, G. A., Israel, G. L., Belfiore, A., Bernardini, F., Esposito, P., Pintore, F., De Luca, A., Papitto, A., Stella, L., Tiengo, A., Zampieri, L., Bachetti, M., Brightman, M., Casella, P., D'Agostino, D., Dall'Osso, S., Earnshaw, H. P., Fürst, F., Haberl, F., Harrison, F. A., Mapelli, M., Marelli, M., Middleton, M., Pinto, C., Roberts, T. P., Salvaterra, R., Turolla, R., Walton, D. J., and Wolter, A. (2020). Discovery of a 2.8 s Pulsar in a 2 Day Orbit High-mass X-Ray Binary Powering the Ultraluminous X-Ray Source ULX-7 in M51. *Astrophysical Journal*, 895(1):60. 1.4.2, 2.5.3, 2.5.4, 3.1, 5.1

Russell, D. G. (2002). The H I Line Width/Linear Diameter Relationship as an Independent Test of the Hubble Constant. *ApJ*, 565(2):681–695. 2.4

Sathyaprakash, R., Roberts, T. P., and Siwek, M. M. (2019a). Observational limits on the X-ray emission from the bubble nebula surrounding Ho IX X-1. *MNRAS*, 488(4):4614–4622. 4.7

Sathyaprakash, R., Roberts, T. P., Walton, D. J., Fuerst, F., Bachetti, M., Pinto, C., Alston, W. N., Earnshaw, H. P., Fabian, A. C., Middleton, M. J., and Soria, R. (2019b). The discovery of weak coherent pulsations in the ultraluminous X-ray source NGC 1313 X-2. *MNRAS*, 488(1):L35–L40. 1.4.2, 1.15, 2.5.4, 3.1, 4.7, 5.1

Schwarzschild, K. (1916). Über das Gravitationsfeld eines Massenpunktes nach der Einsteinschen Theorie. *Sitzungsberichte der Königlich Preussischen Akademie der Wissenschaften*, pages 189–196. 1.3.2

Servillat, M., Farrell, S. A., Lin, D., Godet, O., Barret, D., and Webb, N. A. (2011). X-Ray Variability and Hardness of ESO 243-49 HLX-1: Clear Evidence for Spectral State Transitions. *ApJ*, 743(1):6. 1.4.2, 3.1, 3.4, 3.6

Shakura, N. I. and Sunyaev, R. A. (1973). Black holes in binary systems. Observational appearance. *A&A*, 24:337–355. 1.4.2, 1.4.2, 2.5.2, 4.4.1

Shapiro, S. L. and Teukolsky, S. A. (1983). *Black holes, white dwarfs and neutron stars. The physics of compact objects*. 1.3.2

Shu, Y., Koposov, S. E., Evans, N. W., Belokurov, V., McMahon, R. G., Auger, M. W., and Lemon, C. A. (2019). Catalogues of active galactic nuclei from Gaia and unWISE data. *MNRAS*, 489(4):4741–4759. 2.3.1, 3.2

Smith, J. F. and Courtier, G. M. (1976). The Ariel 5 Programme. *Proceedings of the Royal Society of London Series A*, 350(1663):421–439. 1.1

Song, X., Walton, D. J., Lansbury, G. B., Evans, P. A., Fabian, A. C., Earnshaw, H., and Roberts, T. P. (2020). The hunt for pulsating ultraluminous X-ray sources. *MNRAS*, 491(1):1260–1277. 2.3.1

Soria, R., Kuntz, K. D., Winkler, P. F., Blair, W. P., Long, K. S., Plucinsky, P. P., and Whitmore, B. C. (2012). The Birth of an Ultraluminous X-Ray Source in M83. *ApJ*, 750(2):152. 2.3.1

Stobbart, A. M., Roberts, T. P., and Wilms, J. (2006). XMM-Newton observations of the brightest ultraluminous X-ray sources. *MNRAS*, 368(1):397–413. 1.4.2, 2.4.2, 2.5.2, 2.5.4, 4.4.1

Strohmayer, T. E. and Mushotzky, R. F. (2009). Evidence for an Intermediate-mass Black Hole in NGC 5408 X-1. *ApJ*, 703(2):1386–1393. 1.4.2

Strüder, L., Briel, U., Dennerl, K., Hartmann, R., Kendziorra, E., Meidinger, N., Pfeffermann, E., Reppin, C., Aschenbach, B., Bornemann, W., Bräuninger, H., Burkert, W., Elender, M., Freyberg, M., Haberl, F., Hartner, G., Heuschmann, F., Hippmann, H., Kastelic, E., Kemmer, S., Kettenring, G., Kink, W., Krause, N., Müller, S., Oppitz, A., Pietsch, W., Popp, M., Predehl, P., Read, A., Stephan, K. H., Stötter, D., Trümper, J., Holl, P., Kemmer, J., Soltau, H., Stötter, R., Weber, U., Weichert, U., von Zanthier, C., Carathanassis, D., Lutz, G., Richter, R. H., Solc, P., Böttcher, H., Kuster, M., Staubert, R., Abbey, A., Holland, A., Turner, M., Balasini, M., Bignami, G. F., La Palombara, N., Villa, G., Buttler, W., Gianini, F., Lainé, R., Lumb, D., and Dhez, P. (2001). The European Photon Imaging Camera on XMM-Newton: The pn-CCD camera. *A&A*, 365:L18–L26. 1.2.2, 2.3.2.1

Sunyaev, R. A. and Titarchuk, L. G. (1980). Comptonization of X-Rays in Plasma Clouds - Typical Radiation Spectra. *A&A*, 86:121. 1.3.3

Sunyaev, R. A. and Truemper, J. (1979). Hard X-ray spectrum of CYG X-1. *Nat*, 279:506–508. 1.3.3

Sutton, A. D., Roberts, T. P., Gladstone, J. C., Farrell, S. A., Reilly, E., Goad, M. R., and Gehrels, N. (2013a). A bright ultraluminous X-ray source in NGC 5907. *MNRAS*, 434(2):1702–1712. 3.1

Sutton, A. D., Roberts, T. P., Gladstone, J. C., and Walton, D. J. (2015). The hyperluminous X-ray source candidate in IC 4320: another HLX bites the dust. *MNRAS*, 450(1):787–793. 2.3.3, 3.1

Sutton, A. D., Roberts, T. P., and Middleton, M. J. (2013b). The ultraluminous state revisited: fractional variability and spectral shape as diagnostics of super-Eddington accretion. *MNRAS*, 435(2):1758–1775. 3.4

Sutton, A. D., Roberts, T. P., and Walton, D. J. (2011). Key results from an XMM-Newton and Chandra study of a new sample of extreme ULXs from the 2XMM catalogue. *Astronomische Nachrichten*, 332(4):362. 4.1

Sutton, A. D., Roberts, T. P., Walton, D. J., Gladstone, J. C., and Scott, A. E. (2012). The most extreme ultraluminous X-ray sources: evidence for intermediate-mass black holes? *MNRAS*, 423(2):1154–1177. 2.3.3, 2.4.2, 5.1

Swartz, D. A., Ghosh, K. K., Tennant, A. F., and Wu, K. (2004). The Ultraluminous X-Ray Source Population from the Chandra Archive of Galaxies. *ApJS*, 154(2):519–539. 2.1, 2.3

Swartz, D. A., Soria, R., Tennant, A. F., and Yukita, M. (2011). A Complete Sample of Ultraluminous X-ray Source Host Galaxies. *ApJ*, 741(1):49. 2.3.1, 2.4.1, 2.3

Swartz, D. A., Tennant, A. F., and Soria, R. (2009). Ultraluminous X-Ray Source Correlations with Star-Forming Regions. *ApJ*, 703(1):159–168. 2.4

Tao, L., Feng, H., Grisé, F., and Kaaret, P. (2011). Compact Optical Counterparts of Ultraluminous X-Ray Sources. *ApJ*, 737(2):81. 1.4.3

Tauris, T. M. and van den Heuvel, E. P. J. (2006). Formation and evolution of compact stellar X-ray sources. In *Compact stellar X-ray sources*, volume 39, pages 623–665. 1.3.3

Theureau, G., Hanski, M. O., Coudreau, N., Hallet, N., and Martin, J. M. (2007). Kinematics of the Local Universe. XIII. 21-cm line measurements of 452 galaxies with the Nançay radiotelescope, JHK Tully-Fisher relation, and preliminary maps of the peculiar velocity field. *A&A*, 465(1):71–85. 2.4

Tranin, H., Godet, O., Webb, N., and Primorac, D. (2022). Probabilistic classification of X-ray sources applied to Swift-XRT and XMM-Newton catalogs. *A&A*, 657:A138. 2.7.2, 5.1

Tranin, H., Webb, N., Godet, O., and Quintin, E. (2024). Statistical study of a large and cleaned sample of ultraluminous and hyperluminous X-ray sources. *A&A*, 681:A16. (document), 1.5, 2, 2.7, 2.7.1, 2.7.2, 2.6, 2.7.2, 2.7.3, 2.8, 2.9, 2.7, 3.1, 3, 3.2, 5.1

Truemper, J. (1982). The ROSAT mission. *Advances in Space Research*, 2(4):241–249. 1.1

Tsygankov, S. S., Mushtukov, A. A., Suleimanov, V. F., and Poutanen, J. (2016). Propeller effect in action in the ultraluminous accreting magnetar M82 X-2. *MNRAS*, 457(1):1101–1106. 2.3.1, 4.7

Tully, R. B., Courtois, H. M., and Sorce, J. G. (2016). Cosmicflows-3. *AJ*, 152(2):50. 2.2, 2.5

Turner, M. J. L., Abbey, A., Arnaud, M., Balasini, M., Barbera, M., Belsole, E., Bennie, P. J., Bernard, J. P., Bignami, G. F., Boer, M., Briel, U., Butler, I., Cara, C., Chabaud, C., Cole, R., Collura, A., Conte, M., Cros, A., Denby, M., Dhez, P., Di Coco, G., Dowson, J., Ferrando, P., Ghizzardi, S., Gianotti, F., Goodall, C. V., Gretton, L., Griffiths, R. G., Hainaut, O., Hochedez, J. F., Holland, A. D., Jourdain, E., Kendziorra, E., Lagostina, A., Laine, R., La Palombara, N., Lortholary, M., Lumb, D., Marty, P., Molendi, S., Pigot, C., Poindron, E., Pounds, K. A., Reeves, J. N., Reppin, C., Rothenflug, R., Salvetat, P., Sauvageot, J. L.,

Schmitt, D., Sembay, S., Short, A. D. T., Spragg, J., Stephen, J., Strüder, L., Tiengo, A., Trifoglio, M., Trümper, J., Vercellone, S., Vigroux, L., Villa, G., Ward, M. J., Whitehead, S., and Zonca, E. (2001). The European Photon Imaging Camera on XMM-Newton: The MOS cameras. *A&A*, 365:L27–L35. 1.2.2, 2.3.2.1

Urquhart, R. and Soria, R. (2016). Optically thick outflows in ultraluminous supersoft sources. *MNRAS*, 456(2):1859–1880. 3.6

Urquhart, R., Soria, R., Johnston, H. M., Pakull, M. W., Motch, C., Schwope, A., Miller-Jones, J. C. A., and Anderson, G. E. (2018). Multiband counterparts of two eclipsing ultraluminous X-ray sources in M 51. *MNRAS*, 475(3):3561–3576. 1.4.3

van der Klis, M. (1994). Similarities in Neutron Star and Black Hole Accretion. *ApJS*, 92:511. 1.11

van Haaften, L. M., Maccarone, T. J., Rhode, K. L., Kundu, A., and Zepf, S. E. (2019). Discovery of a transient ultraluminous X-ray source in the elliptical galaxy M86. *MNRAS*, 483(3):3566–3573. 2.3.1

Vasilopoulos, G., Haberl, F., Carpano, S., and Maitra, C. (2018). NGC 300 ULX1: A test case for accretion torque theory. *A&A*, 620:L12. 2.4.1, 2.5.3

Vasilopoulos, G., Petropoulou, M., Koliopanos, F., Ray, P. S., Bailyn, C. B., Haberl, F., and Gendreau, K. (2019). NGC 300 ULX1: spin evolution, super-Eddington accretion, and outflows. *MNRAS*, 488(4):5225–5231. 2.4.1

Verner, D. A., Ferland, G. J., Korista, K. T., and Yakovlev, D. G. (1996). Atomic Data for Astrophysics. II. New Analytic FITS for Photoionization Cross Sections of Atoms and Ions. *ApJ*, 465:487. 2.5.2

Véron-Cetty, M. P. and Véron, P. (2010). A catalogue of quasars and active nuclei: 13th edition. *A&A*, 518:A10. 2.3.1, 3.2

Voges, W., Aschenbach, B., Boller, T., Bräuninger, H., Briel, U., Burkert, W., Dennerl, K., Englhauser, J., Gruber, R., Haberl, F., Hartner, G., Hasinger, G., Kürster, M., Pfeffermann, E., Pietsch, W., Predehl, P., Rosso, C., Schmitt, J. H. M. M., Trümper, J., and Zimmermann, H. U. (1999). The ROSAT all-sky survey bright source catalogue. *A&A*, 349:389–405. 1.3

Walton, D. J., Bachetti, M., Fürst, F., Barret, D., Brightman, M., Fabian, A. C., Grefenstette, B. W., Harrison, F. A., Heida, M., Kennea, J., Kosec, P., Lau, R. M., Madsen, K. K., Middleton, M. J., Pinto, C., Steiner, J. F., and Webb, N. (2018a). A Potential Cyclotron Resonant Scattering Feature in the Ultraluminous X-Ray Source Pulsar NGC 300 ULX1 Seen by NuSTAR and XMM-Newton. *ApJ*, 857(1):L3. 2.4.1

Walton, D. J., Fuerst, F., Harrison, F., Stern, D., Bachetti, M., Barret, D., Bauer, F., Boggs, S. E., Christensen, F. E., Craig, W. W., Fabian, A. C., Grefenstette, B. W., Hailey, C. J., Madsen, K. K., Miller, J. M., Ptak, A., Rana, V., Webb, N. A.,

and Zhang, W. W. (2013). An Extremely Luminous and Variable Ultraluminous X-Ray Source in the Outskirts of Circinus Observed with NuSTAR. *ApJ*, 779(2):148. 1.4.2

Walton, D. J., Fürst, F., Bachetti, M., Barret, D., Brightman, M., Fabian, A. C., Gehrels, N., Harrison, F. A., Heida, M., Middleton, M. J., Rana, V., Roberts, T. P., Stern, D., Tao, L., and Webb, N. (2016a). A 78 Day X-Ray Period Detected from NGC 5907 ULX1 by Swift. *ApJ*, 827(1):L13. 3.1, 3.6

Walton, D. J., Fürst, F., Heida, M., Harrison, F. A., Barret, D., Stern, D., Bachetti, M., Brightman, M., Fabian, A. C., and Middleton, M. J. (2018b). Evidence for Pulsar-like Emission Components in the Broadband ULX Sample. *ApJ*, 856(2):128. 1.4.2, 4, 2.5.4

Walton, D. J., Gladstone, J. C., Roberts, T. P., Fabian, A. C., Caballero-Garcia, M. D., Done, C., and Middleton, M. J. (2011a). Comparing spectral models for ultraluminous X-ray sources with NGC 4517 ULX1. *MNRAS*, 414(2):1011–1022. 2.5.2, 2.5.4

Walton, D. J., Harrison, F. A., Grefenstette, B. W., Miller, J. M., Bachetti, M., Barret, D., Boggs, S. E., Christensen, F. E., Craig, W. W., Fabian, A. C., Fuerst, F., Hailey, C. J., Madsen, K. K., Parker, M. L., Ptak, A., Rana, V., Stern, D., Webb, N., and Zhang, W. W. (2014). Broadband X-Ray Spectra of the Ultraluminous X-Ray Source Holmberg IX X-1 Observed with NuSTAR, XMM-Newton, and Suzaku. *ApJ*, 793(1):21. 1.4.2, 2.5.2, 2.5.4

Walton, D. J., Heida, M., Bachetti, M., Fürst, F., Brightman, M., Earnshaw, H., Evans, P. A., Fabian, A. C., Grefenstette, B. W., Harrison, F. A., Israel, G. L., Lansbury, G. B., Middleton, M. J., Pike, S., Rana, V., Roberts, T. P., Rodriguez Castillo, G. A., Salvaterra, R., Song, X., and Stern, D. (2021). A new transient ultraluminous X-ray source in NGC 7090. *MNRAS*, 501(1):1002–1012. 2.3.1, 2.5.3

Walton, D. J., Mackenzie, A. D. A., Gully, H., Patel, N. R., Roberts, T. P., Earnshaw, H. P., and Mateos, S. (2022). A multimission catalogue of ultraluminous X-ray source candidates. *MNRAS*, 509(2):1587–1604. (document), 2, 2.7.2, 2.6, 2.7.2, 2.7.3, 2.8, 2.9, 2.7, 3, 3.1, 3.2, 3.3, 3.1, 3.2, 3.5.2.1, 3.5, 3.6, 3.5.2.2, 3.7, 5.1

Walton, D. J., Middleton, M. J., Pinto, C., Fabian, A. C., Bachetti, M., Barret, D., Brightman, M., Fuerst, F., Harrison, F. A., Miller, J. M., and Stern, D. (2016b). An Iron K Component to the Ultrafast Outflow in NGC 1313 X-1. *ApJ*, 826(2):L26. 1.4.2, 2.5.4

Walton, D. J., Middleton, M. J., Rana, V., Miller, J. M., Harrison, F. A., Fabian, A. C., Bachetti, M., Barret, D., Boggs, S. E., Christensen, F. E., Craig, W. W., Fuerst, F., Grefenstette, B. W., Hailey, C. J., Madsen, K. K., Stern, D., and Zhang, W. (2015). NuSTAR, XMM-Newton, and Suzaku Observations of the Ultraluminous X-Ray Source Holmberg II X-1. *ApJ*, 806(1):65. 1.4.2, 2.5.4

Walton, D. J., Roberts, T. P., Mateos, S., and Heard, V. (2011b). 2XMM ultra-luminous X-ray source candidates in nearby galaxies. *MNRAS*, 416(3):1844–1861. 2.1, 2.2, 2.3.2.1, 2.4.2, 2.3, 2.7.1, 2.7.2, 2.7.3, 3.2, 5.1

Wang, S., Qiu, Y., Liu, J., and Bregman, J. N. (2016). Chandra ACIS Survey of X-Ray Point Sources in Nearby Galaxies. II. X-Ray Luminosity Functions and Ultraluminous X-Ray Sources. *ApJ*, 829(1):20. 2.4.1

Webb, N., Cseh, D., Lenc, E., Godet, O., Barret, D., Corbel, S., Farrell, S., Fender, R., Gehrels, N., and Heywood, I. (2012). Radio Detections During Two State Transitions of the Intermediate-Mass Black Hole HLX-1. *Science*, 337(6094):554. 1.4.2, 3.1, 3.6

Webb, N. A., Barret, D., Godet, O., Gupta, M., Lin, D., Quintin, E., and Tranin, H. (2023). Tidal disruption events and quasi-periodic eruptions. *Astronomische Nachrichten*, 344(4):e20230051. 3.1

Webb, N. A., Coriat, M., Traulsen, I., Ballet, J., Motch, C., Carrera, F. J., Koliopanos, F., Authier, J., de la Calle, I., Ceballos, M. T., Colomo, E., Chuard, D., Freyberg, M., Garcia, T., Kolehmainen, M., Lamer, G., Lin, D., Maggi, P., Michel, L., Page, C. G., Page, M. J., Perea-Calderon, J. V., Pineau, F. X., Rodriguez, P., Rosen, S. R., Santos Lleo, M., Saxton, R. D., Schwope, A., Tomás, L., Watson, M. G., and Zakardjian, A. (2020). The XMM-Newton serendipitous survey. IX. The fourth XMM-Newton serendipitous source catalogue. *Astronomy and Astrophysics*, 641:A136. 2.1, 2.3.2.1, 2.4.2, 2.7.1

Webb, N. A., Godet, O., Wiersema, K., Lasota, J. P., Barret, D., Farrell, S. A., Maccarone, T. J., and Servillat, M. (2014). Optical Variability of the Accretion Disk around the Intermediate-mass Black Hole ESO 243-49 HLX-1 during the 2012 Outburst. *ApJ*, 780(1):L9. 3.1

Weissenborn, S., Sagert, I., Pagliara, G., Hempel, M., and Schaffner-Bielich, J. (2011). Quark Matter in Massive Compact Stars. *ApJ*, 740(1):L14. 1.3.2

Weisskopf, M. C., Brinkman, B., Canizares, C., Garmire, G., Murray, S., and Van Speybroeck, L. P. (2002). An Overview of the Performance and Scientific Results from the Chandra X-Ray Observatory. *PASP*, 114(791):1–24. 1.2, 2.1

White, N. E., Nagase, F., and Parmar, A. N. (1995). The properties of X-ray binaries. In *X-ray Binaries*, pages 1–57. 1.3.3

Willingale, R., Starling, R. L. C., Beardmore, A. P., Tanvir, N. R., and O'Brien, P. T. (2013). Calibration of X-ray absorption in our Galaxy. *MNRAS*, 431(1):394–404. 3.5.1.1, 4.4.1

Wilms, J., Allen, A., and McCray, R. (2000a). On the Absorption of X-Rays in the Interstellar Medium. *ApJ*, 542(2):914–924. 2.5.2

Wilms, J., Allen, A., and McCray, R. (2000b). On the Absorption of X-Rays in the Interstellar Medium. *ApJ*, 542(2):914–924. 3.5.1.1, 4.4.1

Witten, E. (1984). Cosmic separation of phases. , 30(2):272–285. 1.3.2

Wood, K. S., Meekins, J. F., Yentis, D. J., Smathers, H. W., McNutt, D. P., Bleach, R. D., Byram, E. T., Chupp, T. A., Friedman, H., and Meidav, M. (1984). The HEAO A-1 X-ray source catalog. *ApJS*, 56:507–649. 1.1, 1.2

XRISM Science Team (2020). Science with the X-ray Imaging and Spectroscopy Mission (XRISM). *arXiv e-prints*, page arXiv:2003.04962. 2.1

Yan, Z. and Yu, W. (2017). A new outburst of ESO 243-49 HLX-1 after being in quiescence for two years. *The Astronomer's Telegram*, 10289:1. 3.1

Zhang, W. M., Soria, R., Zhang, S. N., Swartz, D. A., and Liu, J. F. (2009). A Census of X-ray Nuclear Activity in Nearby Galaxies. *ApJ*, 699(1):281–297. 2.3.1

Zolotukhin, I., Webb, N. A., Godet, O., Bachetti, M., and Barret, D. (2016). A Search for Hyperluminous X-Ray Sources in the XMM-Newton Source Catalog. *ApJ*, 817(2):88. 3.1

Zombeck, M. V., Chappell, J. H., Kenter, A. T., Moore, R. W., Murray, S. S., Fraser, G. W., and Serio, S. (1995). High-resolution camera (HRC) on the Advanced X-Ray Astrophysics Facility (AXAF). In Siegmund, O. H. and Vallerga, J. V., editors, *EUV, X-Ray, and Gamma-Ray Instrumentation for Astronomy VI*, volume 2518 of *Society of Photo-Optical Instrumentation Engineers (SPIE) Conference Series*, pages 96–106. 2.3.2.3